

# **Turbulent Flow Structures Induced by an Engine Intake Port**

## **Dissertation**

zur Erlangung des akademischen Grades

**Doktoringenieur  
(Dr.-Ing.)**

von: Dipl.-Ing. Olivier Imberdis

geb. am: 28.12.1979

in: Verdun, Frankreich

genehmigt durch die Fakultät für Verfahrens- und Systemtechnik  
der Otto-von-Guericke-Universität Magdeburg

Gutachter: Prof. Dr. Eckehard Specht

Prof. Dr. Dominique Thévenin

Prof. Dr. Johannes Janicka

eingereicht am: 13. Januar 2009

Promotionskolloquium am: 19. Oktober 2009







## **Schriftliche Erklärung**

Ich erkläre hiermit, dass ich die vorliegende Arbeit ohne unzulässige Hilfe Dritter und ohne Benutzung anderer als der angegebenen Hilfsmittel angefertigt habe. Die aus fremden Quellen direkt oder indirekt übernommenen Gedanken sind als solche kenntlich gemacht.

Insbesondere habe ich nicht die Hilfe einer kommerziellen Promotionsberatung in Anspruch genommen. Dritte haben von mir weder unmittelbar noch mittelbar geldwerte Leistungen für Arbeiten erhalten, die im Zusammenhang mit dem Inhalt der vorgelegten Dissertation stehen.

Die Arbeit wurde bisher weder im Inland noch im Ausland in gleicher oder ähnlicher Form als Dissertation eingereicht und ist als Ganzes auch noch nicht veröffentlicht.

Paris, 6. Januar 2009



## **Disclaimer**

Publications about the content of this work require the written consent of Volkswagen AG. The results, opinions and conclusions expressed in this work are not necessarily those of Volkswagen AG.





## Acknowledgements

The present thesis arose from my activity as PhD student within the Volkswagen AG Corporate Research Centre in Wolfsburg, Germany, and more particularly in the department for Vehicle Concepts and Computer Aided Engineering methods. This work has been granted by a Marie Curie Fellow in the framework of the Industry Host Fellowship Program financed by the European Commission, a support that I gratefully acknowledge.

I would like to express my sincere gratitude to Dr. Markus Lienkamp, Mr. Oliver Schroeter and Dr. Henry Bensler for their confidence and efforts all along the three and a half year spent in their research department, who offered me the chance to conduct this study in the best conditions.

A particular thank goes to my mentor Professor Dominique Thévenin for his guidance and encouragement throughout this work and his patience during the preparation of this thesis.

The experimental expertise of Dr. Werner Hentschel and his team, as well as Mr. Lars Kapitza, who shared with me their large know-how, their contacts and even their technical facilities for optical measurements, is gratefully acknowledged.

From the numerical side, I would like to sincerely thank the colleagues from the VW CFD team for their intensive support and friendliness, Dr. Axel Winkler, Dr. Maite Abad-Lozano, Mr. Uwe Reisch, without forgetting those who have migrated to Audi, Mr. Diego Lehmann and Mr. Gordon Roettger.

Before closing this chapter, I have to express my deepest gratitude and respect for a person towards which I am greatly indebted, for his large contribution to this research work, his innumerable technical and scientific advices, my supervisor Dr. Michael Hartmann. The time spent by my side and his continuous support, have offered me the chance to give to this work another dimension.

Finally, I feel the urge to remember the endless patience, understanding and encouragement of my family and my friends, who always found the right words to support me, especially during the final phase of this work.



# Zusammenfassung

Unter den letzten Technologien vorhanden hat die Benzin-Direkteinspritzung (BDE) neue Perspektiven für Fremdzündungsmotoren, um wettbewerbsfähig zu bleiben durch Erfüllen der Anforderungen bezüglich  $\text{CO}_2$ -Emissionen, geöffnet, während der Leistung, dank verbesserter Kraftstoffeffizienz, hoch aufrechterhalten ist. Allerdings dieses Brennverfahren und insbesondere geschichtete BDE-Motoren sind mit verschiedenen Problemen wie zyklischen Schwankungen konfrontiert.

Im Rahmen dieser Doktorarbeit, die turbulente Luftströmung, die von einem Saugkanal eines FSI-Motor (Fuel Stratified Injection) indiziert ist, war durch die neuesten numerische und experimentelle Verfahren ausführlich untersucht. Um die instationäre Phänomene, die mit der Luft-Kraftstoff Mischung, und infolgedessen, mit der Stabilität der Verbrennung verbunden sind, besser zu verstehen, sind 3-D CFD Analyse, auf feinere numerische Gitter basiert, angewendet. Ein Vergleich zwischen statistische Formulierung (RANS und URANS), eine innovative URANS-abgeleitete Methode, Scale Adaptive Simulation (SAS), und eine hybride Grobstruktursimulation, Detached Eddy Simulation (DES), war durchgeführt. Hoch aufgelöste Laser-Messungen mittels Stereo-PIV (Particle Image Velocimetry) konnten in einen stationären Drall Optische Prüfstand Informationen über die turbulente Strömung mit einer hohen Aufnahmefrequenz (bis zum 20 kHz Pulse-Rate) liefern. Der Hauptfokus dieser Studie ist auf die hohe Zeitauflösung der Meßdaten, sowie die feine Räumliche-Auflösung der numerischen Gittern zur CFD-Berechnung gelegt.

Obwohl eine gute Übereinstimmung zwischen experimentelle und numerische Ergebnisse für gemittelte globale Variablen gefunden war, die Analyse von instationäre Daten hat mehrere Aspekte hervorgehoben. Sowohl die Qualität von hoch-aufgelösten optische Messungen einer turbulente In-Zylinder-Strömung in realistischen Bedingungen, als auch die Bearbeitung von umfangreichen 3-D CFD generierten Datenbanken, eine große Herausforderung bedeuten. Allerdings, diese Arbeit hat sich an der sorgfältigen Ausführung eines Auswertungsverfahrens ausgerichtet, um die turbulente Phänomene, die in Saugkanal-Strömungen indiziert sind, besser zu Visualisieren und Quantifizieren.

Mit dem Ziel, den physikalischen Ursprung der gelösten Wirbeln zu verfolgen, sind die ausführliche Spektralanalyse von verschiedenen Outputs, die rohen Geschwindigkeiten von einer Seite und den resultierenden Zeitkoeffizienten der POD-Zerlegung auf der anderen Seite, geführt worden, um die charakteristischen Frequenzen or Modi zu erkennen, die zu den Strömungsfluktuationen beitragen. Die Rekonstruktion des mit diesem Frequenzen gefilterten Strömungsfeldes erlaubte, die Quelle der Störung zu bestimmen und eine Korrelation zwischen diesen Wirkungen und der Motorgeometrie zu bilden.

Schließlich ist eine quantitative Methode vorgeschlagen worden, um einen besseren Einblick in die turbulenten Strukturen zu liefern, die sich innerhalb des Zylinders entwickeln. Die umfassende Statistik, die sich aus der Untersuchung der zweiten Invariant des Geschwindigkeitsgradiententensor ergibt, ebenso wie des vollständigen Mapping der Wirbel-Größe-Verteilung in verschiedenen Zylinderabschnitten, bereitstellen eine wertvolle Datenbank für Vergleichstudien zwischen numerischen Modellen und experimentellen Ergebnisse. Diese Auswertungsverfahren bietet eine innovative und effiziente Weise an, das Turbulenz-Niveau veranlasst durch jede Motorgeometrie zu charakterisieren, aber konnte auch zahlreich andere Anwendungen finden, wo turbulente Strömungen dominieren. Bezüglich der erste Anwendung der SAS Turbulenz Modell für In-Zylinder Strömungen, es ist aufgezeigt worden, dass die Benutzung dieses auf einer modifizierten URANS-Formulierung gegründeten Modells eine vielversprechende Alternative zu dem LES-abgeleitenden Modell wie DES bereitstellt.



## Abstract

Amongst the latest technologies available, gasoline direct injection (DI) has opened new perspectives for spark ignition (SI) engines to remain competitive by complying with the CO<sub>2</sub> emission legislations while maintaining high power output thanks to significant improvements in fuel efficiency. However, this injection technique and especially the stratified DISI engines are facing several issues such as the problem of combustion variability from cycle to cycle.

In the framework of this PhD thesis, the turbulent cold airflow induced by the intake port of a production FSI<sup>®</sup> - Fuel Stratified Injection - engine has been intensively investigated thanks to the latest numerical and experimental techniques. In order to better understand the unsteady phenomena associated to air-fuel mixing, influencing the general combustion process and then leading to engine cyclic variations, 3-D CFD analysis was performed for the steady-state flow using standard and advanced turbulence modeling on high resolution numerical meshes. A comparison of statistical formulations (RANS and URANS), an innovative URANS derivative methodology called Scale Adaptive Simulation (SAS) and a hybrid Large Eddy Simulation (LES) method (Detached Eddy Simulation – DES) was carried out. A stationary Tumble Optical Rig (TOR) was used to conduct stereoscopic high speed Particle Image Velocimetry (PIV) measurements of the turbulent flow up to a repetition rate of 20 kHz, corresponding to an effective frequency of 10 kHz for the correlated velocity fields. Thus, the main focus of the work has been put on the high time-resolution of the measured data, as well as on the strong refinement of the numerical mesh and models employed.

Although a good agreement has been found between experimental and numerical results for global averaged variables, the analysis of unsteady data has highlighted several aspects. First of all, highly resolved optical measurements of a turbulent in-cylinder flow in a realistic configuration and secondly the issue of handling the massive database generated by the unsteady CFD simulations are still representing real challenges. However, based on this important set of data, the present work focuses on the elaboration of a general post-processing method in order to facilitate the visualization and the quantification of the turbulent phenomena occurring in engine-port induced flows.

With the objective of tracking the physical origin of the vortices developing in the geometry, the detailed spectral analysis of different outputs, the raw velocities from one side and the time coefficients resulting from a Proper Orthogonal Decomposition on the other side, have been conducted in order to reveal the characteristic frequencies or modes contributing to the flow fluctuations. The reconstruction of the flow field filtered with these frequencies allowed to determine the source of the disturbance and to establish a correlation between these effects and the engine geometry.

Finally, a quantitative method has been proposed to supply a better insight into the turbulent structures evolving within the cylinder. The extensive statistics resulting from the investigation of the second invariant of the velocity gradient tensor as well as the complete mapping of eddy size distribution in various cylinder sections are providing a valuable database for comparative studies between numerical models and experimental results. This post-processing method suggests an innovative and efficient way of characterizing the turbulence level induced by any engine geometry, but could also find numerous other applications where turbulent flows are dominating.

Regarding the first application of the SAS turbulence model for in-cylinder flows, it has been demonstrated that the utilization of this model based on a modified URANS formulation provides a promising alternative to the LES derivative models such as DES.



# Table of Contents

Figures Index .....	III
Tables Index .....	VIII
Nomenclature .....	IX
<b>1 Introduction .....</b>	<b>1</b>
1.1 General.....	1
1.2 Rationales for Current Study.....	1
1.3 Literature Survey .....	2
1.4 Scope of the Work .....	5
<b>2 DISI-Engine In-cylinder Flow.....</b>	<b>7</b>
2.1 Direct Injection and Stratified Combustion in Gasoline Engines .....	7
2.1.1 Operating Modes Description.....	7
2.1.2 Combustion Concept and Charge Motion.....	8
2.1.3 The Volkswagen FSI® Engine.....	10
2.2 Engine Cycle-to-Cycle Variations .....	11
2.2.1 Origins of the Engine Cyclic Variations (ECV) .....	12
2.2.2 Effects of In-Cylinder Flows and Role of Turbulence.....	12
2.3 Outlook for the Current Analysis.....	13
<b>3 Turbulent Flows in Internal Combustion Engines: Description, Modelling &amp; Visualization.....</b>	<b>15</b>
3.1 Description of Turbulence.....	15
3.1.1 Spectral Definition of Turbulent Flows.....	15
3.1.2 Moments Measure of Velocities Distributions .....	17
3.2 Numerical Models and Issues.....	19
3.2.1 Direct Numerical Simulation (DNS).....	20
3.2.2 Statistical Models: Reynolds Averaged Navier-Stokes (RANS) .....	21
3.2.3 Large Eddy Simulation (LES) .....	26
3.2.4 A Hybrid Approach: Detached Eddy Simulation (DES).....	28
3.2.5 An Alternative: Scale Adaptive Simulation (SAS) .....	31
3.3 Selective Visualization of Turbulent Flows .....	33
3.3.1 Coherent Structures .....	33
3.3.2 Flow Pattern Extraction Techniques .....	34
<b>4 Scope of Investigation &amp; Preliminary Studies .....</b>	<b>43</b>
4.1 Research Strategy.....	43
4.2 Tumble-Flap Model .....	44
4.2.1 Presentation of the Geometry.....	45

4.2.2	Zonal Treatment of the DES Model .....	46
4.2.3	Mesh Sensitivity Analysis .....	48
4.3	Simplified Intake-Port Section Model.....	54
4.3.1	Port Model Presentation and Experimental Setup .....	54
4.3.2	Flow Fields Comparison .....	54
4.3.3	Detailed Boundary-Layer and Flow-Detachment Analysis .....	56
4.4	Cylinder-Head Model Without Tumble-Flap.....	61
4.4.1	High-Speed Particle Image Velocimetry (HS-PIV).....	61
4.4.2	Optical Test-Bench Description and Intake-Port Model Presentation .....	62
4.4.3	Comparison Between HS-PIV and DES Results.....	64
4.4.4	2D and 3D Flow Visualization .....	68
<b>5</b>	<b>Analysis of a Production FSI<sup>®</sup> Cylinder-Head.....</b>	<b>73</b>
5.1	Optimized Design of the Steady-State Optical Test-Bench .....	73
5.2	Experimental Setup.....	74
5.2.1	Stereoscopic HS-PIV.....	74
5.2.2	Constant Temperature Anemometry .....	76
5.3	Numerical Simulation .....	79
5.3.1	Meshing Strategy and Sensitivity Analysis .....	79
5.3.2	Data Management and Post-Processing Mesh .....	83
5.4	Averaged Results Comparison .....	84
5.5	Unsteady Results Analysis.....	88
5.5.1	Spectral Analysis.....	88
5.5.2	Comparison with HS-PIV Results.....	93
5.6	POD of Experimental and Numerical Results .....	94
5.6.1	Analysis of the Post-Processing Window Size Influence.....	94
5.6.2	Influence of the Energy Truncation Level.....	99
5.6.3	Analysis of the Time Coefficients Spectra .....	100
5.6.4	Comparison with HS-PIV data.....	106
5.6.5	POD Modes Sizes.....	111
5.7	Visualization of Turbulent Structures .....	122
5.7.1	3-D Visualization .....	122
5.7.2	Turbulence Models Comparison .....	122
5.7.3	2-D Visualization and Quantification of the Turbulent Structures.....	124
<b>6</b>	<b>Summary &amp; Conclusions .....</b>	<b>135</b>
	<b>Bibliography.....</b>	<b>139</b>
	<b>Appendix.....</b>	<b>149</b>
A.1	Sequence of instantaneous PIV acquisitions (§5.5).....	149
A-2	Spectral Analysis of the FSI <sup>®</sup> Intake-Port Induced Turbulent Flow (§5.6.5).....	150
	<b>Lebenslauf.....</b>	<b>157</b>



## Figures Index

Figure 2.1: Operation map of DI gasoline engines.....	7
Figure 2.2: Schematic of the air motion in cylinder. a/ swirl flow, b/ tumble flow (reprinted from [140])...	9
Figure 2.3: Different combustion concepts for DISI engines - 1: spark plug, 2: injector nozzle [20]. ....	9
Figure 2.4: Combustion concept of the Volkswagen FSI® engine [61].....	10
Figure 2.5: Schematic influence of the tumble control flap position on the in-cylinder air-flow pattern.....	11
Figure 3.1: Energy spectrum for homogeneous isotropic turbulence. ....	15
Figure 3.2: Two-layer model for turbulent boundary layers.....	24
Figure 3.3: Velocity profile of a turbulent boundary layer (reprinted from [127]).....	24
Figure 3.4: Blending functions for the SST model as a function of the non-dimension wall distance $y/\delta$ (left: $F_1$ , right: $F_2$ ) (reprinted from [95]).....	30
Figure 3.5: Left / Schematic of a mixing layer between two parallel flows of respective velocity $\vec{U}_1$ and $\vec{U}_2$ - development of a Kelvin-Helmholtz instability. Right / Vorticity modulus of the same type of instability obtained with Large Eddy Simulation (reproduced from Lesieur et al. [82]).....	35
Figure 3.6: a/ Contours of normalized pressure $p/(\rho U^2)$ in an axial cross-section; b/ Isosurface of instantaneous low-pressure $p = -0.22\rho U^2$ representing the vortex rings in the wake of a sphere (reprinted from Seidl et al. [116]).....	36
Figure 3.7: Representation of the resolved turbulent structures for a cylinder in cross-flow – Isosurface of $Q$ -criterion with $Q = 10^5 \text{ s}^{-2}$ (Menter & Egorov [93]).....	37
Figure 3.8: Schematic view of a/ the classical POD, b/ the snapshot POD (reprinted from [29]).....	40
Figure 4.1: Research strategy employed for analyzing the turbulent flow induced by a DISI engine intake port .....	43
Figure 4.2: Presentation of the tumble-flap model geometry used for optical measurements.....	45
Figure 4.3: Technical drawing and section view of the experimental model (all dimensions in mm).....	46
Figure 4.4: Different zonal treatment of the DES model according to the blending functions used: blue color for LES resolved area and red color for URANS mode. a/ default settings offering a URANS driven resolution, rather protective; b/ user specified parameters, with higher turbulence sensitivity (larger LES mode).....	47
Figure 4.5: Comparison of the flow vorticity contour (X-component) for the two different blending functions settings presented in the previous figure .....	47
Figure 4.6: Different meshes used for the sensitivity analysis: a/ full hexahedral; b/ hybrid tetra / hexa / prisms; c/ full tetrahedral.....	49
Figure 4.7: Different cells geometries and sizes present in the three former meshes.....	50
Figure 4.8: Comparison of the recirculation length between the 3 different mesh types – Superimposition of the averaged velocity Z-component and the null velocity contour line (black line).....	50
Figure 4.9: Blending function comparison between the three different meshes .....	51
Figure 4.10: Comparison of the ratio between the smallest turbulent structures resolved by the DES model ( $L_t$ ) and the local mesh length-scale ( $\Delta_{mesh}$ ) .....	51

Figure 4.11: Position of the different velocity profiles in the duct for comparison with LDA measurements .....	52
Figure 4.12: Profiles of the Z-velocity component: comparison between LDA measurements and CFD simulation results – Position 0 is the lower bound of the duct .....	53
Figure 4.13: Experimental setup: simplified intake-port model and LDA system .....	54
Figure 4.14: Position of the different planes measured.....	55
Figure 4.15: Horizontal velocity component comparison between a) CFD URANS, b) CFD DES, c) LDA grid 1 (1mm resolution), d) grid 2 (0,2mm resolution) and grid 3 (0,5mm resolution) .....	56
Figure 4.16: Position of the measured profiles (4mm, 16mm and 19mm from the coordinates origin) .....	57
Figure 4.17: Profile 4 – a) X-Velocity component, b) RMS of the X-Velocity component, c) Zoom in the boundary layer for the X-Velocity component, d) corresponding zoom for the RMS .....	57
Figure 4.18: Profile 16 – a) X velocity component, b) RMS of the X velocity component, c) zoom in the boundary layer for the X velocity component, d) corresponding zoom for the RMS.....	58
Figure 4.19: Profile 19 – a) X velocity component, b) RMS of the X velocity component, c) Zoom in the boundary layer for the X velocity component, d) corresponding zoom for the RMS.....	59
Figure 4.20: 2-Components PIV general setup .....	62
Figure 4.21: Experimental setup and model: left, the Tumble Optical Test-Bench; right, the flow-box and the cylinder in Perspex (reprinted from [69]).....	63
Figure 4.22: Positions of the two different measured planes: 1 – cylinder middle-plane, 2 – valve plane ..	64
Figure 4.23: Averaged velocity vectors and scalar fields in the cylinder middle-plane (velocity magnitude ranging from 0 $\rightarrow$ $U_{max}$ ).....	65
Figure 4.24: Averaged velocity vectors and scalar fields in the valve-plane (velocity magnitude ranging from 0 $\rightarrow$ $U_{max}$ ).....	65
Figure 4.25: HS-PIV instantaneous velocity fields at four consecutive time steps in the valve middle-plane (same colours and vectors scaling for all figures, from 0 $\rightarrow$ $U_{max}$ ).....	66
Figure 4.26: HS-PIV data analysis (50 kg/h, 10 mm, valve middle-plane): a/ standard deviation (equal $R(x,y,z,t)$ ) of the Y-velocity component, b/ number of valid data per point over the sample size (here 100 time-steps), c/ time-correlation of the Y-component and d/ correlation coefficient $\rho$ ( $\rightarrow$ $Rho$ ).....	67
Figure 4.27: CFD results - Various cross-sections of the flow: a) left valve middle-plane, b) right valve middle plane, c) flow cross-section in the Y direction and d) cross-section plane in the Z direction.....	69
Figure 4.28: Isosurface of low value of normalized pressure ( $P = -2.1\rho U_0^2$ ) .....	70
Figure 4.29: Valve middle-plane shaded with vorticity magnitude and low normalized pressure contour lines .....	71
Figure 4.30: Valve middle-plane shaded with vorticity magnitude and positive $Q$ contour lines .....	71
Figure 5.1: Optical test-bench optimization.....	73
Figure 5.2: a/ Variation of the Plexiglas reflectance according to the light-ray angle of incidence – b/ energy of a single oscillator as a function of the laser pulse repetition rate.....	74
Figure 5.3: a/ Experimental setup for stereoscopic PIV, b/ Top-view of the optical system showing the Forward-Forward scattering method .....	75
Figure 5.4: Light scattering by a 1 $\mu$ m oil particle in air (reprinted from Raffel et al. [104]).....	76
Figure 5.5: CTA setup for velocity profile measurement in the intake extrusion – a/ Position of the two different CTA probes, the L-form one for the vertical profile and the straight probe for the horizontal profile; b/ cross section view of the channel with the vertical and horizontal lines followed .....	77

Figure 5.6: Different mini-CTA X wire probes employed (from Dantec) – a/ straight probe (55P61) for measurements in the direction of the main flow; b/ probe for cross-flow measurements (55P62).....77

Figure 5.7: Comparison of the velocity profiles measured and computed at a distance of 210mm from the engine intake port – a/ horizontal profile and b/ vertical profile of the streamwise component.....78

Figure 5.8: a/ 3-D model used for the numerical simulation; b/ cross-section of the hybrid mesh; c/ zoom in the valve-clearance region showing the Low-Reynolds wall treatment with variable prisms layer height .....80

Figure 5.9: Sensitivity analysis – Left: comparison of the advection scheme influence on the total pressure drop between the intake and outlet of the fluid domain; Right: RANS simulation convergence for the three meshes with high-resolution advection scheme (measured value: 3650 Pa) .....82

Figure 5.10: Mesh sensitivity analysis – Averaged RANS-SST simulation results obtained with the High-resolution advection scheme .....83

Figure 5.11: Diagram illustrating the different meshes employed for the various post-processing operations conducted later.....84

Figure 5.12: Comparison of average velocity magnitude and vectors (100C3: 100 kg/h, 3mm valve-lift) ..85

Figure 5.13: Average velocity magnitude superimposed with vectors. The dots in each quadrant are representing the tumble center positions .....85

Figure 5.14: a/ Comparison between measured and calculated profiles of the total velocity magnitude – b/ Representation of the absolute difference normalized with the average velocity magnitude .....87

Figure 5.15: a/ Comparison of the measured and calculated profiles of the vertical velocity component – b/ Representation of the absolute velocity difference normalized with the average vertical velocity component.....88

Figure 5.16: Root-Mean-Square (RMS) value of the vertical velocity component (SAS 100C3 results) – definition of the Regions Of Interest 1 and 2 (ROI 1 and ROI 2) .....90

Figure 5.17: Skewness of the vertical velocity component (SAS 100C3 results) – definition of the 3<sup>rd</sup> Region Of Interest (ROI 3) .....90

Figure 5.18: DES results – Characteristic spectra of the vertical velocity component computed in each of the ROI defined.....91

Figure 5.19: SAS results – Characteristic spectra of the vertical velocity component computed in each of the ROI defined.....91

Figure 5.20: Reconstructed velocity field (vertical component) filtered with the first frequency mode  $f_1 = 1.5 \text{ kHz}$ .....92

Figure 5.21: Reconstructed velocity field (vertical component) filtered with the second frequency mode  $f_2 = 2.5 \text{ kHz}$ .....92

Figure 5.22: Reconstructed velocity field (vertical component) filtered with the third frequency mode  $f_3 = 3.6 \text{ kHz}$ .....93

Figure 5.23: Cumulative energy distribution of the POD modes and relative difference - DES 100C3 (valve plane) results with: a/ the full range of modes and b/ a zoom in the 30 most energetic modes - c/ and d/ corresponding SAS results.....95

Figure 5.24: Cumulative sum of the kinetic energy up to the truncation mode indicated in each graph normalized with the total kinetic energy resulting from the 300 modes .....96

Figure 5.25: Visualization of the 1<sup>st</sup> POD mode of the flow (DES100C3) – Velocity vectors and kinetic energy: a/ full valve cross-section plane b/ PIV window .....97

Figure 5.26: Visualization of the 2<sup>nd</sup> POD mode of the flow (DES100C3) – Velocity vectors and kinetic energy: a/ full valve cross-section plane b/ PIV window .....98

Figure 5.27: Visualization of the 3 <sup>rd</sup> POD mode of the flow (DES100C3) – Velocity vectors and kinetic energy: a/ full valve cross-section plane b/ PIV window .....	98
Figure 5.28: Visualization of the 4 <sup>th</sup> POD mode of the flow (DES100C3) – Velocity vectors and kinetic energy: a/ full valve cross-section plane b/ PIV window .....	99
Figure 5.29: Analysis of the truncation influence on the quality of the reconstructed velocity field (DES 100C3 – valve-plane) .....	100
Figure 5.30: Spectrogram resulting from the FFT of the time coefficients associated to the different POD modes – Comparison between DES and SAS results, case 100C3, full valve plane and PIV window. The marked regions represent the modes domains showing a particular spectral activity for the three frequencies of interest.....	101
Figure 5.31: Reconstruction of the velocity field filtered by the frequency of 3600Hz for the full valve-plane – a/ with modes 45-53 (full plane modes) – b/ with modes 96-146 (PIV-window modes).....	103
Figure 5.32: Reconstruction of the velocity field filtered by the frequency of 3600Hz for the “PIV-window” – a/ with modes 45-53 (full plane modes) – b/ with modes 96-146 (PIV-window modes).....	103
Figure 5.33: Reconstruction of the velocity field filtered by the frequency of 3600Hz – a/ full valve-plane: modes 45-53 (full plane modes) – b/ “PIV-window”: modes 96-146 (PIV-window modes).....	104
Figure 5.34: Reconstruction of the velocity field filtered by the frequency of 2500Hz – a/ full valve-plane: modes 62-88 – b/ “PIV-window”: modes 111-189 .....	105
Figure 5.35: Reconstruction of the velocity field filtered by the frequency of 1500Hz – a/ full valve-plane: modes 55-121 – b/ “PIV-window”: modes 58-125 .....	106
Figure 5.36: Difference of spatial resolution between various post-processing grids: a/ fine mesh b/ coarse mesh / “PIV-like” resolution (see also the diagram presented in Figure 5.11) .....	106
Figure 5.37: PIV results in the valve plane – Top: raw data, Bottom: interpolated velocity field (over space and time) .....	107
Figure 5.38: : Influence of the sample size on the cumulative fluctuating kinetic energy convergence (from 301 modes to 901 modes).....	108
Figure 5.39: Windowing effect on CFD results – comparison with PIV measurements in the valve-plane .....	109
Figure 5.40: Eigenvalues comparison between both numerical results (DES and SAS) and experimental results for the case 100C3, in the valve plane – a/ 300 modes; b/ Zoom in the 30 first modes.....	109
Figure 5.41: Linear representation of the spectrogram of the time coefficients associated to the 300 POD modes. Left: PIV results (distinction between a confidence area and a noisy, scattered region bordered by the dashed red lines, in the upper right-hand-side of the graph), right: DES .....	110
Figure 5.42: Logarithmic representation of the spectrogram from Figure 5.41 – Left: PIV results; Right: DES results.....	111
Figure 5.43: Diagram of the “zero-crossings” calculation principle .....	112
Figure 5.44: Example of zero-crossings determination for the Y-velocity component in the Z-direction (case 100C3 and the reconstructed velocity field fluctuating with 1.5kHz) – a/ reconstructed velocity field with vectors; b/ PIV results: sign of the Y-component (red: >0, blue: <0); c/ DES results; d/ SAS results .....	113
Figure 5.45: Influence of the spatial resolution on the zero-crossings computation and consequently, on the structure size – SAS original resolution (red), SAS low resolution (black), and PIV results (blue) ....	113
Figure 5.46: Comparison of count number of zero-crossings (a) and averaged characteristic length of the structures (b) for the Y velocity component along the Z direction .....	114
Figure 5.47: Comparison of count number of zero-crossings (a) and averaged characteristic length of the structures (b) for the Z velocity component along the Y direction .....	114

Figure 5.48: Averaged structures diameter according to the velocity component normal to the direction considered.....	116
Figure 5.49: Diameter of turbulent structures reconstructed (red curve) and structures size contained in each mode (blue curve). The X-axis corresponds to the mode number for the blue curve and to the time step for the red curve (time dependant mean diameter).....	117
Figure 5.50: Summary of average structure diameters and their corresponding fluctuation frequency for the four different configurations investigated and the two planes post-processed – Based on the zero-crossings analysis of the Y-component / Z-direction (VP: Valve Plane; CC: Cylinder Center plane; 50kg/h or 100kg/h flow rate; closed flap; 3mm or 9mm valve lift) .....	118
Figure 5.51: Overall comparison of the interpolated results obtained for the structure diameters in the valve plane and in the cylinder central plane .....	119
Figure 5.52: 3D visualization of turbulent structures – half-section of an isosurface of positive $Q$ ( $Q = 7e+06s^{-2}$ ) shaded with the vorticity .....	122
Figure 5.53: Ratio between the smallest turbulent structures resolved by the two different turbulence models and the local mesh length scale .....	123
Figure 5.54: Comparison of the ratio between the turbulent kinetic energy resolved and the total amount of this value .....	124
Figure 5.55: Different section views of the isovolume of $Q$ , representing the development of the turbulent structures within the cylinder, colored with the vorticity .....	125
Figure 5.56: Instantaneous representation of the global $Q$ invariant parameter distribution along two perpendicular directions of the cylinder. a/ Section cuts showing the two axis and the intersection area with the $Q$ -isovolume ( $Q = 7e06 s^{-2}$ ); b/ $Q$ distribution along the two axis defined in a/ .....	126
Figure 5.57: Probability function of the $Q$ invariant calculated on each post-processing planes for the DES 100C3 simulation results (where $Q_c$ is the criterion – $Q_c = 7e06 s^{-2}$ ).....	126
Figure 5.58: Probability function of the $Q$ invariant calculated on each post-processing planes for the different SAS simulations (mass flow: 100 and 50 kg/h; valve-lift: 3 and 9 mm; $Q_c = 7e06 s^{-2}$ ) .....	127
Figure 5.59: Superimposition of the probability function of the $Q$ -invariant for the four different SAS simulations on each horizontal cylinder cross-sections.....	129
Figure 5.60: Distribution of the approximate radius of the 2-D turbulent structures defined by the selected range of $Q$ – Mass flow = 100 kg/h (X-axis: radius [mm], Y-axis: count number [-]) .....	130
Figure 5.61: Distribution of the approximated radius of the 2-D turbulent structures defined by the selected range of $Q$ – Mass flow = 50 kg/h (X-axis: radius [mm], Y-axis: count number [-]) .....	131
Figure 5.62: Normalized distribution of the turbulent structures according to the $Q$ -factor definition....	132

## Tables Index

Table 3-1: Empirical estimation for scales of turbulence [5].....	17
Table 3-2: Modeling constants of the SST model (subscript 1 is used for the $k - \omega$ model constants, subscript 2 for the $k - \epsilon$ model constants).....	26
Table 5-1: Summary of the main characteristics of the three different meshes investigated.....	81
Table 5-2: Principal simulation settings and boundary conditions.....	81
Table 5-3: Distance between the tumble centres obtained, comparing PIV with the different simulations.....	86
Table 5-4: Total pressure drop between inlet and outlet (100C3 and 100C9 stand for a mass-flow of 100 kg/h and a valve-lift of 3 mm and 9 mm respectively).....	86
Table 5-5: Comparison of the main characteristic frequencies resulting from DES and SAS simulations.....	91
Table 5-6: Modes associated to the different frequencies for various CFD results and post-processing windows.....	102
Table 5-7: Comparison of zero-crossings count number statistics.....	115
Table 5-8: Comparison of approximated structures size.....	115
Table 5-9: Summary of main characteristic frequencies observed for each investigated cases – SAS Valve-plane.....	121
Table 5-10: Summary of the global distribution and extreme values of the variable Q according to different criteria on every post-processing plane (SAS results).....	127

# Nomenclature

## Abbreviations

AFR	air/fuel ratio
BDC	bottom dead centre
CFD	computational fluid dynamic
DES	detached eddy simulation
DISI	direct-injection spark-ignition
DOP/TOP	Drall Optischer Prüfstand (swirl optical test-bench) / Tumble Optischer Prüfstand (tumble optical test-bench)
DNS	direct numerical simulation
ECV	engine cyclic variations
FFT	fast Fourier transformation
FSI	fuel stratified injection
HS-PIV	high-speed particle image velocimetry
ICE	internal combustion engine
LDA	laser Doppler anemometry
LES	large eddy simulation
LNS	limited numerical scales
PIV	particle image velocimetry
POD	proper orthogonal decomposition
RANS	Reynolds averaged Navier-Stokes
SAS	scale adaptive simulation
SGS	subgrid scale
SST	shear-stress transport
SVD	singular value decomposition
TDC	top dead centre
TOP	Tumble optische Prüfstand (Tumble optical rig)
TR-PIV	time-resolved particle image velocimetry
URANS	unsteady Reynolds averaged Navier-Stokes

## Latin symbols

$a_1$	constant of the SST turbulence model – Eq. (3.38)
$C$	Courant number
$C_1, C_2, C_k, C_\epsilon$	constants of the $k - \epsilon$ model
$C_S$	Smagorinsky constant
$C_\mu$	constant for the spatial scheme of the $k - \epsilon$ model – Eq. (3.31)
$c_K$	universal Kolmogorov constant, $c_K = 1.5$
$CD_{k\omega}$	cross-diffusion function used in the blending function $F_1$ of the $k - \omega$ SST turbulence model
$E$	energy function of the wavenumber in the turbulent energy spectrum, $\text{m}^3/\text{s}$
$F_j$	external forces, N
$F_{DES}$	blending function of the DES hybrid turbulence model
$F_{DES-CFX}$	specific blending function of the DES turbulence model implemented in CFX
$F_{SST}, F, F_1, F_2$	blending functions of the SST turbulence model
$f_d$	characteristic frequency of the most dissipative eddies, 1/s
$f_e$	characteristic frequency of the energy containing eddies, 1/s
$f_K$	characteristic frequency of the Kolmogorov size eddies, 1/s
$f_l$	characteristic frequency of the largest eddies, 1/s
$h$	spatial increment or grid spacing, m
$k$	turbulent kinetic energy, $\text{m}^2/\text{s}^2$
$L_t$	turbulent length scale, m
$L_{vK}$	von Kármán length scale, m
$l_*$	turbulence length unit ( $= \nu / v_*$ ), m
$l_d$	length scale of the most dissipative eddies, m
$l_e$	length scale of the energy containing eddies, m
$l_K$	Kolmogorov length scale, m
$l_L$	length scale of the largest eddies, m
$l_t$	integral length scale, m
$p$	pressure, Pa
$Q$	2 <sup>nd</sup> invariant of the velocity gradient tensor, $1/\text{s}^2$
Re	Reynolds number
$S$	invariant of the strain-rate tensor ( $= (2S_{ij}S_{ij})^{1/2}$ ), 1/s
$S_{ij}$	strain-rate tensor – symmetric part of the velocity gradient tensor, 1/s
Sr	Strouhal number
$t$	time, s
$t_K$	Kolmogorov time scale, s
$u_i$	$i^{\text{th}}$ -component of velocity, m/s
$u_\tau$	wall- or friction velocity, m/s



$v_*$	wall- or friction velocity, m/s
$x_i$	$i^{\text{th}}$ -component of the Cartesian coordinate, m
$y^+$	normalized wall distance

## Greek symbols

$\alpha, \alpha_1, \alpha_2$	coefficients of the SST turbulence model
$\beta, \beta', \beta^*$	coefficients of the SST turbulence model
$\delta_{ij}$	Kronecker delta
$\Delta t$	transient simulations time-step, s
$\varepsilon$	dissipation rate of turbulent kinetic energy $k$ , J/(kg.s)
$\eta$	Kolmogorov length scale of turbulence, m
$\kappa$	wave number ( $= 2\pi / \lambda$ ), 1/m
$\kappa_{vK}$	von Kármán constant, $\kappa_{vK} = 0.41$
$\lambda$	wave length, m
$\mu$	dynamic viscosity, kg/(m.s)
$\mu_t$	dynamic turbulent viscosity, kg/(m.s)
$\nu$	kinematic viscosity ( $= \mu / \rho$ ), m <sup>2</sup> /s
$\nu_t$	kinematic turbulent viscosity, m <sup>2</sup> /s
$\xi, \xi_1, \xi_2$	modelling constants in the SST turbulence model
$\rho$	density, kg/m <sup>3</sup>
$\sigma, \sigma^*, \sigma_k, \sigma_\omega$	diffusion constants of the SST turbulence model
$\tau$	integral time scale, s
$\tau_{ij}$	viscous stress tensor, N/m <sup>2</sup>
$\omega$	turbulent eddy frequency, 1/s
$\Omega$	rotation tensor – anti-symmetric part of the velocity gradient tensor, 1/s

## Subscripts and superscripts

*	dimensionless, perturbation quantities <i>or</i> conjugate complex of a vector
+	dimensionless quantities in the near wall region
$i$	component $i$ , running index
$j$	running index
SGS	subgrid scale

**Other symbols**

-	conventional time average
$\langle \rangle$	ensemble average, time average
' or ''	fluctuation quantity

# 1 Introduction

## 1.1 General

After more than one century of uncontested reign over the domain of transportation as the only economically viable energy source available, the various pressures acting nowadays on fossil oil are incessantly tightening the vice on combustion engines.

The two petroleum shocks from 1973 and 1979 have drawn the attention of all main actors ranging from industrial to governmental entities on this major raising problematic and have highlighted the risks related to such a strong dependency on this single energy mode. The successive wars and diplomatic crises occurring with the oil producing countries are pushing the barrel prices to new irreversible spheres and contracting the global production. However, the ever-increasing demand reinforced by the additional needs from the emerging and developing countries such as China or India are boosting the global consumption to a value of about 30 billions of barrels per year. Under these conditions, the most optimistic estimations are foreseeing a period of approximately 40 years of oil reserves from now on (International Energy Agency – IEA [68]).

Besides this issue of oil supply, another major parameter is gaining influence, the environmental concern. This aspect, and more particularly the greenhouse gases emissions with their effect on global warming, is stressing the transportation industry, which is responsible for more than one fourth of the total amount of CO<sub>2</sub> produced [68]. Stringent measures are being introduced by most of the leading countries to limit and even reduce those emissions in a short to mid term future. Following that purpose, taxes systems and other financial means are employed to support the proliferation of environmental-friendly vehicles by setting limitations on carbonate dioxide emissions. Politics are preventing vehicles from entering large cities by introducing tollgates with gradual rates according to their emission level; governments are favouring the purchase of “eco-cars” through price rebates; and very deterrent taxes are awaiting the OEM’s (Original Equipment Manufacturer’s – here the car manufacturers), which are not complying with the average fleet emissions targets as soon as on the horizon of 2012 as for Europe [40]. Oil natural reserves, technical and industrial issues, geopolitical situation, financial and environmental consequences are all the influencing parameters that are leading the way of tomorrow’s transportation solutions and more than that, of the global economy. Although it seems inevitable that a drastic change must occur in the vehicles propulsion technology, it also does not make any doubt for most of the experts that the next twenty to thirty years will still be ruled by internal combustion engines evolutions.

## 1.2 Rationales for Current Study

During the last decades, the automotive industry has been widely marked by increasing efforts from the OEM’s and their suppliers to improve engine efficiency and the combustion process. Indeed, tightening pollutants emission legislations as well as evolving users’ expectations for lower fuel consumption and higher performances have prompted these continuous developments in internal combustion engines. Recently, interesting headways have been realized in the domain of homogeneous and stratified lean-burn combustion, calling for better knowledge of the in-cylinder flow structure. Actually, charge motion within the engine cylinder is one of the main influential factors on the global combustion process, enabling to control and optimize the air-fuel mixing.

This last observation is even more relevant in the Direct-Injection Spark-Ignition (DISI) engines offering the adjustable combustion strategy mentioned before. This engines concept, although presenting a great potential in terms of reduction of fuel consumption, or in other terms of CO<sub>2</sub>-

emissions, has unfortunately shown its sensitivity to cyclic variations (see Chapter 2). The combustion process in the lean burn functioning domain is becoming more complex than during the homogeneous mode, due to the need to direct properly the ignitable mixture in the vicinity of the spark plug. Different ways have been investigated in order to optimize this particular mode of operation. The technique implemented and unveiled by Volkswagen in its FSI<sup>®</sup> engines in 1999, was a tumble-based, air/wall guided process. An organized flow motion was generated by the intake-port and amplified by an actuated flap in order to “push” the flow through the upper side of the valves and then increase the tumble-ratio. The position of the injector and the shape of the piston bowl gave to the fuel spray a contra-rotating direction with regards to the dynamic of the intake charge. Then both the air motion and the wall geometry are guiding the mixture. Despite this innovative and interesting solution, large cycle-to-cycle variations were still observed in the stratified mode, leading to an unbalanced engine performance, and even causing misfire and incomplete combustion with high raw emissions. Therefore, the reduction of cyclic fluctuations and the improvement of process reliability have become of major importance since then. The flourishing number of references found in the literature, which are related to this topic, also supports this idea.

The turbulent flow condition induced by the intake system and the fluctuations in flow velocity are of first interest in order to better understand the origin of the engine cyclic variations. The objective to obtain a reproducible mixture movement with high kinetic energy needs to be fulfilled to stabilise the engine operation and prevent the fluctuations of the combustion process. However, the complexity of the fluid flow developing in DISI engines requires advanced experimental and numerical tools, which will allow the developers to improve the systems.

### **1.3 Literature Survey**

Recent computational resources advances and improved numerical and physical models are providing a viable starting point for applying “Eddy Capturing Methods” such as Large Eddy Simulation (LES) to flows of realistic complexity and direct industrial interest. Indeed, extensive developments have brought these approaches at a stage where it warrants, under certain restrictions, successful applications in various domains such as computation of turbulent flows, sprays, mixing and combustion processes for practical engine configurations, even through several engine cycles.

Although Computational Fluid Dynamics (CFD) has become a key-point in the global product development process, the only method available until now to investigate these concrete industrial applications was restricted to the Reynolds Averaged Navier-Stokes (RANS) methods. In fact, the issue of simulating high Reynolds number turbulent flows in particularly complex geometries would have been solved with the accurate Direct Numerical Simulation (DNS) techniques if sufficient computational resources had been available. However, due to the broad range of scales that need to be fully resolved, the computational cost for a three dimensional DNS is scaling as  $Re^{9/4}$  (see §3.2.1), which is far from the actual or foreseeable computational performances.

On the other hand, even if the contribution of 2-equations based RANS or URANS (Unsteady RANS) models to the progresses in Internal Combustion Engines (ICE) cannot be underestimated ([18], [23] and [106] for example), their weaknesses have also been regularly demonstrated in the literature. First of all, its lack of universality has been shown in Leschziner and Lien et al. [82, 84] in the sense that the good performance for one particular engine configuration could not be maintained for other geometries or conditions. The second main drawback of RANS, and associated methods, lies in its own nature and the averaging process that describes it. This statistical method cannot take into account the highly unstable nature of turbulent flows induced by intake ports and valve-trains of ICE.

Even though engineers and industrial users are now recognizing the potential of LES to tackle the problems related to the simulation of in-cylinder applications, where the geometrical complexity is accompanied by a highly transient flow field, exposed to rapid strain, the relatively coarse grid resolutions presented in the literature are restricting the overall quality of the predictions. This observation made in 2001 by Celik et al. [24] in their good and rather exhaustive review of LES applications for in-cylinder turbulence, is still valid today. Actually, although the global performances have continuously improved since the publication of this review, the major contributions that appeared since this date are still pretty limited in terms of spatial resolution.

Engineers dealing with engine flows simulations are faced with the dilemma to make a compromise between either a very fine resolution to solve smaller scales, or to take more physical phenomena into account. Theoretically, LES would be able to simulate the most complex cases, in an affordable time, but for this purpose, it must be massively parallel. Like Poinsot [104] mentioned it after having shown the results of an extreme application, the simulation of a large combustion chamber of a turbine, fitted with 24 burners and run on the IBM BlueGene machine in 2005 on 32.000CPU's, "*LES is not slow... it is only expensive!*". However, industrial needs are concerned with other constraints and cannot afford such expenses for their daily standard computations. This is one of the reasons to explain the constant interest for coarser grids for engineering problems. On the other hand, some studies have argued that meshes between  $10^5$  and  $10^6$  computational elements associated to a second-order spatial discretization are already sufficient to capture 80-90% of the flow's kinetic energy [59]. Thus, with only few modifications of numerical methodology, a reformulation of the turbulent stress model and accurate inflow/outflow boundary conditions, LES delivers significantly more information than a corresponding RANS, and provides a more realistic representation of the in-cylinder turbulent flow.

Under these fundamentals, LES is getting an almost exponential growth of interest, especially for engine applications, where it opens new opportunities for investigation in previously inaccessible physical phenomena such as the cycle-to-cycle variability. Researchers and developers are focusing their work on different aspects in order to examine the origins of those fluctuations, which can be classified into two groups, as described in Chiriac and Apostolescu [27]. The first group concerns the natural "random" phenomena such as gas motion or charge mixture, and are referred as stochastic effects. This first group is directly correlated to the inherent nature of the flow, and its turbulent characteristics. The second group is described as a deterministic effect and is related to the combustion quality, driven by the prior cycle's influence such as incomplete combustion, residual gases composition and quantity. Then, the numerous works found in the literature can be clustered in two main categories, the one dealing with cold flows and the others with reacting flows.

For the first category and the study of non-reacting flows, the investigators are operating in several steps. First of all, they concentrate their work on the intake stroke and the geometry of the intake system by studying the flow pattern generated in a stationary configuration. Then they implement a moving mesh strategy in order to consider the full engine cycle and the interaction existing between the air, induced by the intake port, and the moving valves and piston. The complete gas dynamic is taken into account during the full cycle, adding the effects of the compression and exhaust phases to the steady geometry analysis. In the diversity of sources found in the literature, while studying the generation and decay of turbulence in the combustion chamber of ICE, two main directions are crystallizing. Some authors, like Celik et al. [25], after having observed a rapid distortion of the turbulent eddies inside the cylinder during the intake stroke, do think that the majority of the turbulence influencing the combustion is regenerated during the compression and expansion phases, when the piston is near Top Dead Centre. Even if the turbulence generated during the intake stroke is much larger than the one induced by the piston-bowl assembly at TDC, they assume that the dynamics of squish flow and the design of

bowl geometry are playing a dominant role in enhancing the combustion. This analysis supports the conclusion of Haworth [58], who sees the cycle-to-cycle variability as an intrinsic part of the (filtered) Navier-Stokes equations of motion, and is “*nothing more than large-length-scale long-time-scale turbulence*”. According to him, this large-scale turbulence would correspond to the only residual influence of the intake flow dynamics observed around TDC, under the form of a large rotational structure known as swirl or tumble depending on the direction of the main axis of revolution.

Based on these observations or assumptions, some researchers are then concentrating their efforts on the analysis of motored and fired engines, favouring the effects of other physical phenomena such as the fuel injection and the global combustion process to explain the occurrence and amplitude of engine cyclic variations. The importance of the injection strategy and the interaction existing between the jet and the mean flow before compression have been investigated in Devesa et al. [38] and Pischinger et al. [103], showing the crucial role of injection in the load location and energy transfer between mean and fluctuating flow. Generally speaking, the mixing process is representing a main vector of interest in the way to identify the potential sources for engine cyclic variations and has been the object of many numerical investigations as can be read in [61, 123, 124]. Consequently, as a normal extension of the works aforementioned, some scientists are combining the simulation of multiphase flows with combustion models to observe the influence of the thermodynamic reactions on the engine stability. Obviously, the increased complexity of the phenomena to be accounted for, once again, does not allow the use of refined meshes. In the last advances observed in the literature, none of the simulations has been realised with pure LES, but a wall function is always required. The results summarized in [28, 131, 133], all using the same CFD code AVBP from CERFACS (European Centre for Research and Advanced Training in Scientific Computation) and IFP (French research institute in energetics), establish the dependency of the complete cycles simulation quality to the inflow conditions given. Indeed, by considering different components of the real geometry, such as the full intake manifold or the silencer at the outlet, the displacement of the boundary conditions further away from the combustion chamber are improving the overall quality of the simulation. Despite the compromise of employing a relative coarse mesh definition in the boundary layer to maintain affordable computational costs, the authors are underlining the necessity to simulate a larger amount of cycles in order to generate reliable statistics on fired engines. However, based on their activities on combustion simulation, some researchers are yet pointing out the fact that the cycle-to-cycle variations observed are very sensitive to the intake flow and port geometry. Indeed, aside the former legitimate trend consisting on devoting the CFD resources on the simulation of combustion over many cycles to the detriment of the boundary layer resolution, numerous studies are sustaining the argument that intake port induced turbulence is of major importance for the generation of engine cyclic variations.

In 2005, Goryntsev et al. [52, 54] have published several papers demonstrating the importance of accurately modelling the intake port, the valves region, as well as the jet flow dominated by strong shear effects. Despite a rather low grid resolution and the use of a standard Smagorinsky constant for the subgrid scale (SGS) model, they were able to observe the sensitivity of the cyclic variations to the intake port and valves geometry. Even if they did not establish a concrete correlation between the turbulence generated during the intake phase with the one remaining in the cylinder at the end of the compression stroke, they expressed the hypothesis that the valve-port region might be the possible origin of the cyclic variations of the flow field. More recently, the same authors have continued their research by studying the influence of the cycle-to-cycle variations on the fuel-air mixing and combustion in a DISI engine [53]. The simulation of a realistic motored engine with fuel spray modelling has shown the impact of the cycle-to-cycle velocity fluctuations on the mass fraction distribution within the cylinder.

Based upon the suggestion that flow instabilities occurring during the intake phase can be a source of engine cyclic variation, a general statement made its way within the CFD community. It

seemed obvious that accurate near wall treatment is fundamental in determining correct prediction of boundary-layer separation and associated flow perturbations. Unfortunately, the use of pure LES involving resolution of turbulence through to the wall boundary still remains prohibitively expensive. For this reason, some hybrid methods combining the advantages of URANS and LES formulations have been developed (please refer to §3.2.4 for a detailed description of the Detached Eddy Simulation model). Thanks to these hybrid models and the adoption of URANS method for the near wall, two different strategies can be implemented to handle the boundary layer, namely the conventional High-Reynolds wall function method or the Low-Reynolds turbulence near wall method. In the first case, the use of an empirical law to describe the viscous sub-layer of the wall boundary allows to eliminate the need for a fine mesh to resolve the gradients approaching the wall. Although it is widely acknowledged that this conventional method has severe limitations in terms of accuracy and predictive capability of port-flows [17], CFD simulations using High-Re wall function have found widespread acceptance as a tool to aid design of engine intake ports. On the other hand, the Low-Reynolds technique rests on the integration of the turbulence equations up to the wall and therefore requires a relatively fine numerical grid, with at least 16 near wall cells within the boundary layer [6]. In a recent paper from Campbell et al.[22], the emphasis has been put on the importance of the near wall behaviour for engine port simulations, demonstrating the performance of a URANS Low-Reynolds method associated to a  $k-\omega$  SST turbulence model [89] to accurately predict the flow separation location around the valve seat of a Diesel engine. The authors even concluded that *“reliance on the High-Reynolds wall function method is a source of considerable error and does not provide a predictive capability when examining novel geometry features”*.

Nevertheless, as described earlier in this chapter, the resulting common requirement for unsteady simulations in internal combustion engines, which is to resolve in an accurate way the boundary layer, cannot be followed in most of the industrial investigations published recently due to the perpetual seek for economically viable solutions. Indeed, the actual trend focusing on the simulation of motored engines for a more realistic observation of the in-cylinder turbulent flow is often based on moving mesh strategies using High-Reynolds wall function formulations or other wall adapting linear models. These methods are the only possibilities to conduct LES or derivative hybrid simulations over multiple engine cycles, while maintaining affordable computational expenses. Studies intending to consider a sufficiently large amount of cycles to generate reliable statistics about the cycle effects do not have any other chance as to employ coarser meshes without refinement in critical regions where the boundary layer activity is yet of first importance.

## **1.4 Scope of the Work**

Considering the rather elusive character of recent transient CFD studies in predicting intake port flows and their deficiency in accurate determination of boundary layer separation and associated flow instabilities, the present work shows a further determined effort to validate simulations of stationary port-valve flow rig tumble measurements, employing latest state-of-the-art industrial CFD and measurement methodologies. Through this study, a contribution to the characterization of turbulence induced by DISI intake ports, and thus, to the understanding of the process deemed to be a major source of in-cylinder flow fluctuations, and later of combustion cyclic variations, is provided.

A general description of the operating modes of DISI-engines and the presentation of the major challenges existing with this particular technology will be given in Chapter 2, complementing the background of engine cyclic variations already tackled in the present chapter.

After having depicted the main physical characteristics of turbulence, the state-of-the-art of turbulence modelling based on the underlying governing equations for fluid mechanics will be reviewed in Chapter 3. Although the broad panel of numerical treatments of the Navier-Stokes

equations available is presented, ranging from RANS to DNS, the focus will be put on the description of two modern methods, namely the Detached Eddy Simulation and the Scale Adaptive Simulation. Then, the emphasis will be put on the presentation of different techniques available to characterize and visualize coherent structures in cylinder. Several flow pattern extraction methods employed to filter the numerical and experimental data will be introduced, such as some energy-based decomposition tools (Proper Orthogonal Decomposition – POD) or selective visualization processes to identify vortices in engines and valve-ports.

The several steps and preliminary studies undertaken in order to gradually increase the complexity of the geometries investigated and to get the sensibility of the turbulence model employed to various parameters is summarized in Chapter 4.

Finally, Chapter 5 is dedicated to the detailed analysis of turbulent flows induced by the cylinder head of a Volkswagen series production FSI<sup>®</sup> engine. For this exhaustive investigation in the aerodynamic origins of port flow perturbations, high definition geometry description, multi-million cell models, costly low Reynolds wall treatment and innovative turbulence modelling have been employed. From the experimental point of view, the latest high-end transient optical measurement techniques have been implemented to generate the required 3-d time-resolved validation data.

Based on these detailed information of the flow, a novel post-processing method for transient CFD and experimental results is proposed, intending to provide an objective comparison basis for assessing the performance of ICE ports.



## 2 DISI-Engine In-cylinder Flow

Although direct fuel injection technology has been widely applied to *compression ignition* (Diesel) engines since several decades, first in the field of marine and heavy-duty engines, before to become a standard for passenger car engines in the early nineties as well, the *spark ignition* (gasoline) engines have been longer dominated by external mixture formation mechanisms. The main reasons for this dominance have been the relatively simple control mechanisms ensuring reliable ignition and combustion under all operating conditions. Moreover, the after treatment of the exhaust gases was made much easier by the stoichiometric combustion.

However, considering the global trend for lower CO<sub>2</sub> emissions and subsequently for lower fuel consumption, engineers had to resort to new technologies, offering more flexibility to control and optimize the performance of this type of engines. After the technology breakthrough from Daimler-Benz in the 50's, the first automotive manufacturer to offer the so-called direct-injection spark-ignition (DISI) technology (or gasoline direct injection – GDI) in a series production passenger car was Mitsubishi in 1997.

### 2.1 Direct Injection and Stratified Combustion in Gasoline Engines

As indicated before, DISI engines have a number of advantages, one of them being the absence of throttling losses (or pumping losses) usually found in homogeneously operated SI engines due to the regulation system of the air/fuel mixture. Actually, the objective behind this injection strategy is to control the combustion process not through the quantity of premixed air/fuel mixture admitted into the cylinder but through the exclusive quantity of fuel injected, similar to Diesel engines. Thus, the greatest attractiveness of DISI engines lies in the much larger charge stratification offered by this technology, compared to the port fuel injection engines (PFI).

#### 2.1.1 Operating Modes Description

The driving force of the DISI technology rests on its ability to offer stratified charging, depending on the engine speed and load, as shown in Figure 2.1. For low to moderate engine revolutions, and for part load conditions, the engine is functioning in stratified charge mode. Above a certain domain, a standard homogeneous mode is employed to guarantee the combustion quality at higher engine speeds.

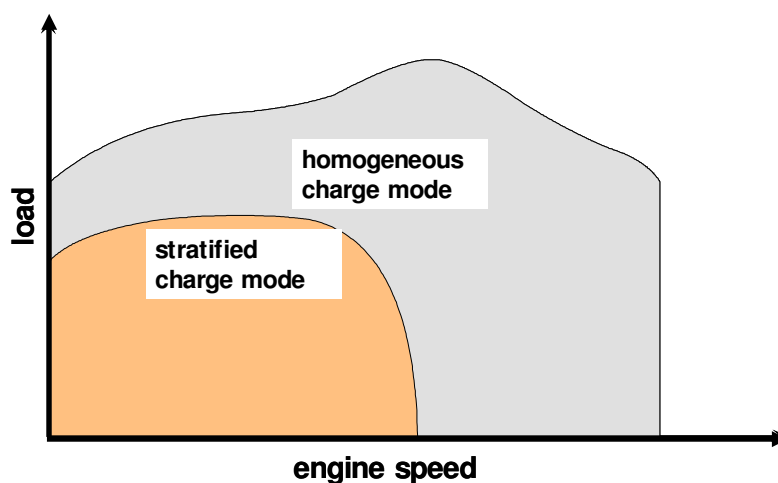


Figure 2.1: Operation map of DI gasoline engines.

Under idling and partial loads, the stratified mode is characterized by a large global air/fuel ratio (AFR) in the cylinder, typically around 2 to 3 but in some extreme cases up to 10 [78], for which no ignition is possible. Therefore, to ensure a reliable inflammation and thereby, a stable combustion, a sophisticated interaction of fuel injection directly into the combustion chamber, a suitable combustion chamber and piston shape, combined with the fluid dynamics of the flow in the cylinder are used to form an ignitable mixture in the spark plug vicinity ( $0.6 < \text{AFR} < 1.4$ , [20]). Everywhere else in the combustion chamber exists nearly pure air.

Thanks to this charge stratification, the combustion is getting lean, which enables the engine to be unthrottled and then, to drastically reduce the pumping losses. Another main characteristic of the lean or heterogeneous nature of the combustion is that the same amount of energy is released into a larger mass of gas, producing a lower temperature rise, and lower heat losses. Furthermore, the greater distance between the local combustion region and the walls, as well as the additional cooling effect induced by the injection of fuel directly into the cylinder and its evaporation, are resulting in a reduction of the heat losses through the wall and an increased volumetric efficiency [88]. The combined effect of absence of throttling and lower temperature in the combustion chamber allows using higher compression ratios, which finally increases the global engine efficiency.

However, besides the important thermodynamic advantages, the DISI technology takes also large benefits from the flexibility offered by new electronic control strategies and the use of common-rail systems. Thus, all injection parameters (injection timing, duration, mass and pressure) can be precisely adjusted in order to confer to the engine the optimal operating conditions in both homogeneous and heterogeneous modes.

In the stratified mode, under low loads, the DISI engine operates by injecting a small fuel charge late in the compression stroke, shortly before the ignition time. The management of the flow in the cylinder and the design of the spray nozzle, contrives to keep this fuel charge isolated from most of the air present in the cylinder. This implies complex combustion chamber geometry, involving squish and cavities in the piston crown, as it will be presented in the following paragraph.

As the load increases, the injection timing is moved earlier and earlier into the intake stroke, and the fuel mixes more and more with the air in the cylinder, until a certain operating domain. Over this limit, the charge is becoming homogeneous up to full load. Indeed, at higher engine speeds and loads, the time available for the mixture formation is too short and the fuel quantity required too large to employ successfully a stratified charge operation mode. Thus, for these particular operating ranges, the fuel is already injected during the induction event.

### **2.1.2 Combustion Concept and Charge Motion**

A major challenge while designing an engine able to work in homogeneous as well as in heterogeneous charge is to ensure the quality and the reproducibility of the mixture formation in order to maintain a cloud of ignitable vapor near the spark plug, no matter what the load. In order to fulfill these objectives, several combustion concepts have arisen, including different injector nozzle positions and various charge motions.

With regards to the last point, the underlying idea is to use a large rotating flow structure in the cylinder, in order to encapsulate and keep the kinetic energy induced by the intake flow throughout the compression phase. This energy will be transferred to smaller turbulent scales, down to the molecular scale where the reacting process is taking place. Thus, the charge motion, through this complex cascade phenomenon, is supporting the transport and mixing process necessary to realize ignition, speed-up the flame front displacement and ensure the combustion

propagation. The exact role of turbulence on the physical combustion process will be treated later in this chapter.

The two principle large scale motions employed for internal combustion engines are differentiating from each other through their rotational axis. If the axis of the large vortex is parallel to the cylinder axis, this shape is called *swirl*, whereas a rotational structure with a main axis perpendicular to the cylinder axis is named *tumble*, as presented in Figure 2.2.

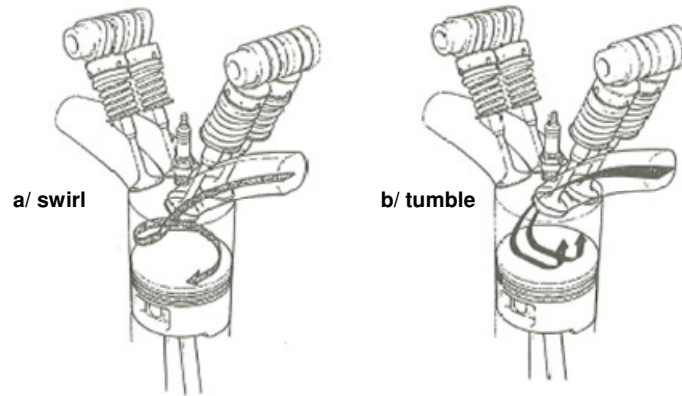


**Figure 2.2: Schematic of the air motion in cylinder. a/ swirl flow, b/ tumble flow (reprinted from [141]).**

As far as the Diesel engines are concerned, swirl is almost the unique flow motion applied. In this case, turbulence is generated as the piston approaches top dead centre through the interaction of the tangential velocity and the inward radial flow induced by the squish region [64]. Even if this flow management has proven its benefits for auto ignition engines, it is not well dedicated to stratified combustion concepts. Indeed, the radial shape of the flow is not favorable to a spark plug positioned in the centre of the cylinder, for which the convection velocity induced by the swirl would be inefficient [47].

Thus, although both flow patterns can be employed for gasoline direct injection engines, tumble is the most popular motion encountered in this type of engines. This large-scale motion appeared with the development of multi-valves cylinder heads. In opposition to swirl flows, which required a particular intake port and manifold shape to produce the radial velocities, tumble flows can be obtained by using simpler geometries.

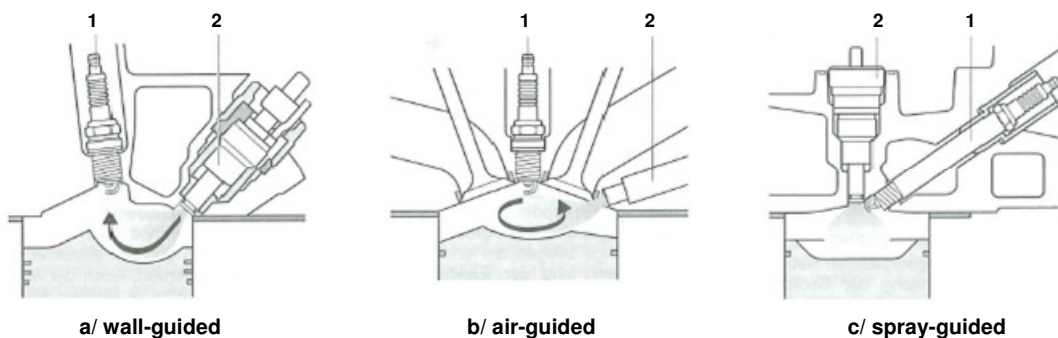


**Figure 2.3: Different combustion concepts for DISI engines - 1: spark plug, 2: injector nozzle [20].**

Figure 2.3 above is presenting the three main concepts available nowadays to control the combustion process, taking place in DISI engines. As their names indicate, the major difference between them is the method used to direct the fuel toward the spark plug.

At the first sight, it is possible to observe that both wall-guided and air-guided techniques are showing the same engine architecture, with a rather long distance between the injector nozzle, positioned underneath the intake port, and the spark plug. In the first case, the fuel is injected

directly towards the piston crown with a certain inclination angle. Then, thanks to its particular geometry and the presence of a so-called fuel-cavity, the piston deflects the fuel flow to direct it to the spark plug. Despite the advantage of injecting fuel on a hot surface, improving the evaporation process, under certain conditions, a wall-film can form, yielding an incomplete combustion and an increase of the HC and soot-emissions.

In the case of an air-guided concept, the fuel spray is completely isolated from the surrounding surfaces by the airflow, which is driving the fuel near the ignition region. The absence of contact with the walls prevents the creation of a liquid film and, therefore, reduces the HC emissions. However, this technique is very sensitive to the in-cylinder flow and its stability.

The last concept presented in Figure 2.3 is the so-called spray-guided one. On the contrary to the two first methods described before, in this case, the nozzle is placed in the centre of the cylinder head, very close to the spark plug, and the shape of the piston is much simpler. The performance of this combustion strategy is strongly dependent on the characteristics and the quality of the fuel spray. The stratification and then the creation of an ignitable mixture in the vicinity of the spark plug can also be influenced by the manufacturing or assembly tolerances. This last point represents the main issue of this method, since a slight variation of the injector orientation or angle due to some tolerances can affect the spray in a direct manner. Recent advances in the injector technology with new spray and jet formation have allowed the introduction of new DISI engines with stratified mode onto the passenger cars market. In 2006, Daimler brought into series a newly developed spray-guided Stratified-Charged Gasoline Engine (CGI), based on optimized piezo-actuated fuel injectors' technology, allowing for a broaden stratified operating mode and improved fuel savings and pollutants emissions. BMW is following the same trend, and presented in 2007 its new 4-cylinder engine based on a similar technology.

### 2.1.3 The Volkswagen FSI<sup>®</sup> Engine

The combustion process of the Volkswagen FSI<sup>®</sup> engine investigated during the present work is a tumble-based, air-/wall-guided process. Volkswagen unveiled the technology presented here in 1999 and has applied it to different engines size and capacity.

The mixture is guided simultaneously via the air motion and the piston bowl, as indicated in Figure 2.4.

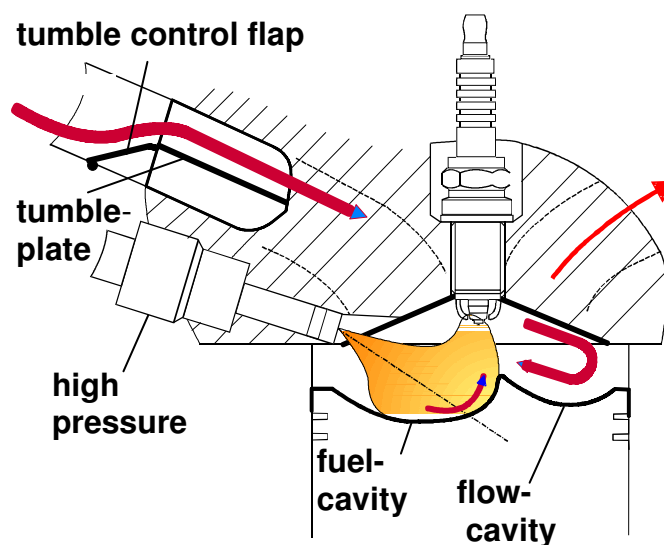
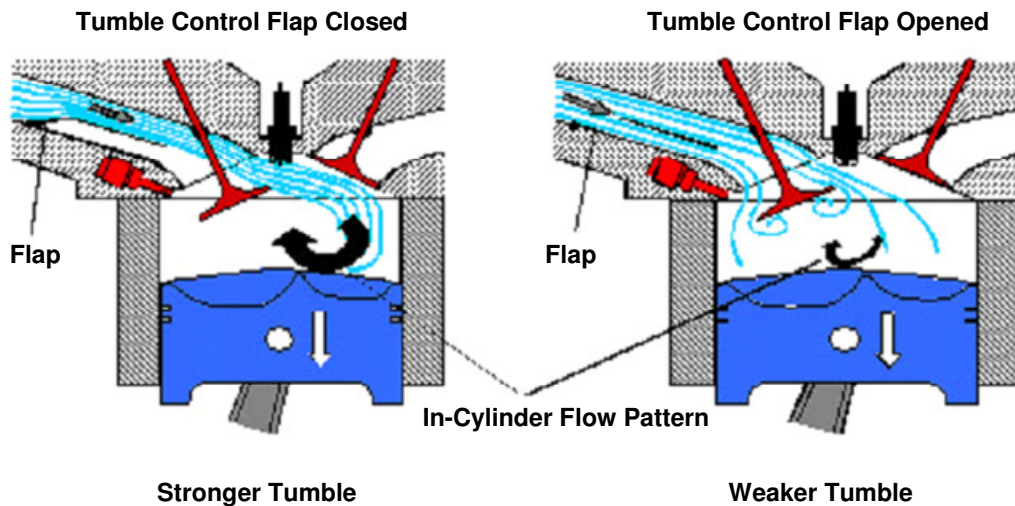


Figure 2.4: Combustion concept of the Volkswagen FSI<sup>®</sup> engine [62]

The induction port is designed as a charge port with moderate tumble intensity, and is divided into an upper and lower half by a cast-in tumble plate. For generating the charge motion in the lean stratified charge mode, a variable tumble system with a tumble control flap is used in the intake port, upstream of the intake valves. As a result, in stratified charge operation while the flap is closed, the flow in the upper part of the port cross-section is accelerated and tends to enter the combustion chamber preferably over the upper edge of the valve, generating an intensive tumble flow (Fig. 2.5).

The piston is presenting a particular shape, with a fuel cavity on the inlet side and a flow cavity on the exhaust side. The direction of the tumble flow during the compression stroke is influenced to a large extent by the port geometry and by the inclination of the flow cavity. Thus, the common action of the fuel cavity and the competing tumble flow is generating and directing the inflammable “cloud” close to the ignition point. Under these conditions, the engine is operating in lean combustion mode. Alternatively, at higher loads of the engine, a homogeneous mixture is used, no longer requiring this strong localisation of the flow.



**Figure 2.5: Schematic influence of the tumble control flap position on the in-cylinder air-flow pattern**

Although the main objective of all these different combustion concepts were to achieve major fuel consumption savings (up to 15% according to certain sources under the European driving cycle, compared to an equivalent Port Fuel Injection engine), large cycle-to-cycle variations were observed, especially in the stratified lean mode, leading to an unbalanced engine performance, and even causing misfire and incomplete combustion with high raw emissions.

## **2.2 Engine Cycle-to-Cycle Variations**

The engine cycle-to-cycle variations are recognised as a major limitation of the performances of the direct-injection spark-ignition engines, and more particularly at lean-burn operating conditions (see for example [7, 44, 88]). Diesel engines are lesser exposed to this problem than gasoline engines, due to the difference of ignition process. In the case of gasoline engine, the reason is the fixed location of the external ignition source, namely the spark electrode, whereas in the Diesel case, the combustion is ignited at the position with the optimal thermodynamic conditions.

All the internal engine processes such as the in-cylinder airflow or the fluid phase motion are characterized by their turbulent nature. The resulting stochastic variations are leading to variable conditions for the combustion to initiate and propagate. Finally, the cycle-to-cycle variations observed in the combustion process are influencing the global engine stability and its emissions level. These emissions can only be partially reduced using exhaust aftertreatment systems, however this represents an important issue, since the emissions need to be significantly decreased in order to fulfil future regulations. Therefore, the understanding of the origins of cyclic variations is of primary interest to be able to control and reduce them.

### **2.2.1 Origins of the Engine Cyclic Variations (ECV)**

The presence of cycle-to-cycle variations in internal combustion engines (ICE) is inherent to their operating mode and to the large amount of parameter at stake in the combustion process. Although engineers and scientists have been aware of this phenomenon very early in the history of ICE, the systematic investigation of engine cyclic variations only started from the beginning of the sixties.

From that period, the effects of cyclic variations in combustion and subsequent pressure development have been measured in various ways, ranging from flame front displacement speed, to maximum rates of pressure rise in cylinder, peak pressures and their crank-angle occurrences, to such integral parameters as indicated mean effective pressure (IMEP). An exhaustive literature survey about this early phase of investigations in ECV can be found in the work of Young [143]. Even if those studies were based on homogeneous spark-ignition engines, their phenomenological observations stated the premises for future investigations.

As main output of these research works, a categorization between the origins of ECV has been formulated, differentiating the influencing factors from chemical nature to the physical ones. Thus, such factors as the equivalence ratio, the quantity of burnt gases, or the fuel type are considered as chemical factors, mostly influencing the mixture quality or the dilution, and impacting the flame speed. Any modification of these parameters, away from the “best-power” conditions, will slow down the flame kernel development and increase the cyclic variations. Also related to these parameters, dealing with the combustion quality, the concept of prior cycle’s influence (or history) appeared later (see Chiriac and Apostolescu [27]). This concept describes the deterministic effect of an incomplete combustion or of the composition and quantity of residual gases on the successive cycle fluctuations.

On the other hand, physical factors are also recognized to strongly influence the occurrence of cycle-to-cycle variations. Amongst them, the mixture motion and preparation, ignition characteristics with the spark location, number of ignition sources, or spark timing, as well as the combustion chamber geometry and the compression ratio are playing a major role.

However, above all of these different factors, it was already assumed that cycle-to-cycle fluctuations in mixture motion, and more explicitly in the velocity field, was the main cause of cyclic combustion variations. Some experimentalists such as Broeze [21], Vichnievsky and Sale [134], Soltau [122] or Patterson [100] have identified the stabilizing effect of an organized in-cylinder flow motion such as swirl on combustion and pressure development.

But at that time, neither experimental nor numerical solutions were then available to get the required insight into the fluid mechanics of the gas motion to support their observations.

### **2.2.2 Effects of In-Cylinder Flows and Role of Turbulence**

Since the mixture motion was deemed most responsible for the cyclic variations, in-cylinder flow investigations have intensified. Numerous works showing evidences of the importance of in-cylinder fluid flows for controlling the combustion process have been published in the last

decades (as, for examples, in [11, 63, 79, 142]). For that purpose, local velocity correlations were mostly used, being measured by punctual systems such as Hot Wire Anemometry or optical techniques like Laser Doppler Velocimetry.

But the continuous improvements in terms of non-intrusive optical measurement techniques associated to the emergence of Computational Fluid Dynamics offered new efficient tools to the researchers in order to better understand the processes related to in-cylinder flow fluctuations. Thus, techniques such as Particle Image Velocimetry have been applied to internal engine applications, in order to capture the full velocity field in 2-dimensional 2-components (2D 2C) and 3-dimensional 3-components (2D 3C). One of the first detailed PIV analyses in an engine has been realized by Reuss et al. [108], who described the turbulent flow according to the strain rate and the vorticity, since these flow properties were known to affect the burning rate of both laminar and turbulent flames [65, 140]. In a following publication [109], the same authors reaffirmed that the small-scale structures that they found in the filtered velocity, vorticity and strain-rate distributions, are measures of coherent structures that exist in the flow.

Successive qualitative and quantitative flow visualization experiments, such as the work from Khalighi [74], are highlighting the fact that generating a large vortex in the engine cylinder during the intake process is probably the most promising way to achieve fast burning rate. Indeed, it has been shown that a well defined swirl or tumbling flow structure is providing a more stable engine running process, breaking up later in the combustion phase, and therefore, giving higher turbulence during combustion. Additionally, they were able to observe the strong influence of the intake configuration, or design, on the in-cylinder flow structure.

With the last point mentioned above, is rising the question of intake port-flow stability. Based on the former observations, according to the role of the in-cylinder flow and turbulence on the overall combustion performance, it can be supposed that most of the instabilities are induced by the intake-port conditions. The works of Bensler et al. [15] has demonstrated that the swirl motion generated by the intake port of a gasoline engine was actually suffering large fluctuations even under stationary flow conditions. The objective of the authors was to propose a method to characterize cylinder heads by computing a so-called Swirl or Tumble Stability Number. The main advantage of their technique was the possibility to study the instantaneous behaviour of the rotational vortex within the cylinder, as well as the evolution of the swirl (or tumble) number over time. Their observations draw a direct link between the intake port induced perturbations, upstream of the cylinder, and the fluctuations observed in the swirl (or tumble) process, supposed to assist in establishing an organised structured flow field inhibiting undesirable fluctuations and improving engine cyclic stability.

### **2.3 Outlook for the Current Analysis**

In spite of all the progresses realised in the combustion process lately, cycle-to-cycle variations are still encountered in direct injection spark ignition engines. The lean stratified-charge generated by an air-/wall-guided concept, thus using internal aerodynamics to control the mixture formation, are particularly sensitive to intake-flow conditions. Hentschel et al. [62], after having studied the spray formation under constant and reproducible conditions in a pressure chamber, and its influence on mixture formation in a transparent DISI motored engine, concluded that the higher level of cyclic variations measured in the real engine were related to the fluctuations of the in-cylinder flow, not to the fuel spray.

Although a multitude of investigations have been conducted in this type of engines, no concrete elements concerning the origins of cycle-to-cycle variations could be stated. One of the main reasons is that, from an aerodynamic simulation perspective, a DISI intake manifold/port is an extremely major challenge. Indeed, it combines, inside a wall-bounded geometry, many of those difficult flow features such as high streamline curvature, pressure gradients, stagnation regions,

separation and re-circulation. Under such stringent conditions, it is difficult to differentiate the sources of perturbations, which can combine themselves, later in the cylinder. The number of bluff-body features in the geometry of a gasoline intake port, such as the one investigated later, that create separated wake flows and associated unsteady vortex shedding structures is rather high. Amongst these features, the tumble control flap, the horizontal flow splitter (or cast-in tumble plate), the port elbow, the valve stem or the valve head itself can all constitute potential flow perturbation sources.

In order to distinguish the contribution of each of the previously mentioned geometrical features to the fluctuations of the tumble structure in cylinder, a stationary port flow rig can be utilised, as discussed by Campbell et al. in [22]. Even if the information obtained in such a system is obviously not corresponding to the final conditions reigning at the end of the compression stroke, when the piston nears TDC, the turbulence development so obtained is responsible for the creation and the stability of the tumble structure, as can be found in a motored engine. Indeed, Shuliang et al. [118] have compared the in-cylinder tumble characteristics delivered by the analysis of a steady flow rig and the corresponding SI motored engine. They have shown that the tumble speed and resulting tumble ratios were very well matching for a given piston position range (crank angle range) and under consideration of some required corrections due to the compression ratio and the volumetric efficiency.

Thus it will be possible to characterize the instantaneous velocity field and turbulence structures, which are directly influencing the tumbling flow. The tumble motion is ensuring the transport of kinetic energy throughout the compression phase until it breaks-up again in smaller scales through the *Kolmogorov cascade* (see §3.1.1), and contributes to the mixing process and later the development of the flame kernel.



### 3 Turbulent Flows in Internal Combustion Engines: Description, Modelling & Visualization

As described earlier, turbulence is playing a key-role in the complete engine cycle process, directly influencing the general flow pattern, as well as the fuel / air mixture, and finally the combustion stability. According to this observation, the need to accurately model the phenomenon has increased and is of first interest nowadays in order to develop more reliable simulation tools. Before getting into the presentation of the different numerical models, some precisions concerning the nature of turbulence have to be given.

#### 3.1 Description of Turbulence

##### 3.1.1 Spectral Definition of Turbulent Flows

Although turbulence is not precisely defined, it is possible to describe it according to the common characteristics of the turbulent flows due to the fact that most flows occurring in nature are turbulent (laminar behaviour being an exception).

Turbulence is an eddying motion that exists at high Reynolds numbers, which means when the inertial forces are much larger than the viscous ones. As presented in Figure 3.1 below, turbulence has a wide spectrum of eddy sizes with a corresponding spectrum of fluctuation frequencies. At this point, it is important to notice that a continuous spectrum is characteristic of turbulent flows in contrast to the spectra with discrete frequencies in unsteady laminar flows. Turbulence has prevailing rotational motion that can be thought of as a tangle of vortex elements with highly unsteady vorticity vectors that are aligned in all directions. The largest eddies have sizes on the same order of magnitude as the flow domain, low frequencies, and are effected by the boundaries and the mean flow. The smallest eddies, on the other hand, are determined by the viscosity of the fluid and their high frequency fluctuations. As the Reynolds number of a given flow increases, the width of the spectrum, or the difference between the largest and smallest eddies, increases.

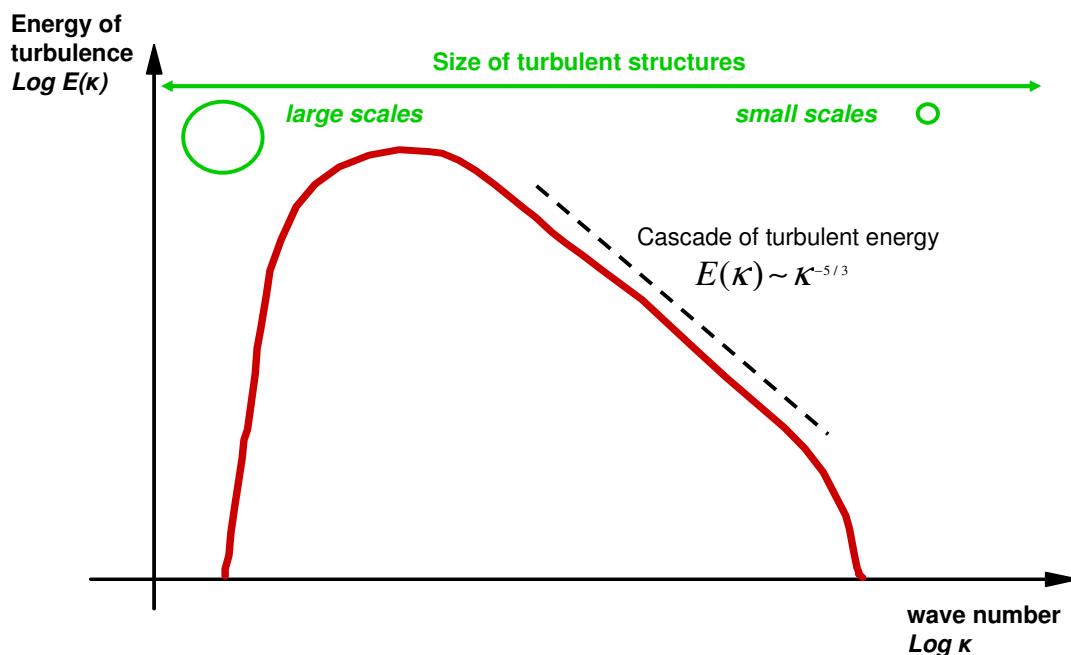


Figure 3.1: Energy spectrum for homogeneous isotropic turbulence.

The large eddies extract kinetic energy from the mean motion and feed it to the large-scale turbulent motion. The eddies may be considered as vortex elements that stretch each other. Due to this vortex stretching, energy is passed down the *cascade* to smaller and smaller eddies until viscosity causes the dissipation of the eddies. The slope of the cascade process has been revealed by the investigations in isotropic turbulence carried out by Kolmogorov [77] and his *similarity considerations*, setting a relation between the turbulent energy and the wave length uniquely determined by  $\epsilon$ :

$$E(\kappa) = c_K \epsilon^{2/3} \kappa^{-5/3}, \quad (3.1)$$

where  $c_K = 1.5$  is the universal Kolmogorov constant. This relation is also known as the “-5/3 – power-law”.

Other similarities have been established, notably by Heisenberg [60], who shown that the shape of the spectrum for the highest wave numbers can be defined by  $E(\kappa) \sim \kappa^{-7}$ .

The rate of energy dissipated is determined by the large-scale motion although dissipation occurs at the smallest scales. It is important to note that viscosity does not determine the amount of dissipated energy, but only the scale at which dissipation occurs.

Since the size of the large eddies is on the order of the flow domain, their motion strongly depends on the boundary conditions of a problem. The preferred flow direction of the mean flow is imposed on the large-scale turbulent motion, which makes the flow strongly anisotropic. With the cascading process, the direction sensitivity of the flow is diminished, and at high Reynolds number flows, the small-scale dissipative motion is isotropic. According to the work of Kolmogorov [76, 77], the *locally isotropic turbulence* is uniquely determined by the two quantities  $\nu$  and  $\epsilon$ , namely the kinematic viscosity and the eddy dissipation rate. They yield as a length scale of the fine structure of the turbulence, the *Kolmogorov length*:

$$l_K = \eta = \left( \frac{\nu^3}{\epsilon} \right)^{1/4}, \quad (3.2)$$

and the *Kolmogorov time scale*:

$$t_K = \left( \frac{\nu}{\epsilon} \right)^{1/2}. \quad (3.3)$$

Thanks to the scale-invariance of the eddy dissipation rate  $\epsilon$ , the characteristic length associated to the larger integral eddies can be derived and yields:

$$l_i = \frac{k^{3/2}}{\epsilon}, \quad (3.4)$$

with  $k$ , the turbulent kinetic energy, defined by the integral of the turbulent energy over the complete range of wave numbers (corresponds to the area under the red curve on Figure 3.1):

$$k = \int_0^{\infty} E(\kappa) d\kappa. \quad (3.5)$$

Then, similarly with the Kolmogorov scales, the integral time scale can be determined and reads:

$$\tau = \frac{k}{\varepsilon}. \quad (3.6)$$

For practical purpose and, more precisely, for the first approximation of the time-step required to setup the transient simulation of a wall bounded turbulent flow, the estimates presented in Table 3-1 are very useful.

**Table 3-1: Empirical estimation for scales of turbulence [5]**

Category	Characteristic Length	Frequency
Largest Eddies	$l_L \approx \frac{d}{2}$	$f_l \approx 0,4 \frac{\bar{u}}{d} \text{Re}^{\frac{1}{8}}$
Energy Containing Eddies	$l_e = 0,005d \text{Re}^{\frac{1}{8}}$	$f_e \approx 4 \frac{\bar{u}}{d}$
Most Dissipative Eddies	$l_d = 20d \text{Re}^{-0,78}$	$f_d \approx 0,02 \frac{\bar{u}}{d} \text{Re}^{0,56}$
Kolmogorov Eddies	$l_K = \eta = 4d \text{Re}^{-0,78}$	$f_K = \frac{v}{\eta} \approx 0,06 \frac{\bar{u}}{d} \text{Re}^{0,56}$

In the table above,  $d$  represents a characteristic length of the geometry considered (channel height, duct diameter...).

According to the estimate of the characteristic frequency of the most dissipative scales and the experience gained with the numerical tool used in this work, CFX, it is possible to determine a time-step, based on the criterion that at least twenty iterations per period are required

$\left( \Delta t = \frac{1}{20 \cdot f_d} \right)$ . An estimation of the total simulation time can also be obtained by defining a

duration of ten times the period of the largest eddies  $\left( t = 10 \cdot \frac{1}{f_l} \right)$ .

### 3.1.2 Moments Measure of Velocities Distributions

The physical phenomenon of turbulence is considered as random, which means that each time history of the phenomenon of interest, obtained per measurement or simulation in a finite time, represents a unique set of circumstances. In other words, this set of data is not likely to be repeated in other independent acquisitions or computations of the phenomenon. Consequently, to fully define all properties of the flow investigated, it is necessary to consider the ensemble of all time history information available that, for usual engineering applications, is tending towards infinite. Hence, the instantaneous amplitude of the phenomenon at a specific time in the future or from different experiment or simulation cannot be determined from an exact equation, but instead, can be described in statistic or probabilistic terms.

For concrete applications, the properties of the instantaneous velocity field of a turbulent flow can often be closely approximated through the knowledge of only two average properties that describe the central tendency and dispersion of the data. But different quantities reflecting the distribution of fluctuations within the flow can also be examined to improve the understanding of in-cylinder flow turbulence.

In the following paragraph, only the principal definitions of the statistical terms of interest will be given. For more details about this particular description of turbulence, the reader is advised to refer to [14, 130].

The statistical description of turbulence is supplying the definitions of various terms, based on the probability density function applied to the instantaneous velocity field. Thus, for an instantaneous velocity field,  $\tilde{u}$ , the Reynolds decomposition reads:

$$\tilde{u}(x,t) = U(x) + u(x,t) \quad (3.7)$$

with  $U$  the mean value and  $u$  the fluctuation of the velocity.

By averaging the probability density function (pdf),  $f(\tilde{u})$ , over time, some mean values are defined as power of  $\tilde{u}$  and are called *moments*.

The first moment is the familiar mean value, defined by:

$$U \equiv \int_{-\infty}^{\infty} \tilde{u} f(\tilde{u}) d\tilde{u} \quad \text{where} \quad \int_{-\infty}^{\infty} f(\tilde{u}) d\tilde{u} = 1 \quad (3.8)$$

The second central moment is also a very familiar quantity to describe the amplitude of fluctuations and is known as the variance (square of the standard deviation  $\sigma$  or rms):

$$\sigma^2 \equiv \overline{u^2} = \int_{-\infty}^{\infty} u^2 f(\tilde{u}) d\tilde{u} \quad (3.9)$$

These two first moments are the most popular probabilistic criteria used to describe a turbulent flow; the mean value defines the central tendency of the random process, while the variance defines its dispersion. Thus, the variance constitutes a measure of how steady or unsteady the flow is. It has statistical relevance as well as physical, as it is related to the turbulent kinetic energy  $\overline{u^2}$ .

In the same way, some higher order central moments can be defined. An interesting factor is the third central moment due to the fact that this value is representative of the asymmetry of the function. The common formulation of this parameter is written as follows:

$$skew = \frac{\overline{u^3}}{\sigma^3} = \frac{1}{\sigma^3} \int_{-\infty}^{\infty} u^3 f(\tilde{u}) d\tilde{u} \quad (3.10)$$

where the skewness,  $skew$ , is a dimensionless measure of the asymmetry of the pdf. Indeed, this criterion is an indicator of the general shape of the pdf, and as soon as  $skew \neq 0$ , it means that the probability function has a non-Gaussian distribution. A physical interpretation of this phenomenon is the presence of a preferred domain for the velocity fluctuations, either in the upper or in the lower range. In certain cases, where a succession of positive and negative skew can be observed, one can even speak about flow intermittency, with eddying structures in contra-rotating directions.

However, at this stage, it has to be mentioned that, obviously, the higher the order of the moment is, the higher the uncertainty rises. Therefore, some precautions need to be taken by analyzing the skewness variable since the 3rd order can accentuate some numerical errors occurring during, for example, a CFD computation.

### 3.2 Numerical Models and Issues

In general, multidimensional flow problems, such as turbulence, are governed by conservation principles for mass, energy and momentum. The application of these principles yields a set of partial differential equations in terms of time and space, known as the Navier-Stokes equations. Thus, these governing equations for fluid mechanics are “simply” a mathematical realization of conservation of mass, conservation of linear momentum and, in non-isothermal flows, conservation of energy (first law of thermodynamics). In the case of compressible flows, the Navier-Stokes equations are taking the following form for mass conservation

$$\frac{\partial \rho}{\partial t} + \frac{\partial}{\partial x_i}(\rho u_i) = 0, \quad (3.11)$$

and conservation of momentum, based on the principle that the temporal change of the momentum equals the sum of all external forces acting on the control volume considered

$$\frac{\partial u_j}{\partial t} + u_i \frac{\partial u_j}{\partial x_i} = -\frac{1}{\rho} \frac{\partial p}{\partial x_j} + \frac{1}{\rho} \frac{\partial \tau_{ij}}{\partial x_i} + F_j, \quad j = 1, 2, 3 \quad (3.12)$$

The first term on the right hand side of Eq. ( 3.12 ) denotes the pressure gradient in direction  $x_j$ , the second term includes the stress tensor

$$\tau_{ij} = \begin{pmatrix} \tau_{x_1 x_1} & \tau_{x_1 x_2} & \tau_{x_1 x_3} \\ \tau_{x_2 x_1} & \tau_{x_2 x_2} & \tau_{x_2 x_3} \\ \tau_{x_3 x_1} & \tau_{x_3 x_2} & \tau_{x_3 x_3} \end{pmatrix}, \quad (3.13)$$

and  $F_j$  represent the external forces.

The viscous stress tensor  $\tau_{ij}$  accounts for momentum transfer due to friction. For Newtonian fluids, Stokes' postulation (1845) states that the shear stresses are proportional to the velocity gradients, with the molecular viscosity as the proportionality factor:

$$\tau_{ij} = \mu \left( \frac{\partial u_i}{\partial x_j} + \frac{\partial u_j}{\partial x_i} \right) - \delta_{ij} \frac{2}{3} \mu \frac{\partial u_i}{\partial x_i}. \quad (3.14)$$

$\delta_{ij}$  is the Kronecker delta. Since most of the flows studied here are considered incompressible ( $\partial u_i / \partial x_i = 0$ ) the second term on the right hand side of Eq. ( 3.14 ) cancels out, such that Eq. ( 3.12 ) becomes

$$\frac{\partial u_j}{\partial t} + u_i \frac{\partial u_j}{\partial x_i} = -\frac{1}{\rho} \frac{\partial p}{\partial x_j} + \frac{\mu}{\rho} \left( \frac{\partial^2 u_j}{\partial x_i \partial x_i} \right) + F_j, \quad j = 1, 2, 3. \quad (3.15)$$

In the following paragraphs, the structure of the presentation of the different turbulence models does not reflect any increasing level of complexity, but more on the chronology of their implementation in the software employed.

### 3.2.1 Direct Numerical Simulation (DNS)

This method represents the simplest conceptual approach and also the most accurate one to solve the fluid mechanics governing equations. As its name indicates, DNS is proposing to treat the Navier-Stokes equations directly on a discretized grid that has to be fine enough to resolve the smallest length scales of the flow problem without the need of any turbulence model. These smallest length scales are defined by the size of the smallest eddies, which are of the order of the Kolmogorov scale, and are representing the most dissipative turbulent structures for turbulent kinetic energy (see Chapter 3.1).

The strong dependency of the turbulence scales with the Reynolds number constitutes the principal limiting factor of the method as they are becoming smaller for increasing Reynolds numbers. Indeed, in order to resolve the whole range of spatial and temporal turbulence scales, the numerical grid has to fulfil several requirements.

First of all, the number of grid points  $N$  along a given mesh direction with increment  $h$  must be superior to  $L$  so that the integral scale is contained within the computational domain. This gives the following relation:

$$Nh > L \quad (3.16)$$

On the other side of the range, the Kolmogorov scale needs to be taken into account, which gives a constraint on the grid point spacing:

$$h \leq \eta \quad (3.17)$$

Since

$$\varepsilon \approx \frac{u'^3}{L} \quad (3.18)$$

where  $u'$  is the Root Mean Square (RMS) of the velocity, by injection in the previous expressions and substitution with the Reynolds number definition

$$\text{Re} = \frac{u' L}{\nu} \quad (3.19)$$

it implies that a three-dimensional DNS requires a number of points,  $N^3$ , satisfying

$$N^3 \geq \text{Re}^{9/4} \quad (3.20)$$

This very high spatial requirement is accompanied with a constraint on the time integration of the solution, which has to “catch” the displacement of the fluid particles of not more as a fraction of the spacing increment  $h$ . Thus the chosen time step  $\Delta t$  must comply with the following condition on the Courant number [1, 31]:

$$C = \frac{u' \Delta t}{h} < 1, \quad (3.21)$$

and the total simulated time interval is proportional to the turbulence time scale  $\tau = \frac{L}{u'}$ .

By combining the previous relations with Eq. ( 3.17 ), it derives that the number of  $\Delta t$  is proportional to  $L/(C\eta)$ . Finally, while considering the definition of  $Re$ ,  $\eta$  and  $L$  given earlier, it follows that

$$N_{\Delta t} \sim \frac{L}{\eta} \sim Re^{3/4}. \quad (3.22)$$

To summarize the former observations, both the grid size and the time integration are growing as a power law of the Reynolds number, implying huge requirements in terms of storage memory and a total number of numerical operations scaling with  $Re^3$  [102].

Consequently, even with the expected rapid progress in computer systems and massive parallel clusters, DNS will not be suitable for solving engineering problems in the foreseeable future. This method is constrained to fundamental research applications with relatively low Reynolds number flows and geometrically simple domains. In these particular conditions, DNS is providing an invaluable quantitative and qualitative data base for any variable of interest and can be considered as a numerical experiment. In this sense, DNS results can be used to get a better understanding of the complex flow phenomena taking place in turbulence development, and to validate other numerical models.

### 3.2.2 Statistical Models: Reynolds Averaged Navier-Stokes (RANS)

RANS simulation is by far the most applied method in engineering problems to solve the Navier-Stokes equations. Proposed by Osborne Reynolds over a century ago, this statistical description of turbulent flows is based on a decomposition of the instantaneous values of the conserved quantities into a time-averaged (or ensemble-averaged) mean denoted by an overbar ( $\bar{\quad}$ ) and a fluctuating part denoted by the superscript ( $'$ ):

$$u_i(x,t) = \bar{u}_i(x) + u'_i(x,t). \quad (3.23)$$

Then, RANS method represents an ensemble average over the entire range of turbulent eddies, while modeling turbulence effects without a need for the resolution of the turbulent fluctuations. Simulation of the RANS equations greatly reduces the computational effort compared to a Direct Numerical Simulation and for this reason is generally adopted for practical engineering calculations. However, the averaging procedure introduces additional unknown terms containing products of the fluctuating quantities, which act like additional stresses in the fluid. When the Reynolds approach, Eq. ( 3.23 ), is substituted into the conservation equations specified earlier in this chapter, Eq. ( 3.15 ), in absence of external forces, the resulting RANS equations contain one additional term commonly interpreted as the turbulent shear, or Reynolds stress tensor

$$\rho \left( \frac{\partial \bar{u}_j}{\partial t} + \bar{u}_i \frac{\partial \bar{u}_j}{\partial x_i} \right) = - \frac{\partial \bar{p}}{\partial x_j} + \frac{\partial}{\partial x_i} \left( \bar{\tau}_{ij} - \rho \overline{u'_i u'_j} \right). \quad (3.24)$$

The last term above is used to represent the enhancement of the viscous stresses of the conserved momentum by the presence of turbulent eddies in the flow, and is the subject of turbulence modeling. Additional equations of known quantities are required in order to achieve the “closure” of the problem. Closure implies that there are a sufficient number of equations for all the unknowns, including the Reynolds-Stress tensor which resulted from the averaging

procedure. The number and the nature of equations used to close the system define the type of turbulence model, ranging from zero- to multi-equation models. Considering the methods of interest that will be presented and implemented later in this work, only a brief overview of some relevant two-equation models will be given. For further details on other RANS models, refer to [42].

The most widely used modeling strategy is based on the eddy viscosity hypothesis, also known as the Boussinesq approximation (1877), which assumes that the Reynolds stress tensor may be modeled as the viscous stress tensor in Eq. ( 3.14 )

$$-\overline{\rho u'_i u'_j} = \mu_t \left( \frac{\partial \bar{u}_i}{\partial x_j} + \frac{\partial \bar{u}_j}{\partial x_i} \right) - \delta_{ij} \frac{2}{3} \rho k, \quad (3.25)$$

where  $\mu_t$  is referred to as the turbulent viscosity and  $k$  is defined as the kinetic energy of the turbulent fluctuations

$$k = \frac{1}{2} \overline{u'_i u'_i} = \frac{1}{2} \left( \overline{u_1'^2} + \overline{u_2'^2} + \overline{u_3'^2} \right) \quad (3.26)$$

In the contrary to the fully algebraic models or even the one-equation models, the two-equation ones are solving both velocity and length scale using separate transport equations. The following models description is referring mostly to their implementation in the commercial code CFX from ANSYS.

### ***k-ε Model***

As its name indicates, this method is based on the resolution of transport equations for two scalar properties of turbulence. The  $k$ -equation is a model of the transport equation for the turbulent kinetic energy, and the  $\varepsilon$ -equation is a model for the dissipation rate of turbulent kinetic energy. Originally, the  $k-\varepsilon$  model was developed to improve the mixing-length model and to avoid the algebraic prescription of the turbulent length scale in complex flows. Different versions of this model are reported in the literature, notably in [73, 80, 111, 138]. The formulation presented thereafter is resulting from the derivation of the conservation equation for  $k$  as described in various textbooks of fluid mechanics, e.g. [42, 136]. After several mathematical operations, it yields:

$$\frac{\partial k}{\partial t} + \bar{u}_i \frac{\partial k}{\partial x_i} = \frac{\partial}{\partial x_i} \left( \frac{\nu_t}{C_k} \frac{\partial k}{\partial x_i} \right) + \nu_t \frac{\partial \bar{u}_j}{\partial x_i} \left( \frac{\partial \bar{u}_j}{\partial x_i} + \frac{\partial \bar{u}_i}{\partial x_j} \right) - \varepsilon, \quad (3.27)$$

$$\text{with} \quad \nu_t = \mu_t / \rho \quad (3.28)$$

$$\text{and} \quad \varepsilon = \frac{k^{3/2}}{L_t}. \quad (3.29)$$

The former relation takes into account the fact that there is an energy cascade from the largest scales to the smallest ones, and that the energy transferred to the smallest structures is dissipated. Although the derivation of the conservation equation for dissipation is not straightforward and rather complex, it is nevertheless feasible. However, for standard  $k-\varepsilon$  models, a similar



equation as the one developed for  $k$ , Eq. (3.27), is used for the transport of the turbulent kinetic energy dissipation rate, as follows:

$$\frac{\partial \varepsilon}{\partial t} + \bar{u}_i \frac{\partial \varepsilon}{\partial x_i} = \frac{\partial}{\partial x_i} \left( \frac{\nu_t}{C_\varepsilon} \frac{\partial \varepsilon}{\partial x_i} \right) + C_1 \frac{\varepsilon}{k} \nu_t \frac{\partial \bar{u}_j}{\partial x_i} \left( \frac{\partial \bar{u}_j}{\partial x_i} + \frac{\partial \bar{u}_i}{\partial x_j} \right) - C_2 \frac{\varepsilon^2}{k}. \quad (3.30)$$

According to the present formulation, the relation for the turbulent viscosity is the following

$$\mu_t = C_\mu \rho \frac{k^2}{\varepsilon}. \quad (3.31)$$

Even if the five empirical constants used within this model are not universal, some recommended values could be found in the literature, see [42, 128].

Although  $k - \varepsilon$  models and derivatives such as renormalization group models (RNG) have been (and are still) successfully implemented in numerous engineering applications, insuring a strong numerical stability and fast results, some limitations of the method have been demonstrated. Over estimation of the turbulence level in stagnation regions, or under prediction of the turbulence dissipation in detached regions are counting among the main drawbacks of this methods, which make it not well dedicated for flows under adverse pressure gradient or wall-bounded flows.

### ***k- $\omega$ and Shear-Stress-Transport (SST) Models***

This model has been mainly developed in order to compensate the problem related to the boundary layer definition of the  $k - \varepsilon$  model, which requires the use of complex non-linear damping functions in order to model the flow in the near-wall region. As depicted in Figure 3.3, in the turbulent boundary layer, according to the representation of the non-dimensional velocity  $u^+$  (normalized with  $u_\tau$ ), as a function of the non-dimensional wall distance,  $y^+$ , the thickness of the viscous sublayer is very small ( $y^+ \leq 5$ ).

A standard  $k - \varepsilon$  model would require a low-Reynolds mesh definition in the vicinity of the wall with a resolution of  $y^+ < 0.2$ , whereas a low-Reynolds with  $k - \omega$  formulation would only require  $y^+ < 2$  [6].

As it has been mentioned in the literature survey, §1.2, only low-Reynolds turbulence near wall methods allow to accurately predict the local flow separations occurring in engine ports and influencing the in-cylinder flow. However, in order to guarantee the quality of the flow computation, a fine and relatively expensive resolution of the boundary layer is necessary. When implementing a Low-Reynolds mesh with a  $k - \omega$  SST model, at least 16 points are required within the boundary layer.

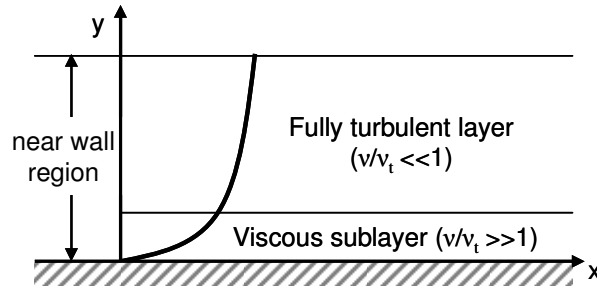


Figure 3.2: Two-layer model for turbulent boundary layers

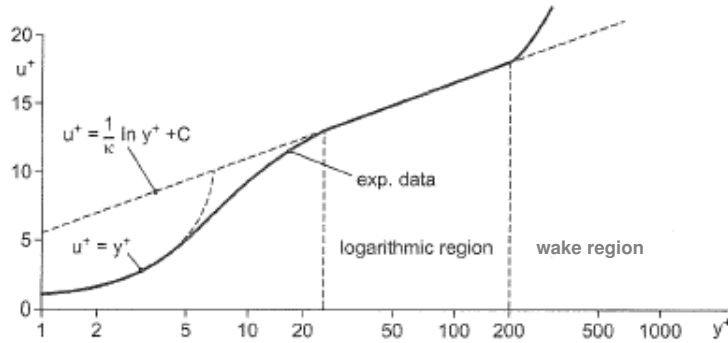


Figure 3.3: Velocity profile of a turbulent boundary layer (reprinted from [128])

However, for most of the industrial applications with wall-bounded flows, even this criterion ( $y^+ < 2$ ) cannot always be fulfilled, this is the reason why some near-wall treatments have been developed for  $k - \omega$  models.

Basically, these models are also solving two different transport equations for two chosen variables, the turbulent kinetic energy  $k$  and the specific dissipation  $\omega$ , also known as the turbulent frequency. In the Wilcox's formulation [137], the turbulence viscosity is modelled as  $\nu_t = k / \omega$  and the two transport equations read

$$\frac{\partial k}{\partial t} + \bar{u}_i \frac{\partial k}{\partial x_i} = \tau_{ij} \frac{\partial \bar{u}_j}{\partial x_i} - \beta^* k \omega + \frac{\partial}{\partial x_i} \left[ (\nu + \sigma^* \nu_t) \frac{\partial k}{\partial x_i} \right], \quad (3.32)$$

and

$$\frac{\partial \omega}{\partial t} + \bar{u}_i \frac{\partial \omega}{\partial x_i} = \alpha \frac{\omega}{k} \tau_{ij} \frac{\partial \bar{u}_j}{\partial x_i} - \beta \omega^2 + \frac{\partial}{\partial x_i} \left[ (\nu + \sigma \nu_t) \frac{\partial \omega}{\partial x_i} \right]. \quad (3.33)$$

A first drawback of the Wilcox model is its strong sensitivity to the free stream and boundary conditions. Indeed, significant variations in the results provided by this method can be observed, depending on the value given for  $\omega$  at the inlet of the fluid domain. In order to prevent this problem from happening, a blending between the  $k - \omega$  in the wall vicinity and the  $k - \epsilon$  model in the outer region has been developed by Menter [90]. This method consists of a transformation of the  $k - \epsilon$  model to the  $k - \omega$  formulation by multiplying the Wilcox model equations by a blending function  $F_1$  and the transformed  $k - \epsilon$  equations by a function  $(1 - F_1)$  before adding the corresponding  $k$ - and  $\omega$ -equations. The blending function depends on the wall-distance: it

is equal to one near the surface and switches over to zero close to the edge of the boundary layer, where the  $k - \varepsilon$  model is recovered.

The blending function  $F_1$  is defined by the following expression:

$$F_1 = \tanh \left\{ \left( \min \left( \max \left( \frac{\sqrt{k}}{\beta^* \omega y}, \frac{500\nu}{y^2 \omega} \right), \frac{4\rho k}{CD_{k\omega} \sigma_{\omega 2} y^2} \right) \right)^4 \right\} \quad (3.34)$$

where  $y$  is the distance to the closest wall,  $\nu$  is the kinematic viscosity,  $\beta^* = 0.09$  and

$$CD_{k\omega} = \max \left( 2\rho \frac{1}{\sigma_{\omega 2} \omega} \frac{\partial k}{\partial x_i} \frac{\partial \omega}{\partial x_i}, 1.0 \times 10^{-10} \right) \quad (3.35)$$

In Eq. (3.35),  $CD_{k\omega}$  stands for cross-diffusion in the  $k - \omega$  model. The blending driven by the function  $F_1$  takes place in the wake region of the boundary layer.

Finally, the Baseline (BSL)  $k - \omega$  model can be written as follows:

$$\frac{\partial k}{\partial t} + \bar{u}_i \frac{\partial k}{\partial x_i} = \tau_{ij} \frac{\partial \bar{u}_j}{\partial x_i} - \beta^* k \omega + \frac{\partial}{\partial x_i} \left[ (\nu + \sigma_k \nu_t) \frac{\partial k}{\partial x_i} \right] \quad (3.36)$$

and

$$\frac{\partial \omega}{\partial t} + \bar{u}_i \frac{\partial \omega}{\partial x_i} = \alpha \frac{\omega}{k} \tau_{ij} \frac{\partial \bar{u}_j}{\partial x_i} - \beta \omega^2 + \frac{\partial}{\partial x_i} \left[ (\nu + \sigma_\omega \nu_t) \frac{\partial \omega}{\partial x_i} \right] + (1 - F_1) 2\sigma_\omega \frac{1}{\omega} \frac{\partial k}{\partial x_i} \frac{\partial \omega}{\partial x_i} \quad (3.37)$$

This BSL model combines the advantages of the Wilcox and  $k - \varepsilon$  models presented before, but still shows some weaknesses. It has been already proved in [90] that this model fails to properly predict the onset and amount of flow separation from smooth surfaces. According to Menter [90], the main reason for this deficiency is that both models (Wilcox and  $k - \varepsilon$ ) do not account for the transport of the turbulent shear stress. In other terms, this means that there is an over prediction of the eddy-viscosity, calling for the use of a limiter within the eddy-viscosity formulation as follows:

$$\nu_t = \frac{a_1 k}{\max(a_1 \omega, |\bar{S}| F_2)} \quad (3.38)$$

$$\text{where } \nu_t = \mu_t / \rho \quad (3.39)$$

According to Eq. (3.38), where  $|\bar{S}|$  represents an invariant of the strain rate,  $|\bar{S}| = (2S_{ij}S_{ij})^{1/2}$ , the maximum value of the eddy viscosity is limited (in turbulent boundary layers) by forcing the turbulent shear stress to be bounded by the turbulent kinetic energy times the constant  $a_1$  ( $a_1 = 0.31$ ). This effect is achieved with an auxiliary function  $F_2$  defined as a function of wall distance  $y$  as:

$$F_2 = \tanh \left\{ \left( \max \left( \frac{2\sqrt{k}}{\beta^* \omega y}, \frac{500\nu}{y^2 \omega} \right) \right)^2 \right\} \quad (3.40)$$

To sum up, the SST model developed and implemented in CFX is based on the  $\omega$ - equation and provides an analytical expression for  $\omega$  in the viscous sub-layer. This turbulence model allows for a near-wall formulation, which gradually and automatically switches from wall-functions to low-Reynolds near-wall formulations.

Finally, all the required model coefficients  $\alpha, \beta, \sigma_k$  and  $\sigma_\omega$  denoted in Eq. (3.41) with the symbol  $\xi$  are defined by blending the coefficients of the original  $k - \omega$  model, denoted as  $\xi_1$ , with those of the transformed  $k - \varepsilon$  model, denoted as  $\xi_2$ , according to the relationship:

$$\xi = \xi_1 F_1 + \xi_2 (1 - F_1) \quad (3.41)$$

**Table 3-2: Modeling constants of the SST model (subscript 1 is used for the  $k - \omega$  model constants, subscript 2 for the  $k - \varepsilon$  model constants)**

$\alpha_1$	$\beta^*$	$\alpha_1$	$\beta_1$	$\sigma_{k1}$	$\sigma_{\omega 1}$	$\alpha_2$	$\beta_2$	$\sigma_{k2}$	$\sigma_{\omega 2}$
0.31	0.09	5/9	0.075	2	2	0.44	0.0828	1	1/0.856

According to the results of an intensive comparison of the performances of various turbulence models (one-equation model from Spalart and Allmaras, two-equations models from Wilcox, Launder-Sharma and Menter), Bardina et al. [10] concluded that the  $k - \omega$  SST model from Menter can be considered as the best model since it did the best overall job in predicting the complex flows involving separation while giving results comparable with the best of the other models for simple flows.

This model has been used as kernel in the CFX solver to develop the DES and the SAS turbulence models employed and described later in this work.

### 3.2.3 Large Eddy Simulation (LES)

Considering the limitations of the different turbulence models evoked earlier, either not suitable for transient flows or computationally speaking prohibitive, another trend has emerged in the 1960's. Some atmospheric scientists developed a technique based on the attractive idea, which was to use temporal and spatial integration schemes of sufficient accuracy to resolve the larger turbulent scales, more relevant and problematic to their meteorological simulations. This leaves the turbulence model (a sub-grid scale model – SGS) to account just for the effects of the more universal and isotropic smaller scales. This is the basis of the Large Eddy Simulation approach. LES is then the methodology of choice to allow the calculation to capture the instability of the shear layer and the development of the coherent structures in the wake, with more accurate prediction of the unsteady forces than can be obtained by steady or unsteady RANS methods.

The separation of scales required between the scales that will be modelled and those that will be solved directly, is made by filtering the flow field. The general form of the filtering operation that will be applied to the governing equations to generate the filtered equations of motion reads [81]:

$$\bar{f}(x) = \int_D f(x') G(x; x') dx', \quad (3.42)$$

where the overbar on  $f$  denotes the filtered (or resolved, or large-scale) variable,  $D$  is the entire domain and  $G$  is the filter function. The filter function determines the cutoff scales under which the smaller structures will be modelled.

Many filters have been developed and used in the past, but the most commonly-used are the sharp Fourier cutoff filter, the Gaussian filter and the tophat filter in real space (see [102, 113] for a detailed description). All of them are presenting advantages and disadvantages, but their selection depends on the numerical technique employed by the solver of choice. For example, some filters such as the tophat function are more appropriate for finite-difference or finite-volume schemes. Independently of the nature of the filter, they all contain a characteristic filter size  $\bar{\Delta}$ . In finite-volume schemes, the filter length scale is represented by a mesh length scale computed from the grid spacing in axial, transverse and spanwise directions, according to the following expression:

$$\bar{\Delta} = (\Delta x \Delta y \Delta z)^{1/3}. \quad (3.43)$$

But another, more conservative, approach can be found and consists on taking the maximum length scale of the computational cell:

$$\bar{\Delta} = \max(\Delta x, \Delta y, \Delta z). \quad (3.44)$$

After having applied the filtering operation (3.42) to the governing equations, the filtered equations of motion, for an incompressible flow of a Newtonian fluid, are taking the following form:

$$\frac{\partial \bar{u}_i}{\partial x_i} = 0. \quad (3.45)$$

$$\frac{\partial \bar{u}_i}{\partial t} + \frac{\partial}{\partial x_j} (\bar{u}_i \bar{u}_j) = -\frac{1}{\rho} \frac{\partial \bar{p}}{\partial x_i} - \frac{1}{\rho} \frac{\partial \tau_{ij}}{\partial x_j} + \nu \frac{\partial^2 \bar{u}_i}{\partial x_j \partial x_j}. \quad (3.46)$$

The filtered Navier-Stokes equations, written above, govern the evolution of the large, energy-carrying, scales of motion. The effect of the small scales appears through a subgrid-scale (SGS) stress term,

$$\tau_{ij} = \overline{\rho u_i u_j} - \rho \bar{u}_i \bar{u}_j, \quad (3.47)$$

that must be modelled.

The definition of the SGS Reynolds stress model is decisive in the implementation of a LES method since it controls its ability to accurately estimate the local mean fluctuations of the small-scale turbulence. Many papers [101, 115, 116, 125, 135] and books [42, 46, 101, 113] have covered and described the concept of filtering and the key issues related to subgrid models. Most of the models, which have been proposed, are semi-empirical SGS models. The simplest and most widely used model is the one due to Smagorinsky [120] that is an adaptation of the RANS mixing length model to LES:

$$\tau_{ij} = -2\rho\nu_{SGS}\bar{S}_{ij} = -2\rho(C_S\bar{\Delta})^2|\bar{S}|\bar{S}_{ij}, \quad (3.48)$$

where the local resolved rate-of-strain tensor is defined by:  $|\bar{S}| = \sqrt{2(\bar{S}_{ij}\bar{S}_{ij})}^{1/2}$ .

The single model coefficient,  $C_S$  or *Smagorinsky constant*, in the case of isotropic turbulence with inertial range spectrum,

$$E(\kappa) = C_\kappa \varepsilon^{2/3} \kappa^{-5/3}, \quad (3.49)$$

takes the following form:

$$C_S = \frac{1}{\pi} \left( \frac{2}{3C_\kappa} \right)^{3/4} \approx 0.17. \quad (3.50)$$

The constant-coefficient Smagorinsky model is the one applied in the numerical solver employed throughout the present study. For the particular application considered and its strong wall-bounded nature, a lower value of  $C_S$  has been used, by setting this coefficient to 0.1.

Obviously, like every empirical method, the need of adaptation of the model according to the flow conditions or even in different regions of a single flow, confer to this approach a lack of universality. This deficiency, as well as the requirement that the filter width  $\bar{\Delta}$  be specified explicitly motivated the search for a more general approach. Even if interesting advances in this field have been done, particularly with the development of dynamic models such as the one proposed by Germano et al. [48] or the more recent deconvolution models (see [41] for a review), there has still not been proved that a single model will be capable of predicting a wide variety of flows without modification.

On the other hand, as can be read in [6], despite the acknowledged limitations of the Smagorinsky constant model, *it has been observed that it is easy to blame the model constant, when other shortcomings, such as a bad representation of the upstream conditions, can affect the flow just as much as a change in the constant value.*

### 3.2.4 A Hybrid Approach: Detached Eddy Simulation (DES)

DES appeared among the CFD environment in the late nineties, with the main objective to conciliate the advantages of LES in “detached” flow regions and the RANS formulation in the “attached” regions, i.e. for the eddies located in the boundary layer. Some important computational cost savings were expected, compared to the prohibitive application of pure LES to complete vehicles simulations or complex wall-bounded flows. DES belongs to the category of *seamless* hybrid turbulence models, such as the Limited-Numerical-Scales (LNS) from Batten et al. [12] or the Two-Scale Method from Willems [139], in opposition to the *zonal* methods (for more details please refer to [8, 35]). Both categories are differentiating from each other by the transition between RANS and LES formulations and the treatment of the so-called *grey area* existing in this particular region.

From the time of emergence of hybrid approaches, the main issue was to define the parameters controlling the transition between the two different models used. In 2001, Strelets [129] developed a so-called SST-DES formulation based on the idea to switch from the Shear-Stress Transport (SST) RANS model, from Menter [89], to a LES model in regions where the turbulent length,  $L_t$ , predicted by the RANS model is larger than the local grid spacing.

The equation of the turbulent kinetic energy ( $k$ ) from the SST model reads:

$$\frac{\partial(\rho k)}{\partial t} + \frac{\partial}{\partial x_i}(\rho \bar{u}_i k) = \underbrace{\tilde{P}_k}_{\text{Production term}} - \underbrace{\beta^* \rho k \omega}_{\text{Dissipation term}} + \underbrace{\frac{\partial}{\partial x_i} \left[ (\mu + \sigma_k \mu_t) \frac{\partial k}{\partial x_i} \right]}_{\text{Diffusion term}} \quad (3.51)$$

The DES modification from Strelets is occurring in the destruction term as follows:

$$\varepsilon = \beta^* k \omega \rightarrow \beta^* k \omega \cdot F_{DES} \quad (3.52)$$

with

$$F_{DES} = \max\left(\frac{L_t}{C_{DES} \Delta}, 1\right) \quad (3.53)$$

where  $L_t$  is the turbulence length scale predicted by the RANS model,  $L_t = \sqrt{k} / (\beta^* \omega)$ ,  $\Delta$  is the local grid spacing,  $\beta^*$  and  $C_{DES}$  are two constants.

The model used in this paper is the one implemented in CFX 10 from Ansys, which is offering an improved formulation of the zonal treatment of DES [96]. The former models (Spalart and Strelets) were lacking a mechanism for preventing the limiter to become active in the attached portion of the boundary layer, a phenomenon that could lead to grid-induced flow separation [96]. In order to avoid or reduce this counter-effect, the present model is using the blending factors employed by the zonal formulation of the SST model to shift between the  $k$ - $\omega$  model in the wall vicinity to  $k$ - $\varepsilon$  away from it. This differentiation between the boundary layer and the free flow field can also be used here as blending functions for the DES limiter.

$$F_{DES-CFX} = \max\left\{\frac{L_t}{C_{DES} \Delta} (1 - F_{SST}), 1\right\} \quad (3.54)$$

with

$$F_{SST} = 0, F_1 \text{ or } F_2 \quad (3.55)$$

In the equation above,  $F_{SST}=0$  recovers the Strelets model;  $F_1$  and  $F_2$  are the two blending functions of the SST model given in Eq. (3.34) and (3.40). By forcing the solver to work with one function or the other allows the control of the sensitivity of the model in shifting between RANS and LES.

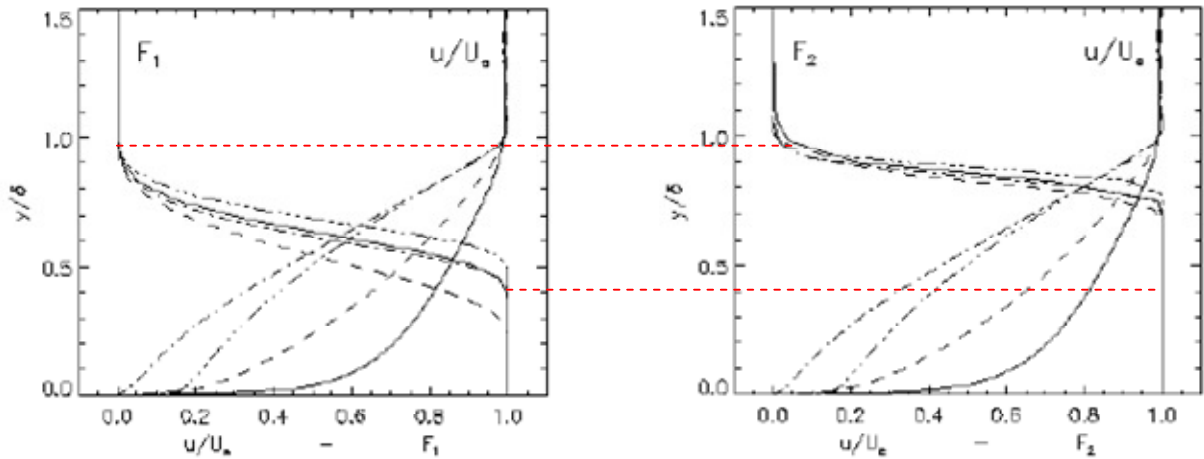


**Figure 3.4: Blending functions for the SST model as a function of the non-dimension wall distance  $y/\delta$  (left:  $F_1$ , right:  $F_2$ ) (reprinted from [96])**

Figure 3.4 is showing the evolution of the two different blending functions used by the SST model and allows comparing the difference of sensitivity between both functions for the shift between  $k-\omega$  and  $k-\varepsilon$ .

Considering that the DES SST model is based on both the  $k-\omega$  and  $k-\varepsilon$  models, the constant  $C_{DES}$  from Eq. (3.54) needs to be calibrated for each of them separately. Then, a blending is used to generate the overall model constant as follows:

$$C_{DES} = C_{DES}^{k-\omega} \cdot F_{SST} + C_{DES}^{k-\varepsilon} \cdot (1 - F_{SST}). \quad (3.56)$$

According to the work of Strelets [129], for the hybrid model employed later in this study, these two constants are taking the following values:

$$C_{DES}^{k-\omega} = 0.78 \text{ and } C_{DES}^{k-\varepsilon} = 0.67. \quad (3.57)$$

With regard to the numerical treatment of the DES model in CFX, the same numerical schemes as the one suggested by Strelets [129] are used, that is to say a second-order upwind-biased scheme for the RANS region and a second-order central difference scheme for the LES region. This is necessary to avoid excessive numerical diffusion in the LES regions resulting from an upwind biased scheme.

Most of the references available in the literature are referring to applications related to external aerodynamics or bluff-body flows. This is mainly due to the original motivation of industrials and researchers to develop an alternative to LES for aeronautical cases, especially to perform full aircraft calculations at flight Reynolds numbers. Some complementary and quite exhaustive surveys are given in [102, 114, 126]. As general conclusion from the various analyses of massively separated flow fields, it was stated that DES is presenting some very positive features. Indeed, it has been observed that DES naturally provides unsteady information of the turbulent flow, since small-scale turbulence is generated by the shear-layer instabilities present in this type of flows. But it has been shown that the good performance of a DES simulation is strongly connected to the grid quality and refinement in critical regions. This is the only way to ensure, in the RANS region, the mixing length to be much smaller than the grid size, while in the LES region, where the resolved eddies dominate the momentum and energy transport, the opposite must occur.



On the other hand, only few reports are concerned with internal flows and those are mainly dealing with simulations of academic channel flows. For real industrial applications of wall-bounded flows, where turbulent separation in a complex 3-d geometry occurs, modelling errors in the RANS region may become significant.

This could be the case in engine applications and more particularly in the intake port, where flows separation in the flow splitter or in the port elbow may occur. In the work from Sohm [121], the potential of DES to predict engine cyclic variations has been investigated. Despite the lack of validation data, encouraging results have been obtained, showing the capability of this hybrid model to account for the turbulence development and resulting fluctuations of the velocity field within the cylinder. Nevertheless, for this study, some hypotheses and compromises had to be made in order to be able to compute several engine cycles. Among those “restrictions”, the author had to use rather coarse grids (up to 3 million elements at the Bottom Dead Centre), especially in the engine port, upstream of the valves. The low treatment of the engine in-flow probably affected the computations based on a steady configuration (without moving boundaries). The assumption that the flow characteristics in the cylinder are essentially driven by the shear layer induced turbulence in the wake of the valves was utilized to justify the use of RANS modelling in the intake port region. This led to the conclusion that the discrepancy observed in different sections of the cylinder was likely to be related to some manufacturing tolerances. This work also pointed out the difficulty to represent and quantitatively compare instantaneous results of fluctuating quantities.

The present study will be based on the same SST-DES model implemented in ANSYS-CFX. The focus will be put on the accurate resolution of the intake flow condition, with high mesh-densities for a precise resolution of both the core of the flow and the boundary layers. Some new post-processing methods will also be proposed in order to better visualize and quantify the turbulent structures developing in Direct Injection Spark-Ignition engines.

### 3.2.5 An Alternative: Scale Adaptive Simulation (SAS)

The SAS turbulence model first appeared in 2003, in a paper published by its inventors, Menter and coworkers [97]. They have demonstrated that a derivation of RANS model, the SAS formulation, was able to detect the already resolved structures in the flow and thereby to allow the evolution of a turbulent spectrum in unstable flow regions.

Usually, a main characteristic of any RANS formulation such as the well-known two-equation models is their intrinsic dissipative nature. Consequently they are not very sensitive to instabilities that could lead to a fully developed unsteady flow, unless the instabilities are above a certain critical level.

However, with regards to the fundamental similarity existing between the momentum equations resulting from RANS or from LES approach, there is no reason for an improved RANS model not to be able to predict turbulent structures. According to Menter [97], the major problem only rests on the level of eddy viscosity provided by the turbulence model, which is overestimated by the standard 2-equations formulations in unsteady conditions. Thus, the idea behind the SST  $k - \omega$  based SAS model is to add a production term to the  $\omega$  -equation, which is sensitive to resolved fluctuations.

Basically, when the flow equations resolve turbulence, the length scale based on the velocity gradients is much smaller than the one based on time-averaged quantities. It is for this reason that Menter proposed to use the von Kármán length scale,  $L_{vK}$ , as scale determining variable for his SAS model. Hence, the information provided by the von Kármán length-scale allows the SAS model to dynamically adjust the resolved structures in a URANS simulation, which results in a

LES-like behavior in unsteady regions of the flow field. At the same time, the model provides standard RANS capabilities in stable flow regions.

It has been shown by Menter and Egorov [92] that the second derivative of the velocity field, and thereby,  $L_{vK}$ , introduced by the exact transport equation for the turbulent length-scale, as derived by Rotta [112], is of first interest for inhomogeneous flows. Without repeating the development of the complex equations (which can be found in [92]), one can just summarize the different steps leading to the important terms and the actual form of the SAS model.

The starting point of the transformation process was the formulation of the two-equation  $k - \Phi$  model, with the variables  $k$  and  $\Phi = \sqrt{k}L$ . The formulation of the model based on Rotta's theory revealed the presence of the second derivative of the velocity formulated as follow:

$$U'' = \sqrt{\frac{\partial^2 U_i}{\partial x_j \partial x_j} \frac{\partial^2 U_i}{\partial x_k \partial x_k}} \quad (3.58)$$

This is the relevant term around which the SAS model is built, making the turbulence length scale now largely proportional to the von Kármán length-scale  $L_{vK}$ . For shear-flows, it reads:

$$L \sim L_{vK} = \kappa_{vK} \frac{S}{U''} = \kappa_{vK} \left| \frac{\partial U / \partial y}{\partial^2 U / \partial y^2} \right| \quad (3.59)$$

where  $S$  is the absolute value of the strain-rate and  $\kappa_{vK} = 0.41$ .

$L_{vK}$  is considered as a natural scale since it adjusts to the already resolved scales in a simulation and provides a length-scale, which is proportional to the size of the resolved eddies. Standard turbulence models, on the other hand, always provide a length-scale proportional to the thickness of the shear layer. They do not adjust to the local flow topology and are therefore overly diffusive.

Finally, in order to provide the SAS capability to the SST model, the  $k - \Phi$  equations have been transformed to the  $k - \omega$  framework according to the expression:

$$\Phi = \frac{1}{c_\mu^{1/4}} \frac{k}{\omega} \quad \text{with} \quad c_\mu = 0.09 \quad (3.60)$$

Consequently, the resulting SST-SAS model also benefits from the usage of the von Kármán length-scale, working in pure SST mode in the RANS region, and activating the SAS formulation in the URANS region.

Since this model is relatively recent, the literature relating to applications of SAS are rather limited. Nevertheless, some important contributions have been brought by Menter and coworkers in a series of papers [93, 95, 97]. Despite its young existence, this RANS derivative model has been applied to several flow configurations, ranging from academical cases up to complete aircrafts [95] and the analysis of some aeroacoustic noise induced by side view car mirror [13].

Through these various applications, the SST-SAS model has proven its ability to provide similar results to SST-DES, while avoiding some of the uncertainties resulting from an explicit usage of the grid spacing. This means that the application of the SAS model in complex geometries is less grid sensitive than the DES formulation.

A second advantage of SAS is its greater tolerance towards the selection of the time step. A comparison between LES and SAS simulations run on the same grid but with different time steps have highlighted the characteristic of the SAS concept to allow the model to adjust to the scales resolved by the grid and the time step and produce turbulence structures suitable for the given resolution. This performance is provided by the introduction of the von Kármán length scale in the model, which is an appropriate quantity for detecting unsteadiness and trigger the resolution of turbulence, without any explicit dependency on the grid spacing, as observed by Davidson in [33, 34].

However, this last point could also represent a drawback in the sense that the SAS model cannot be forced by grid refinement into unsteadiness. It has been observed through the different references listed in this paragraph, that, if the flow instability is not strong enough, the SAS model will simply remain in steady mode, whereas the DES model can be influenced by reducing the grid spacing and can be triggered to produce unsteady solutions.

To the author's best knowledge, apart from the present study and a corresponding publication from the same author and coworkers in 2007 [71], no other applications of the SST-SAS model for Internal Combustion Engine could be found in the literature to date.

### **3.3 Selective Visualization of Turbulent Flows**

In the description of turbulence given in §3.1, a characteristic element of these particular type of flows has been mentioned, the vortices or eddies. In accordance with the theory of Kolmogorov [77] and its *turbulence cascade*, turbulent flows are constituted by a continuous spectrum of scales, the largest ones extracting the kinetic energy from the mean motion and feeding it to the large scale turbulent motion.

After a brief presentation of the main eddies characteristics, and more particularly the definition of coherent structures, different methods used to extract flow patterns and to visualize them will be reviewed.

#### **3.3.1 Coherent Structures**

In describing turbulence, many researchers refer to eddying motion, which is a local swirling motion where the vorticity can often be very intense. These turbulent eddies, of a wide range of sizes as described in the spectral definition of turbulence earlier in this chapter, appear and generate vigorous mixing and effective turbulent stresses.

A main feature of turbulence is represented by the notion of *coherent structures*. The basic concept associated is that a coherent structure is a recognizable form seen amid the “apparent” disorderly motion of the surroundings. Consequently, this characteristic structure is providing a valuable insight into the properties of turbulent flows via its contribution in terms of vortex kinematics and dynamics. In that sense, a coherent structure associates a concrete form to the term *eddy*. Understanding this type of vortices can be then used to help understand why a flow behaves as it does and can help in understanding how to control the turbulence.

Nevertheless, studying coherent structures is nothing but trivial. Indeed, the idea of structure is strongly dependent on how they are visualized, in which coordinates frame, and according to which criterion. Experimentally, smoke or particle displacements are often used to visualize the velocity field and then to identify structures as dominant flow patterns. However, the extent to which recognizable forms can be identified, and the value of the criterion used, have been a subject of controversy and animated debates. The very low signal-to-noise ratio observed in many flows, which is decreasing with increasing Reynolds number, as well as the absence of universal threshold or objective criterion, make the eduction or retrieval of the coherent structures one of the most challenging task while studying turbulent flows.

Usually, this particular category of structures is associated with the notion of *large eddies*, corresponding to the energy-containing scales of motion. However, the designation *large eddies* does not only include coherent vortices but also some other less definitive patterns of fluid movement.

The different pattern recognition or eduction techniques presented thereafter will have to face the issues previously mentioned and to exploit the characteristics of coherent structures in order to distinguish those dominant eddying motions from the bunch of perturbing smaller scales.

### 3.3.2 Flow Pattern Extraction Techniques

Visualization and characterization of the turbulent structures developing in complex flows such as the ones induced by engine intake ports are of high interest. Indeed, the evolution of vortices in engines has to be carefully controlled in order to generate the required amount of turbulence at the right position in the cylinder. Fluctuations of these structures are strongly influencing the general combustion process which in turn affects the overall engine stability.

A common practice to observe vortical structures generated by simulation or experimental results of turbulent flows has long been done through the visualization of instantaneous flow fields. The representation of the isosurface of instantaneous velocities or even the corresponding velocity vector fields, although full of details, are only providing a qualitative insight into the prevailing flow patterns.

Even if an intuitive understanding of the flow is fundamental, further techniques need to be implemented to track the vortices in the fluid domain and establish, in an objective way, the origins of these flow fluctuations.

#### 3.3.2.1 High-Vorticity Magnitude

A very important quantity for characterizing turbulence and its rotational structures is the vorticity vector  $\vec{\omega}$  defined as:

$$\vec{\omega} = \vec{\nabla} \times \vec{u}. \quad (3.61)$$

In the case depicted in Figure 3.5, the quasi-discontinuity between two parallel flows of velocity  $\vec{U}_1$  and  $\vec{U}_2$  gives rise to a vortex sheet. The main vorticity component, in the plane of interest, reads:

$$\omega_z = \frac{\partial v}{\partial x} - \frac{\partial u}{\partial y}. \quad (3.62)$$

The vorticity sheet existing in the mixing layer between both flows is violently unstable under small perturbations and rolls-up into spiral Kelvin-Helmholtz vortices into which vorticity has concentrated. These vortices may undergo secondary successive instabilities, leading to a virulent direct kinetic-energy cascade toward small scales, or they may also be responsible for inverse energy cascades through pairings. Usually, the Kelvin-Helmholtz-type instabilities are the source of turbulence in many hydrodynamic as well as external and internal aerodynamic applications.



**Figure 3.5:** Left / Schematic of a mixing layer between two parallel flows of respective velocity  $\vec{U}_1$  and  $\vec{U}_2$  - development of a Kelvin-Helmholtz instability. Right / Vorticity modulus of the same type of instability obtained with Large Eddy Simulation (reproduced from Lesieur et al. [83]).

Therefore, vorticity is often used in engineering problems in order to detect regions of high vortical activity, where a particular control of turbulence may be of first interest.

Indeed, since vorticity is linked to flow topology, the time evolution of the vorticity field expresses changes in flow topology, a process that can be identified through visualization. For this purpose, the representation and animation of 3-d isosurface of a selected vorticity value allow to track the dominating structures / patterns of the turbulent flow field.

This criterion presents the great advantage to stick closely to the core of the vortical structures, since eddies can be characterized by a large increase of the intensity of vorticity. However, this effect could also be generated by a large shear stress in a shear layer, where there is actually no vortex. Based on these remarks, it can be concluded that the *high-vorticity magnitude* criterion is a necessary condition to describe a vortex but, alone, is not sufficient. Therefore, the information provided needs to be complemented or detailed by another finer criterion.

### 3.3.2.2 Low Pressure

Pressure minima at vortex centres are one of the different *point-based* criteria developed to detect the presence of the vortical structures and to identify their core location. The normalized low-pressure quantity can be defined as follows:

$$\frac{p}{\rho U^2} = a < 0, \quad (3.63)$$

where  $p$  is the instantaneous absolute pressure and  $a$  is a negative constant.

By selecting an appropriate value for the low-pressure isosurface, it is possible to filter the flow field and to represent the envelop of the vortical structures developing in the domain.

This technique has been already widely implemented, as presented by example in [83, 117], where the use of low-pressure isosurface enabled, in Seidl et al. [117], to characterize the strong vortex rings developing and breaking down in the wake of a sphere (see Figure 3.6), or, in Lesieur and

coworkers [83], to visualize the complex helical pairing occurring in an incompressible spatial mixing layer under particular boundary conditions.

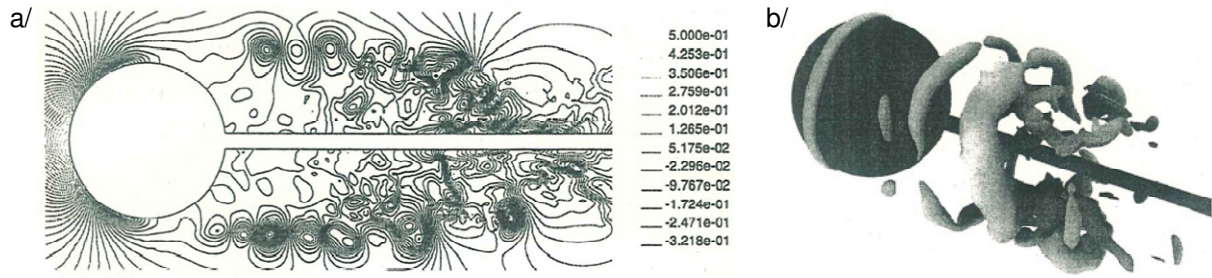


**Figure 3.6:** a/ Contours of normalized pressure  $p/(\rho U^2)$  in an axial cross-section; b/ Isosurface of instantaneous low-pressure  $p = -0.22\rho U^2$  representing the vortex rings in the wake of a sphere (reprinted from Seidl et al. [117]).

As can be found in [132], pressure minima are usually very well performing for 2-d flows but are showing some weaknesses in case of 3-d configurations. Among its greatest advantages, this technique is detecting the actual rotating structures, and is really non-sensitive to shear layers on the contrary to the vorticity-based method presented earlier.

However, the pressure difference is quite dependent to the eddies size. For this reason, smaller vortices are more difficult to identify with pressure minima than larger scales, for which the pressure difference is much larger.

Finally, a last issue related to this technique is the difficulty to obtain valuable measurement data for pressure fields. This makes the low pressure method much more dedicated to simulation data, guarantying the spatial resolution required and the information at each numerical node.

Although this visualization method is rather convenient and straightforward to apply, due to its *point-based* nature, it may sometimes fail to detect obvious vortices, or find non-vortical structures. A reason for this could be that vortex is essentially a macroscopic or regional phenomenon, and the point samples underlying the low-pressure criterion do not always translate into regional characteristics.

### 3.3.2.3 Second Invariant of the Velocity Gradient Tensor

The notion of a vortex is widely used in fluid dynamics and vortices are often thought of as regions of high vorticity. However, there is no universal threshold over which vorticity is to be considered high, or any non-ambiguous definition to distinguish the core of a vertical region. Furthermore, some misleading interpretation of high vorticity in flow regions dominated by a high shear could attribute the presence of vortices where there is none.

The problems related to this simple and controversial definition of a vortex has been addressed by several authors, including Lugt [85], Jeong and Hussain [72], and Cucitore et al. [32].

In 1995, Jeong and Hussain [72] stressed the need for a Galilean-invariant vortex criteria, i.e., criteria that remain invariant under coordinate changes. For a three-dimensional smooth velocity field  $v(x, t)$ , available Galilean-invariant vortex criteria use the velocity gradient decomposition:

$$\nabla v = S + \Omega, \quad (3.64)$$

where  $S = \frac{1}{2}[\nabla v + (\nabla v)^T]$  is the rate-of-strain tensor, and  $\Omega = \frac{1}{2}[\nabla v - (\nabla v)^T]$  is the vorticity tensor.

Among the different criteria used to detect and represent vortices, positive values of the second invariant,  $Q$ , of the velocity gradient tensor have been recognized as vortical regions first by Hunt et al. [67] (see also [72, 102]). This commonly used parameter, called  $Q$ -criterion, is defined as follows:

$$Q = -\frac{1}{2}(S_{ij}S_{ij} - \Omega_{ij}\Omega_{ij}) = -\frac{1}{2}\frac{\partial u_i}{\partial x_j}\frac{\partial u_j}{\partial x_i} \quad (3.65)$$

where  $\Omega_{ij}$  and  $S_{ij}$  are the anti-symmetric and the symmetric parts of the velocity gradient respectively, as defined in Eq. (3.64).

Therefore, in regions where  $Q > 0$ , the Euclidean norm of the vorticity tensor dominates that of the rate-of-strain.

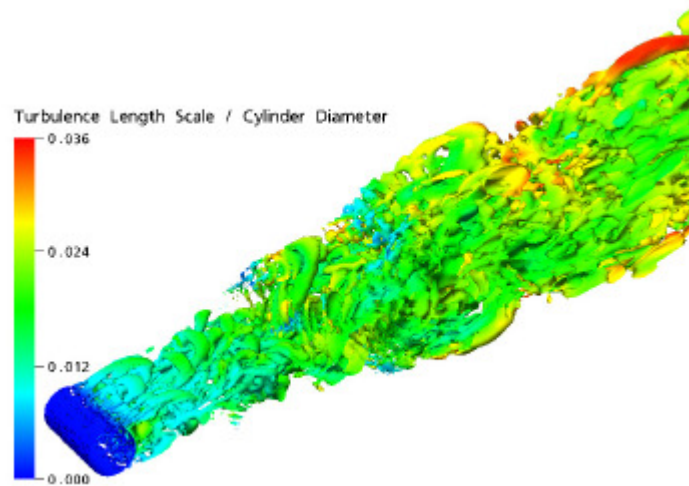


**Figure 3.7: Representation of the resolved turbulent structures for a cylinder in cross-flow – Isosurface of  $Q$ -criterion with  $Q=10^5 \text{ s}^{-2}$  (Menter & Egorov [94]).**

This variable is often employed to represent the 3-dimensional turbulent structures resolved by the numerical model and constitutes a useful criterion to compare the level of resolution achieved, as can be seen from the example presented in Figure 3.7.

For wall-bounded flows more particularly, where the turbulent flow is strongly dominated by shear effects, the results are likely to be masked by the large strain-rate, which needs to be filtered out. In engine applications for example, this phenomenon will be a major issue while post-processing the results. The selection of an appropriate value of  $Q$  and the representation of the corresponding isosurface should allow observing the vortex structures developing and decaying within the cylinder.

### 3.3.2.4 Proper Orthogonal Decomposition

Some other sophisticated methods have been proposed for education and modeling of the coherent structures observed in most turbulent flows. Amongst them, Proper Orthogonal Decomposition (POD) technique, as introduced in the late sixties by Lumley [86], is quite attractive in terms of identification of coherent structures.

Indeed, before going deeper in detail, its fundamental principle lies basically on the optimal decomposition of the dominant features of the flow, classified in a set of basis functions according to the amount of kinetic energy contained by those structures. This criterion for flow pattern recognition is well matching with the nature of the coherent structures, which are defined as the largest energy containing eddies. Some studies of different flow configurations (see [43]) have shown that the relative energy content of the coherent structures as compared to the total turbulent energy can represent from 10% (for boundary layers, far jets), up to 20% (far wakes, plane mixing layers) or even 25% (near wakes or jets). Thus, compared to many other classical methods used for large scales identification, such as flow visualization described earlier, no a priori or other conditions are needed with POD for the eduction scheme. Here, the coherent structures are defined in an objective and unique manner as the flow realization that processes the largest projection onto the flow field. This property of POD will be highlighted below, while presenting briefly the main steps of this decomposition technique. However, a complete review on theory and applications of POD to turbulence is out of the scope of this work, but can be found in several other references (please refer to [16, 26, 29, 51, 66, 98]).

According to the Reynolds decomposition of the vector field, the instantaneous velocity can be divided into two components, one representing the average value, the other representing the turbulent fluctuations (Eq. 3.7). Thanks to the Proper Orthogonal Decomposition method, it is possible to decompose the original signal into a spatial-dependent component and a time-dependent one. Thus, in the context of turbulence and other complex spatio-temporal fields, these will typically be patterns in space and time. Indeed, POD can be used to analyze experimental as well as numerical data with a view to extracting dominant flow features. On the other hand, POD, through its property of optimality, is also able to capture the dominant components of an infinite-dimensional process with only finite “modes”. Therefore, POD can also be used to provide a set of basis functions with which can be defined a low-dimensional subspace on which to construct a dynamical model of the coherent structures by projection on the governing equations [29].

As it was firstly introduced by Lumley in 1967 [86] as a derivate from the more general *Karhunen-Loeve expansion*, POD consists in finding among a set of realizations of the flow field, the realization which maximizes the mean square energy. According to Lumley [86], a coherent structure is the structure that has the largest mean square projection of the velocity field. This maximization leads to a Fredholm integral eigenvalue problem:

$$\int_D R_{ij}(X, X') \Phi_j^{(n)}(X') dX' = \lambda^{(n)} \Phi_i^{(n)}(X) \quad (3.66)$$

where  $R_{ij}(X, X') = \langle u_i(X) u_j(X') \rangle$  is the two-point space-time correlation tensor of the velocity field,  $u(X)$ , with  $X = (x, t_n) \in [D = \mathfrak{R}^3 \times \mathfrak{R}^+]$ . Thus,  $u(X)$  denotes the set of observations (also called *snapshots*) obtained at  $N_t$  different time steps  $t_n$  over a spatial domain of interest (2- or 3-dimensional). These snapshots could be experimental measurements or numerical solutions of velocity fields.

For bounded integration domain  $D$ , it can be shown that Eq. (3.66) does not have a unique solution, but a denumerable infinity of solutions. Thus, each eigenfunction  $\Phi_i^{(n)}(X)$  is associated with a real positive eigenvalue  $\lambda^{(n)}$  of order  $n=1, 2, 3, \dots, +\infty$ . Each eigenfunctions  $\Phi_i^{(n)}(X)$  form a complete orthogonal set, that is, the random vector field  $u_i$ , can be reconstructed in the following way:



$$u_i(X) = \sum_{n=1}^{+\infty} a^{(n)} \Phi_i^{(n)}(X), \quad (3.67)$$

where the coefficients  $a^{(n)}$  of different order are mutually uncorrelated,

$$\langle a^{(n)} a^{*(m)} \rangle = \begin{cases} \lambda^{(n)}, & (n = m) \\ 0, & (n \neq m) \end{cases}. \quad (3.68)$$

An important consequence of (3.68) is that the contribution of each structure to the turbulent kinetic energy and the turbulence stresses can be determined:

$$\langle u_i(X) u_j(X) \rangle = \sum_{n=1}^{+\infty} \lambda^{(n)} \Phi_i^{(n)}(X) \Phi_j^{(n)}(X), \quad (3.69)$$

$$\text{and } \int_D R_{ii}(X, X) dX = \sum_{n=1}^{+\infty} \lambda^{(n)} = E, \quad (3.70)$$

where  $E$  corresponds to the total Turbulent Kinetic Energy (TKE) integrated over the domain  $D$ . The interpretation of this equation is that every structure of order  $n$  makes an independent contribution to the TKE. Then, the amplitude of the eigenvalues  $\lambda^{(n)}$  measures the relative importance of the different structures present within the flow.

Practically, the set of observations has a finite dimension, which means that the total number of snapshots is limited, and then Eq. (3.67) can be rewritten as follows:

$$u(x, t) \approx \sum_{n=1}^K a^{(n)}(t) \phi^{(n)}(x). \quad (3.71)$$

This form represents the POD under the general context of approximation theory. Indeed, it is expected that this approximation becomes exact for  $K \rightarrow +\infty$ . Based on this last observation, while an approximation to any desired accuracy can always be obtained if  $K$  can be chosen large enough, one may like to find a sequence of orthonormal functions  $\phi^{(n)}(x)$  in such a way that the approximation for each  $K$  is as good as possible in a least square sense. The approximation formulation can be then resumed to a *minimization problem*. An exhaustive description of this minimization problem and its practical solution methods are given in [29]. In order to summarize the various ways to solve this new formulation of the problem, a brief description of the three main methods available will follow, covering the Singular Value Decomposition, the classical POD (or direct method) and the snapshot POD.

Basically, for all three methods, the first common step of the process is to reformulate the minimization problem in a matrix approximation context with an arrangement of the set of data in a general Snapshot Data Matrix, and to factorize it. Through this factorization, the global matrix can be written as the product of two singular vectors by the diagonal matrix containing the singular values of the Snapshot Data Matrix. The main difference existing between the diverse methods enumerated earlier lies on the determination of these singular values and, finally, the size of the matrices or the number of operations required.

The SVD solves directly the singular values problem by carrying simultaneously a spatial and temporal correlation, making this approach rather costly for applications with fine spatial or temporal resolution.

Both POD methods are computing the singular values as well as the right and left singular vectors of the rectangular Snapshot Data Matrix by solving symmetric eigenproblems instead of computing directly the singular values. This technique represents a non negligible saving of time in terms of numerical treatment efforts while considering large data sets (in time or space). Afterward, the selection between a classical and a snapshot method only lies in the particular data set available for the evaluation of the kernel of the eigenvalue problem.

As depicted in Figure 3.8, the classical POD method is carrying an average over time and is only dealing with a two-point spatial correlation, whereas the snapshot approach is averaging over the domain, while conducting a two-point temporal correlation. Concretely, this means that in the first case, the size of the eigenvalue problem is of the dimension of the number of spatial points of the snapshots data, whilst, in the second case, the size is equal to the number of acquisitions,  $N_t$ .

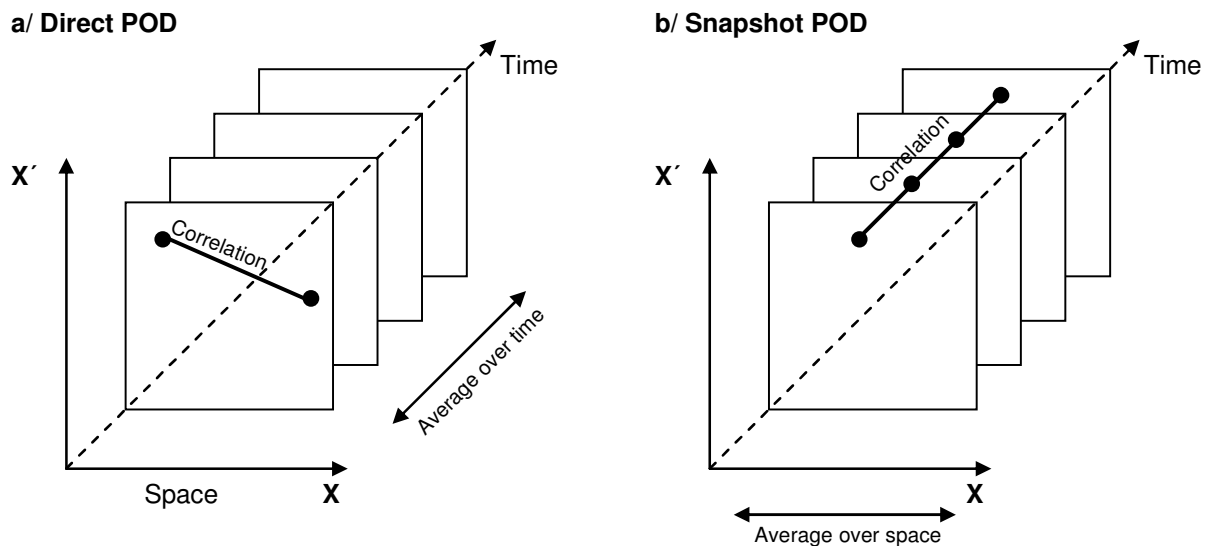


**Figure 3.8: Schematic view of a/ the classical POD, b/ the snapshot POD (reprinted from [29]).**

In conclusion, every time the spatial resolution is larger than the temporal one, the snapshot POD will be preferred. This is the case with data obtained by numerical simulations like Direct Numerical Simulation or Large Eddy Simulation, which are often highly resolved in space and time, but, due to computational costs considerations, only a very short time sample is simulated. On the other hand, for experimental data obtained with High-Speed PIV or similar approaches, with very fine resolution in time, classical POD is more dedicated.

Amongst the scientific and industrial community, POD has already been used in various domains in order to obtain approximate, low-dimensional descriptions of turbulent flows, structural vibrations, damage detection... thanks to its advantages in image processing, signal analysis and data compression. By decreasing the dimension of the complex system and allowing the extraction of the most energetic structures, the snapshot technique has often been implemented in bounded flow applications for flow pattern recognition, and, subsequently, to study the dynamical behavior of the structures according to their scale (as shown, for instance, in [9, 87, 119]).

For engine flow applications, the purpose of most of the investigations found in the literature to date is to understand the process associated to large-scale cycle-to-cycle fluctuations and to analyze the structures break-up taking place over the different engine phases. Previous POD applications based on the in-cylinder flow database can be found in [37, 39, 45, 55, 107].

While Raposo et al. [107] employed POD of 2-d PIV acquisitions in a steady water test rig to gain some qualitative indications about the swirl structure developing during the intake stroke, Graftieaux et al. [55] and later, Deslandes and coworkers [37] proposed some preliminary investigations of cycle-to-cycle variations. They decomposed the flow fluctuations into three different parts through a particular truncation of the POD modes, separating the mean cycle-averaged velocity field from the large-scale cycle-to-cycle fluctuations and the remaining turbulent part. However, a major issue was the selection of the truncation mode to differentiate the cyclic variability from the turbulent fluctuations. In 2004, Fogleman et al. [45] investigated the stability and the complexity of the tumble flow by analyzing the number of modes required to describe it, at each engine phase. Then they applied a so-called phase-invariant POD approach to study the tumble breakdown process more accurately in a time-varying domain. In a more recent paper, Cosadia et al. [30] applied a snapshot POD decomposition to the circulation data (integral value of a vertical component of the vorticity over a disk of radius  $R$ ) in order to study the swirling flow in a Diesel engine. By using this integral variable they tried to alleviate the problem related to POD modes truncation and the associated detection of a “cut-off” between the different structure scales. Based on this methodology they studied two engine events in detail, namely the mid-compression time and the Top Dead Centre position, to observe the effect of turbulent diffusivity induced by the squish motion.

Although the interest for POD for engine flows is intensifying and the diversity of research works is already offering an interesting insight into the turbulent process occurring in cylinders, numerous investigation fields or perspectives are still open.

The present work is proposing an innovative approach based on the POD treatment of numerical and experimental data of a production FSI engine intake port and cylinder head. An objective criterion for a selective truncation of the eigenmodes will be unveiled, based on the spectral analysis of the time coefficients, thus providing a filtering of the turbulent structures according to their fluctuation frequency.



## 4 Scope of Investigation & Preliminary Studies

### 4.1 Research Strategy

As already mentioned in chapter one, the objective of this work is to describe and predict the turbulent flow conditions induced by the intake system of a FSI<sup>®</sup> engine in order to better understand the origins of the engine cyclic variations.

However, the complexity of the fluid flow developing in DISI engines and the large number of influencing parameters at stake require the development of a particular research strategy. This strategy should allow to decompose the processes and to simplify the problem by considering first of all some simple cases, to investigate the fundamentals and set up the numerical and experimental models, before to gradually increase the complexity and then to tackle the real phenomena encountered in full engines.

Following this “guideline”, the final analysis process has been proposed as depicted in Figure 4.1 thereafter.

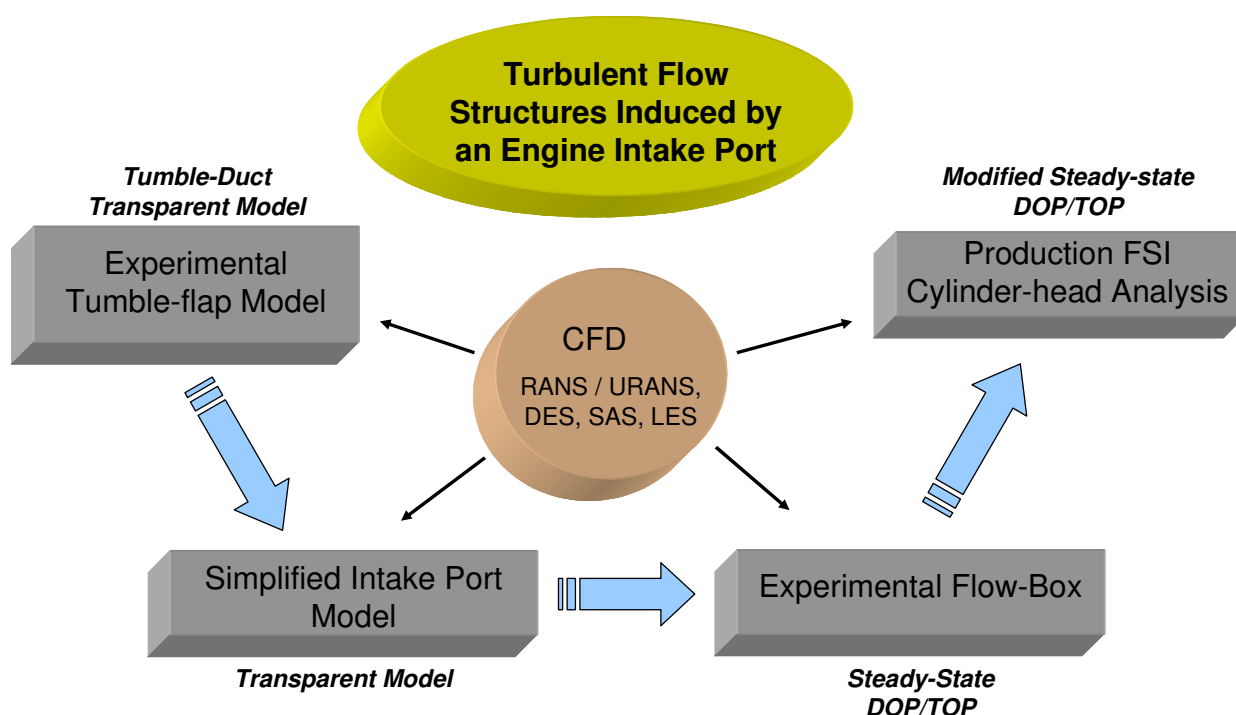


**Figure 4.1:** Research strategy employed for analyzing the turbulent flow induced by a DISI engine intake port

Thus, the global analysis of the turbulent flow generated by this type of engines has been divided in four main steps. The first three ones could be seen as preliminary studies, more fundamental than the last one, taking into account the full geometry of a production cylinder head. The know-how obtained by the study of simpler engine components models must improve the settings of the different numerical methods employed for the simulation, after having been validated through the different experiments conducted.

All along the four stages of the presented research strategy, both numerical and experimental techniques have been continuously improved in order to always stay up to date with the latest

developments and to obtain the most accurate and complete results that either the software or the hardware were able to deliver.

As far as the flow measurements techniques are concerned, the systems available nowadays can be divided into three categories: intrusive, based on physical probes introduced in the flow; partially intrusive, based on flow markers injected into the flow and completely non-intrusive, based on the optical detection of light scattering properties of the flow.

With regards to the first category, pressure and temperature probes as well as hot wire anemometers are used to provide local measurements of the flow, under high temporal resolution. The main drawback of these techniques relies on their fundamental limitations of interfering with the measured flow and creating local disturbances, especially at high speeds. On the other hand, optical methods such as Laser Doppler Anemometry (LDA), Doppler Global Velocimetry (DGV) and Particle Image Velocimetry (PIV) can be generally regarded as non-intrusive, since the size and concentration of the particles introduced in the flow as seeding is too small to change the flow behaviour. Finally, examples of totally non-intrusive technique are Interferometry and Laser Induced Fluorescence (LIF), which are based on the optical properties of the flow itself and are mostly used in combustion applications.

In the following paragraphs, the focus is given on the particular techniques implemented during the various stages of the analysis of single-phase cold flows developing in engine components. Except for the validation of the intake boundary conditions during the investigation in the production FSI cylinder head, where an intrusive technique (CTA) has been employed, the rest of the measurements have been conducted with optical systems. Therefore, another classification of the diagnostics methods can be used to differentiate them, depending on the acquisition principle: pointwise techniques for LDA in opposition to planar techniques as offered by PIV.

Although the firstly mentioned techniques are offering a very high time accuracy at the point of measurement considered, the information is spatially restricted, which is a real drawback when larger fields of view need to be investigated. For this reason, further developments in the domain of non-intrusive velocity measurement for whole field acquisition have been realized. Particle Image Velocimetry (PIV), which appeared in the mid-eighties, is ranking among the most used planar methods nowadays. Since the literature describing the principles of the method as well as its main historical developments is rather large and exhaustive, only the relevant issues and trends regarding the present application will be highlighted during the next paragraphs. Then for further details about the theory and history of PIV, refer to [3, 4, 50, 56, 105, 110].

Besides the spatial resolution aspect, an emphasis will be brought on the ability of the systems to accurately measure the highly transient processes involved in the turbulent flows considered.

With regards to the numerical simulation, the CFD methods developed by the software manufacturer chosen for this study have continuously evolved during the period of the project and have been applied here. Thus, the different numerical results presented in the following chapters have served as test cases for the implementation of the last turbulence models available as, for example, the first application of Scale Adaptive Simulation for in-cylinder flows.

## **4.2 Tumble-Flap Model**

In the diagram presented in Figure 4.1, the main steps of the investigations are described, starting from the upper left-hand side with the study of the turbulence induced in a “tumble-flap” model. This model is aiming at reproducing the effect of the variable tumble flap used in the intake port of the FSI<sup>®</sup> engines, as it has been already described in chapter 2.

It is then intended to reinforce the tumble flow pattern generated within the cylinder under certain functioning conditions such as the stratified combustion mode at low engine loads and revolutions. For this particular operating point, the mixture is lean everywhere inside the cylinder

except in the vicinity of the spark plug where the mixture has to be ignitable (typically for a lambda value between 0.8 and 1.2).

This first step of the preliminary study must be seen as a pure numerical analysis, based on the geometry of a formerly developed experimental model. Even though a direct comparison between CFD- and experimental results is taking place later in this chapter, the divergence in initial and boundary conditions employed, or the incapacity to get the original information and data did not allow to realize a quantitative analysis. For this reason, the comparison conducted is considered as indicative, only showing the general trend taken by the average flow within the geometry investigated.

However, this simple model offered the opportunity to observe in detail the influence of the advanced parameters proposed in the numerical program to adapt the zonal treatment behaviour of the turbulence model, and secondly, to analyse the general mesh sensitivity. The emphasis of the study has then been put on the numerical aspect, to give some directions in terms of model's settings and mesh characteristics for the forthcoming investigations.

### 4.2.1 Presentation of the Geometry

Fundamental investigations of the turbulent flow induced by the variable tumble flap of the intake port equipping the VW FSI<sup>®</sup> engines have led the experimentalists to develop a simplified model dedicated to optical measurements [57]. This model has been employed, under certain modifications that will be stated later, for the CFD study described in this chapter.

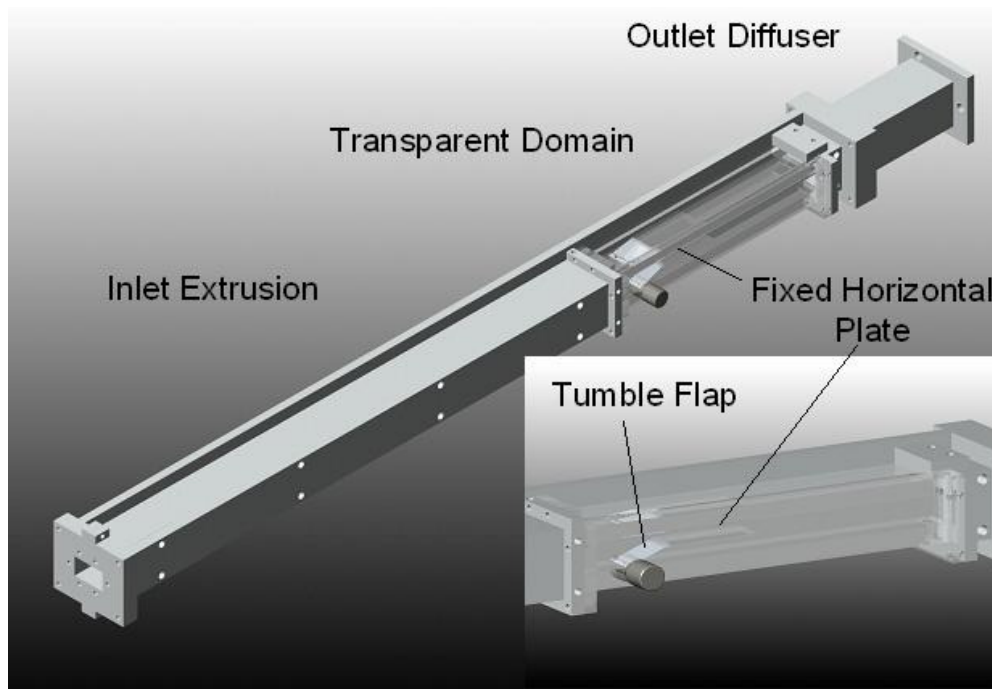
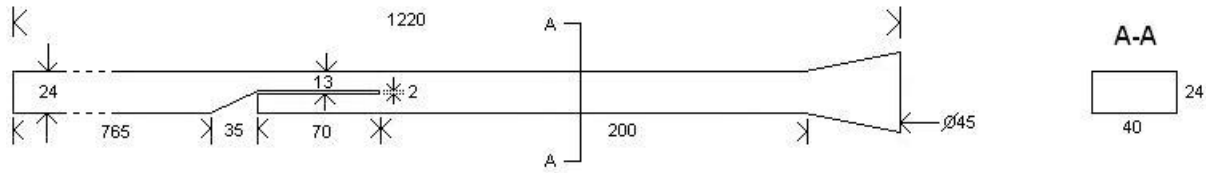


Figure 4.2: Presentation of the tumble-flap model geometry used for optical measurements



**Figure 4.3: Technical drawing and section view of the experimental model (all dimensions in mm)**

As depicted in Figure 4.2 and 4.3 above, the experimental model is composed by inlet and outlet extrusions in order to ensure well-established flow conditions all along the measurement volume. In the present study-case, all the results, boundary conditions and settings used are corresponding to a steady-state flow rate of  $40\text{m}^3/\text{h}$ . Thus, in the inlet extrusion where the averaged velocity is about  $11,5\text{ m}\cdot\text{s}^{-1}$  and the cross-sectional dimensions are  $24\text{mm} \times 40\text{mm}$ , the turbulent flow should be fully developed according to the value of the Reynolds number,  $\text{Re}=22800$ , defined by the hydraulic diameter  $D_H = (2 \times L \times l) / (L + l) = 30\text{ mm}$ .

#### 4.2.2 Zonal Treatment of the DES Model

The Detached Eddy Simulation (DES) model implemented in the CFD code Ansys CFX is offering the possibility to modify the zonal treatment of the fluid domain computed. Indeed the sensitivity of the model towards the shift between URANS in the wall vicinity and LES modelling in the core of the flow can be adjusted thanks to the so-called Blending Functions (BF). A detailed description of these functions has already been given in §3.2.2 and §3.2.4. According to the value set in the solver, the transition between both models can vary from rather protective when the default value is used,  $F = F_2$ , to a pure Strelets model, when  $F = 0$ . For the last case, the boundary layer is not “protected” against an activation of the DES limiter, which can be the source of grid-induced flow separation.

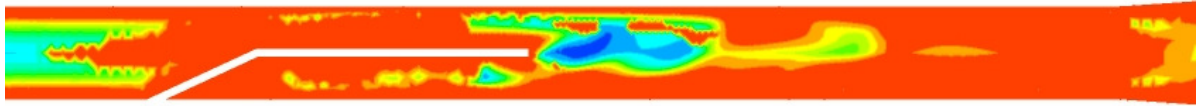
The present preliminary study is aiming at comparing the influence of the value chosen for the blending function on the simulated results and then to estimate the capacity of the DES model to properly catch the multi-scales turbulence decaying process.

The default configuration, which insures the highest level of protection and then the lowest sensibility of the model, is compared to a user-defined configuration, where the blending function is defined by  $F = \beta F_1$ , with  $\beta$  a coefficient chosen between 0 and 1. After several attempts, the best compromise has been obtained for a coefficient of 0.7. In Figure 4.4, the value of the resulting blending function employed by the DES model is plotted along the model investigated. All the regions represented in red are corresponding to a blending function of 1, which means that the model is running in RANS mode, whereas the blue colour corresponds to a LES operating mode. The difference between both settings is rather eloquent, demonstrating the conservative nature of the default parameter.

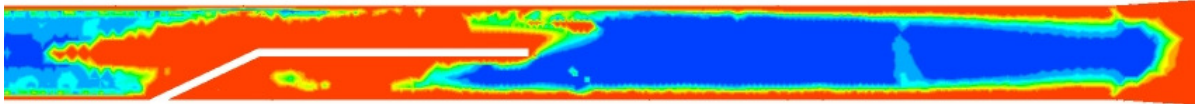
In the results presented thereafter, both simulations have been conducted on the same mesh (Low-Reynolds hybrid mesh), under the same boundary conditions; hence the effect of the blending function could be isolated from the other influencing factors.



a/ Config. 1: default settings



b/ Config. 2: User specified settings



Blending function for DES model [-]

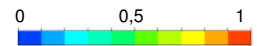


Figure 4.4: Different zonal treatment of the DES model according to the blending functions used: blue color for LES resolved area and red color for URANS mode. a/ default settings offering a URANS driven resolution, rather protective; b/ user specified parameters, with higher turbulence sensitivity (larger LES mode)

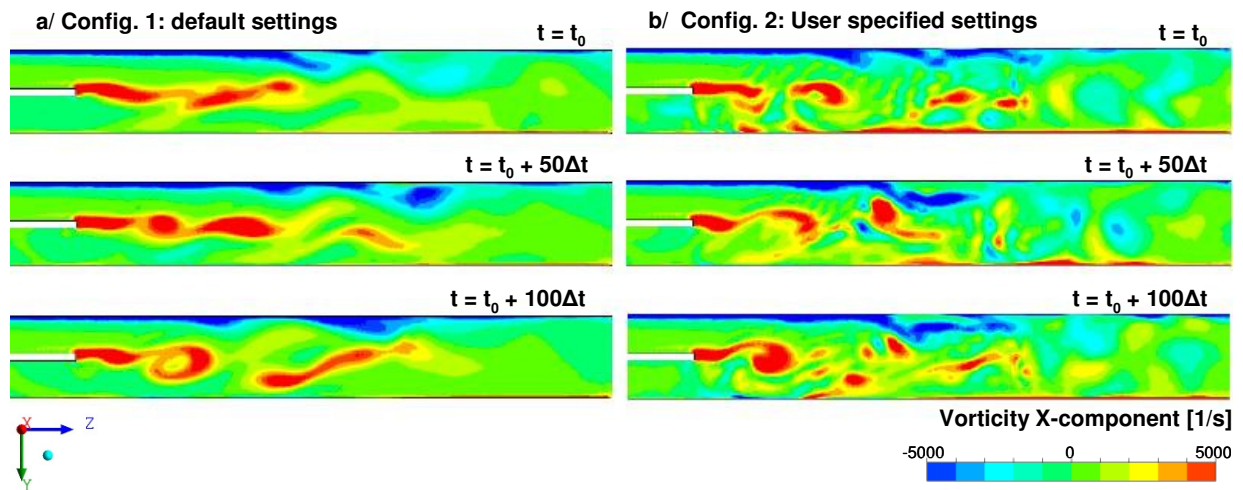


Figure 4.5: Comparison of the flow vorticity contour (X-component) for the two different blending functions settings presented in the previous figure

The structures developing in the wake of the obstacle are characteristic of the Kelvin-Helmholtz instability, which is induced by the shear layer existing between the upper and the lower parts of the flow. The contra-rotating eddies, typical from this last phenomenon, can be observed in Figure 4.5, displaying the X-component of the flow vorticity. It is then possible to differentiate the positive rotational structures from the negative ones, and to examine their oscillation downstream of the horizontal plate.

From the two different results plotted in the former figure, a major discrepancy is the level of structures resolved by the numerical model. In the default configuration, where most of the domain is computed with a URANS formulation, “single-mode” structure decay can be observed, coinciding with the damping nature of the model. In the second configuration, a much finer resolution is obtained, presenting a multi-scale shedding of the vortices. Another interesting aspect is the length of development of the turbulent structures, which is directly related to the quality of resolution of the shear layer. Even with the same mesh structure and size, a significant discrepancy is taking place only due to the settings of the blending function.

For the following studies, this parameter will have to be adjusted in order to guaranty the best level of sensitivity of the numerical model and subsequently, to enable the turbulence structures to develop and decay until the scales desired.

### 4.2.3 Mesh Sensitivity Analysis

Three different types of meshes have been considered in the present study in order to analyze their influence on the DES model results. As depicted in Figures 4.6 and 4.7, the meshes employed are covering the span of possibilities offered by IcemCFD in term of cells structures, from pure hexahedral mesh to fully tetrahedral, also using the “tet2hex” function, transforming the tetrahedral cells in the core of the domain into hexahedral.

Although the total numbers of elements are not similar, the number of control volumes used by the node-based solver scheme has been kept almost constant to a value of around 1 million. The dimensionless wall-distance variable  $y^+$  is always maintained below 5 which indicates that the treatment of the boundary-layer is sufficient to guarantee the low-Reynolds nature of the grids. In order to comply with this criterion,  $y^+ < 5$ , the distance of the first grid point from the wall has been previously calculated according to the relation between  $y^+$  and its dimensional form  $y$ :

$$y^+ = y/l_* \quad \text{with} \quad l_* = \nu/v_* \quad (4.1)$$

with  $l_*$ , the length unit and  $\nu$ , the kinematic viscosity. The former definition of the length unit is requiring the knowledge of the friction velocity,  $v_*$ , sometimes also denominated  $u_\tau$ . Several empirical estimations of this variable can be found in the literature according to the application considered. For pipe flows, Blasius' law of skin friction [19] describes the wall velocity as follows:

$$2\left(\frac{v_*}{u_0}\right)^2 = 0.054 \text{Re}^{-1/4} \quad (4.2)$$

whereas another slightly different expression for channel flows application can be found in [36]:

$$2\left(\frac{v_*}{u_0}\right)^2 = 0.073 \text{Re}^{-1/4} \quad (4.3)$$

In the present case, for a mass-flow of 50 kg/h,  $u_0 = 7.6$  m/s and  $\text{Re} \sim 15000$  in the cross-section upstream of the tumble-flap, which yields with equation (4.2)  $v_* = 0.375$  m/s and consequently  $l_* = 40.3$   $\mu\text{m}$ . While considering equation (4.3),  $v_* = 0.436$  m/s, which leads to  $l_* = 34.65$   $\mu\text{m}$ . Since the geometry investigated here is not exactly matching the assumption of any of these two definitions (it is actually a channel flow but not bounded by two infinite parallel plates like the assumption of Dean, and the cross section is rectangular, not cylindrical, like Blasius' case), the most constraining one will be used to compute the grid criterion; this means the second formulation as it is supplying the smaller length unit. Then, it is possible to compute the condition on  $y$ . It reads:  $y^+ < 5 \Rightarrow y < 5l_*$ , which finally gives  $y < 0.17$  mm.

Based on this criterion and by making sure that several grid points are contained in the viscous sub-layer of the flow, the meshes so obtained can be considered as low-Reynolds grids, avoiding the use of wall-functions. As far as the physical model is concerned, to guaranty the reliability of the comparison between numerical and experimental results, the quality of the walls surfaces is of

first interest. Indeed, all the surfaces have to comply with the condition evoked on  $y$  above, in order to be considered hydraulically smooth.

The numerical treatment of the region at the wake of the plate where the shear stress is maximum between the upper and lower flows is also of high interest. Indeed, the turbulent structures developing downstream of the tumble flap are originating there; the form and size of the grid cells have a strong influence on the accuracy of the simulation. In this region, a particular type of instability known under the name of Kelvin-Helmholtz is occurring. Large contra-rotating eddies are developing in high shear flow regions and then shedding in smaller structures. In order to properly resolve this phenomenon, an appropriate mesh refinement must be employed. Figure 4.6 shows the different strategies implemented for this study, using various mesh density blocks to refine the mesh in regions of interest. According to the increasing refinement obtained with the three meshes, a sensible variation in the final results is expected.

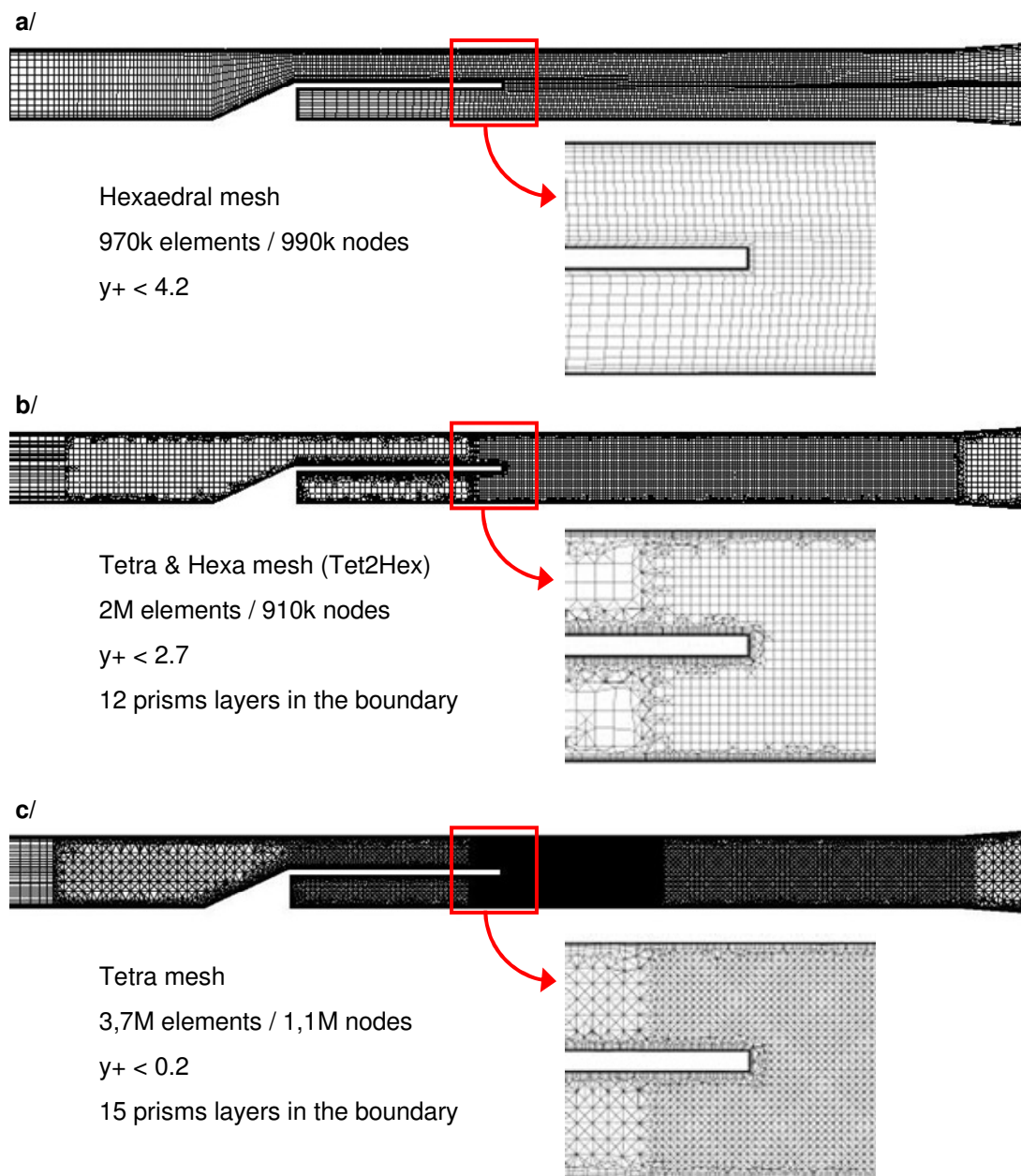


**Figure 4.6: Different meshes used for the sensitivity analysis: a/ full hexahedral; b/ hybrid tetra / hexa / prisms; c/ full tetrahedral**

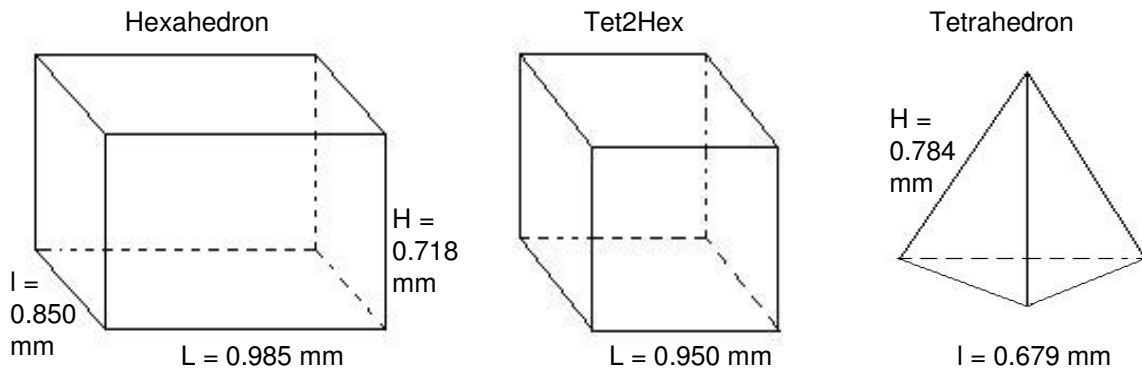


Figure 4.7: Different cells geometries and sizes present in the three former meshes

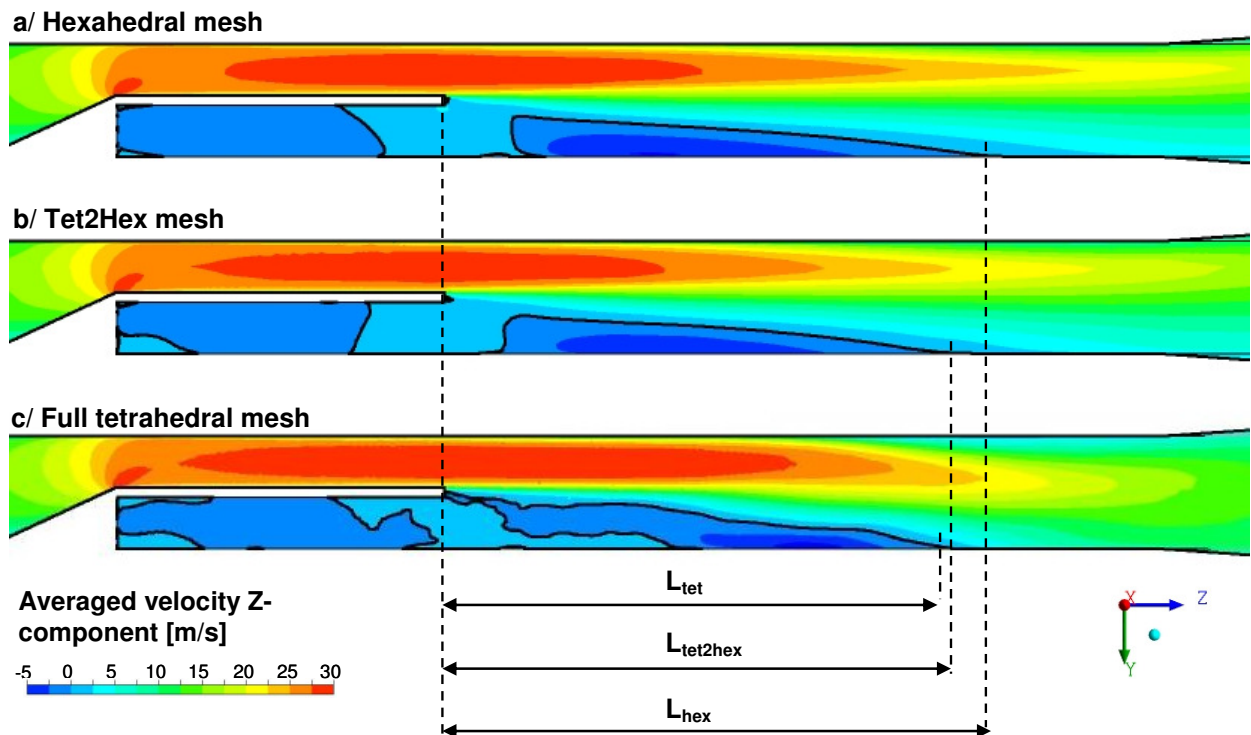


Figure 4.8: Comparison of the recirculation length between the 3 different mesh types – Superimposition of the averaged velocity Z-component and the null velocity contour line (black line)

In Figure 4.8, the recirculation length predicted with the different meshes is showing a certain discrepancy. Although both tetrahedra based grids are rather close to each other, giving a recirculation length of about  $8.2H_{\text{step}} (= L_{\text{tet2hex}})$  for the Tet2Hex mesh and  $8.1H_{\text{step}} (= L_{\text{tet}})$  for the full tetrahedral grid, in comparison with them, the hexahedral mesh “overestimates” this length with a value of  $8.9H_{\text{step}} (= L_{\text{hex}})$ .

Before studying in detail the velocity profiles in different sections of the domain, some quantities can bring relevant information about the quality of the mesh employed here.

First of all, while considering the evolution of the blending function across the domain, as presented in Figure 4.9, although all three meshes are providing similar results, a slight variation of the wall treatment can still be observed. As a matter of fact, even with the same blending function settings, the fully tetrahedral mesh is offering the broadest LES operating mode, with a

much thinner RANS treatment close to the wall. This could have an impact on the flow detachment downstream the horizontal plate, from the upper wall.

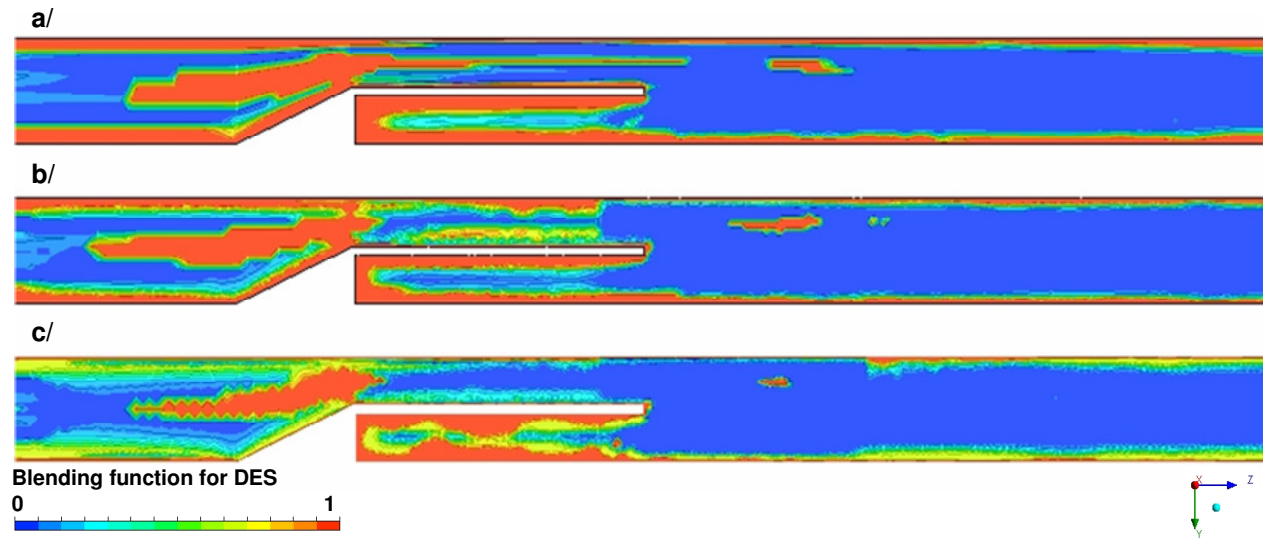


Figure 4.9: Blending function comparison between the three different meshes

The second criterion employed to determine the level of resolution reached by the different simulations is the observation of the turbulence length scale derived from equation (3.60) with

$\Phi = \sqrt{k}L_t$ . It yields:  $L_t = \frac{\sqrt{k}}{c_\mu^{1/4}\omega}$ . This length scale corresponds to the smallest structures

resolved by the turbulence model. Figure 4.10 shows the evolution of this variable (normalized with the local mesh length scale,  $\Delta$ ) within the central longitudinal cut, and gives a comparison between the three different meshes at stake. According to previous studies of the turbulence energy spectrum resolution for isotropic decaying turbulence, the same analysis of the length scale has proven that for a ratio under 0.2, most of the energetic eddies are properly resolved [91].

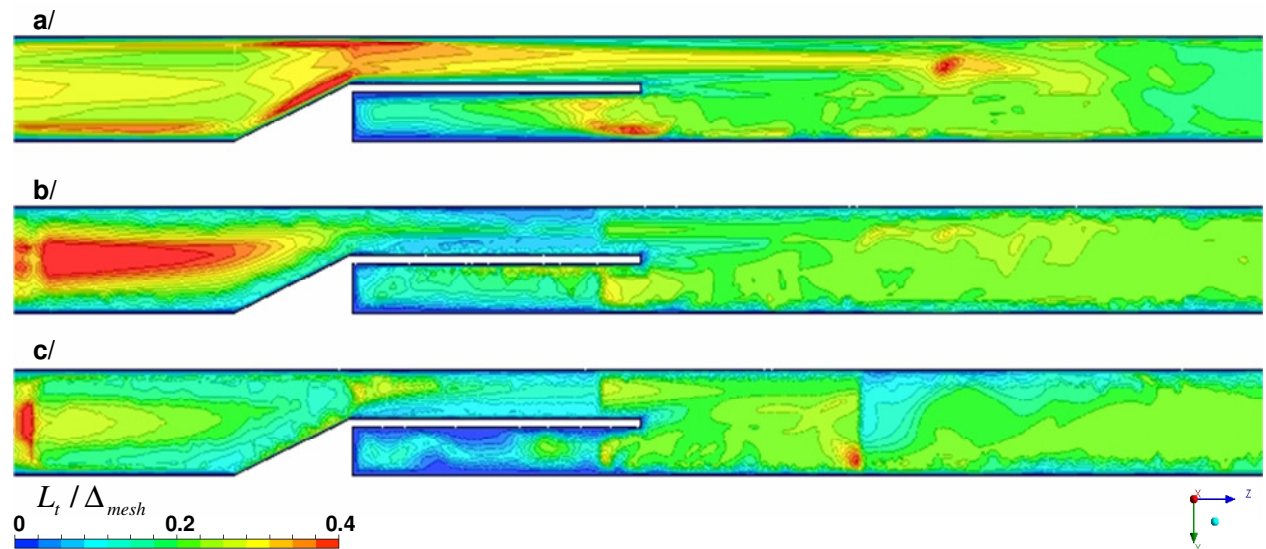
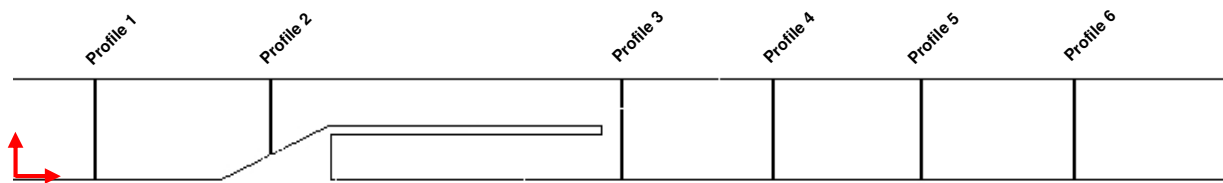


Figure 4.10: Comparison of the ratio between the smallest turbulent structures resolved by the DES model ( $L_t$ ) and the local mesh length-scale ( $\Delta_{mesh}$ )

In the present case, the comparison carried out with the different meshes is showing a clear divergence between the results. In the wake of the plate, both tetrahedral meshes are presenting a better ratio, closer to the target value of 0.2, than the hexahedral mesh. Upstream of the obstacle, a differentiation between the two tetrahedral meshes is appearing, mostly due to the non-homogeneity of the cells and the cell ratio at the border of the refinement block. As far as the hexahedral mesh is concerned, the orientation of the cells and their general elongated shape in the flow stream direction, just before the geometry convergence, is responsible for a higher ratio in this particular region. To conclude with this turbulence length scale ratio analysis, it is possible to assume that, with regards to the average value downstream of the obstacle, where most of the turbulence is induced, all three meshes should be able to deliver satisfying results. However, the full tetrahedral mesh seems to provide a slightly better resolution of the turbulent structures.



**Figure 4.11: Position of the different velocity profiles in the duct for comparison with LDA measurements**

As represented in Figure 4.11 above, six different profiles have been considered along the geometry. Those positions were imposed by the only existing LDA measurements, considerably restricting the amount of information available for the comparison between experimental and numerical results.

The various velocity profiles displayed in Figure 4.12 are comparing the experimental results obtained with LDA for the streamwise velocity component with the three numerical results. As it has already been mentioned before, although there is a certain discrepancy between the geometrical models it selves and probably the boundary conditions, this comparison, without being a real validation reference, gives an indication or a trend and then a benchmark basis. A major issue, which will be obvious during the observation of some profiles in the wake of the horizontal fixed plate (or flow splitter), is the existence of an important offset between the actuable tumble flap and the lateral housing of the model. This enables a certain mass-flow to establish in the lower part of the model, which exerts a non-neglectable influence over the global 3D shape of the flow. In the geometry used for the simulation, the tumble flap is perfectly closing the lower half of the duct.

Profiles 1 and 2 are showing a similar trend for all meshes, with a very high consistency between them, even if they are tendentially overestimating the experimental results. Further in the channel, at profile 3 and 4, the results are taking another inclination. At these positions, the full tetrahedral mesh is not performing as well as the two other meshes, especially in the lower part of the flow, where the recirculation (the negative velocity component values) is not as strong as the one obtained with LDA.

However, the trend is inverted again as the flow is reaching the positions represented by profile 5 and 6 further in the duct. Indeed, the flow detachment from the upper bound of the duct observed in profile 6 is only obtained by the simulation run on the full tetrahedral mesh where the velocity profile is rather different from the profiles obtained with the two other grids. In the first case, the averaged flow pattern is following the trend given by the experimental results, which are showing a clear detachment from the wall and tends to return to a more central configuration.

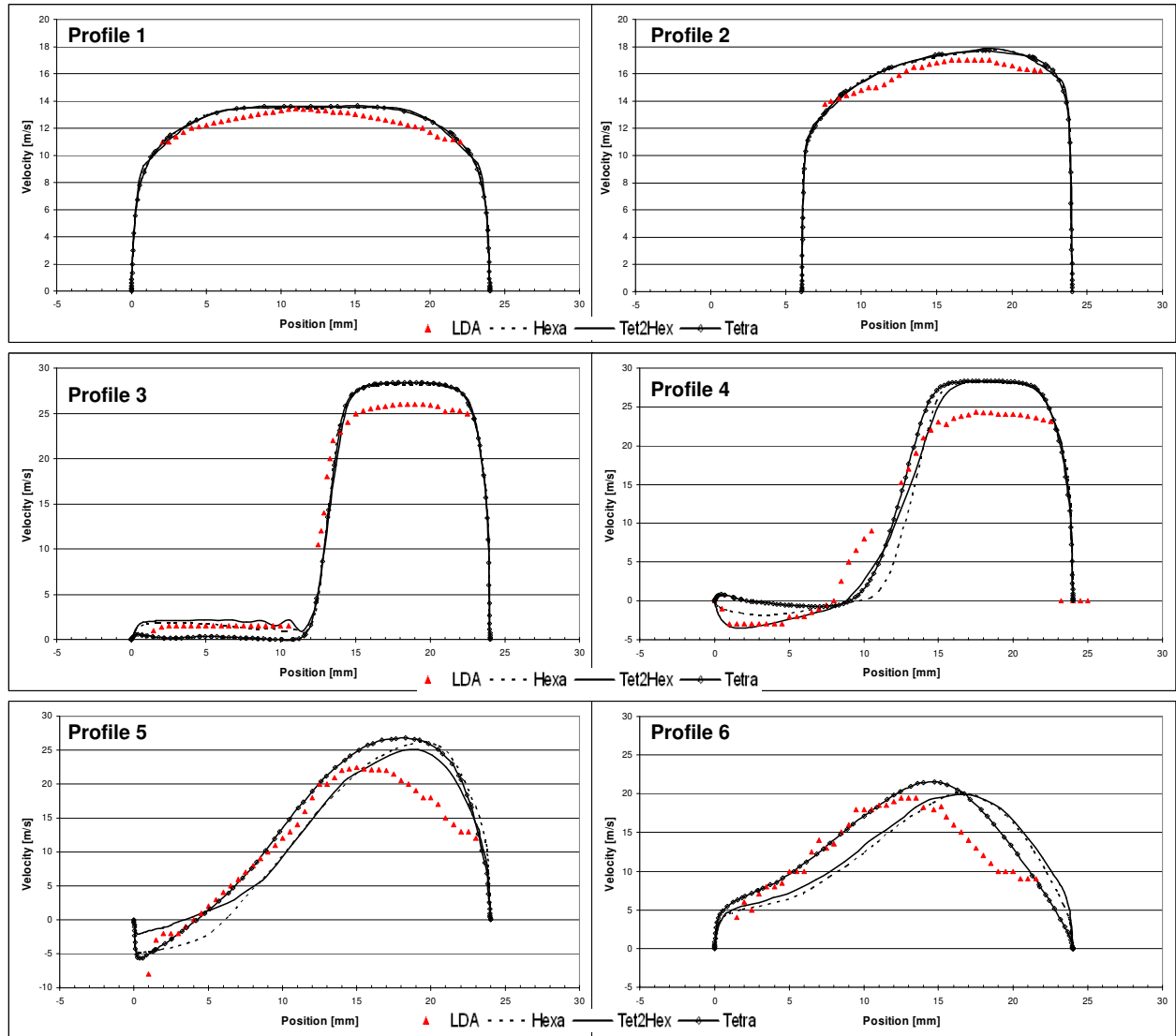


**Figure 4.12: Profiles of the Z-velocity component: comparison between LDA measurements and CFD simulation results – Position 0 is the lower bound of the duct**

### Conclusion

According to these observations and with all the caution required by the use of experimental results based on slightly different conditions, it appears that the quality of the results obtained with meshes from diverse nature is varying along with the location considered in the domain. The present analysis has shown that the hexahedral and the Tet2Hex meshes, despite their drawback in term of turbulence length scale resolution, are properly reproducing the flow right after the tumble plate. However, further in the channel, when the decaying process is taking place, their performance is not as good as the full tetrahedral mesh. Finally, the tendency to pursue for the following steps of the work will be to take the benefit of the different kind of meshes available, depending on the nature of the flow and the importance of the shear effects. Indeed, the higher the flow conditions in a constraining environment, the more important these effects will be. In other words, the turbulence cascade or vortices shedding process will occur in a shorter time, which is pleading for the use of small and isotropic cells such as the tetrahedra. The individual meshing strategy will be presented for each application in the following chapters.

### 4.3 Simplified Intake-Port Section Model

#### 4.3.1 Port Model Presentation and Experimental Setup

A specific experimental port model has been developed (see [69]), offering the optimum geometry to conduct high resolution Laser Doppler Anemometry in the wall boundary layer as well as in the port elbow region. As depicted in Figure 4.13, the port is modeled by two profiles, the upper and the lower wall, which are based on the geometry of a gasoline intake port, preceded by a long extrusion ( $L, W, H$  [mm] = 600, 25, 34 [mm]) to let the flow be fully developed. These flow bounds are constructed thanks to an extrusion of the port contour in the spanwise direction, allowing positioning the control volume of the LDA system as close as possible to the wall, in the middle plane of the model. They are machined in one single block along their full length, avoiding the problem of edge adjustments or flow instabilities due to geometric mismatching.

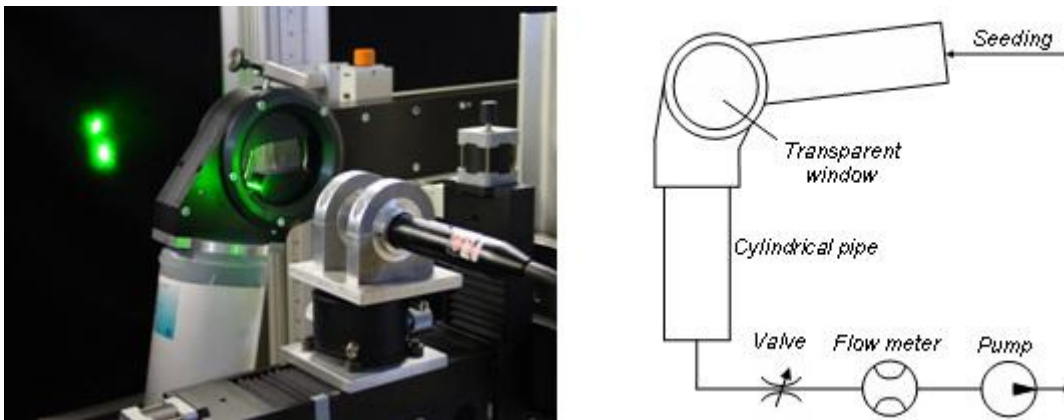


Figure 4.13: Experimental setup: simplified intake-port model and LDA system

The experimental apparatus used were made of a continuous-wave diode-pumped Nd:YAG laser ( $\lambda=532$  nm) and a LDA probe from Dantec Dynamics. The probe is a 1-component FlowLite probe, with an outer diameter of 27 mm, offering a beam diameter of 1.35 mm (beam spacing of 15 mm) and a focal length of 160 mm. In this configuration, the measuring volume had a length of 1.71 mm and a diameter of 0.08 mm. The system was mounted on a 3-axis motorized traverse. Finally, the complete volume was seeded with oil particles (diameter $\sim$ 1-2  $\mu$ m), produced by a Laskin-atomiser, and sucked into the port by a pump. According to the coordinates system defined in Figure 4.14, the X- and Y-components were measured one after the other. Typically, several hundred samples were recorded at each position, except in the recirculation area. Different measurements have been conducted, with different resolutions, as presented in the following section.

#### 4.3.2 Flow Fields Comparison

Even if LDA is not truly dedicated to measure large flow fields, a preliminary study has been carried out to observe the flow in the port elbow region as a whole. As presented in Figure 4.14, several measuring planes, with various spatial resolutions have then been utilized to deliver some qualitative information such as flow detachment, recirculation length, and global velocity magnitude. For this application, a constant valve-lift has been set to 10mm, and the flow rate to 70  $\text{m}^3/\text{h}$ , leading to a Reynolds number of about 26000 (based on the hydraulic diameter and the average velocity in the channel), characteristic of a turbulent flow.



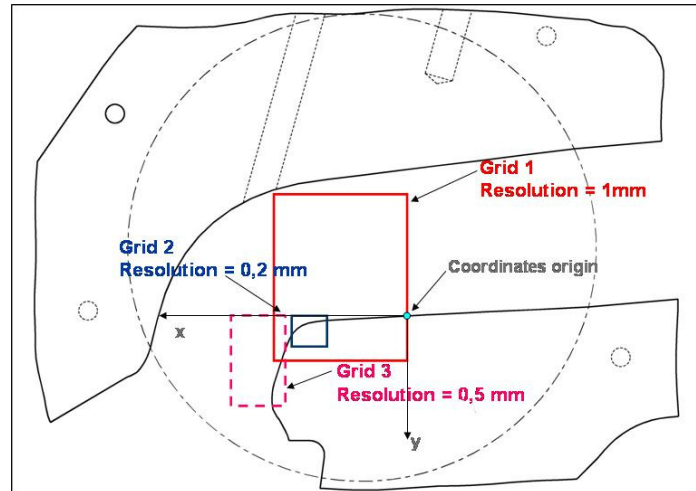


**Figure 4.14: Position of the different planes measured**

In the following figure, Figure 4.15, a comparison is made between the CFD results plotted in the upper side, obtained with URANS and DES methods, and the LDA results in the two other quadrants. From this overall comparison, the general flow structure seems to be properly simulated, giving the same order of magnitude for the horizontal component of the velocity. Although the measured points are not completely covering the wall region in the grid 3, the negative velocities obtained with both methods are proving the presence of a flow recirculation induced by the port geometry. The position of occurrence of the flow detachment is very well matching between both numerical results and is in a good agreement with the LDA measured one presented on grid 2. By comparing this area, which is offering a good precision in the boundary layer, with the much coarser grid 1, it is obvious that the finer the resolution the smaller the extrapolation area is and the more accurate the results.

However, a few discrepancies between URANS and DES results can be noticed in the figure below, a first one in the recirculation area, right downstream of the port elbow. Indeed the URANS solution is underestimating the magnitude of the negative velocity developing in this region, which could lead to an anticipated flow reattachment. Unfortunately the low LDA resolution employed for this plane (grid 3) does not allow a proper validation or refutation of this information. Another difference is occurring in the clearance region between the valve and the cylinder head. There again, URANS is delivering a lower velocity magnitude as to the one obtained with DES. Furthermore, the general flow structure seems to be more complex with the hybrid turbulence model than with the pure URANS method. This open issue would require further experimental investigations to attest one or the other solution.

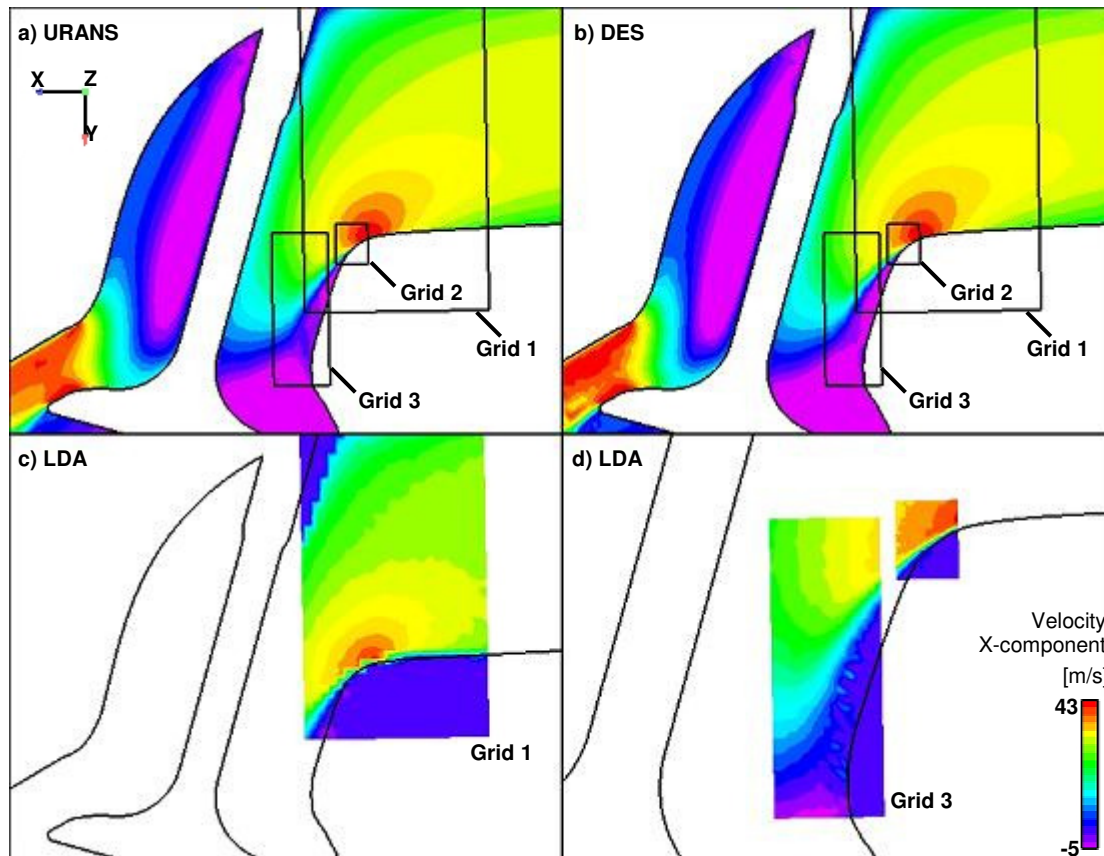


**Figure 4.15: Horizontal velocity component comparison between a) CFD URANS, b) CFD DES, c) LDA grid 1 (1mm resolution), d) grid 2 (0,2mm resolution) and grid 3 (0,5mm resolution)**

### 4.3.3 Detailed Boundary-Layer and Flow-Detachment Analysis

Extensive measurements [49] have been realized in the model in order to study the influence of different parameters such as various flow rates or valve-lifts, and to adjust the experimental setups to guarantee a good optical quality (preventing strong Laser light reflections or adjusting the seeding density). Special care has been given to the boundary layer resolution, using variable spacing along a single profile. In some cases this resolution went down to 0,01mm for the first millimetre, the rest of the profile using 0,5mm accuracy. The following study will concentrate on three profiles as shown thereafter in Figure 4.16. The X- and Y-velocity components are the horizontal and vertical components of the total velocity magnitude, but are not the local projection on the profile considered. Based on the manufacturer's inputs, the accuracy to determine the average velocities should be around  $\pm 1\%$ . However, in particular configurations affecting the control volume orientation, the illumination or the seeding quality, the sample size may be drastically reduced, which directly influences the measurement precision by increasing the results deviation.

As far as the CFD simulations settings are concerned, steady state boundary conditions have been used, with a given static pressure at the inlet and a constant mass-flow at the outlet. The unsteady simulations are initialised by a previously computed RANS flow-field associated to a certain level of turbulence intensity (10%). The approximation of intensity level, as well as the treatment of the wall surface considered as hydraulically smooth could represent two sources of divergence between computed and measured results.

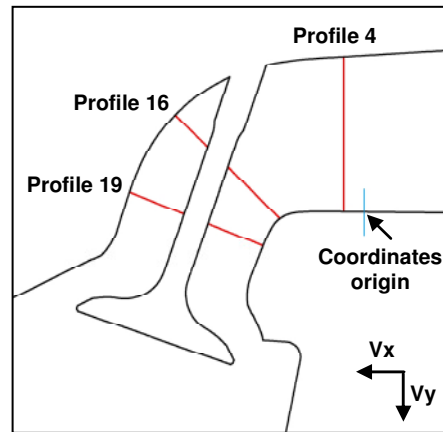


Figure 4.16: Position of the measured profiles (4mm, 16mm and 19mm from the coordinates origin)

In the following profiles, only the main component will be shown, the X-velocity component, with a particular emphasis on the boundary layer.

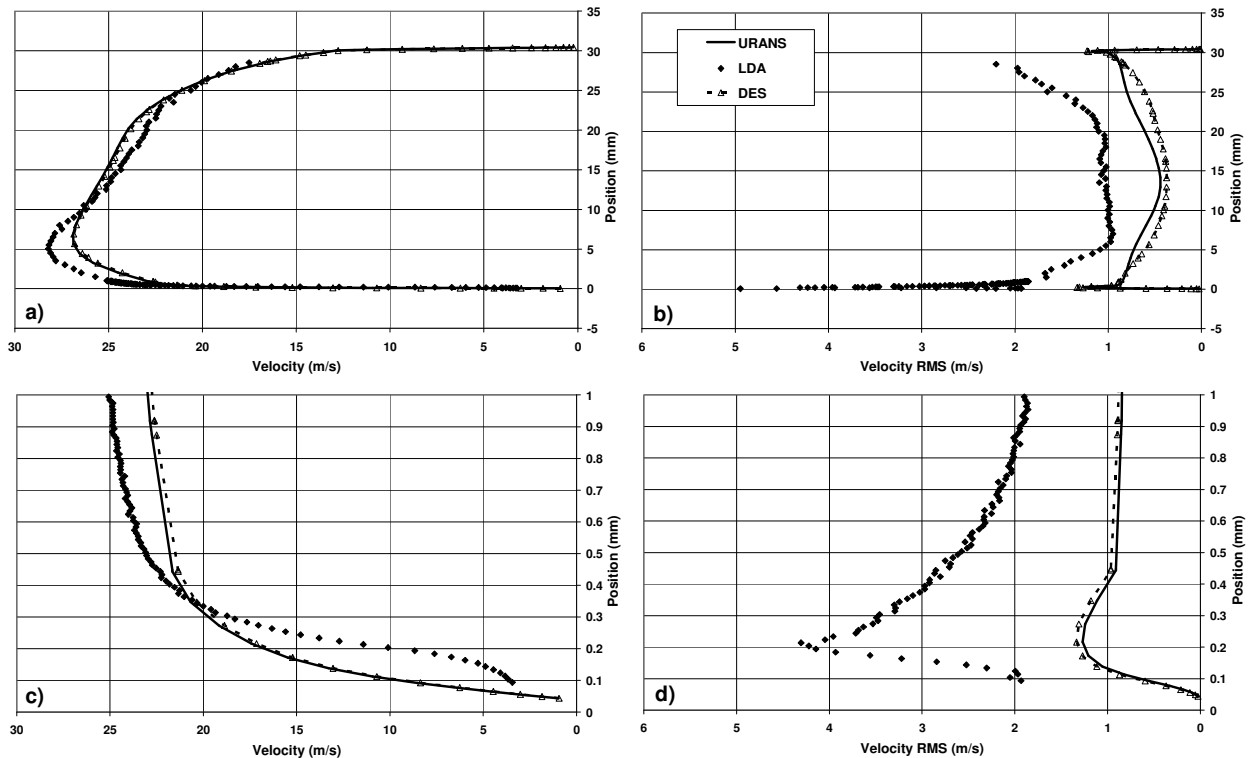
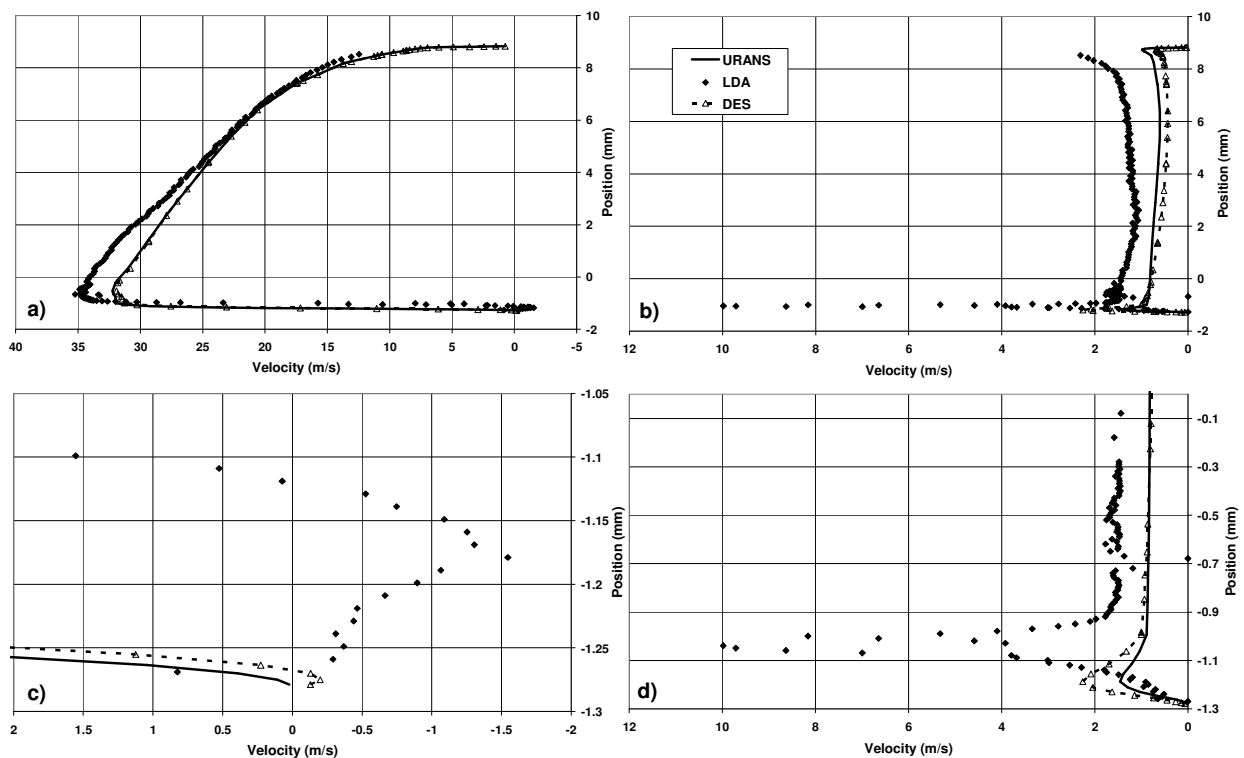


Figure 4.17: Profile 4 – a) X-Velocity component, b) RMS of the X-Velocity component, c) Zoom in the boundary layer for the X-Velocity component, d) corresponding zoom for the RMS

Figure 4.17 above is showing the horizontal component measured by the LDA system, the X-velocity component, compared to the numerical results obtained with URANS and DES modeling. The right hand side is presenting the associated Root Mean Square values (RMS) directly connected to the velocity fluctuations. In the lower part of the figure, a zoom in the boundary layer enables to get further information about the flow development in the vicinity of the wall. The points spacing for the measurements was of 0.01 mm, whereas for the simulation, the boundary layer is modelled by 12 points within 0.4 mm.

At the position considered, profile 4, the two different numerical methods are delivering very similar results due to the fact that the hybrid turbulence model is still working in RANS mode in this part of the duct. Indeed, no important perturbation occurred yet in the flow, whose nature and intensity would force the turbulence model to shift in LES mode. Even though the asymmetry of the profile is well reproduced by both simulations, the discrepancy with experimental data could be seen here as a consequence of the divergence of the boundary conditions mentioned earlier and the presence of numerical dissipation, directly influencing the nature of the flow. Indeed the flow described by the CFD results is not fully developed at this position, in spite of the length of the port. This could also be a reason for the difference in the RMS quantities, the DES model being more sensitive to the nature of the flow and to the boundary conditions as the URANS model. Beside these observations, the X-velocity component's profiles are showing the same trend, with a clear acceleration of the flow at the lower bound. With regards to the RMS values, a short verification is essential to control the accuracy of both measurements and simulation. According to the theoretical definition of the RMS profile for a fully-developed turbulent flow in a pipe (as described by Kim et al. in [75]), the amplitude of the RMS peak should be around three times the wall shear velocity ( $u_\tau$ ) and should be positioned at  $12 \leq y^+ \leq 15$  ( $y^+ = (yu_\tau)/\nu$ ). Based on the value given from the simulation for the wall shear velocity, the experimental RMS peak is about  $(2.63u_\tau)$  and is located at  $y^+ \approx 17$ , which is within a good interval of tolerance. For the numerical results, the position is the same as for the LDA ones, showing a good agreement with the theory, but the amplitude is much lower, about  $(0.82u_\tau)$ . This deviation can be attributed to the nature of the flow, which is probably not fully developed in the simulation case. Indeed, even if the general velocity profile is fully developed, it does not imply that the turbulent fluctuation profiles  $\overline{u'v'}$ ,  $\overline{u'u'}$  or  $\overline{v'v'}$  are also developed.



**Figure 4.18: Profile 16 – a) X velocity component, b) RMS of the X velocity component, c) zoom in the boundary layer for the X velocity component, d) corresponding zoom for the RMS**

While going further in the port, 16 mm downstream of the coordinates origin, the velocity profile for the X-component is developing as plotted in Figure 4.18. At first sight, at this position in the channel, DES and URANS are once again giving similar results. For the maximum velocity magnitude, both of them are presenting a small divergence from the experimental data of about 8.5%, which has to be related to two main factors: first of all, the stronger deviation of experimental results due to seeding irregularities in the elbow region, and secondly to the numerical dissipation. But the notable points that have to be highlighted here are the appearance of flow recirculation with DES (through negative values), and the larger RMS values obtained with this turbulence model. Then, the DES method is starting to show its potential to catch the real nature of the turbulent flow, by taking into account the contribution of the fluctuating quantities. Conversely, URANS is well known to damp these variations and to filter out the relevant information.

For this particular profile, the experimental data are presenting some imperfections, especially in the RMS estimation, where two separated peaks are occurring. A sensible mismatch between measurements and CFD results is also obvious, and should be connected to a slight problem of calibration of the system, or a rotation between both models. Around this position, a slender shift in one or the other direction could quickly lead to large divergence. On the other hand, it has to be mentioned that the numerical mesh quality is playing an important role for the accuracy of the simulation, solving properly the viscous sub-layer and then computing properly the turbulent viscosity. Therefore, it is possible to think that with an even finer mesh at the wall, the performance of both models could be improved and move closer to that of the experiments.

In the following figure, the velocity development within the recirculation region can be observed.

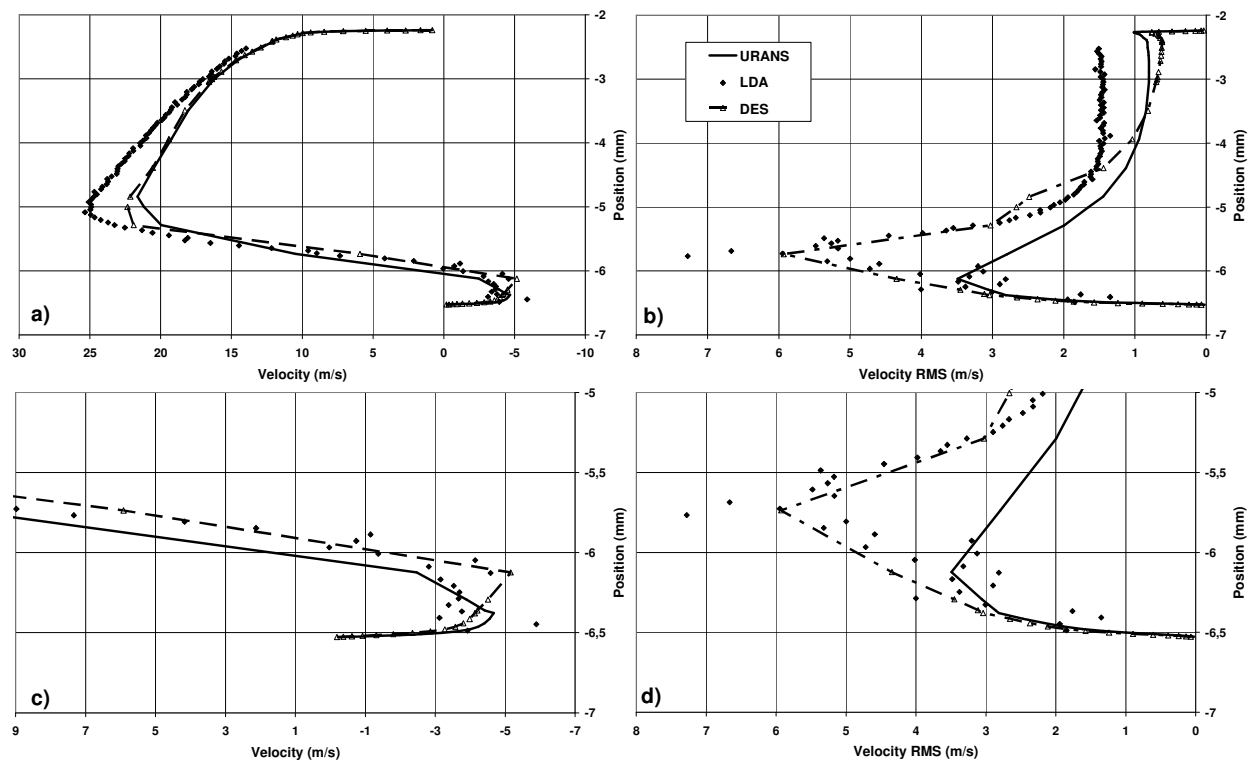


**Figure 4.19: Profile 19 – a) X velocity component, b) RMS of the X velocity component, c) Zoom in the boundary layer for the X velocity component, d) corresponding zoom for the RMS**

Here, a larger discrepancy between the two numerical methods is appearing, showing that DES results are getting closer to the experimental ones. For the X-velocity component, Figures 4.19 a)

and c), the amplitude is matching very well with the measurement data. Even the width of the recirculation region is simulated properly, whereas URANS results are missing the general shape of the flow. Secondly, the RMS values delivered by the DES model are much higher than the URANS ones and in the same order of magnitude as the experimental results. This is reinforcing the idea that hybrid turbulence models like DES can bring large improvement in the way of solving wall-bounded turbulent flows. From the experimental point of view, the LDA results are presenting large fluctuations in the boundary layer, underlining the extreme difficulty to get reliable measurements of the flow in this particular region. Indeed, the curvature of the elbow and the presence of the recirculation are affecting the seeding density and quality in this region, thus preventing the particles to properly follow the flow. Even the use of a longer acquisition time for the first points of the profile in the wall vicinity did not stabilize the results quality as it would have been expected.

### **Conclusion**

The results presented in this section are highlighting several important aspects of the investigation of turbulent flows induced by cylinder-heads and intake ports.

First of all, for the overall averaged results considered here, a good global matching between the velocity fields predicted by both CFD methods and the measured planes with LDA can be observed, validating the trends given by the numerical results. However, despite this good agreement, some discrepancies are occurring while considering the detailed velocity profiles and fluctuating quantities, under the form of the RMS value of the velocity components. Indeed, the maximum velocity peak is always underestimated by the numeric, showing a difference comprises between 5% and 13%, a difference even greater with regards to the RMS values. Until a certain point in the duct, both CFD methods are presenting the same effects, probably related to the boundary and initial conditions employed, the approximation of the wall roughness (hydraulically smooth), as well as the dissipative nature of the turbulence models. Only after a certain point, when the model is shifting from a URANS formulation close to the wall, to a LES mode in the free stream, the DES results are differentiating themselves by approaching the level of turbulence acquired experimentally and delivering a much closer results in term of RMS quantities. This difference between both numerical models could be also an explanation for the better prediction of the recirculation position and length by the hybrid turbulence model compared to the URANS one. For further unsteady flow investigations, by improving their performance thanks to a better triggering of the turbulence model to make it more sensitive and then force it to work in LES mode, only the hybrid method will be able to provide the relevant information required to characterize the turbulent in-cylinder flow.

From the experimental point of view, LDA offers a satisfying measuring precision for the case studied here, as well in time as in space, even if the last aspect is restricted in the boundary-layer regions by the distance of the first measured point in the wall vicinity. A clear restriction of the results also appeared in the elbow region where the strong fluctuations of the measured velocities and RMS highlighted the problem to get the proper seeding conditions in this region. This problem could certainly be alleviated by investing more efforts and more time to improve them but would not meet the other perspectives offered by the last CFD techniques available. As a matter of fact, the major limitation of this experimental method is its point-wise nature, which is obviously not dedicated to the measurement of large planes and then prevent using the great potential of advanced unsteady 3D CFD methods in terms of flow visualization and turbulent structures tracking.

Thus, based on these observations, a planar time-resolved optical system such as High-Speed Particle Image Velocimetry (HS-PIV) will be employed to validate the future simulation results. More details on the development of turbulent flows in engine intake systems will be gained thanks to the combined use of this experimental technique and the results obtained by advanced turbulence models. A particular attention will be given to the 2- and 3-dimensional post-processing of such unsteady data to describe the complex process associated to the origins of turbulence in internal combustion engines.

#### **4.4 Cylinder-Head Model Without Tumble-Flap**

Before detailing the experimental setup developed to characterize the turbulent structures generated by a cylinder head model, a brief description of the HS-PIV technique will be made in order to outline the main advantages of this optical diagnostic method.

##### **4.4.1 High-Speed Particle Image Velocimetry (HS-PIV)**

The PIV technique basically allows one to record images of large parts of flow fields in a variety of applications in gaseous or liquid media and to extract the velocity information out of these images. The evolutions brought to this method during the last decades in terms of data post-processing, the quality of optical systems, the large improvements in laser technology as well as computer capacity have broaden the use of PIV, from qualitative flow visualization to quantitative measurement of complex instantaneous velocity fields.

Recently, even if PIV is commonly recognized and employed within the fluid mechanics research community and almost routinely used in industrial applications, the development process of imaging systems is in no way slowing down. While considering the particular domain of turbulence research activities, the experimental systems have to fulfil the ever-increasing scientists' expectations. Indeed, these studies are calling for a high spatial resolution of the data field in order to resolve large scale as well as small-scale structures in the flow. On the other hand, a second important condition is that the increasing number and the increasing quality of numerical simulations of unsteady flow fields require adequate experimental data for the validation of the numerical codes and their ability to reproduce the physics of the problem. As industrial turbulent flows are concerned, and especially at high Reynolds numbers, beside the spatial resolution evocated earlier, time resolution is playing a crucial role for tracking the broadest range of structures developing and later collapsing within the flow of interest. For this reason, PIV systems described as High-Speed or Time-Resolved systems are becoming very popular, offering high acquisition frequencies, up to tens of kilohertz. The operating frequency range of these systems is increasing at a very high pace, making the terms High-Speed or Time-Resolved relatives to the temporary high-end systems and thus very ephemeral. In the different measurements presented in this paragraph and in Chapter 5 thereafter, the two campaigns took place within less than one year interval, using the latest commercial systems available, and their frequency doubled during the same period.

For this first application of HS-PIV, a 2-components method (2-C PIV) has been employed. 2-C PIV is a whole field measurement technique, providing multi-point, instantaneous acquisitions of the flow-field. Figure 4.20 below briefly describes a typical setup for 2-C PIV recording in a vertical cylinder.

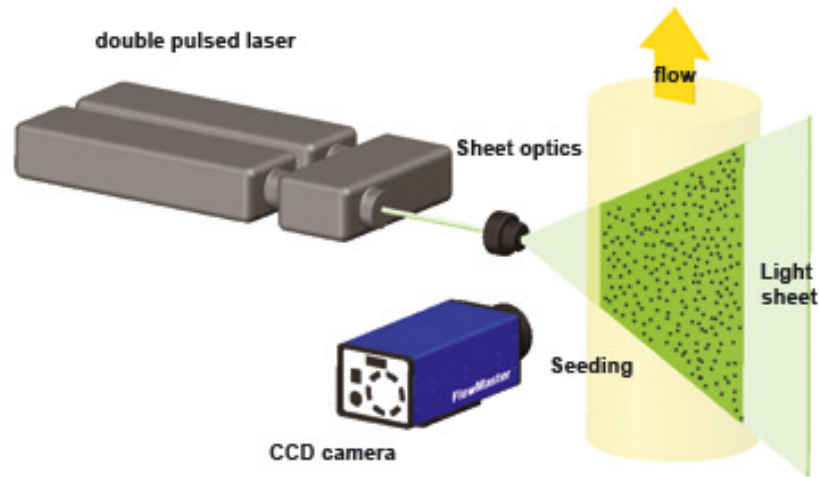


**Figure 4.20: 2-Components PIV general setup**

Small tracer particles are added in the flow and are illuminated by the laser pulses as they are passing in the region of interest. Depending on the nature of the gaseous medium, the light source used and the characteristics of the flow, the particles have to be chosen with good care in order to properly represent the real flow displacement. Indeed, PIV is an indirect velocity measurement technique, strongly dependent on the previously mentioned parameters. The time shift between the two following laser pulses is adapted to the mean flow velocity and the magnification at imaging. An imaging device records the light scattered by the tracer particles via a high quality lens on two separate frames on a special CCD (Charge-Coupled Device) or CMOS (Complementary Metal Oxide Semi-conductor) sensor. The output is stored temporarily on the local buffer memory of the camera before being transferred to a Personal Computer for post-processing.

Based on the same principle, but following some modifications of the hardware as well as the post-processing program, it is also possible to extract the third velocity component of the flow, as will be presented later in Chapter 5.

#### 4.4.2 Optical Test-Bench Description and Intake-Port Model Presentation

In order to observe the formation and development of the turbulent structures induced by an intake-port, a research model derived from a four-valve DISI engine cylinder-head has been machined as a rapid prototyping part (refer to [70]). This “flow-box” was mounted on the so called Tumble-Optical-Test-Bench, basically a square transparent box with an internal cylinder made of Perspex, allowing optical measurements to be carried out (see Figure 4.21; more details on this setup in [15]). In the current case, a cylinder diameter of 84 mm has been used, and placed under the experimental intake-port described above. The two intake valves were manually actuated and positioned at a constant valve-lift (from 3 mm to 10 mm) for each sequence of measurements, corresponding to a specific stationary flow-rate (from 50 kg/h to 150 kg/h) regulated by the speed of the pump. The intake flow sucked into the port was seeded with oil droplets (diameter  $\sim 1 - 2 \mu\text{m}$ ), produced by a Laskin-atomiser.



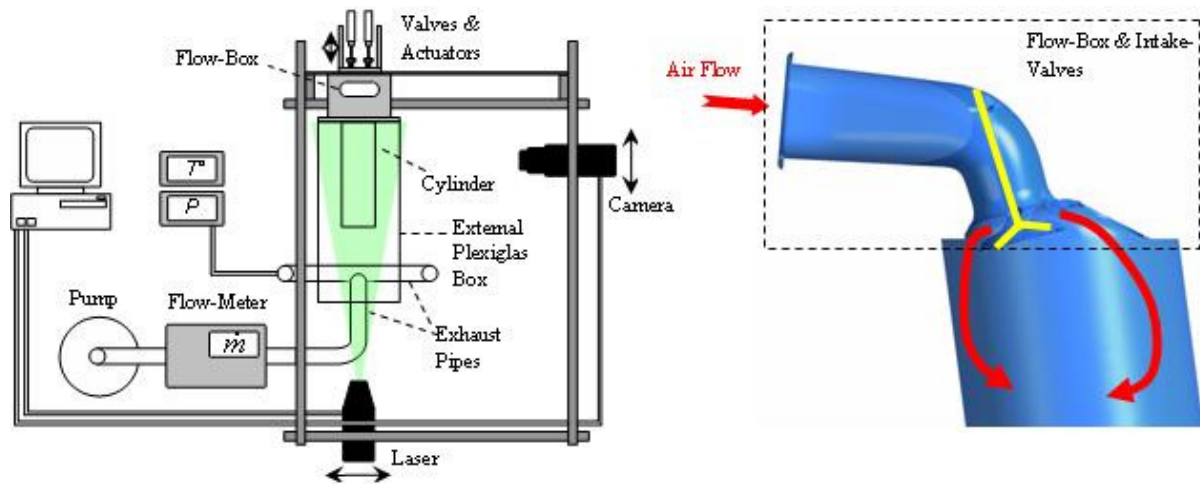


**Figure 4.21: Experimental setup and model: left, the Tumble Optical Test-Bench; right, the flow-box and the cylinder in Perspex (reprinted from [70])**

The acquisition rate of Particle Image Velocimetry (PIV) systems is constantly increasing in order to fulfil experimentalists' requirements. The study of instationary and highly turbulent industrial applications, such as in-cylinder flows in motored engines or high-speed external aerodynamics, will only be made possible if the available systems can overcome the technical limitations of the measuring devices, camera frame-rate and laser pulse repetition-rate.

The system used for these experiments was aiming at evaluating the potential of actual HS-PIV systems in becoming a viable option for research in fluid mechanics, according to industrial requirements and expectations.

The technical features of the HS-PIV system were the following:

*Laser (Pegasus from New Wave):* dual-cavity, diode-pumped, frequency-doubled Nd:YLF laser, 527 nm, 2-3mJ @ 5kHz per cavity

*High-Speed Camera (High-Speed Star 5 from La Vision):* CMOS camera with a resolution of 512x512 pixels @ 10 kHz

The post-processing has been realised thanks to the program DaVis from LaVision. The evaluation of the image pairs was performed with an interrogation area of 32x32 pixels, 50% overlap and the subtraction of a sliding background of 16 pixels.

The subsequently presented experimental results were obtained at a mass flow-rate of 50 kg/h with a valve-lift of 10 mm and a laser pulse time interval of 35  $\mu$ s. A rate of 5 kHz for the vector fields has been achieved.

As far as the numerical simulation is concerned, the zonal turbulence model proposed in ANSYS- CFX, the DES method, has been utilized.

A fully unstructured mesh is employed, mostly made of tetrahedron in the core of the flow, using a typical wall treatment through several prisms layers with an exponential growth. The time step employed for the simulation is set to 10 $\mu$ s, maintaining the Courant number at a value below one (see Equation 3.21 and associated references).

### 4.4.3 Comparison Between HS-PIV and DES Results

The results obtained with a valve-lift of 10 mm and a mass flow-rate of 50 kg/h are qualitatively the most satisfying. Indeed, for this particular configuration, at lower velocities, it is expected to follow some structures convecting within the measured plane with an affordable frequency.

In Figure 4.22 below, two measuring planes are displayed, one in the cylinder middle-plane (plane 1) and the other in a valve middle-plane (plane 2). When using a fast lens (objective aperture = 1.2) in front of the High-Speed camera, the field of view covers the whole central cross section of the cylinder.

First of all, a comparison between the numerical and the experimental results based on the averaged velocity fields will follow.

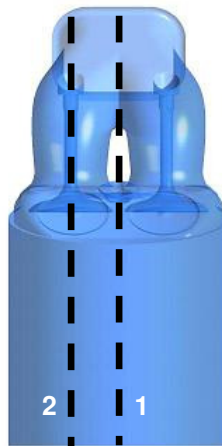


**Figure 4.22: Positions of the two different measured planes: 1 – cylinder middle-plane, 2 – valve plane**

#### 4.4.3.1 Time Averaged HS-PIV and CFD Results Analysis

The following figures are showing the averaged velocity vector and scalar fields in the cylinder- (Figure 4.23) and the valve-plane (Figure 4.24). For a better visualization, a compromise has been found by representing the flow direction by the normalized velocity vectors and the magnitude by the colour. A sample of 100 consecutive time-steps has been used to average the experimental data, whereas the CFD results are averaged over 190 time-steps. This sample size can be proved too small, especially for the PIV measurements, in case that the snapshots employed are not independent from each other. The computation of the time correlation between following timesteps will allow verifying this point. The colour map is related to the total velocity magnitude and the vectors length is kept constant at every position, just giving information about the flow direction. The CFD results have been interpolated on the measurements “grid” (64x64 vectors).

In both cases, measurements and simulation results are presenting the same trend. In the cylinder middle-plane (Figure 4.23), a large rotational structure perpendicular to the cylinder axis is obtained, also called tumble, typical of four-valve pent-roof engines.

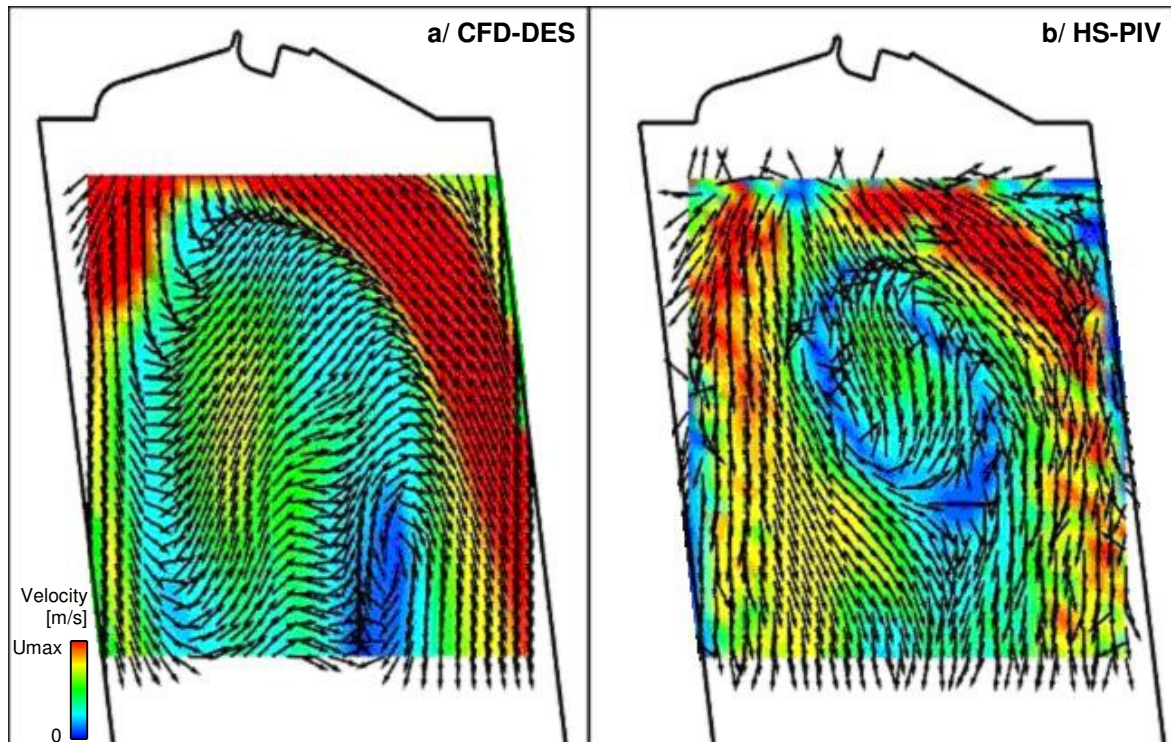


Figure 4.23: Averaged velocity vectors and scalar fields in the cylinder middle-plane (velocity magnitude ranging from  $0 \rightarrow U_{\max}$ )

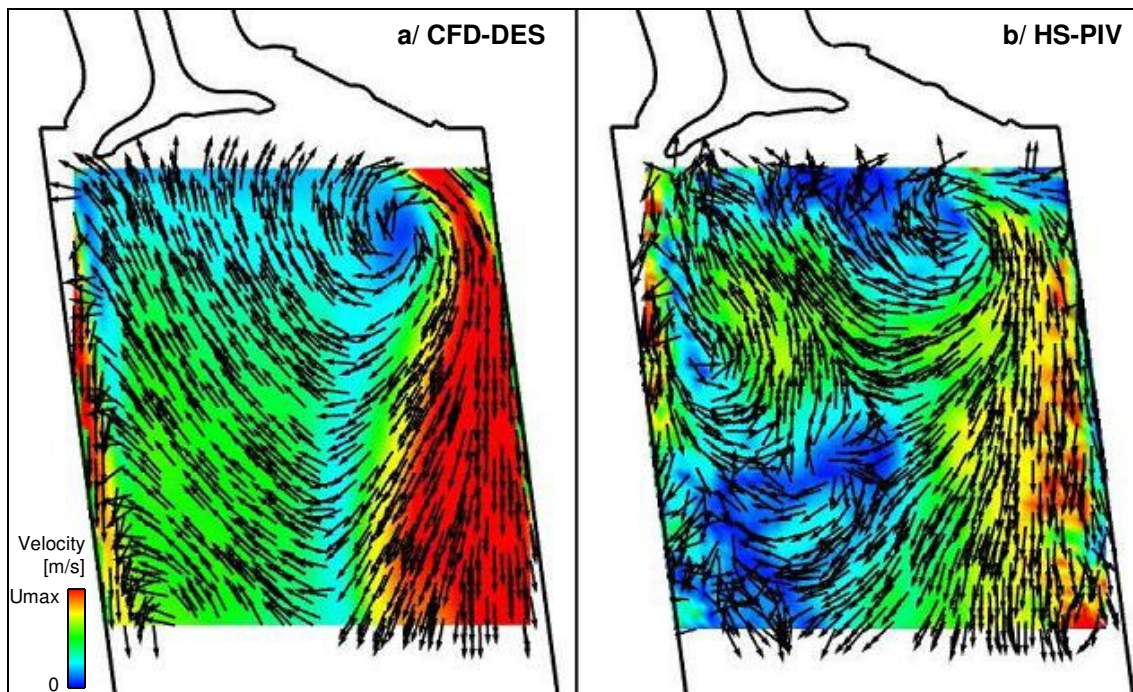


Figure 4.24: Averaged velocity vectors and scalar fields in the valve-plane (velocity magnitude ranging from  $0 \rightarrow U_{\max}$ )

In the valve-plane (Figure 4.24), two strong jets are developing from the upper and the lower tips of the valve, resulting in a rotating structure located in the upper right hand-side of the cylinder. Quantitatively, it is interesting to note that the velocity range is of the same order of magnitude in both cases.

Nevertheless, some discrepancies are occurring in the lower left hand-side for this particular plane, and could be explained by a larger number of non-valid vectors as in the rest of the window. The same observation can be applied to the jet region of the flow along the right-hand side of the cylinder, where the averaged velocity field presents alternatively high and low velocity regions. This implies either that the sample size is not sufficient to get an accurate statistic of the flow or that the quality of the PIV data is not satisfactory.

The former remarks are calling for a detailed analysis of the temporal resolution of the PIV measurements in order to estimate their overall quality and their relevance for further unsteady investigation.

#### 4.4.3.2 Analysis of the PIV Time Resolution

Figure 4.25 thereafter is displaying four consecutive vector fields delivered by the post-processing of the HS-PIV data. The time interval between each of them is  $200 \mu\text{s}$  (5 kHz acquisition rate). In this sequence, chosen randomly among the large amount of data available, it is relatively difficult to recognize any of the vortical structures constituting the flow and ultimately tracking them.

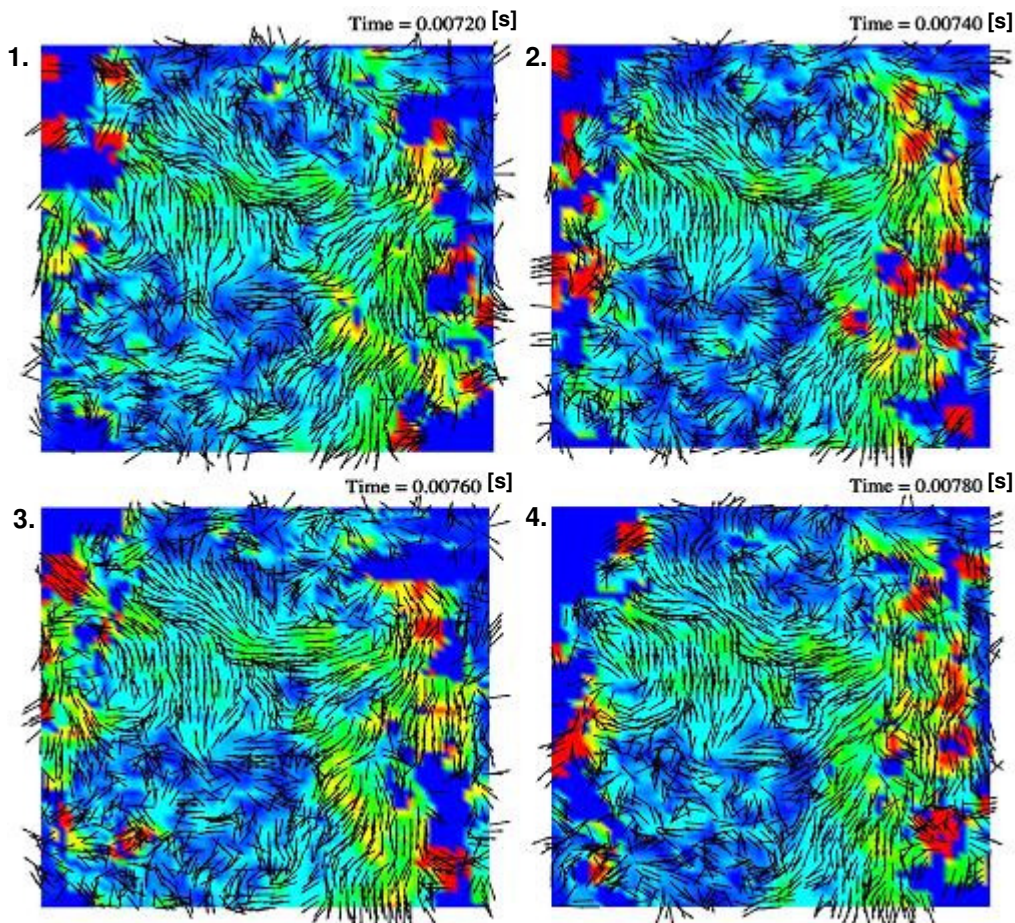


Figure 4.25: HS-PIV instantaneous velocity fields at four consecutive time steps in the valve middle-plane (same colours and vectors scaling for all figures, from  $0 \rightarrow U_{\max}$ )

Indeed, some of the flow regions are not always properly resolved, lacking some vectors at different times, and in turn influencing the accuracy of the results. These regions are principally located in the wall vicinity, where the Perspex curvature is the highest, greatly affecting the optical properties. Moreover, with regards to the vectors displacement between two consecutive shots, the acquisition frequency may be too low to follow them in a resolved manner.

In order to estimate more accurately the capacity of the system to supply time-resolved results, the time-correlation computed between two consecutive “snapshots”,  $R_i(x, y, \Delta t)$ , and its associated correlation coefficient,  $\rho$ , can be considered. These two quantities are defined as follows:

$$R_i(x, y, \Delta t) = \left\langle \left( u_i(x, y, t) - \langle u_i \rangle \right) \left( u_i(x, y, t + \Delta t) - \langle u_i \rangle \right) \right\rangle \quad (4.4)$$

$$\text{and} \quad \rho = \frac{R_i(x, y, \Delta t)}{R_i(x, y, 0)} \quad (4.5)$$

where  $\langle \cdot \rangle$  represents a time averaging operation.

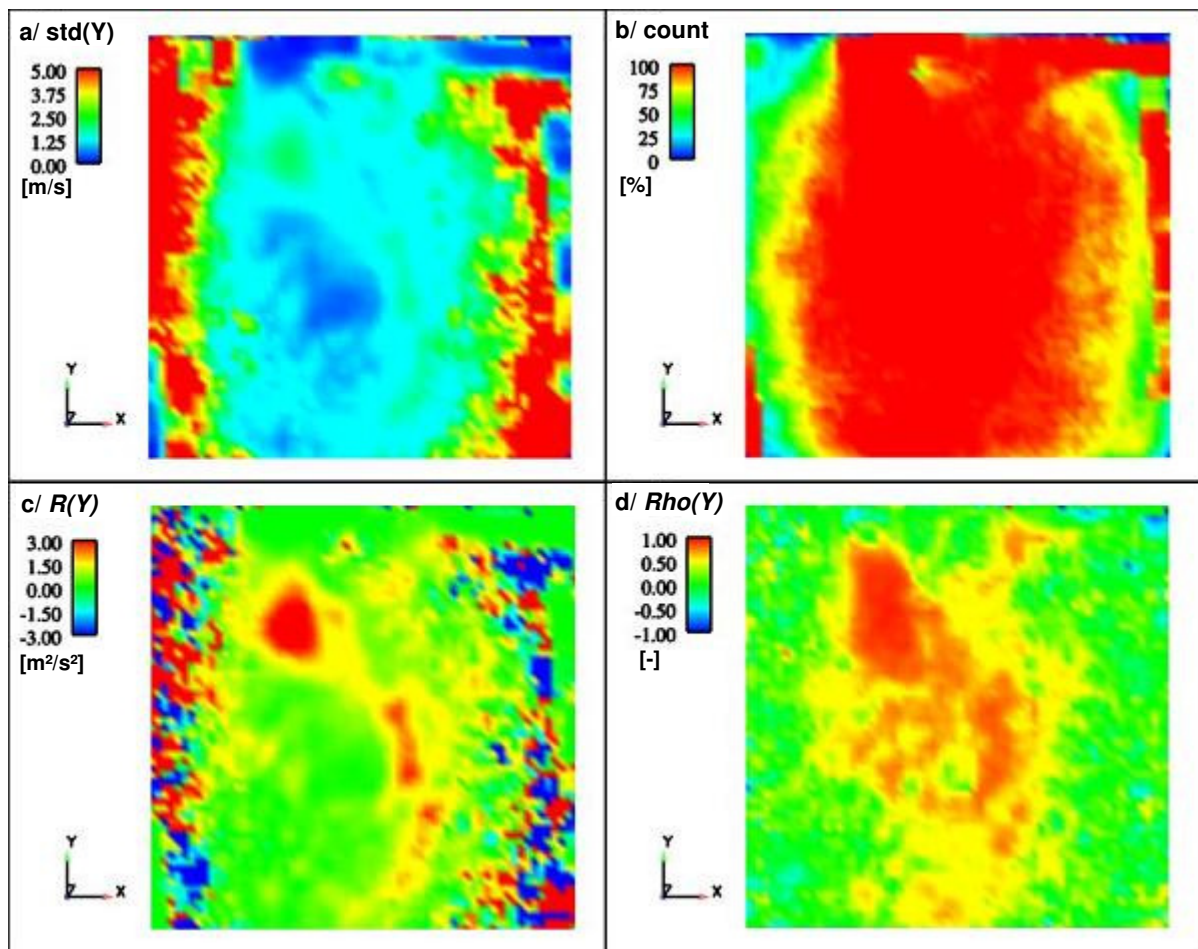


Figure 4.26: HS-PIV data analysis (50 kg/h, 10 mm, valve middle-plane): a/ standard deviation (equal  $R(x, y, \Delta t)$ ) of the Y-velocity component, b/ number of valid data per point over the sample size (here 100 time-steps), c/ time-correlation of the Y-component and d/ correlation coefficient  $\rho$  ( $\rightarrow Rho$ )

In the graph above, in the first quadrant starting from the upper left, the standard deviation of the Y-velocity component presents two regions with high fluctuations, logically located in the jets induced by the valve. These are also the positions where the lower count numbers are observed (upper right-hand side of Figure 4.26), which mean that the reliability in these regions is not very high. As a matter of fact, the former observation also explains why some correlation peaks are obtained at the border of the measuring window, decreasing the clarity of the results. However, by normalizing the correlation function by the square of the standard deviation, the information is filtered and offers a better understanding of the correlation between two consecutive acquisitions. In the present case, the area of maximum correlation corresponds to the portion of the flow which is more stable, around the centre of the window. Most of the interesting information with regards to the turbulent regions is then missing. Indeed, the correlation coefficient is computed at each point of the interpolated acquisition grid, between a time  $t$  and  $t+dt$  and then relates to the dependency existing between two successive time steps. Here, except for the stable central region of the window, the coefficient is equal to zero everywhere. This implies that the fluctuations between two PIV acquisitions are too high to be able to follow the structures.

Considering these restrictions of the HS-PIV data, the rest of this section will focus on the analysis of the numerical results, which have already shown a good correlation in terms of averaged quantities.

#### 4.4.4 2D and 3D Flow Visualization

Based on the simulation results obtained with the zonal turbulence model proposed by CFX10, the DES method, different visualization “tools” have been implemented to detect and track the flow vortices. Before going into detail of this analysis, a quick look into different velocity planes from the numerical model is required to get a better understanding of the global in-cylinder flow pattern.

Figure 4.27, hereafter, shows different section planes in the fluid domain, all of them presenting a strong asymmetry of the flow for the particular time-step chosen. In fact, the short simulation time ( $t_{Tot}=18.6$  ms) did not allow to observe the evolution of this asymmetry, because no other period of oscillation can be resolved (if periodic). Apparently, the same situation happened with the HS-PIV measurements, since the averaged velocity field placed in the valve middle-plane was close to the simulation results. Obviously, some flow instabilities like a “flapping” effect may occur in the port, creating this alternating flow pattern from one side to the other. This phenomenon, while observing instantaneous results or averaging over a too short period, can provoke quiescent flow states in certain regions, whereas others are presenting a high density of turbulent structures. The different cross sections presented in Figure 4.27 are tending to show that this asymmetry is taking its origin in the port elbow and is reinforced through the valve geometry. But this has to be further investigated before being taken for granted. In order to improve the visualization of the vortices developing in the flow, different criteria have been employed here: pressure contours in 2-D as well as isosurface (3-D) of low pressure and the so-called  $Q$ -invariant.

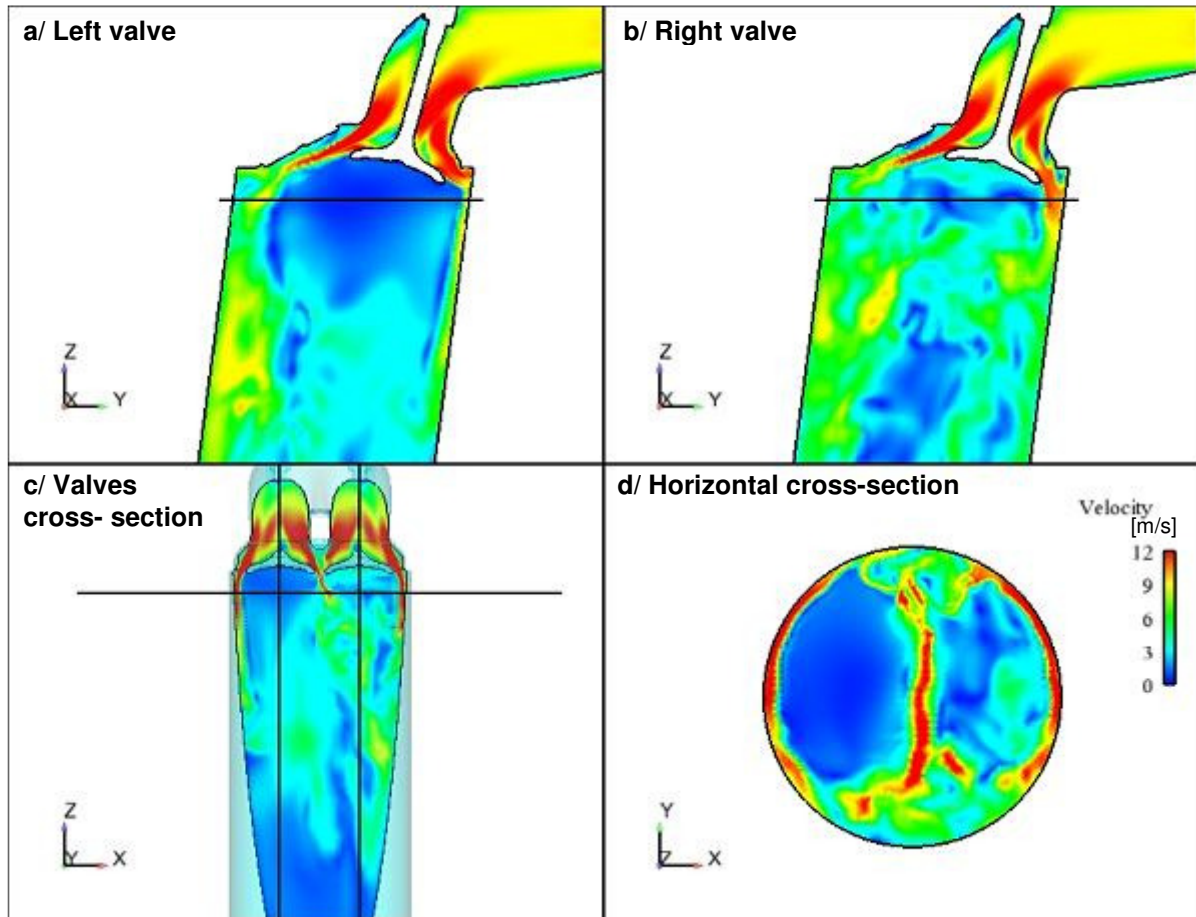
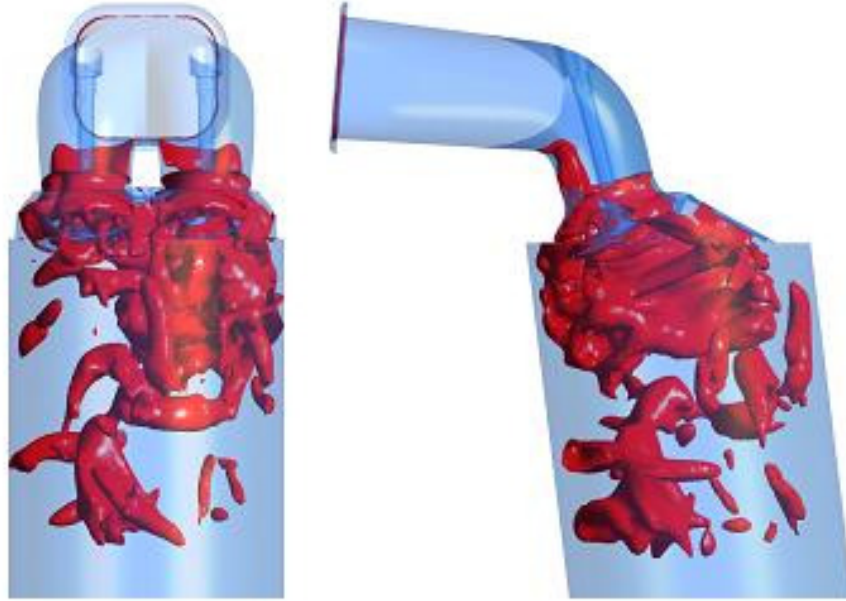


**Figure 4.27: CFD results - Various cross-sections of the flow: a) left valve middle-plane, b) right valve middle plane, c) flow cross-section in the Y direction and d) cross-section plane in the Z direction**

The last criterion, as presented in §3.3.2.3, is defined as the second invariant of the velocity gradient tensor and can be written as follows:

$$Q = \frac{1}{2} \left( |\Omega|^2 - |S|^2 \right) \quad (4.6)$$

where  $\Omega$ , the vorticity tensor, is the anti-symmetric part of the velocity gradient tensor,  $\nabla \bar{u}$ , and  $S$ , the shear-stress tensor, is the symmetric part of the same velocity gradient tensor. As demonstrated from Jeong and Hussain [72], regions of positive  $Q$  are considered vortical regions.



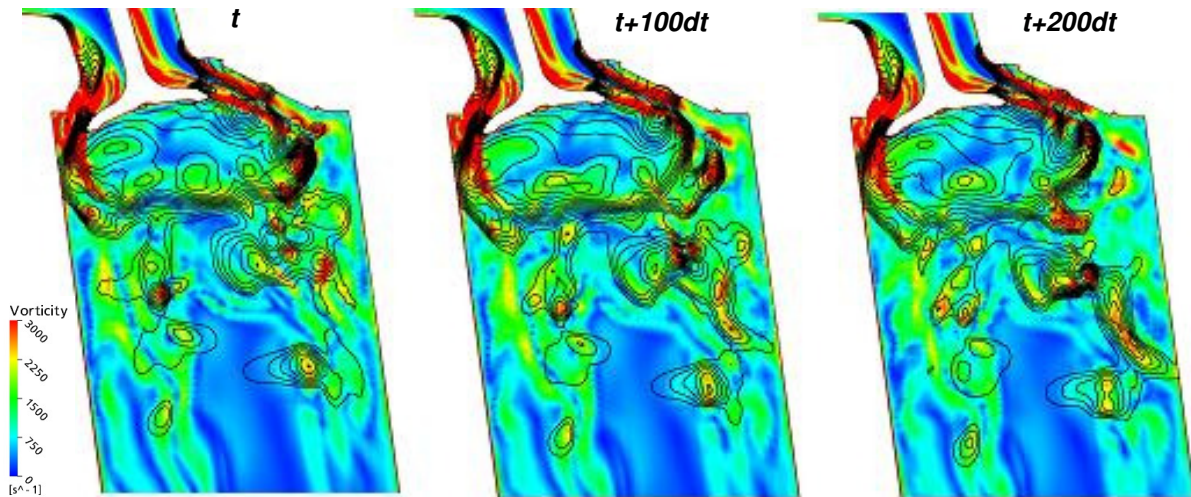
**Figure 4.28: Isosurface of low value of normalized pressure ( $P = -2.1\rho U_0^2$ )**

Figure 4.28 displays a 3-D isosurface of a selected low pressure. This pressure is normalized with  $\rho U_0^2$ . The particular isosurface chosen here,  $P/(\rho U_0^2) = -2.1$ , represents strong vortex tubes and rings taking their origin at the port elbow and developing downstream of the cylinder passing the valves. This representation allows a better insight of the main vortex structures, as well as their positions and distribution to be obtained, highlighting once again the flow asymmetry observed earlier.

The two following figures, Figures 4.29 and 4.30, are showing 2-D vorticity planes in the middle valve section. The regions coloured in red are standing for clockwise or positive rotating eddies, whereas the blue ones are representing the anti-clockwise or negative rotating structures. From Figure 4.29, where the low-pressure contour lines are superimposed to the vorticity, it can be seen that oscillations and roll-up of the shear-layer occurring at the lower and upper part of the valve are associated with alternating low- and high-pressure cores. These pressure cores are also well correlating with the positive  $Q$  isolines from Figure 4.30, which are representing the vortical regions. Nonetheless, the  $Q$ -invariant is presenting a major advantage towards the low-pressure visualization technique. Indeed, physically,  $Q$  represents a local balance between shear strain rate and vorticity magnitude since it is defined by the difference between these two quantities. That is the reason why region of positive values of  $Q$  correspond to regions of swirling flow filtered from the shear layer. This aspect can be easily observed in Figure 4.30, more particularly downstream of the valve-tip, where both shear stress and vorticity are quite high. At this location, only the filter operated with  $Q$  allows distinguishing real vortical structures from the high shear stress.

From a general point of view, by considering the consecutive time-steps presented in both figures, the path of the vortices constituting the turbulent flow can easily be followed thanks to these two visualization criteria, with a consequent advantage for the  $Q$ -invariant.





**Figure 4.29: Valve middle-plane shaded with vorticity magnitude and low normalized pressure contour lines**

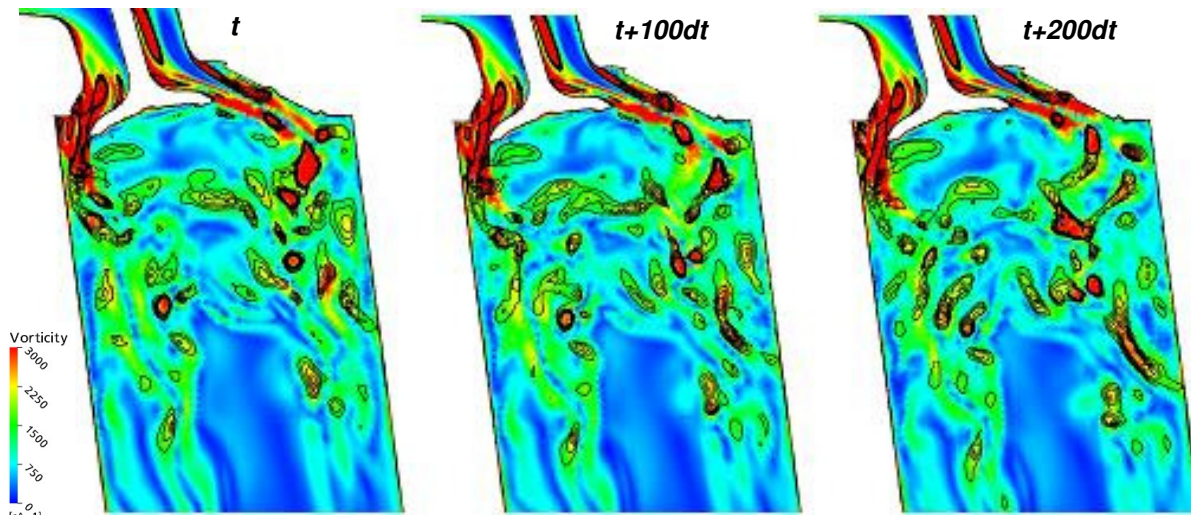


**Figure 4.30: Valve middle-plane shaded with vorticity magnitude and positive  $Q$  contour lines**

### Conclusion

Several important aspects required for the analysis of intake-port induced turbulence have been emphasized all along this last preliminary study. As far as the experimental data are concerned, various questions have to be tackled while measuring the turbulent flow in such a complex environment. First of all, the acquisition frequency has to be sufficient to track the different structures developing and convecting throughout the volume under specific flow conditions. Moreover, the quality of the system calibration is of higher priority, guarantying later a satisfactory imaging quality for further post-processing activities. This has to be done with respect to the numerous light reflections and diffractions occurring by example when the laser beam is traversing the cylinder out of its central position, or when the laser is meeting some reflecting surfaces such as the shafts of the valves. Another important aspect to measure and which will provide valuable validation data is the transverse component that could be obtained in a 3-dimensional measurement.

From the numerical point of view, the potential and efficiency of the hybrid turbulence model, DES, for unsteady flow investigation has been proved once again. As soon as they have been validated thanks to the experimental data, the CFD results can be further investigated in regions

of the flow where no measurements are allowed. In this sense, validation data and unrestricted 3D flow-fields simulations are complementary to study complex industrial geometries. By complying with the numerical requirements to guarantee the level of precision necessary to properly resolved the boundary-layers and the intense shear regions (like at the edge of a solid wall such as the valves tips), unsteady CFD simulation is offering the opportunity to visualize the turbulent structures and their time resolved evolution. Amongst the different criteria presented here, the second invariant of the velocity gradient tensor,  $Q$ , seems to be the most appropriate visualization technique to detect and follow the vortices cores.

According to the former observations, for the next investigation of a production FSI<sup>®</sup> cylinder head, emphasis will be laid on the time-resolution of the experimental results by means of the latest up-to-date High-Speed PIV systems available. Moreover, 3D information will be generated thanks to stereoscopic technique applied to the geometry mounted on an optimized “tumble optical test-bench” (TOP). The visualization method applied here should be further developed in association with other post-processing techniques in order to deliver a better insight in the origin of turbulence induced by the intake port. Thus, based on the  $Q$  invariant representation, a quantitative description of the phenomenon should be obtained, which could be of great use for the purpose of engine intake components optimization.

## 5 Analysis of a Production FSI<sup>®</sup> Cylinder-Head

As final stage of the research strategy developed in the frame of this study, and in order to conciliate the different observations presented earlier, the cylinder-head of a production 1.6l FSI<sup>®</sup> engine has been finally investigated. It is then expected from this analysis to develop a synthesis of the phenomena observed individually within the previous paragraphs.

### 5.1 Optimized Design of the Steady-State Optical Test-Bench

The experience gained with the optical test-bench described in §4.4.2 was suggesting some modifications of its design to improve the acquisition quality of the imaging system. The main objective was to reduce the energy loss through the material as well as the reflection and refraction of light induced by the nature of the material and the curvature of the cylinder.

Indeed, most of the optical problems encountered with the former setup were mainly related to the important thickness of the material through which the laser beam had to go. As presented in Figure 5.1 thereafter, the highest improvement has been achieved thanks to the displacement of the cylinder outside of the surrounding box, preventing the laser to go across a 10 mm-thick wall of Plexiglas. Even the cylinder thickness has been optimized over its total height; after a hand-made treatment, the wall was rubbed down to a width of 2 mm.

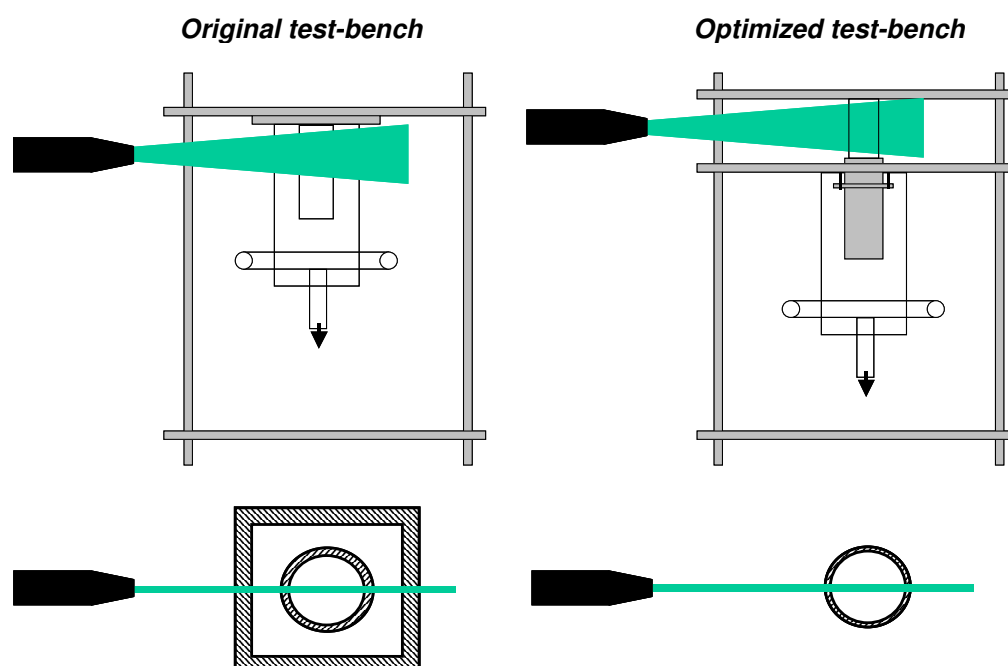


**Figure 5.1: Optical test-bench optimization.**

Plexiglas is a derivative of acrylic with very similar physical and optical properties. Even if this material is well known and used for its unexcelled optical clarity, making it to be a real alternative to the finest optical glass, Plexiglas has still a different refractive index ( $n=1.49$ ) as pure air ( $n=1$ ). Thus light travelling through the air and striking the acrylic surface will be reflected and / or transmitted in different directions depending on the incidence angle. This refraction / reflection phenomenon is responsible for most of the energy losses occurring in this case, a negligible fraction being lost by absorption. Theoretically, the maximum transmittance of a medium such as Plexiglas with its refractive index is 92.5%. Some measurements from the material supplier have shown that approximately 4% of the light energy is lost at each interface with air, and that the

absorbance remains below 0.5% for a material thickness up to 25 mm, which makes an overall energy lost of 8.5%. If the transmitted light energy is assumed to be superior to 91.5% in the worst case, the removal of the external box in Plexiglas is already decreasing the loss by a factor two. The energy saved thanks to these modifications will be of significant importance while considering the extreme repetition rate used during the measurements. Indeed, at very high operating frequencies, the time allocated to each oscillator for the pumping process is drastically reduced, decreasing in the meantime the energy delivered at each pulse (Figure 5.2.b).

On the other hand, a second influencing parameter has to be taken into account during the measurements of different planes, that is the incident beam deviation to the surface's normal. The acrylic material employed here has a critical angle of  $42.2^\circ$  off the normal. Until this value, the reflectance at air / Plexiglas interface is kept almost constant to the value mentioned earlier ( $\sim 8.5\%$ ), but above this critical angle, the reflectance is increasing exponentially, as displayed in Figure 5.2.a. In the present case, the limit reached between the incident laser beam and the normal is not exceeding  $26.4^\circ$  for the valve centre plane, which is guarantying a constant energy loss all along the measurements.

Concerning the reflections occurring within the cylinder, the modification of the thickness is not preventing the apparition of these negative effects but is just modifying the optical path of the beam, shifting the phenomenon. Thus some masking will be required at different positions, depending on the incidence of the light rays to thwart the optical disturbance.

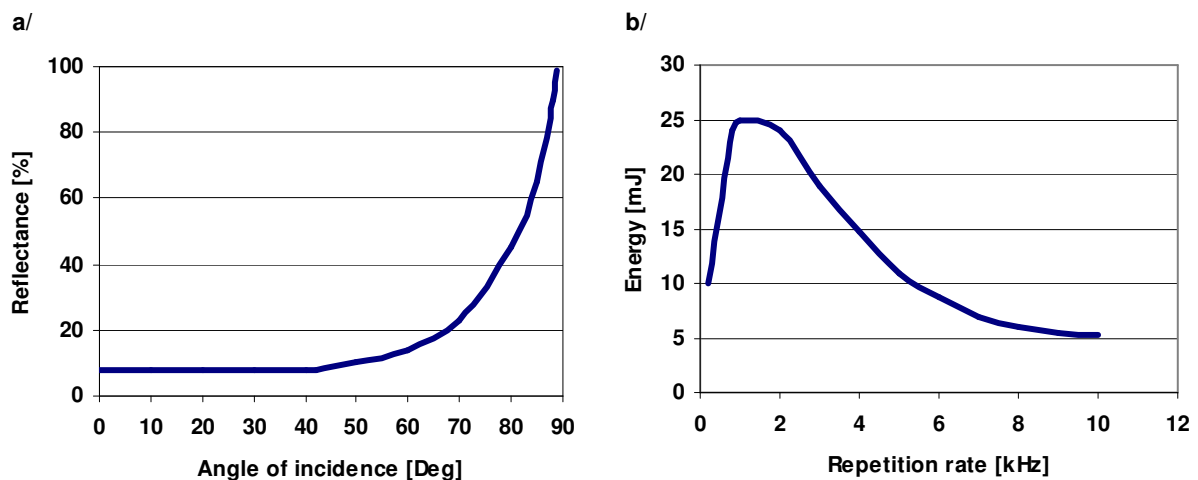


Figure 5.2: a/ Variation of the Plexiglas reflectance according to the light-ray angle of incidence – b/ energy of a single oscillator as a function of the laser pulse repetition rate

## 5.2 Experimental Setup

Several variables or quantities have been measured in order to generate reliable database and boundary conditions for the initialisation and validation of numerical computations. For this purpose, various measuring techniques have been implemented, whose results are summarized in the following paragraphs.

### 5.2.1 Stereoscopic HS-PIV

The cylinder-head of a VW production engine, the four-valve Direct Injection Spark-Ignition (DISI) 1.6L FSI®, is mounted on the previously presented optimized Tumble Optical Test-Bench. As outlined in Figure 5.3, the measuring section consists here on a simple acrylic cylinder

with a thickness of 2 mm, has a diameter of 76.5 mm and 180 mm in height, positioned underneath the cylinder-head, downstream of the valves.

A long intake extrusion ( $L=1500\text{mm}$ ) has been used to ensure the proper development of a fully turbulent velocity profile at the intake port boundary and to keep away the influence of the seeding system. As for the former PIV measurements (see §4.4), the intake flow sucked into the port was seeded with oil droplets (di-2-ethylhexyl-sebacate – DEHS, diameter  $\sim 1 - 2 \mu\text{m}$ ), produced by a Laskin-atomiser.

The two intake valves were manually actuated and positioned at a constant valve-lift (from 3 mm to 9 mm) for each sequence of measurements, corresponding to a specific stationary flow-rate (from 50 kg/h to 150 kg/h) regulated by the speed of the pump. Another parameter available for this study was the variable tumble flap located in front of the port. Thanks to the position of this deflector, it was possible to control the level of turbulence induced by the intake system.

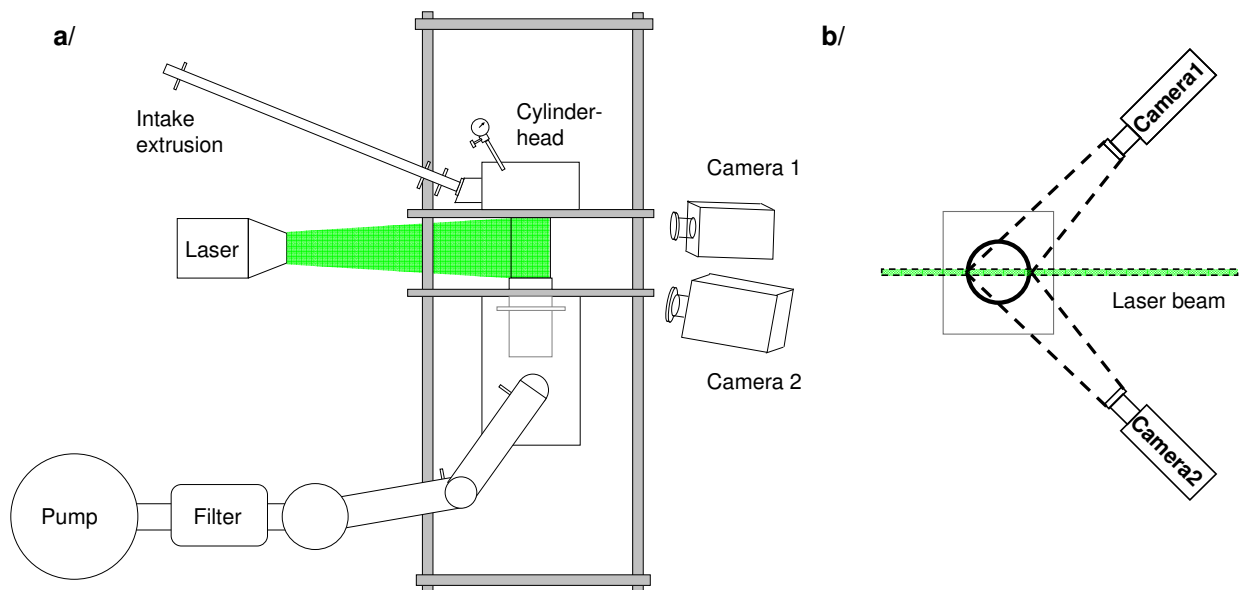


**Figure 5.3: a/ Experimental setup for stereoscopic PIV, b/ Top-view of the optical system showing the Forward-Forward scattering method**

Based on planar domains like the 2-Component PIV exposed in §4.4, the stereoscopic technique is employed in order to extract the third component of the velocity vector (out-of-plane), according to the parallax principle. This method is then taking use of two similar cameras positioned with different angles regarding the measured plane.

Indeed, by placing two cameras so they observe the light-sheet plane from two different angles as shown in Figure 5.3.a, the parallax effect means that one obtains slightly different two-velocity component vector maps from each camera. The differences between them arise from the third, out-of-plane velocity component and the geometrical configuration of the two cameras. After image calibration, this third velocity component can be evaluated. In addition, the two in-plane velocity components can be recalculated, correcting for parallax errors.

However, the relative positioning of the cameras towards the incident light direction has a strong influence on the intensity received by each of them. The sketch in Figure 5.4 is illustrating the phenomenon of light scattering by the seeding particles, showing that the resulting light intensity is not equally or regularly distributed around the moving body. This particular pattern will influence the positioning of the observing cameras, which will be placed in regions of maximum

intensity. Then a compromise has to be found between the best position in terms of light and the reduction of disturbing reflections.

In the present case, the forward-forward spatial arrangement of the cameras (as represented in Figure 5.3.a) was guarantying the best imaging quality.

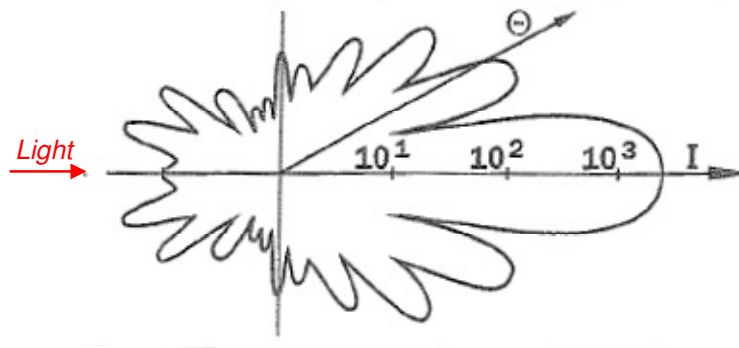


**Figure 5.4: Light scattering by a 1µm oil particle in air (reprinted from Raffel et al. [105])**

As the ever increasing performances of optical acquisition systems are offering new perspectives for a better insight in the complex processes associated with turbulent flows, the present study is employing the cutting-edge technology available in terms of HS-PIV to accurately measure the unsteady flow field developing in an engine cylinder. The technical features of the HS-PIV system were the following:

*Laser Darwin-Duo* (from Quantronix): dual-cavity, diode-pumped, frequency-doubled Nd:YLF laser, 527 nm, 25 mJ @ 1 kHz per cavity

*High-Speed Camera* (High-Speed Star 5 from La Vision): CMOS camera with a resolution of 512x512 pixels @ 10 kHz (same cameras as the one used for the cylinder-head model analysis in §4.4)

By accurately setting the time delay between two consecutive pulses, it is possible to double the overall pulse repetition rate in order to reach a frequency of 20 kHz, which means 10 kHz of effective correlated velocity fields. The post-processing has been realized by the program DaVis 7.2 from LaVision. The evaluation of the image pairs was performed with a multi-pass method, the last interrogation window being of the size of 32 x 32 pixels, with an overlap of 50%. Thanks to these settings, the distance separating two post-processed velocity vectors was equal to 1.86mm. It is yet important to keep in mind that the real post-processing grid independent information is twice less than this last value, about 3.72mm, since the overlapping treatment only interpolates the data between two successive frames.

### 5.2.2 Constant Temperature Anemometry

A strategy has been employed to decrease the size of the numerical domain and subsequently the computational efforts required to simulate the full experimental setup presented before. This was achieved by splitting the geometry shortly upstream of the engine intake port aperture 210 mm before the outlet of the long extrusion. The data delivered by a steady-state simulation in this particular plane were used as intake boundary conditions for the computation of the rest of the model. For this last part of the simulation process, the advanced turbulence models employed are very sensitive to the boundary conditions given at the intake. Indeed, the velocity profile and the level of turbulence supplied have to be as accurate as possible to let the perturbations develop

themselves further in the flow. Thus, it is of high importance to validate the data set delivered by the simulation of the intake extrusion.

Considering the experimental model and its general configuration, amongst the various velocity measurement systems available, Constant Temperature Anemometry (CTA or Hot Wire Anemometry) was offering the required features for a relatively straightforward application, without massive hardware modification. Although this is an intrusive technique, for this first set of measurements, the flow conditions downstream of the plane measured were irrelevant. As depicted in Figure 5.5, two perpendicular profiles have been measured in the plane of interest, both of them along the respective mid-axis of each side of the duct. Two different probes have been used, a straight one for the horizontal axis, and an L-form probe for the vertical one. Even though this last probe was the most effective way to measure a profile at once, the size of the opening necessary to position it was preventing its use for the horizontal profile. As a matter of fact, the diameter of the hole would have been larger than the height of the channel. Consequently, a straight probe has been used for this profile. In this case, the profile had to be split in two parts in order to be able to measure the velocity as close as possible to the wall by entering the duct from the opposite side. A short overlapping between both half profiles was guarantying their matching in the central region of the flow.

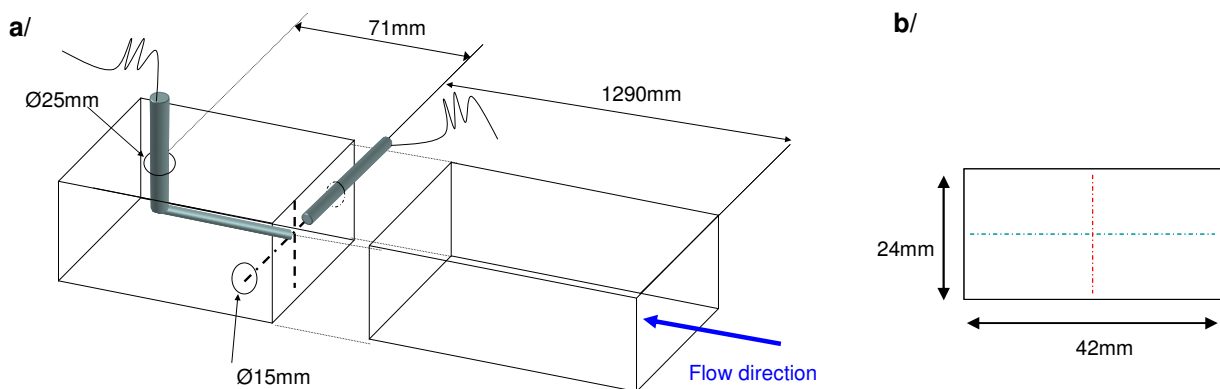


**Figure 5.5: CTA setup for velocity profile measurement in the intake extrusion – a/ Position of the two different CTA probes, the L-form one for the vertical profile and the straight probe for the horizontal profile; b/ cross section view of the channel with the vertical and horizontal lines followed**

Due to the different orientation of the probes toward the flow stream, according to the profile considered, several types of sensors have been used, as presented in Figure 5.6.

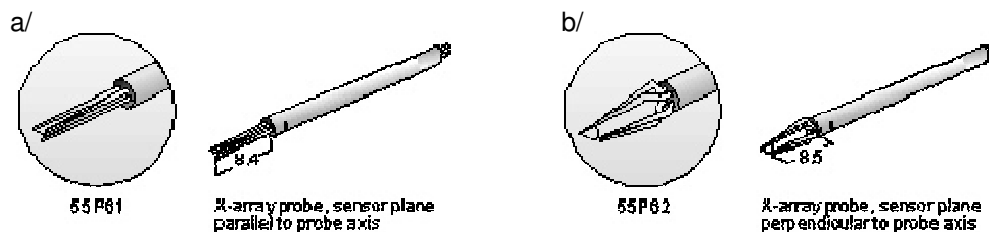


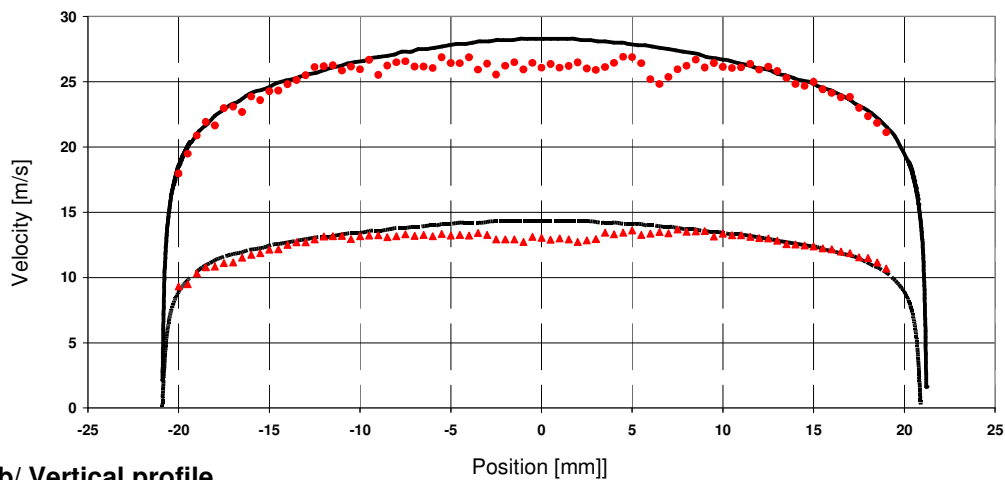
**Figure 5.6: Different mini-CTA X wire probes employed (from Dantec) – a/ straight probe (55P61) for measurements in the direction of the main flow; b/ probe for cross-flow measurements (55P62)**

Both miniatures X wire probes with straight prongs from Dantec are dedicated to different applications. The reference 55P61 (Figure 5.6.a) is used either for free-stream applications or L-form mounted systems, for which the probe axis is parallel to the main flow direction, so that the

predominant flow vector attacks the two wires under  $45^\circ$ . As the 55P62 (Figure 5.6.b) probe is concerned, the layout of the wires is devoted to radial operation, for example in places not readily accessible. In this case, the probe axis is perpendicular to the main flow, but here again, the predominant flow vector makes an angle of  $45^\circ$  with the two wires.

Figures 5.7.a and 5.7.b thereafter are showing the comparison between the averaged velocity profiles measured with the CTA systems described above and the RANS simulations.

#### a/ Horizontal profile



#### b/ Vertical profile

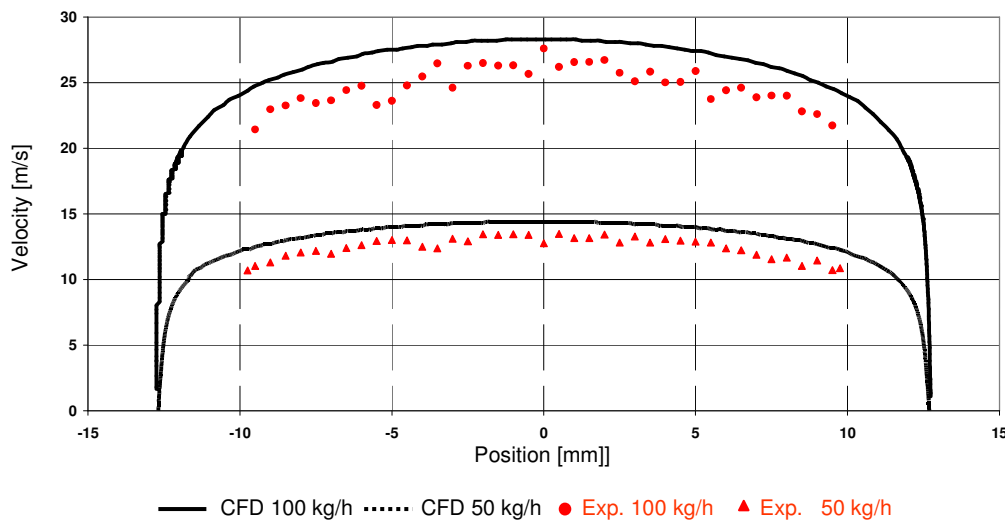


**Figure 5.7: Comparison of the velocity profiles measured and computed at a distance of 210mm from the engine intake port – a/ horizontal profile and b/ vertical profile of the streamwise component**

The horizontal profiles shown in Figure 5.7.a are representative of a well established turbulent flow, with a rather flat shape and a sharp velocity fall close to the walls. Over a broad part of the profile, both numeric and experiment are providing very comparable values except in the vicinity of the channel centre, where a discrepancy of about 6% to 7% can be observed (depending on the mass flow).

With regards to the vertical profiles (Figure 5.7.b), the overall shape of the averaged velocities is maintained between CFD and hot wire anemometry results, showing a similar development of the flow in both cases. However, in the contrary to the horizontal direction, a constant offset of around 7% exists between the measured and computed results over the full profile width.



Those discrepancies between numerical and experimental data may originate from the flow spilling out of the intake extrusion through the CTA probe orifice. This leaking is then directly influencing the mass flow seen at the position considered to measure the velocity profiles presented in Figure 5.7.

Furthermore, due to the geometry of the probe, it was not possible to go as close to the wall as with the straight probes used for the horizontal profiles. This is the reason why approximately 3 mm are missing on both sides of the vertical profiles, corresponding to the radius of the probe housing.

Thanks to the information above, it is possible to determine the range of Reynolds numbers spanned by the different flow conditions. Based on the hydraulic diameter of the duct in a perpendicular cross-section of the flow, it yields:

$$D_H = \frac{2(L \cdot H)}{L + H} = \frac{2 \cdot (24 \cdot 42)}{24 + 42} \approx 30.5 \text{ mm}, \quad (5.1)$$

and then, the following Reynolds number range:

$$(3 \cdot 10^4)_{50 \text{ kg/h}} < \text{Re}_{D_H} < (6 \cdot 10^4)_{100 \text{ kg/h}}. \quad (5.2)$$

From a general point of view, the information delivered by the RANS simulation are complying with the experimental results and will be therefore used to setup the boundary conditions for the computation of the full model. Nevertheless, by setting an unsteady simulation, a certain level of turbulence, also called turbulence intensity, has to be given at the intake, in order to take into account the real nature of the flow entering the geometry. A good indication is given by the time-resolved CTA measurements, providing all variables to determine this quantity. Indeed, the turbulence intensity, which is defined by the ratio between the RMS and the mean value of the velocity, is varying between 5% and 7.5% according to the various measurements conducted. This value will be considered while adjusting the parameter for the unsteady simulation of the full intake port and engine cylinder.

## 5.3 Numerical Simulation

### 5.3.1 Meshing Strategy and Sensitivity Analysis

Amongst the different preliminary studies conducted earlier, a first analysis of the mesh sensitivity towards various parameters has already been presented, showing the dependency of the numerical results on the mesh nature and size (see §4.2.3). For the present geometry, more complex than the tumble-flap model considered before, the emphasis has been put on the mesh quality to guarantee the best spatial resolution achievable with the computer capacity available. Based on the observations made with the former academic case, a hybrid mesh strategy was developed to mesh the cylinder head model and piping system (Figure 5.8). Then, most of the fluid domain constituting the real experimental volume has been taken into account, allowing moving the boundary conditions far away from the region of interest, that means from the cylinder and distribution system (port and valves). More particularly, for the intake condition, where a long extrusion has been used, the distance separating the real pipe inlet from the intake port and valves, enabled using steady-state conditions at that position. Indeed, the perturbations induced by some geometrical changes within the system are much larger and then hide the influence of the fluctuations likely to occur at the intake.

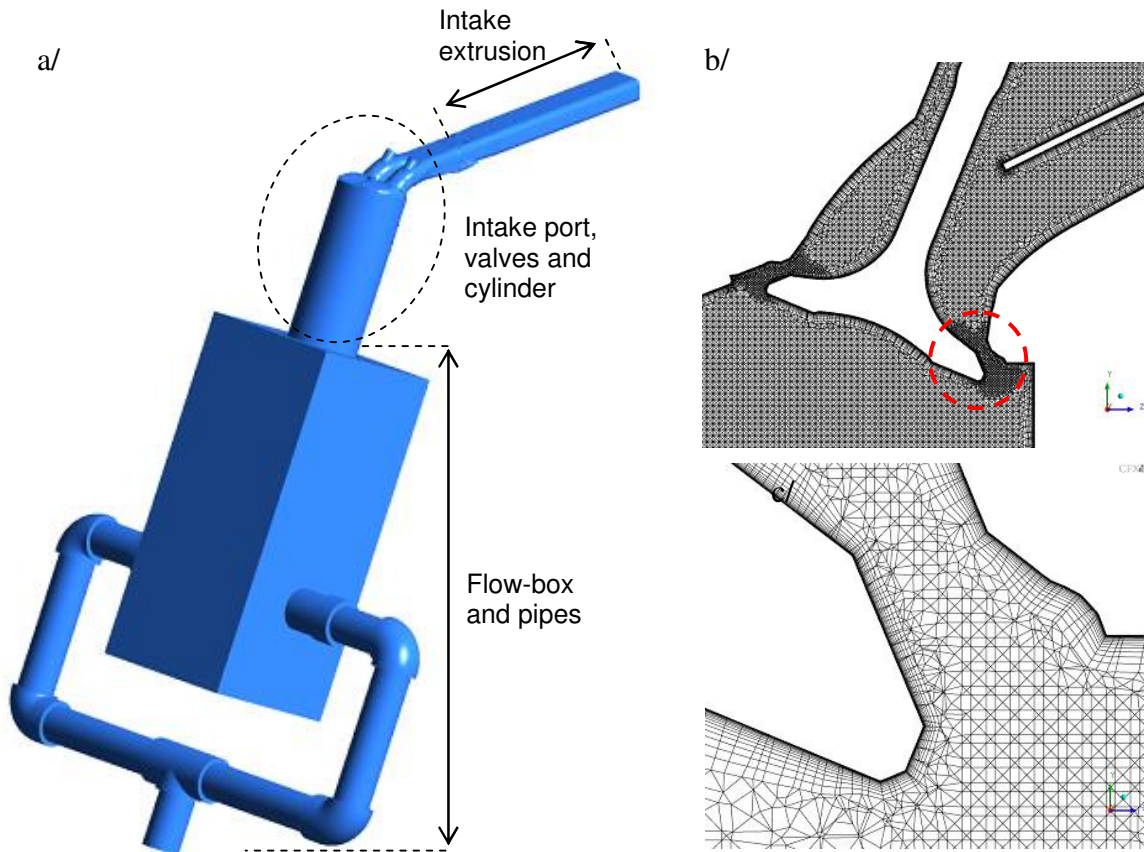


**Figure 5.8: a/ 3-D model used for the numerical simulation; b/ cross-section of the hybrid mesh; c/ zoom in the valve-clearance region showing the Low-Reynolds wall treatment with variable prisms layer height**

For this mesh sensitivity analysis, three different meshes have been developed as summarized in Table 5-1. Two of them are employing the low-Reynolds treatment of the walls, offering a demanding resolution of the boundary-layer and a maximum  $y^+$  number close to the unity. The third one is dedicated to the use of a wall-function, enabling a coarser treatment of the walls and then saving some orders of number of cells in the boundary layer. Two levels of resolution for the core of the domain have been implemented, fine mesh for a better resolution of the free stream, opposed to a coarser mesh. Thus, for the three meshes described thereafter, the following combinations have been investigated: Low Reynolds coarse or fine, and for the fine resolution, either Low Reynolds or Wall Function.

However, even if the total number of cells is varying with a maximum difference of almost 30%, in every case, a particular attention has been given in this work to accurately resolve the turbulent flow developing in the cylinder, taking into account as much details as possible. Therefore, various flow regions were highly resolved in terms of number of cells, such as the gap between the wall and the moving tumble flap with a clearance of barely one millimetre, or even some screw heads in the port. A hybrid mesh was generated, whose strategy has been to divide the global geometry into three main parts: the intake extrusion meshed with hexahedral and prisms elements, the intake port and cylinder modelled with tetrahedrons and prisms layers, and finally the “flow-box” and piping elements, which are exclusively meshed with hexahedral elements.

In the most extreme mesh configuration, a low-Reynolds number resolution of the boundary layers has been generated with 17 prism layers, as it can be seen in Figure 5.8.b. According to the settings employed, the entire mesh consists of 30 million elements corresponding to about 10 million control volumes for a node-based scheme. The tetrahedral cell size in the core of the cylinder was about 0.6 mm, and 0.3 mm in the valve clearance.

**Table 5-1: Summary of the main characteristics of the three different meshes investigated**

	<b>Meshing strategy</b>	<b>Nb of nodes</b>	<b>Nb of prims layers</b>	<b>y+ max</b>
<b>Low Reynolds Fine</b>	<u>Intake extrusion:</u> prisms & hexahedra	10.5M	17	1.5
<b>Low Reynolds Coarse</b>	<u>Port, valves and cylinder:</u> prisms & tetrahedra	8.9M	17	1.5
<b>Wall Function Fine</b>	<u>Flow-box and pipes:</u> hexahedra	7.5M	8	25

For the three different meshes presented in Table 5-1, the sensitivity toward the order of accuracy of the numerical scheme employed has been investigated. The CFD program used for the simulation offers three different differencing schemes to calculate the advection terms in the discrete finite volume equations, the 1<sup>st</sup> order upwind differencing scheme, the “high resolution” scheme and the “specified blend” advection scheme.

The 1<sup>st</sup> order scheme is the most robust option but is suffering from numerical diffusion. High resolution is standing for an automatic numerical treatment of the advection terms, oscillating between a 2<sup>nd</sup> order scheme in locations where the variable gradient is rather low, to a 1<sup>st</sup> order scheme where variations are getting sharper in order to maintain the robustness. The last advection scheme is allowing manual settings of the blending factor employed to shift between 1<sup>st</sup> to 2<sup>nd</sup> order. A blend factor of 0.0 corresponds to the upwind scheme and is consequently very robust, whereas a value of 1.0, its maximum, returns a fully 2<sup>nd</sup> order scheme, more accurate but also more sensitive. However, the blend factor is a continuous parameter and can be adjusted to find the appropriate compromise with regards to the level of accuracy desired.

**Table 5-2: Principal simulation settings and boundary conditions**

<b>Mass flow</b>		100	[kg/h]
<b>Temperature</b>		26	[°C]
<b>Intake</b>	Velocity profile		[m/s]
	Turbulence Kinetic Energy		[m <sup>2</sup> /s <sup>2</sup> ]
	Turbulence Eddy Dissipation		[m <sup>2</sup> /s <sup>3</sup> ]
<b>Outlet</b>	Static pressure	1	[bar]
<b>Wall treatment</b>	Hydraulically smooth & adiabatic		

Considering the size of the meshes at stake for this sensitivity analysis and the large resulting computational costs, the study has been restricted to steady-state simulations of the geometry under the boundary conditions summarized in Table 5-2. The velocity profiles and turbulence information (turbulence kinetic energy and eddy dissipation) given at the intake are generated by the simulation of an individual intake extrusion pipe, as described in §4.2.2. In all cases, a k- $\omega$  based SST (Shear Stress Transport) turbulence model has been used. The time-step used for the simulations was set to a value of 10  $\mu$ s, maintaining the Courant number below unity (see Equation 3.21 and associated references).

As can be seen from Figure 5.9 thereafter, the averaged total pressure drop computed with both low-Reynolds meshes is much higher than the one obtained with the Wall Function meshing strategy, independently from the numerical schemes employed. The reference pressure drop measured between the two extremities of the domain considered was equal to 3650 Pa, discrediting the results of the Wall Function mesh. In addition to the difference observed between the natures of the boundary layer treatment, the actual study was also offering a comparison between the three advection schemes available in CFX. In the present case, for a steady-state RANS simulation, the better results are supplied by the Upwind scheme (1<sup>st</sup> order), followed closely by the High Resolution one. At this point, it must be mentioned that the forced 2<sup>nd</sup> order advection scheme (Blend 1) was not able to converge with the two Low Reynolds meshes. This has probably to be related to the higher sensitivity of the numerical treatment to the nature of the mesh, and the fact that the larger cells and smoother ratios employed with the Wall Function mesh are facilitating the convergence. However, even if the results are converging, the 2<sup>nd</sup> order scheme results are not bringing any improvement as far as the total pressure drop is concerned.

Although the coarse LR mesh is offering a slightly better total pressure drop with the upwind scheme, the use of the High Resolution scheme is inverting the tendency, showing a small advantage for the finer grid. As a matter of fact, only the High Resolution scheme is offering the minimum precision required by the turbulence models employed for unsteady simulations, as it will be presented in the following paragraphs.

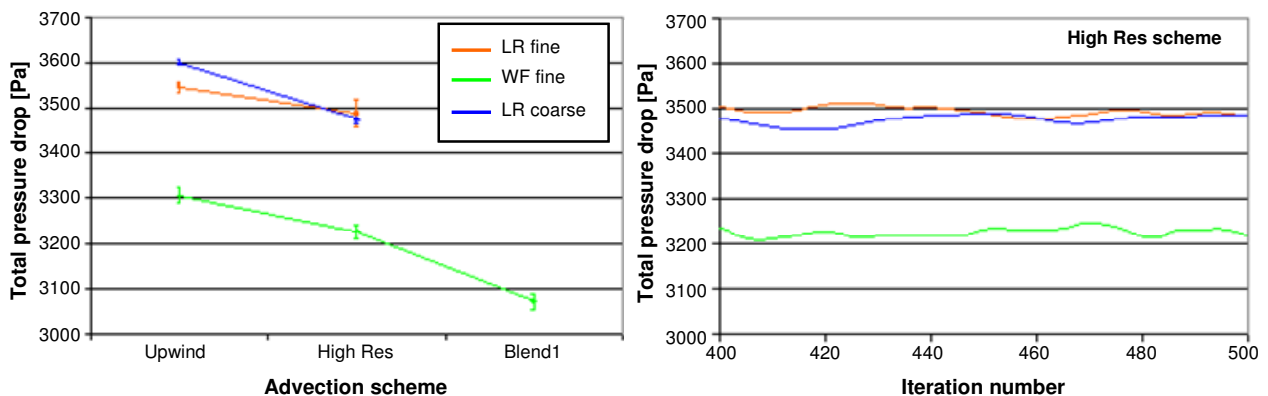


**Figure 5.9: Sensitivity analysis – Left: comparison of the advection scheme influence on the total pressure drop between the intake and outlet of the fluid domain; Right: RANS simulation convergence for the three meshes with high-resolution advection scheme (measured value: 3650 Pa)**

The convergence curves plotted in the right-hand-side of Figure 5.9 are showing the unsteady nature of the pressure drop, and consequently of the flow establishing in the domain computed. The various instabilities induced by the complex geometry are calling for an unsteady simulation of the flow.

In the valve centre section plane represented in Figure 5.10, the comparison of the averaged velocity field is highlighting the main differences occurring with the High Resolution method for the three meshes. The results delivered by the two LR approaches, very similar to each other, are showing a significant discrepancy with the WF results in the three regions marked on the graph. Thus, in the port elbow (region 1), in the wake of the valve-shaft (region 2) or in the shear layer developing at low valve-lifts (3 mm here) downstream of the valve edge, the general structure of the flow obtained is varying, showing the sensitivity of the simulation accuracy towards the wall treatment employed. Indeed, in this kind of applications with wall-bounded flows, where the shear effects are playing a very important role, the boundary layer treatment is a deciding factor, also influencing the global values as can be seen from this first steady-state analysis.

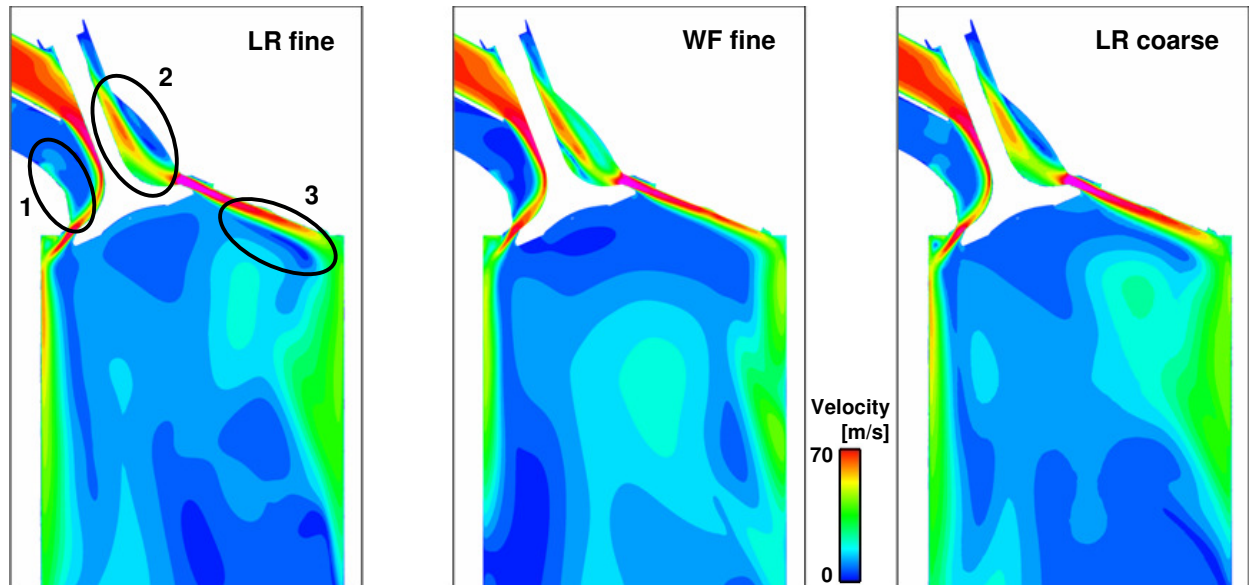


**Figure 5.10: Mesh sensitivity analysis – Averaged RANS-SST simulation results obtained with the High-resolution advection scheme**

Based on these former observations, the use of advanced turbulence models on the LR fine grid combined with the High Resolution scheme should deliver reliable results as well as a deeper view in the turbulence structures developing in a DISI engine and their origins.

### 5.3.2 Data Management and Post-Processing Mesh

A major issue arising while dealing with highly resolved meshes like the one presented earlier is the huge amount of data generated by the unsteady simulation. For a relatively short total physical time computed and even by restricting the number of variables written after each iteration, the usage of very small time-steps associated to a large nodes density is delivering result files of several hundreds of gigabytes. Besides the obvious problem of storage capacity, the numerical post-treatment of the data is becoming a real concern. Indeed, the different operations conducted to study the turbulent flow induced by the cylinder head, such as POD, spectral analysis with Fourier Transform, or the structures visualization thanks to the Q-invariant calculation are requiring important numerical efforts. This is making data management a foremost challenge to deal with from now on, according to the ever-increasing complexity of the geometries investigated as well as the level of details desired.

The chart presented thereafter is showing the strategy developed during this study in order to alleviate this problem and to improve the post-processing. The original CFD mesh developed with a high level of resolution in the boundary- and shear-layers is not suitable for the post-treatment operations undertaken later. Therefore, in order to decrease drastically the size of the files to manipulate, the main planes of interest have been extracted from the original data set, according to two different mesh densities. Both of them are produced thanks to the post-processing program Enight 8.2, by generating the intersection between a plane with a given density for the orthogonal mesh to be exported and the original CFD volume mesh. According to the level of details to be captured and the objectives of the post-processing operation, the CFD outputs have been mapped or interpolated either on a finer grid, the so-called High-Resolution mesh, or on a coarser one, the Low-Resolution mesh. The first one has a nodes repartition similar to the one in the core of the CFD mesh, and thanks to its restricted amount of exported planes (11 volume sections) offers a data reduction of a factor 30. On the other hand,

the newly defined orthogonal Low-Resolution mesh presents only the same resolution as the post-processed High-Speed PIV data and ensures a saving of 1.400 times less nodes.

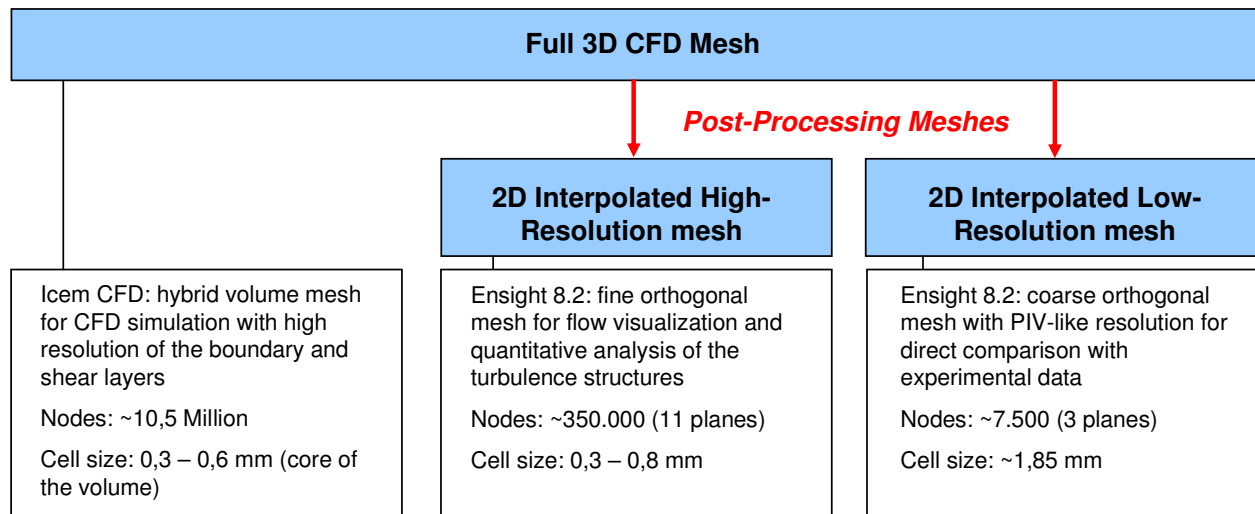


**Figure 5.11: Diagram illustrating the different meshes employed for the various post-processing operations conducted later**

The data simplification and reduction process described in this chapter is an essential optimization step aiming to keep the complex and expensive post-processing at an affordable cost in terms of computational time and storage capacity.

## 5.4 Averaged Results Comparison

Although both experimental and numerical methods implemented here are dedicated to time-resolved analysis of unsteady flows, a first comparison of the averaged results is still inevitable to control the overall quality of the different techniques. Figure 5.12 displays the velocity vectors in the cylinder central plane shaded with the total velocity magnitude obtained by High-Speed PIV with an acquisition rate of 10 kHz (the frequency mentioned here refers to the post-processed information rate, i.e. half of the acquisition frequency), compared to the CFD results from RANS, DES and SAS simulations. An identical colour-scale is employed to facilitate comparisons. At a first sight, considering the region measured by HS-PIV 10 kHz as the comparison area, one can say that the global velocity range is relatively well matching between the simulations and the experimental results. A clear swirling structure perpendicular to the cylinder axis, the so called tumble shape typical from DISI engines, can also be observed in each case except for the RANS results. Indeed, the converged RANS simulation presented here is lacking the general flow pattern and is proving once again the limitation of such statistical methods to reproduce the complex phenomena associated with engine flows.

Figure 5.13 is offering a closer view to the center of the large rotating structure in order to compare their accurate position in the different quadrants. The large dots are representing the center position of the individual tumble pattern structures, and the dashed square is adjusted to plot the reference position (tumble centre of the HS-PIV 10kHz case) in the three other quadrants. By computing the relative distance between the different points, as given in Table 5-3, one can first remark that the DES simulation is providing the best matching with the experimental tumble center. Presenting a relatively higher discrepancy, the SAS model is still delivering satisfying results, particularly while considering the post-processed vectors spacing obtained with the PIV results. Obviously, RANS is absent from this table since no large eddy structure is present in this case.

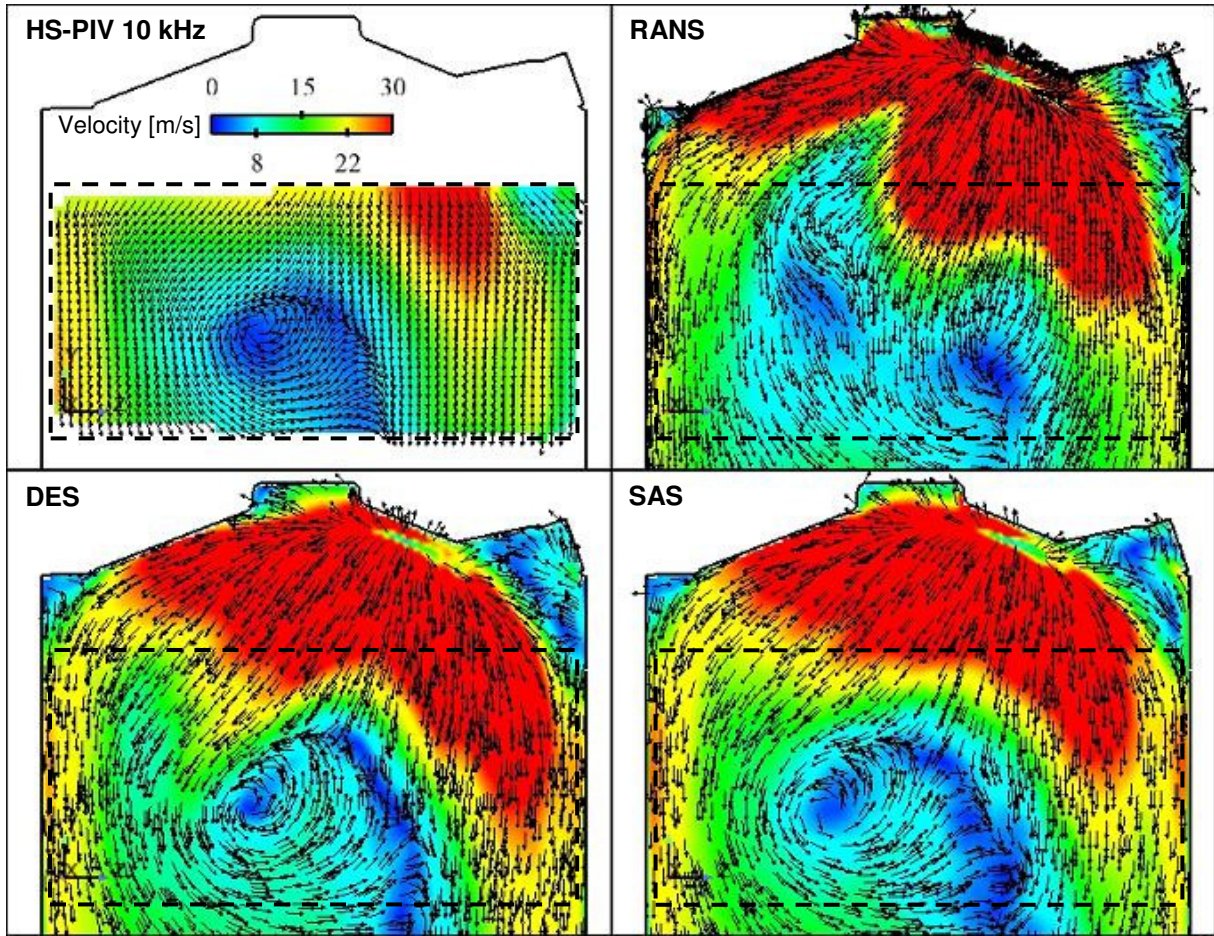


Figure 5.12: Comparison of average velocity magnitude and vectors (100C3: 100 kg/h, 3mm valve-lift)

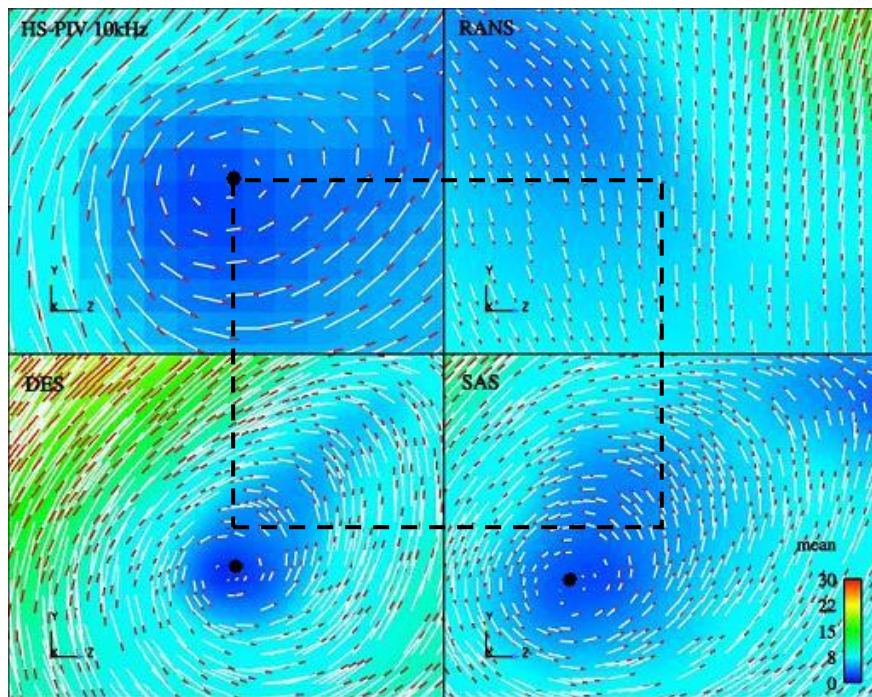


Figure 5.13: Average velocity magnitude superimposed with vectors. The dots in each quadrant are representing the tumble center positions

**Table 5-3: Distance between the tumble centres obtained, comparing PIV with the different simulations**

<i>Distance [mm]</i>	DES	SAS
PIV 10kHz	1,7	4,2
SAS	3,6	-

When focusing on the general flow pattern and the velocity vectors orientation, SAS seems to offer a better answer than DES. In the DES case, the vector's rotation around the tumble center position follows an ellipsoid whose greatest axis is forming an angle with the horizontal of about 45°. In contrast, the shape obtained with SAS is rather circular and closer to the HS-PIV 10kHz results.

In order to quantitatively compare the experimental and numerical results, velocity profiles were extracted along the z-axis in the center of the large tumble structure observed in the HS-PIV 10 kHz averaged results (taken as reference position for the different cases). The comparison of the profiles for the total velocity magnitude and for the Y-component can be seen in Figures 5.14.a and 5.15.a. Although the measured and the simulated results differ slightly due to an over-prediction of the velocity maxima, the general tendencies of the flow are found in both methods. However, as it is confirmed by the representation of the absolute difference between numerical and experimental results normalized with the respective average velocities (Figures 5.14.b and 5.15.b), SAS results are showing a better concordance with the experimental ones.

**Table 5-4: Total pressure drop between inlet and outlet (100C3 and 100C9 stand for a mass-flow of 100 kg/h and a valve-lift of 3 mm and 9 mm respectively)**

$\Delta P$ total [Pa]				
	Exp.	RANS	DES	SAS
Case 100C3	3650	3480	3595	3665
<i>Variation [%]</i>	-	-4.7	-1.5	0.4
Case 100C9	2475	2445	-	2450
<i>Variation [%]</i>	-	-1.2	-	-1

Table 5-4, which displays the total pressure drop computed between the inlet and the outlet of the complete model (experimental as well as numerical), provides another criterion to identify the quality of both models. According to these results, SAS seems to be a good alternative to the hybrid turbulence model DES as far as averaged results are concerned. However, the real challenge is to investigate the ability of the model to properly reproduce the unsteadiness of the flow in all its complexity.



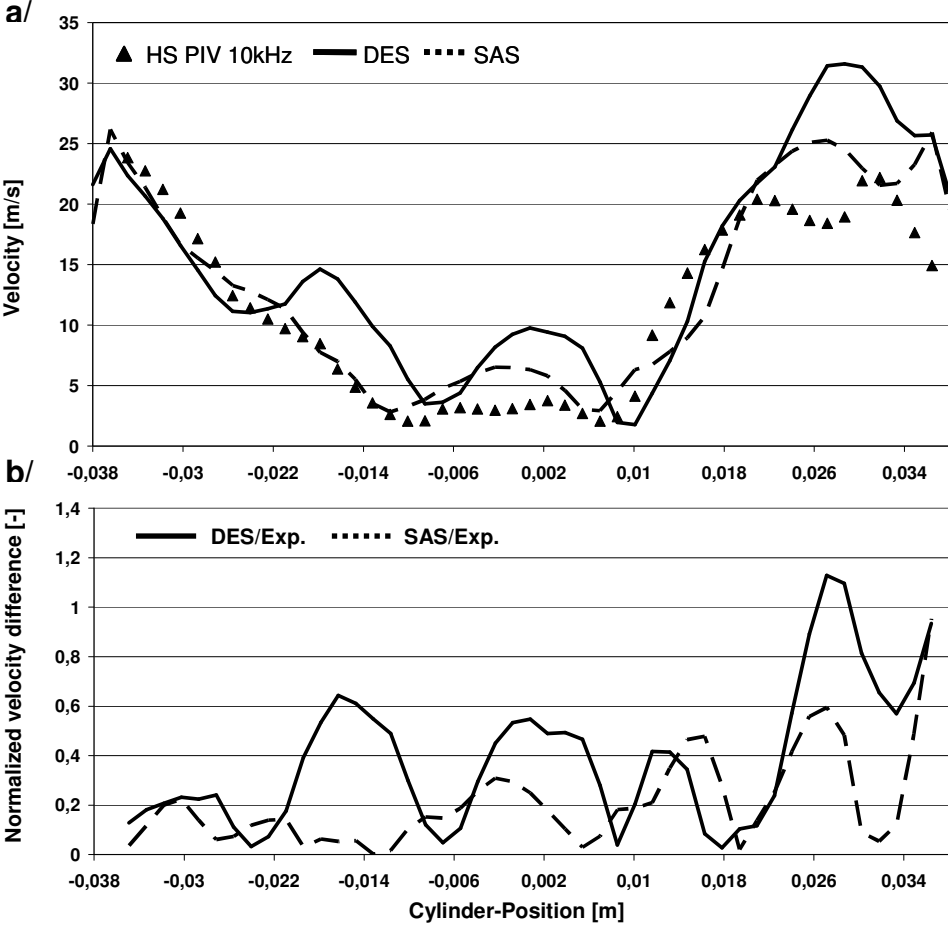


Figure 5.14: a/ Comparison between measured and calculated profiles of the total velocity magnitude – b/ Representation of the absolute difference normalized with the average velocity magnitude

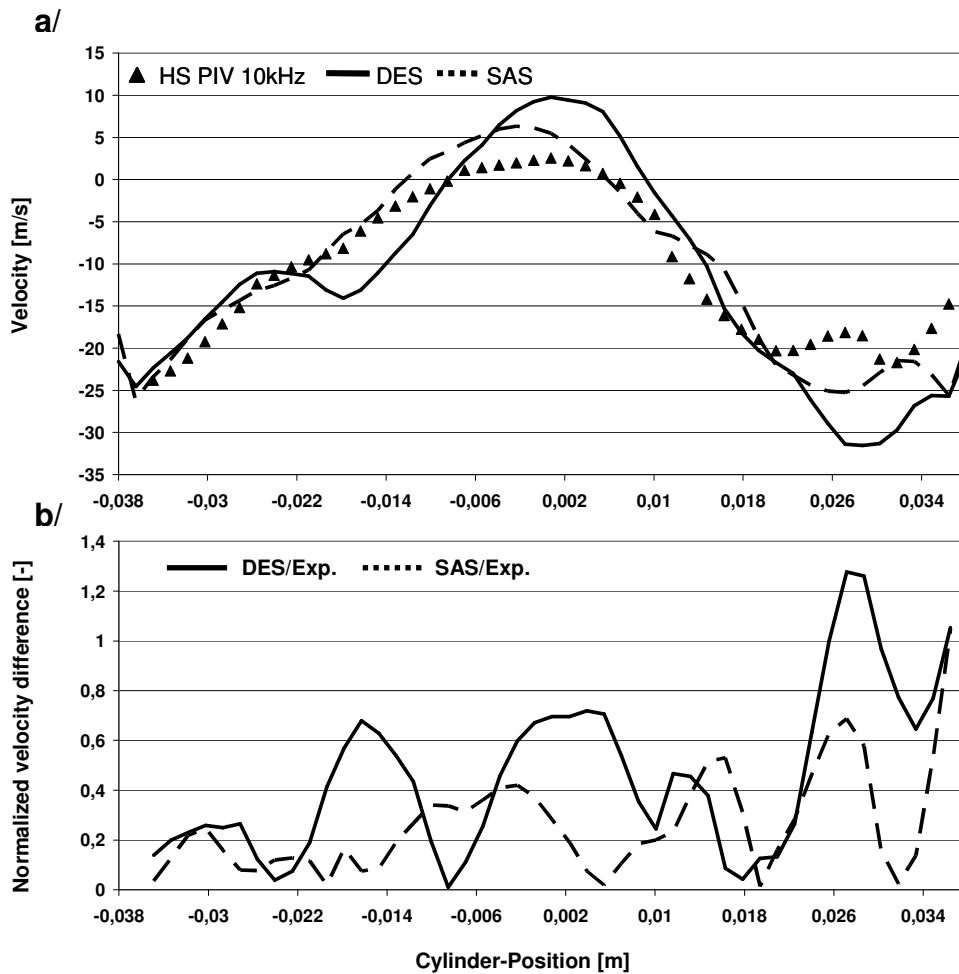


Figure 5.15: a/ Comparison of the measured and calculated profiles of the vertical velocity component – b/ Representation of the absolute velocity difference normalized with the average vertical velocity component

## 5.5 Unsteady Results Analysis

The comparison of unsteady results from CFD computations with PIV data extracted from an ensemble at a particular time is everything but obvious. Several factors such as the boundary conditions for the CFD computation or the post-processing filters used for PIV data may induce strong variations between both results. Although the general turbulent structures observed in the numerical and experimental studies are showing an important level of similarity, other comparison techniques have to be implemented to get a better evaluation of the reliability of the methods. Indeed, animations (see Figure A.1 in Appendix for a sequence of successive snapshots) of the time-resolved laser measurements allow to follow some eddies convecting through the window within the time frame considered, but better quantitative information would be gained by conducting a spectral analysis of the different data sets and observing their correlation.

### 5.5.1 Spectral Analysis

In order to identify the origins of the velocity fluctuations induced by the intake port considered, and then later to determine the relevant geometric parameters for optimization purpose, a

detailed spectral analysis would deliver an interesting amount of information. First of all, some regions of interest (ROI) have to be defined, where the flow is showing a particular behavior containing some characteristic frequencies. Thanks to the representation of the second and third moments of the velocity fluctuations as defined in Eq. (3.9) and (3.10), different regions of the flow are differentiating themselves from the rest of the domain. As depicted in Figures 5.16 and 5.17, representing the SAS results, two remarkable regions are made visible by the RMS analysis, where the jet regions formed around the valve tip are showing strong fluctuations due to a high shear strain (Region-Of-Interest - ROI - 1 and 2 on the graph). From the skewness representation, another area seems to be remarkable, located downstream of the valve-shaft on its left side (ROI 3). In Figure 5.17, particular attention has to be given to the small quadrant in the left-hand upper part (quadrant (a)) showing the two valves from the front view. Under the valves in the mixing region between the flows coming from both sides of the intake port, one can observe alternately positive and negative values of *skew*, attributed to a large spatial gradient of this quantity in this region. This phenomenon is characteristic of the jet flapping effect occurring between the two valves, where the flow is oscillating from one side to the other [99, 127]. This last effect is also assumed to have a great influence on the general in-cylinder flow stability and consequently on the engine cyclic variations.

In addition, the observation of this flow instability between the valves is supporting the assumption expressed in §4.4.4, which explains the asymmetry obtained with the short simulation time. Hence, the flow did not have a sufficient time to show the periodic nature of the fluctuation and was instead going in an arbitrary direction.

The spectra of the vertical velocity components have been computed on the three different regions defined previously. In each case the mean value has been withdrawn from the instantaneous velocity field before calculating the FFT spectrum of the points contained in the ROI. As far as the frequency range is concerned, the Nyquist criterion is giving a maximal frequency of  $1/2\Delta t = 5\text{kHz}$ . Indeed, the result files have been written every tenth time-step, giving an effective  $\Delta t$  of  $1\text{e-}04\text{ s}$ . This value is also corresponding to the time interval separating two following post-processed PIV vector-fields, therefore offering the same frequency range for the spectral analysis. The spectra obtained with CFD results are plotted in Figures 5.18 and 5.19 thereafter, for the DES and the SAS results respectively. In both cases, a total number of  $N = 256$  timesteps have been used to compute the FFT of the signal, giving a frequency resolution of  $\Delta f = 1/(N\Delta t) = 39\text{Hz}$ . This  $\Delta f$  corresponds to the precision of the spectral analysis and represents the limiting factor, or the averaging window, used for the peak detection process. It should be noted here, that a pure FFT of the full data set without any windowing process has been employed. Although this crude signal treatment can lead to aliasing effect influencing the information located at both extremities of the spectrum, the relatively small number of samples did not allow any windowing application, which would have reduced the frequency resolution.

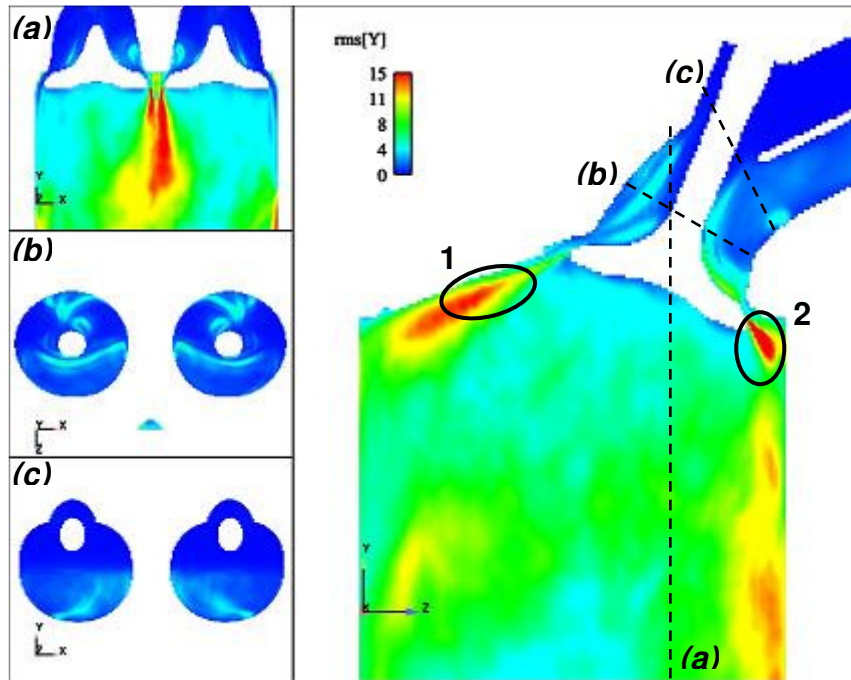


Figure 5.16: Root-Mean-Square (RMS) value of the vertical velocity component (SAS 100C3 results) – definition of the Regions Of Interest 1 and 2 (ROI 1 and ROI 2)

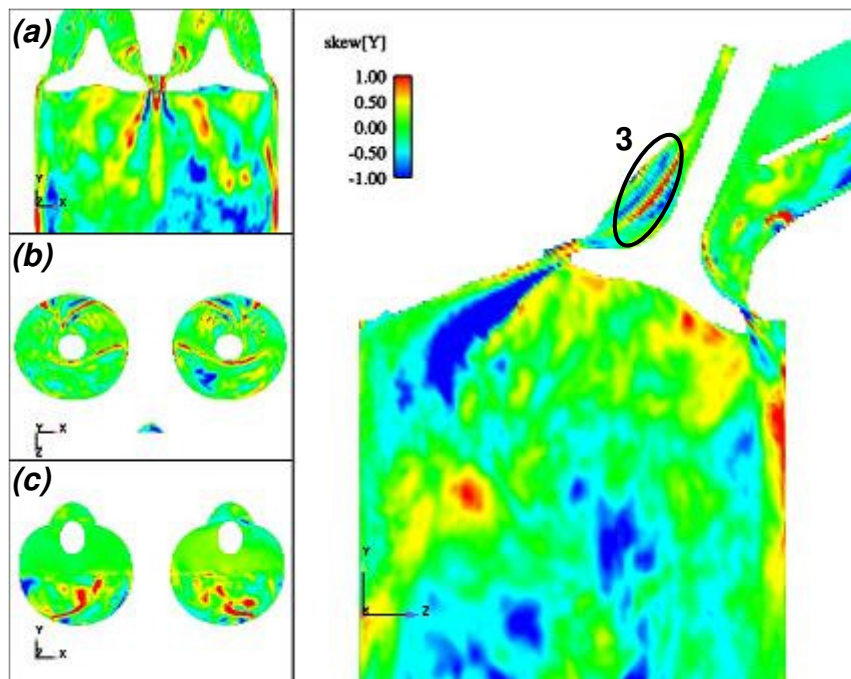


Figure 5.17: Skewness of the vertical velocity component (SAS 100C3 results) – definition of the 3<sup>rd</sup> Region Of Interest (ROI 3)

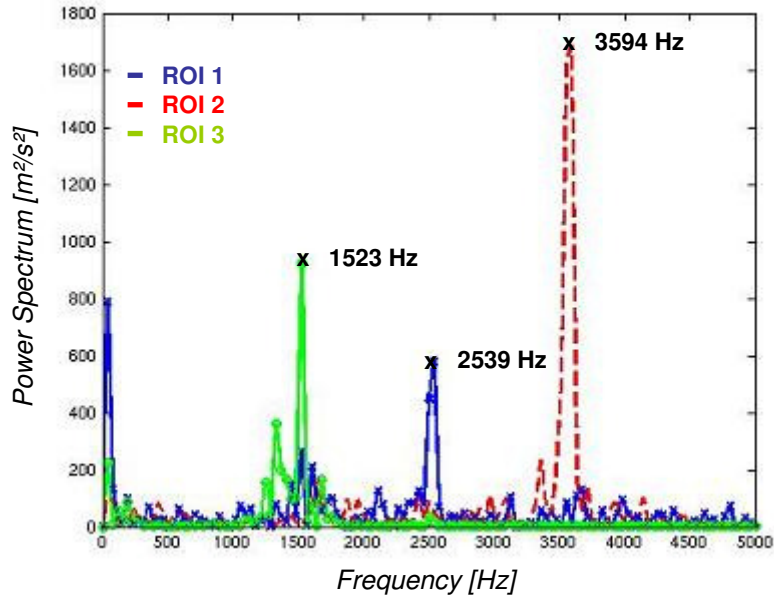


Figure 5.18: DES results – Characteristic spectra of the vertical velocity component computed in each of the ROI defined

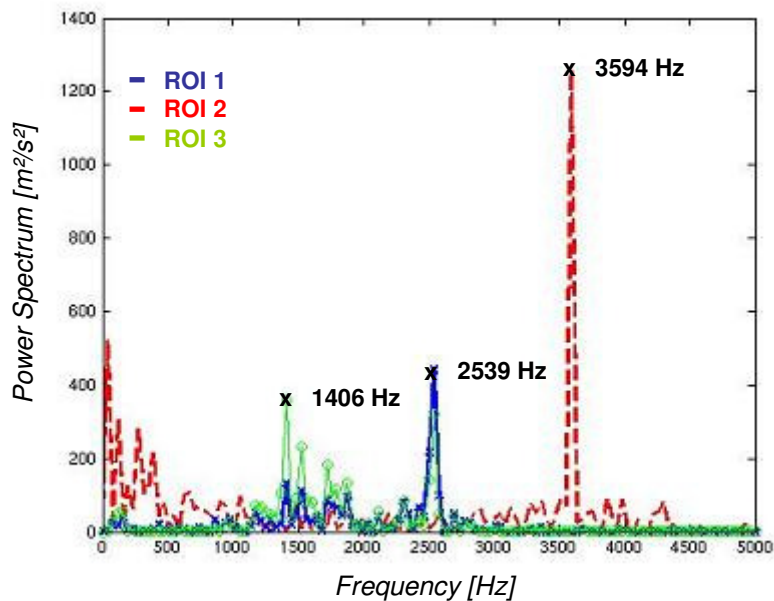


Figure 5.19: SAS results – Characteristic spectra of the vertical velocity component computed in each of the ROI defined

Table 5-5: Comparison of the main characteristic frequencies resulting from DES and SAS simulations

Frequency [Hz]	ROI 1	ROI 2	ROI 3
DES	2539	3594	1523
SAS	2539	3594	1406

With a very good agreement between both turbulence models employed here, the three regions selected are showing a clear and distinct frequency peak (with respect to the frequency resolution used for the FFT) as summarized in Table 5-5.

The presence of these single peaks suggests the proximity to the source. However, the influence of these characteristic frequencies should be also found in other regions downstream, in the cylinder. By reconstructing the velocity field filtered by each of these values, it is then possible to observe the influence of each individual phenomenon and above all to track the resulting perturbations back to their origin. This method can be seen as a spectral decomposition followed by a reconstruction of the flow.

The different modes obtained with the three frequencies from the DES results are reproduced in Figures 5.20 to 5.22.

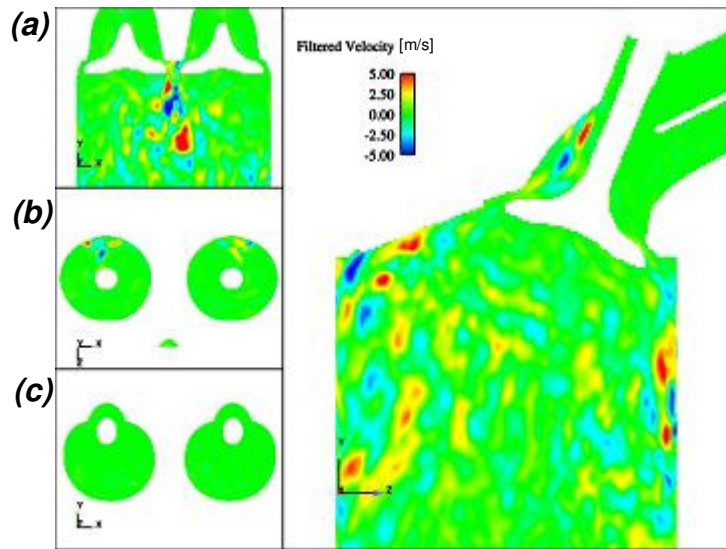


**Figure 5.20: Reconstructed velocity field (vertical component) filtered with the first frequency mode  $f_1 = 1.5 \text{ kHz}$**

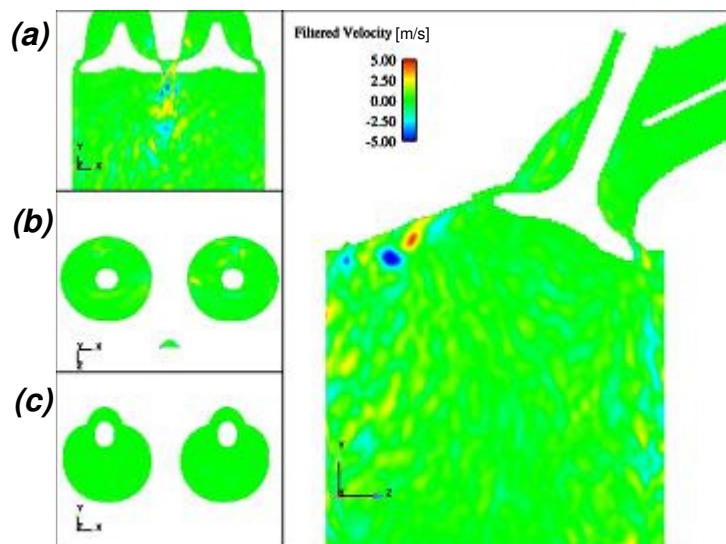


**Figure 5.21: Reconstructed velocity field (vertical component) filtered with the second frequency mode  $f_2 = 2.5 \text{ kHz}$**

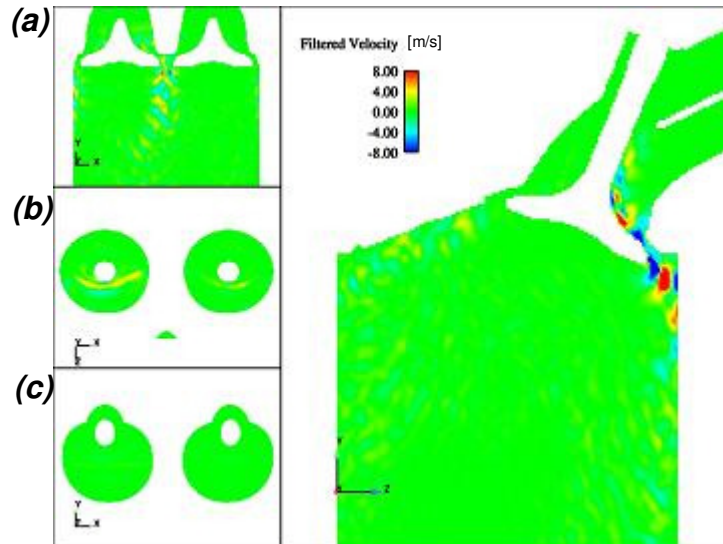


**Figure 5.22: Reconstructed velocity field (vertical component) filtered with the third frequency mode  $f_3 = 3.6$  kHz**

For the first mode corresponding to the frequency of approximately 1.5 kHz, it appears that the flow perturbation is originating from the valve shaft. According to the definition of the Strouhal number, providing an empirical formulation to compute the oscillation frequency of the vortices induced by a cylinder,  $Sr = fD/U$ , the result obtained with a diameter of 6 mm, a mean velocity of about 45 m/s and  $Sr = 0.2$  (approximation for a flow around a cylinder and a  $Re < \sim 1.10^5$  [2]) is corroborating this assumption ( $f = 1500$  Hz). From the reconstructed velocities plotted in Figure 5.20, the location of some structures developing between the valve and the shaft are indeed suggesting the influence of this component as main source for the fluctuations considered. Another section plane perpendicular to the shafts in the port, Figure 5.20.b, is clearly localizing the velocities on one side only, supporting the previously supposed origin.

The same analysis conducted for the next two modes is leading to the conclusion that the second mode with a frequency of 2.5 kHz is related to the valve opening and may be influenced by the distance to the valve-seat, that means the valve-lift, and finally, the structures oscillating with a frequency of about 3.6 kHz are clearly generated by the tumble plate in the port.

Based on this valuable information, some influencing parameters can be highlighted, giving some directions for further geometrical optimizations.

### 5.5.2 Comparison with HS-PIV Results

Although the PIV time resolution was high enough to enable observing turbulent structures developing and traveling within the acquisition domain, the results were still suffering two major issues. The first one was concerning the optical access. As a matter of fact, even in the measurement configuration allowing the highest position in the cylinder, the field of view was restricted to a window located 20mm beneath the valves, far enough for the flow fluctuations to decrease their intensity. Nevertheless, for this measured region, both numerical and experimental results have been subjected to the same spectral analysis, with various processing areas of variable size and position. An averaging process of the spectra contained within these domains was used to filter the signals. Over the full PIV plane, by comparison between the different numerical and experimental results, only few regions are presenting some significant spectra, with pronounced frequency peaks. Outside of these few locations, no relevant information can be taken out of the spectra. The remaining interesting domains are mostly located on the upper corners of the PIV window, close to the cylinder wall, where the number of missing data is the highest. Although

considerable efforts were invested to increase the overall imaging quality, missing information remains an issue encountered with the current set of PIV data. In the particular flow regions considered, the FFT analysis is greatly affected by the lack of information at certain timesteps and, to alleviate these difficulties, one of the most common methods would be to interpolate the results. However, this operation also influences the quality of the computed spectrum.

Nevertheless, the promising information provided by the PIV data in some flow regions still needs to be confirmed through further spectral investigations before conclusion concerning their reliability can be made. A major improvement to the analysis described in the precedent paragraph could be gained by studying the global flow field's spectra instead of some local information. For this purpose, the spectral analysis of the time coefficients delivered by a Proper Orthogonal Decomposition of the flow would fulfill this task, as it will be discussed in the next paragraph.

## **5.6 POD of Experimental and Numerical Results**

POD analysis is thought to bring valuable information about the turbulent processes associated with the in-cylinder flow. Among the different utilizations and interpretations of POD outcomes, the main objective here was to demonstrate the capacity of the method implemented to identify the characteristic flow frequencies such as the one found by spectral analysis of the complete data set (see §5.5.1). Thus, based on a certain range of spatial modes, whose time signals are showing the desired spectrum, it would be possible to reconstruct the corresponding velocity field, and to track the origins of the flow fluctuations. One of the main advantages provided by the spectral analysis of the time signals associated with the spatial modes is the fact that one can compute a spectrum for the full flow field at a particular mode. This yields to a more global analysis compared to the local study presented in the previous paragraph.

This data filtering technique informs about the scale and the location of the structures concerned with the fluctuations induced by the cylinder head, and constitutes a finite “low order” dimensional basis to describe the complex phenomenon of turbulence.

First of all a sensitivity analysis of the decomposition technique to the post-processing window size and resolution is presented. In the following study, the valve cross-section plane has been chosen as region of interest, on which different windows have been applied. Three cases are considered: the full cross-section domain with a relatively fine equidistant post-processing grid, then a window corresponding to the PIV acquisition region and finally, the same PIV-area but with the identical spatial resolution as for the experimental results (coarser resolution).

### **5.6.1 Analysis of the Post-Processing Window Size Influence**

Following the POD theory, described in §3.3.2.4, the kinetic energy obtained with the different modes has been computed and plotted on Figure 5.23. As commonly employed in POD applications, a “mean-shift” has been realized here, in other words, the averaged mean flow was subtracted from the original data set before performing the POD analysis. This subtraction does not normally alter the form of the POD modes due to the large energy associated with the mean flow. Indeed, a preliminary test based on the present data is coinciding with other observations for similar studies in the literature, where the mean flow is appearing as the highest energy mode, without changing the structure of the following modes. Finally the shift operated ensures that the data are centred on the origin (as advised in [26] to improve the interpretation of the POD results).



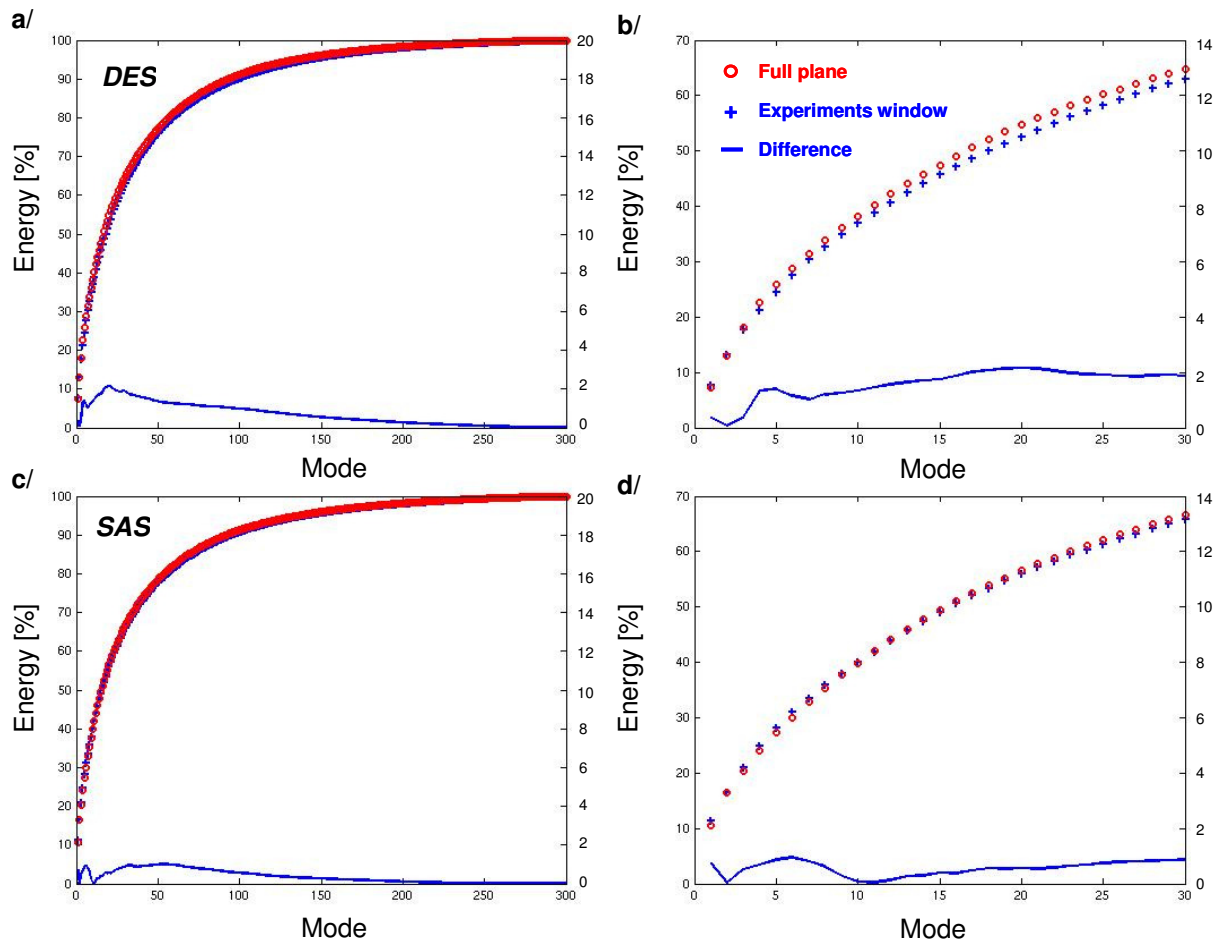


**Figure 5.23: Cumulative energy distribution of the POD modes and relative difference - DES 100C3 (valve plane) results with: a/ the full range of modes and b/ a zoom in the 30 most energetic modes - c/ and d/ corresponding SAS results**

The representation in Figure 5.23 offers an overview over the convergence of the modes resulting from the decomposition process. The comparison of the energy contained in the 300 modes chosen for this analysis is showing a different behaviour towards the windowing effect between DES and SAS results. Apparently, DES results are more sensitive to the window size than the SAS ones. Indeed, in graphs a/ and b/, one can observe that the difference between the full valve-plane and the restricted window is reaching its maximum around the 20<sup>th</sup> mode at about 2% with the DES model and then decreasing slowly with the amount of modes taken into account, down to a value of almost 1% after 100 modes. For the SAS model results, graphs c/ and d/, this difference stays below 1% at its maximum, which is around the 50<sup>th</sup> mode and is already below 0.5% after 100 modes. Another diverging point between these two models is the amount of energy contained in the first mode. In the DES decomposition, the first mode contains approximately 7.5% of the total fluctuant kinetic energy, whereas in the SAS case the same mode is representing more than 10% of the total energy. However, on a more global perspective, beside the light discrepancies mentioned before, the two different post-processing windows are providing very similar results for each model.

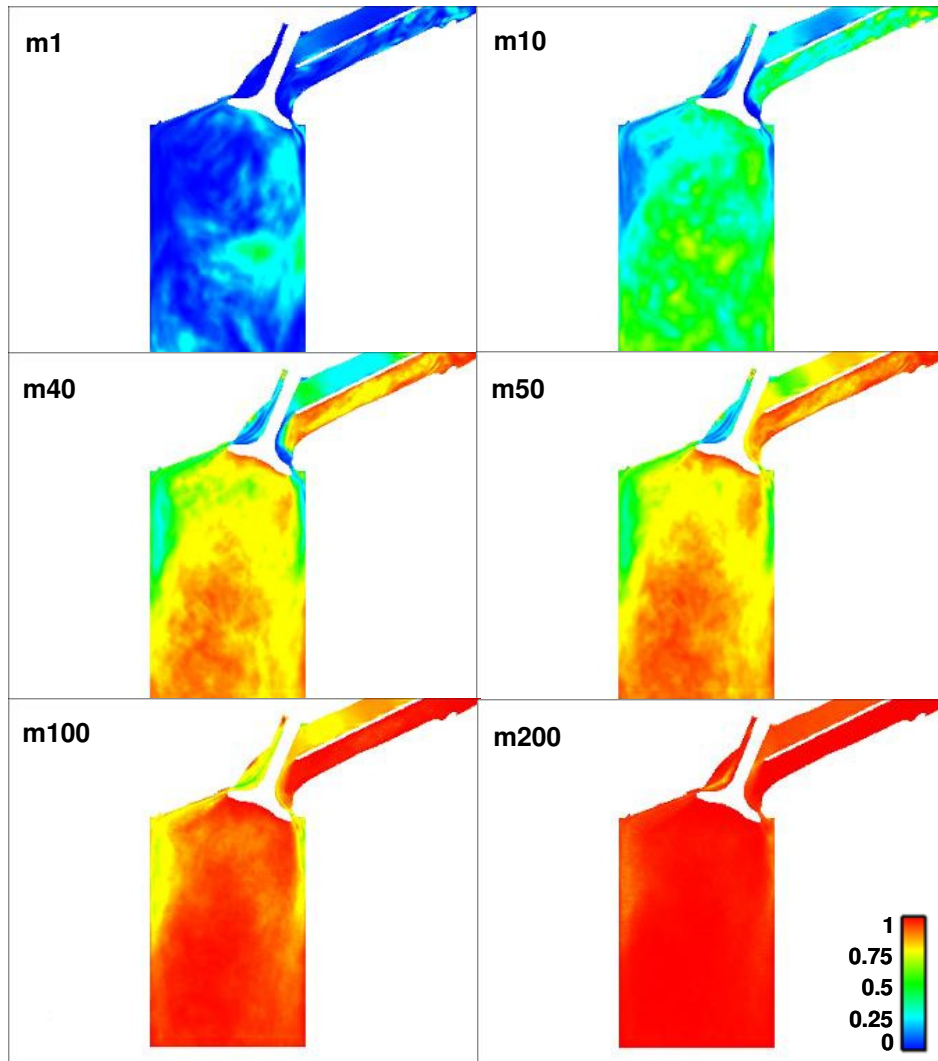


**Figure 5.24: Cumulative sum of the kinetic energy up to the truncation mode indicated in each graph normalized with the total kinetic energy resulting from the 300 modes**

Figure 5.24 above shows the sum of the kinetic energy obtained thanks to the truncation mode indicated in the upper left hand side corner, normalized with the total energy resulting while considering the maximum number of modes (in the present case, 300 modes). The ratio defined

as  $\sum_{i=1}^{N_t} k_i / \sum_{j=1}^N k_j$ , where  $N_t$  is the truncation mode and  $N = 300$ , offers another representation

of the convergence of the different modes. It is then possible to associate the different flow regions with a faster or slower energy convergence. For example, from the plot previously mentioned, one can observe a relatively fast convergence in the core of the cylinder or in the flow region located under the flow splitter in the intake port. These regions are also the most quiescent regions, where the flow is most stable. On the opposite, positions with high shear stress or undergoing large fluctuations, such as around the valve-shaft or starting from the valves tip and along the wake of the plate, are the last regions to converge. This aspect is representative of the high complexity of the flow developing in the cylinder head, where the large number of degrees of freedom, or in other words the dimension of the problem, requires taking into account a large number of modes to reproduce properly the phenomenon.

Another interesting aspect is observed between modes 40 and 50, in the right hand side of the valve-shaft where the energy is suddenly converging within less than ten modes. A more detailed

analysis will shed light on the precise modes and frequencies at which this rapid change is occurring.

The following figures (Figure 5.25 to 5.28) are showing the topology of the spatial modes (shaded with the kinetic energy) obtained for the DES results, classified by POD level from the most energetic, large scale structures, mode 1 in Figure 5.25, to the smaller ones (here until the fourth mode, Figure 5.28). While comparing the two different post-processing fields, apart from the first mode showing high similarities in both planes, some clear discrepancies are appearing for the next modes. Although the energy distribution plotted formerly in Figure 5.23 is really comparable in both cases, the spatial modes are showing some differences. On a global aspect, some similarities exist with regards to the resolved structures at each mode, but their location does not always match with each other. A more quantitative analysis of the spatial structures corresponding to the different modes will be presented later in this chapter.

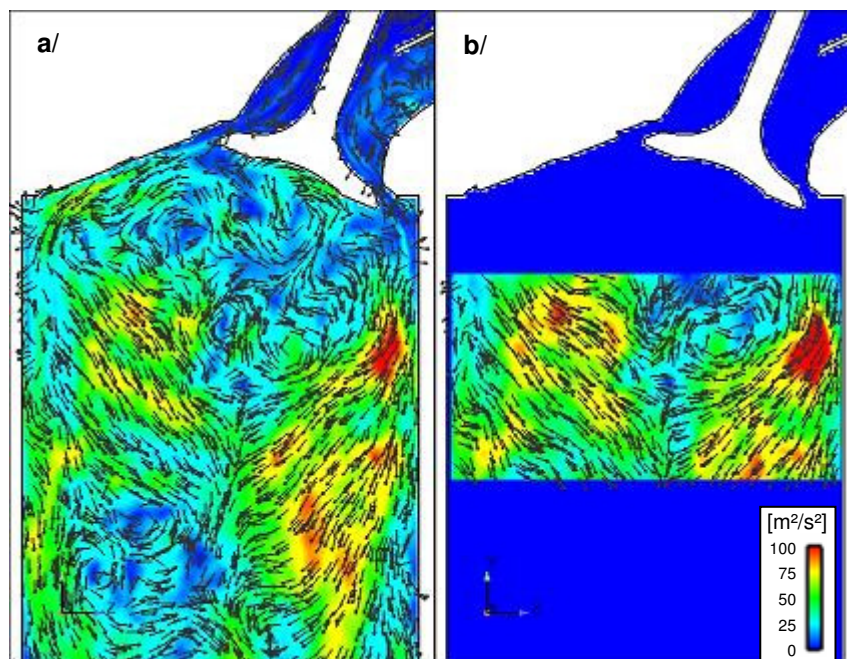


**Figure 5.25: Visualization of the 1<sup>st</sup> POD mode of the flow (DES100C3) – Velocity vectors and kinetic energy: a/ full valve cross-section plane b/ PIV window**

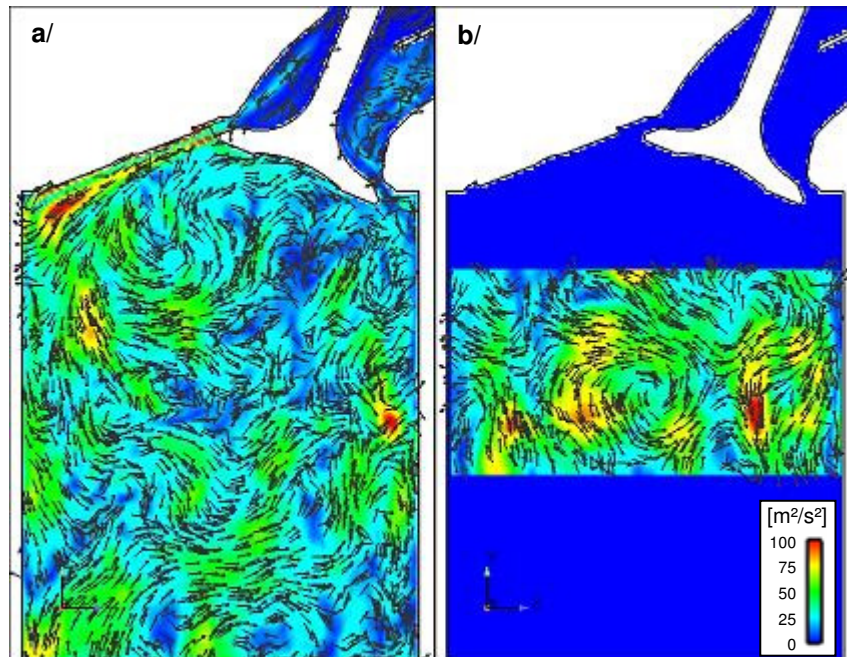


Figure 5.26: Visualization of the 2<sup>nd</sup> POD mode of the flow (DES100C3) – Velocity vectors and kinetic energy: a/ full valve cross-section plane b/ PIV window

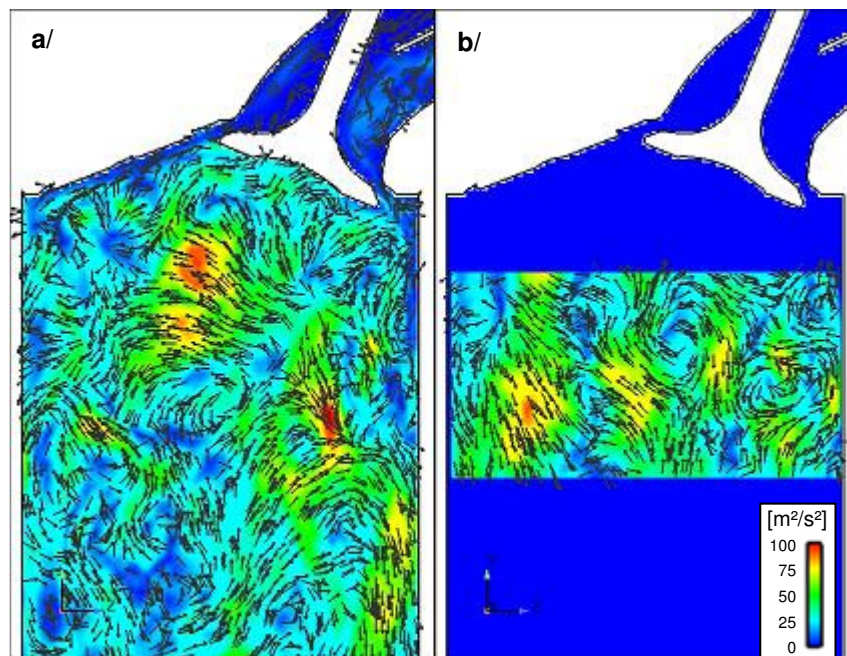
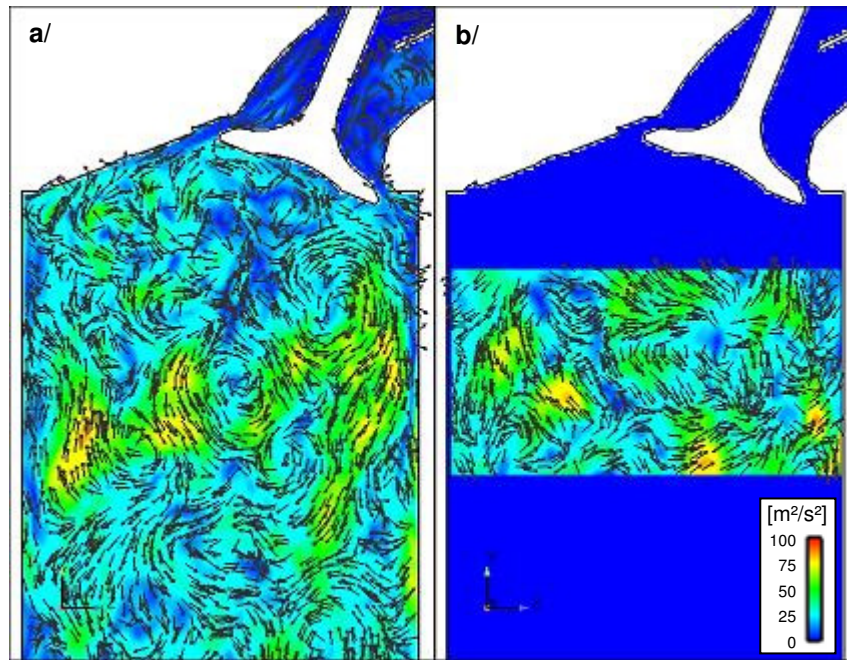


Figure 5.27: Visualization of the 3<sup>rd</sup> POD mode of the flow (DES100C3) – Velocity vectors and kinetic energy: a/ full valve cross-section plane b/ PIV window



**Figure 5.28: Visualization of the 4<sup>th</sup> POD mode of the flow (DES100C3) – Velocity vectors and kinetic energy: a/ full valve cross-section plane b/ PIV window**

Even though the window dimension is influencing, in a certain extent, the shape of the individual modes, the capacity to reconstruct the original velocity field is lying on the combination between spatial modes and their associated time coefficients. Indeed, the structures resulting from the decomposition cannot be considered individually as real structures existing in the flow, but just constitute an optimal N-dimensional basis to reconstruct the original data set.

However, as it will be seen from the following paragraph, by reconstructing the instantaneous velocity fields according to the same truncated modes, both windows are delivering identical results. Although the individual modes are not perfectly fitting together, the reconstruction based on the combination of spatial modes fluctuating in accordance with their time coefficients is giving back the original data set. Thus, the size of the window used for POD should not affect the quality of the decomposition and the reliability of the reconstructed information.

### 5.6.2 Influence of the Energy Truncation Level

The level of truncation chosen to represent the flow field is resulting from a compromise between the dimension of the basis employed to describe the flow of interest and the model accuracy in terms of resolved structures sizes. Once again, the convergence rapidity of the eigenvalues (Figure 5.23) is offering an indication on the complexity of the flow investigated. The number of degrees of freedom available in the flows is directly connected to its complexity, and then to the number of modes required to properly reconstruct the velocity field. Therefore, the faster the eigenvalues are converging, the higher the contribution of the lowest modes to the total flow energy, which indicates that the structure of the flow in such a situation is relatively simple. In the present case, considering the relatively low values of the first eigenvalues and the large number of modes required to reach a sufficient level of energy, one can conclude that this flow is particularly complex and even disorganized.

An example of the influence of the truncation on the reconstructed velocity field is given in Figure 5.29. Three different numbers of modes have been used to reproduce the original data set, each of them corresponding to a certain level of energy. In the upper row of the figure, the two results showing the original data and the reconstructed field by means of the maximum number

of modes are almost completely equivalent, down to the smallest structures. This is already proving the validity of the decomposition method; since the 300 modes used for this operation are containing approximately the full amount of kinetic energy available in this plane, their combination is expected to describe properly the source information.

On the two other quadrants, with a lower number of modes corresponding to a lower level of energy, the results look smoothed. Indeed, in c/, where twenty modes have been used, only 52% of the total fluctuant energy could be obtained (see Figure 5.23b), delivering a reconstructed velocity field close to the averaged results. Most of the smallest structures are filtered out, and only the larger scales are still considered. However, with sixty modes and around eighty percent of the energy, more details of the flow are taken into account, providing more fidelity to the original data.

In the present case, this last level of truncation seems to be most appropriate to reflect the complexity of the geometry and the number of degrees of freedom while keeping the dimension of the problem at an affordable stage.

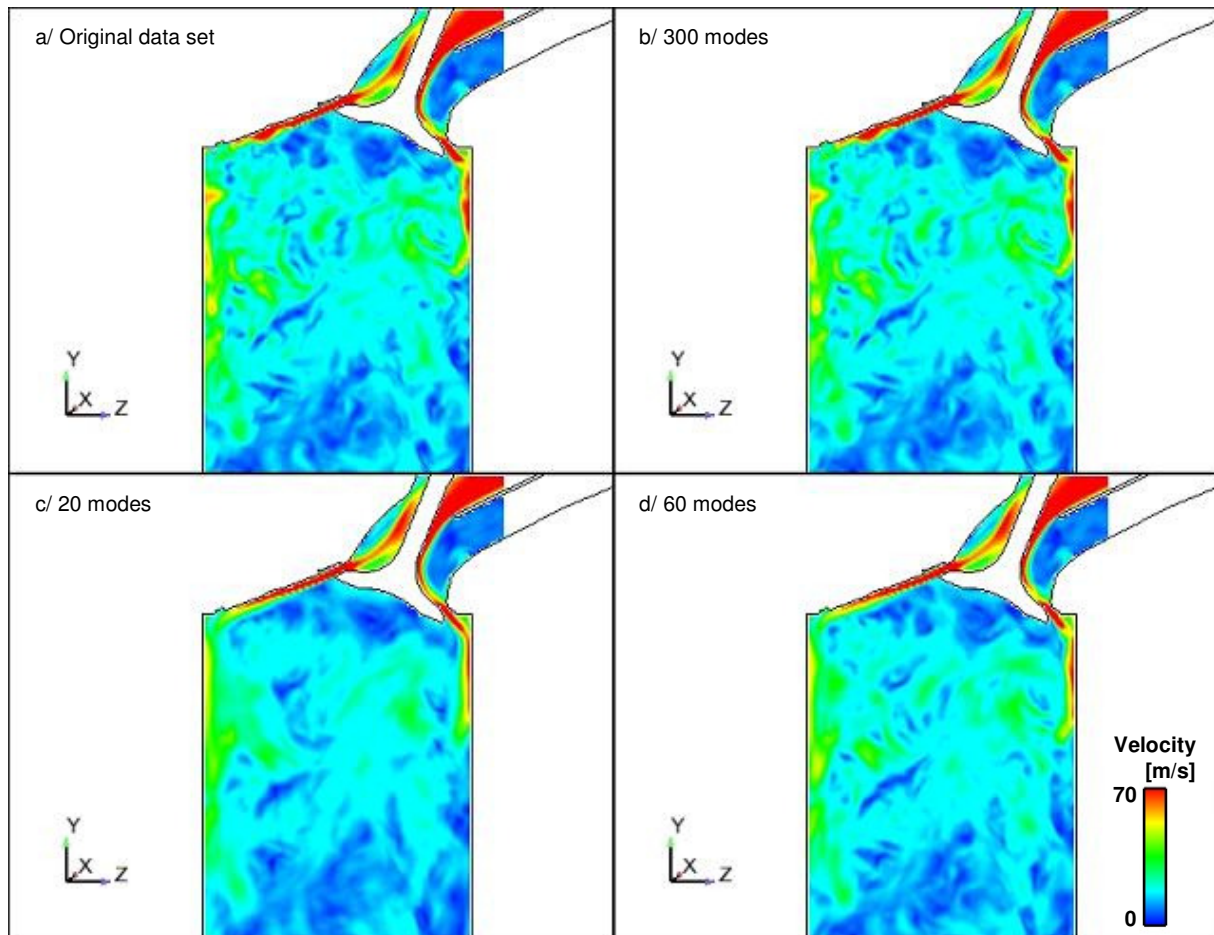


**Figure 5.29: Analysis of the truncation influence on the quality of the reconstructed velocity field (DES 100C3 – valve-plane)**

### 5.6.3 Analysis of the Time Coefficients Spectra

In a further attempt to establish the dependency of the POD method to the post-processing window dimension, the spectral analysis of the time coefficients is another important factor to investigate since it delivers direct information about the fluctuating flow quantities.

A global view of the ensemble of spectra obtained with the different modes can be given by a so-called spectrogram. Thanks to this kind of representation, the full spectral information contained in the 300 modes can be summarized in a frequency map, indicating the principal regions of interest. In the present case, these regions are made of the modes numbers corresponding to a particular frequency peak.

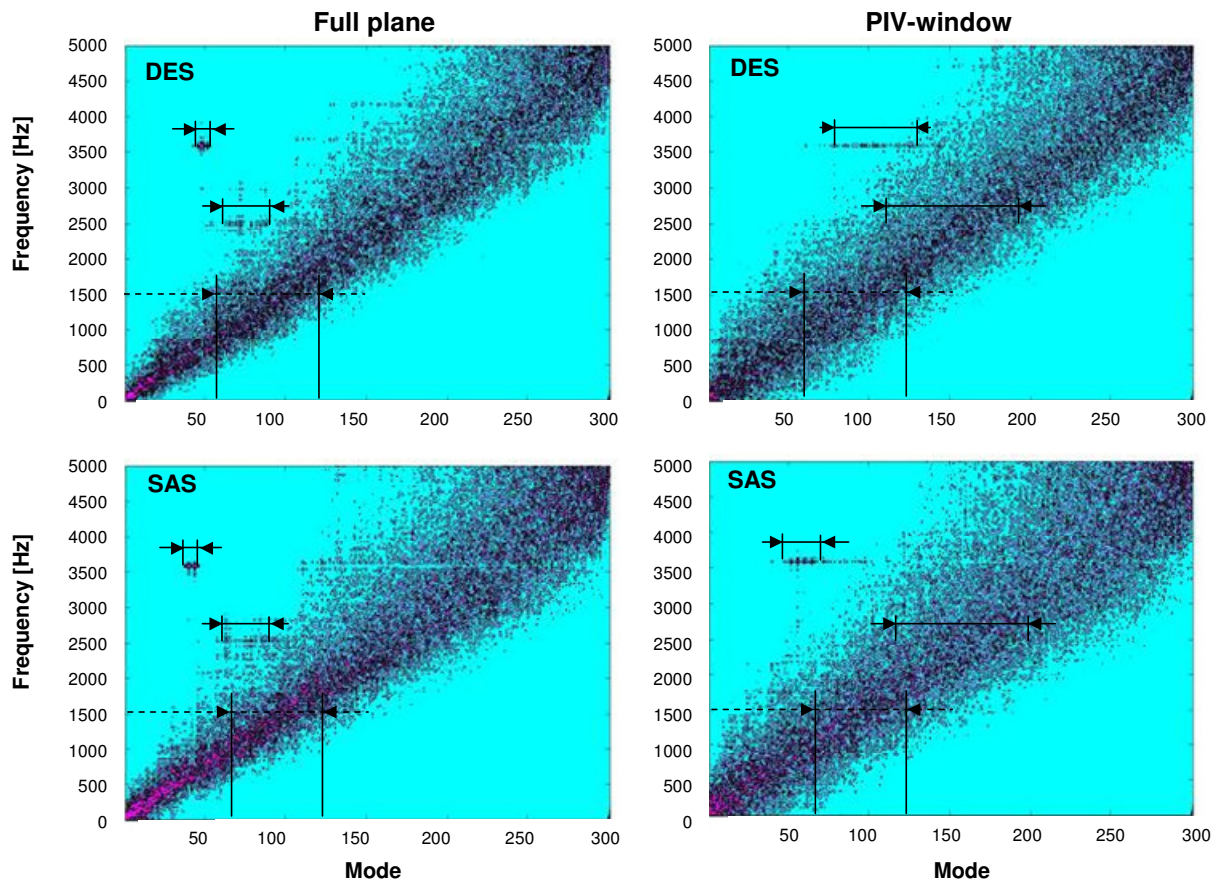


**Figure 5.30: Spectrogram resulting from the FFT of the time coefficients associated to the different POD modes – Comparison between DES and SAS results, case 100C3, full valve plane and PIV window. The marked regions represent the modes domains showing a particular spectral activity for the three frequencies of interest**

In Figure 5.30, at a first sight, a remarkable aspect of the spectrum is its general shape. The dark points or regions of the spectrogram are corresponding to the highest amplitudes of the spectrum for each mode, and are spread along the diagonal of the figure.

In the low-frequency range, the modal distribution of the frequencies is narrower than the distribution of the highest ones. One can easily deduce from this plot that approximately 30 spatial modes are oscillating with a frequency of 500Hz, whereas almost 100 modes are concerned with fluctuations in the frequency range surrounding 4kHz. This observation coincides with the idea that the lowest modes, which are supposed to represent the most energetic and largest structures, are corresponding to the lower frequencies.

On the other hand, the higher modes corresponding to the smaller structures have a broader spectrum, dispersed over numerous high frequencies. Although this general pattern of the frequency distribution is found in both windows (full valve section-plane and PIV-like window), the spectrogram of the PIV window is offering a wider band and is also slightly attenuated in

amplitude. One can explain this difference by the location of the acquisition window. As displayed in the former figures, it is possible to observe that this region is positioned rather far away from the valves and other disturbing geometrical entities. This means that the frequencies associated with the perturbation convecting in the flow may be either damped or even completely absent of this region. Nevertheless, some similarities are occurring between both planes, like, for example, at the high frequency of 3.6 kHz. A really punctual region, constituted by few modes is showing some peaks at this particular frequency in the case of the full plane. In the other case, a horizontal line over a larger number of modes is representing the same frequency. Finally, the size of the window and its position is also influencing the spectral quality of the decomposed modes. Instead of a clear map, a smaller post-processing domain shows roughly the same information but with a somewhat blurred image.

**Table 5-6: Modes associated to the different frequencies for various CFD results and post-processing windows**

Frequency [Hz]	DES		SAS	
	Full valve-plane	PIV window	Full valve-plane	PIV window
3600	45-53	96 - 146	42-48	48-73
2500	62-88	111-189	63-97	125-199
1500	55-121	58-125	68-124	74-134

The information summarized in Table 5-6 is also supporting the observation that the spectrum calculated for the smaller window is spread over a larger number of modes than for the full section plane. A second interesting point is the shift towards the higher modes for the frequency of 3.6kHz with the DES results decomposition. In this particular region, in order to reproduce the flow fluctuations concerned with this frequency, 9 modes are required for the DES results from mode 45 to mode 53, whereas in the SAS case, only 7 modes are necessary, from mode 42 to 48. Since the same numerical mesh has been used for both simulations, this difference could be directly related to the different turbulence models implemented. As a matter of fact, the SAS model, which is a derivative method from the URANS formulation, is supposed to filter the equations governing the flow, and consequently the structures resolved. This would explain the fact that a smaller number of modes are required to reproduce the behaviour of the structures fluctuating with the frequency of 3.6kHz. Thanks to these results, it is now possible to reconstruct the fluctuant velocity fields associated to the frequencies described above: 1.5kHz, 2.5kHz and 3.6kHz.

First of all, a brief comparison is presented between the two different modes ranges determined for each windows and their influence on the reconstructed field. The following plots are showing the reconstructed velocity field filtered according to the modes associated to the frequency of 3.6kHz, once based on the spectrum of the full post-processing plane (subplots a/ thereafter) and then, based on the spectrum of the PIV-window (subplots b/).



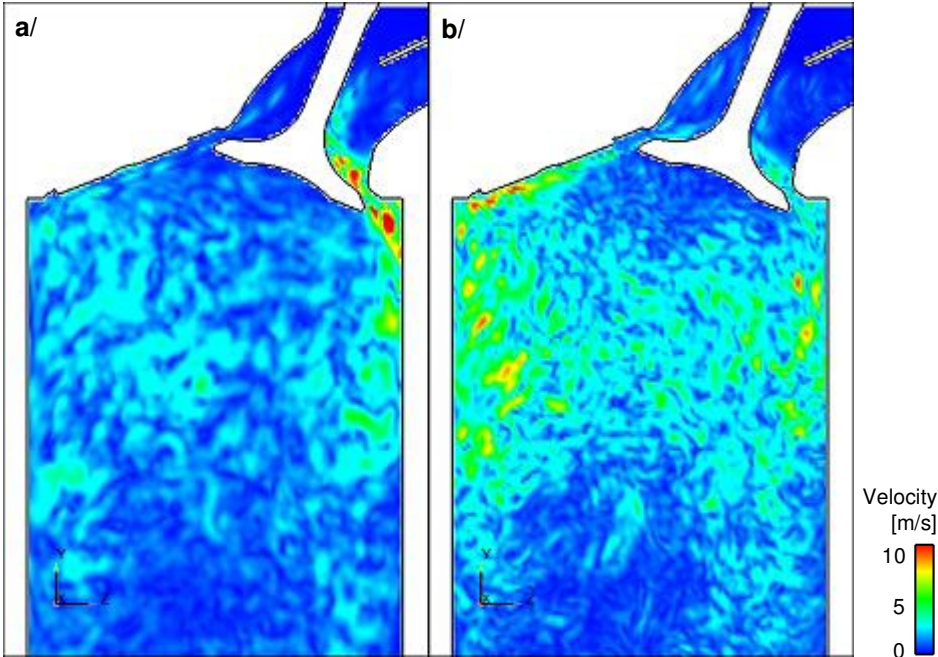


Figure 5.31: Reconstruction of the velocity field filtered by the frequency of 3600Hz for the full valve-plane – a/ with modes 45-53 (full plane modes) – b/ with modes 96-146 (PIV-window modes).

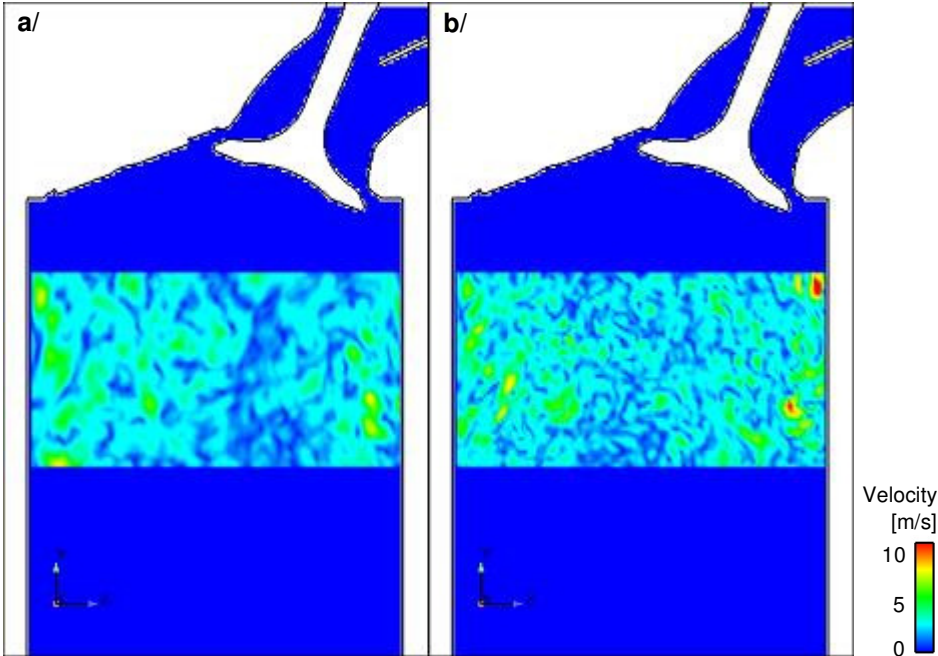
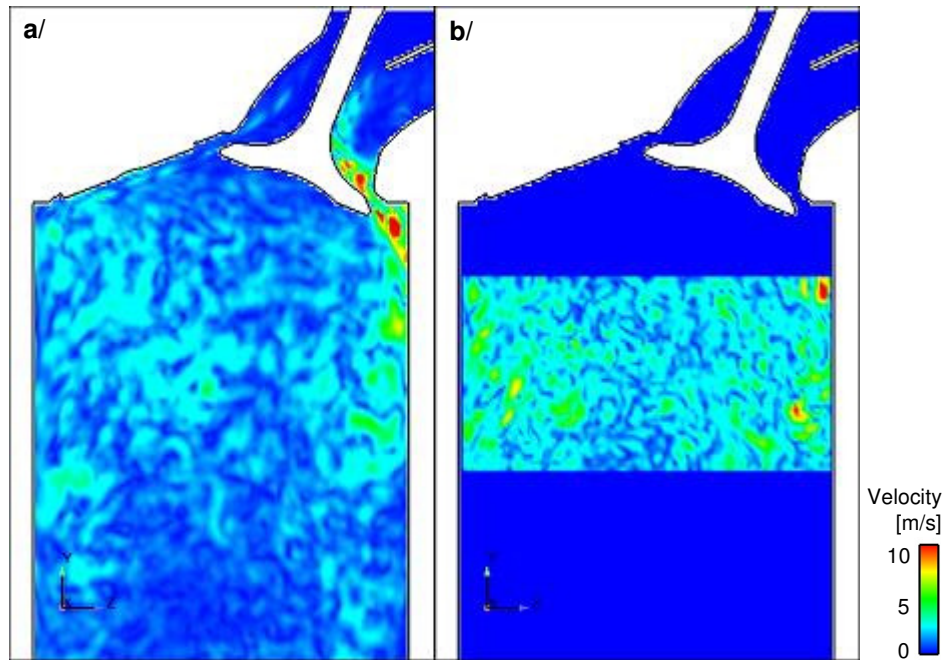


Figure 5.32: Reconstruction of the velocity field filtered by the frequency of 3600Hz for the “PIV-window” – a/ with modes 45-53 (full plane modes) – b/ with modes 96-146 (PIV-window modes).



**Figure 5.33: Reconstruction of the velocity field filtered by the frequency of 3600Hz – a/ full valve-plane: modes 45-53 (full plane modes) – b/ “PIV-window”: modes 96-146 (PIV-window modes).**

The three previous figures are showing the reconstructed field of the velocities fluctuating with the frequency of 3.6 kHz. Figures 5.31 and 5.32 are respectively presenting the reconstructed field on each post-processing window according to the two different modes domains deduced from their spectra. All subplots a/ are obtained thanks to the modes corresponding to the full valve-plane analysis, whereas subplots b/ are related to the PIV window size. Thus, in Figure 5.31, only the left graph presents the appropriate flow reconstruction to which the modes are dedicated, while on the right side, the modes used were defined for the PIV window but applied to the full plane. The opposite situation is occurring in Figure 5.32. Finally, the comparison of the appropriate post-processing windows reconstructed according to their dedicated modes is summarized in Figure 5.33.

For this example, one can clearly localize the fluctuating quantities within the geometry, as it has been already done in §5.5.1. For the full valve-plane, and with the appropriate modes (Figure 5.31.a and 5.33.a), the velocity field reconstruction from the POD method is matching the results obtained in the precedent paragraph, showing that the fluctuation frequency of 3.6 kHz is likely to be induced by the flow splitter installed in the intake port, upstream of the intake valves. Lower in the cylinder, in the PIV window size, the presence of fluctuations with this particular frequency are not so obvious. However, according to the right modes numbers, the reconstruction is showing some regions with an activity in the right side of the cylinder, in the wall vicinity. This is the region where the fluctuations observed earlier are convecting and slowly dissipating.

Some emphasis will be put on this region later as the PIV results will be considered and compared to the CFD results.

The results obtained with the two other frequencies, and plotted thereafter, are also showing a good agreement with the outcomes of the spectral analysis from previous paragraph.

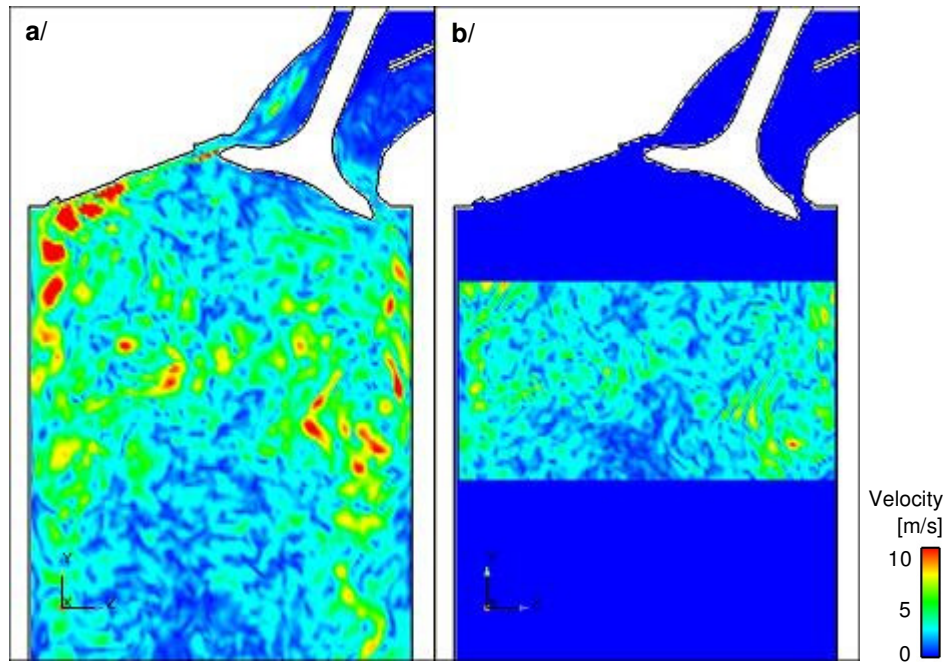


**Figure 5.34: Reconstruction of the velocity field filtered by the frequency of 2500Hz – a/ full valve-plane: modes 62-88 – b/ “PIV-window”: modes 111-189**

Based on the relevant POD modes, the velocity fluctuating with a frequency of 2.5 kHz are confirming the location of their origin at the tip of the intake valve. From Figure 5.34.a, at the particular time-step chosen for this snapshot, one of the highest velocity amplitude regions is just developing on the left side of the valve tip. Then the structures associated to the frequency of interest are traveling within the chamber along the cylinder head before breaking up into several smaller structures.

Generally speaking, for the two cases observed before (for 3.6 kHz and 2.5 kHz), the main variation induced by the windowing effect on the POD decomposition for reconstruction with filtering is an enlargement of the modes range required and a global shift towards the higher modes. This phenomenon yields a reconstructed signal with relatively smaller structures and containing a wider range of frequencies. This lack of sharpness of the resulting field decreases the accuracy of the localization prediction, compared to the full plane analysis. This is a major concern while considering the experimental data for validation of the numerical simulation.

In Figure 5.35, apart from the good matching between the full plane results and the previous local spectral analysis (see §5.5.1, Figure 5.20), which are indicating a strong relation between the oscillation frequency of 1.5 kHz and the valve-shaft, a noticeable point is the presence of clear detached structures in the PIV-like window. Indeed, in contrast to the other two frequencies studied before, the ranges of modes associated with this lower frequency are very similar for both windows, leading to analogous reconstructed fields. This last point is highlighting the inferior sensitivity of the POD decomposition to the window size and position in the lower frequency domain, where the fluctuating quantities can still be found. Considering the outcomes of the present analysis, it is very likely that most of the information delivered by the PIV measurements will be bounded in the lower frequency range, restricting the global field of investigation.

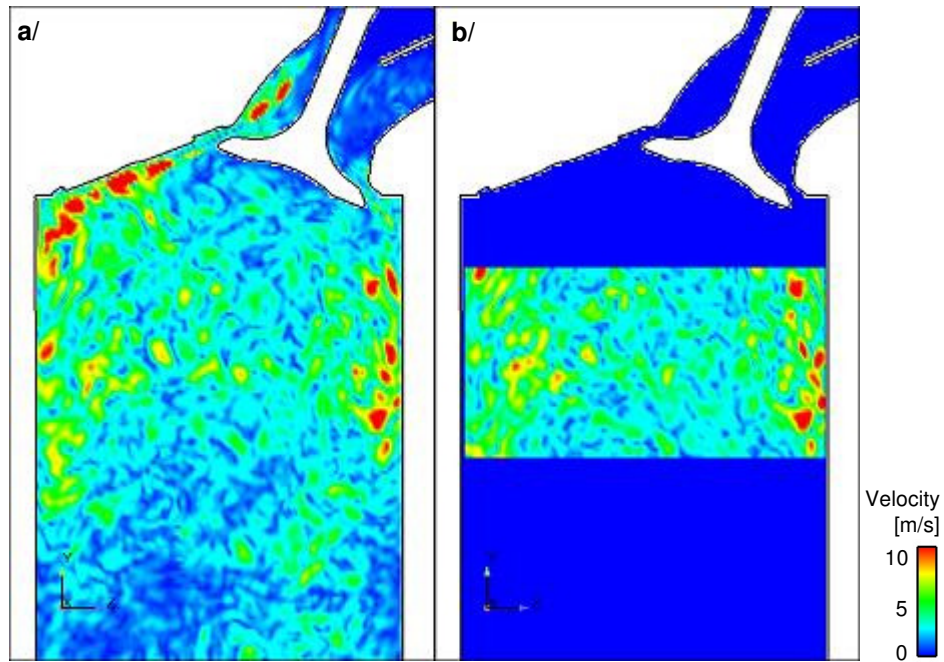


Figure 5.35: Reconstruction of the velocity field filtered by the frequency of 1500Hz – a/ full valve-plane: modes 55-121 – b/ “PIV-window”: modes 58-125

#### 5.6.4 Comparison with HS-PIV data

Before any comparison can be undertaken, a first major difference, the spatial resolution between numerical and experimental data, has to be tackled. Beside the fact that the PIV measuring window is restricted due to a difficult optical access in the upper region of the cylinder, the counterpart of the high acquisition frequency employed was a lower resolution in space.

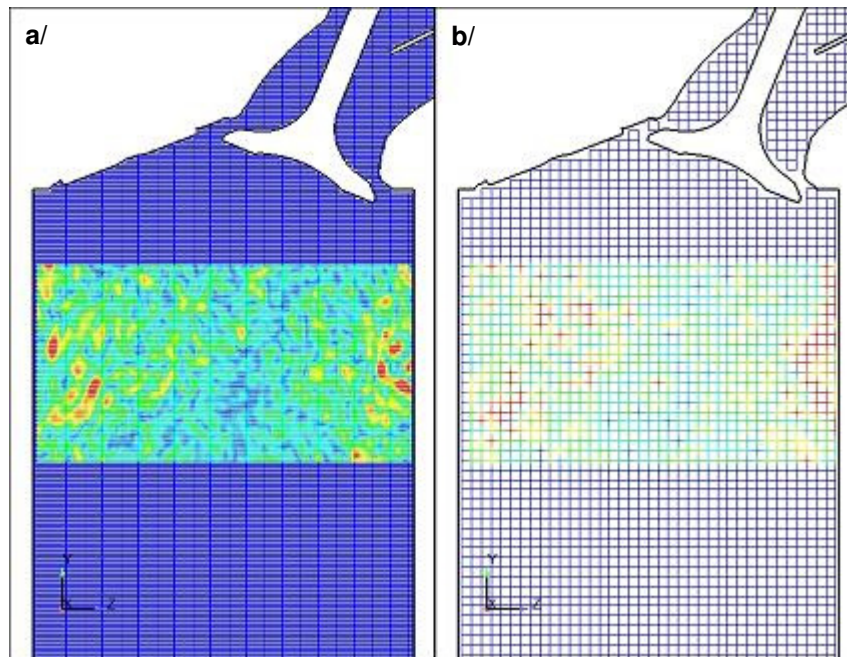
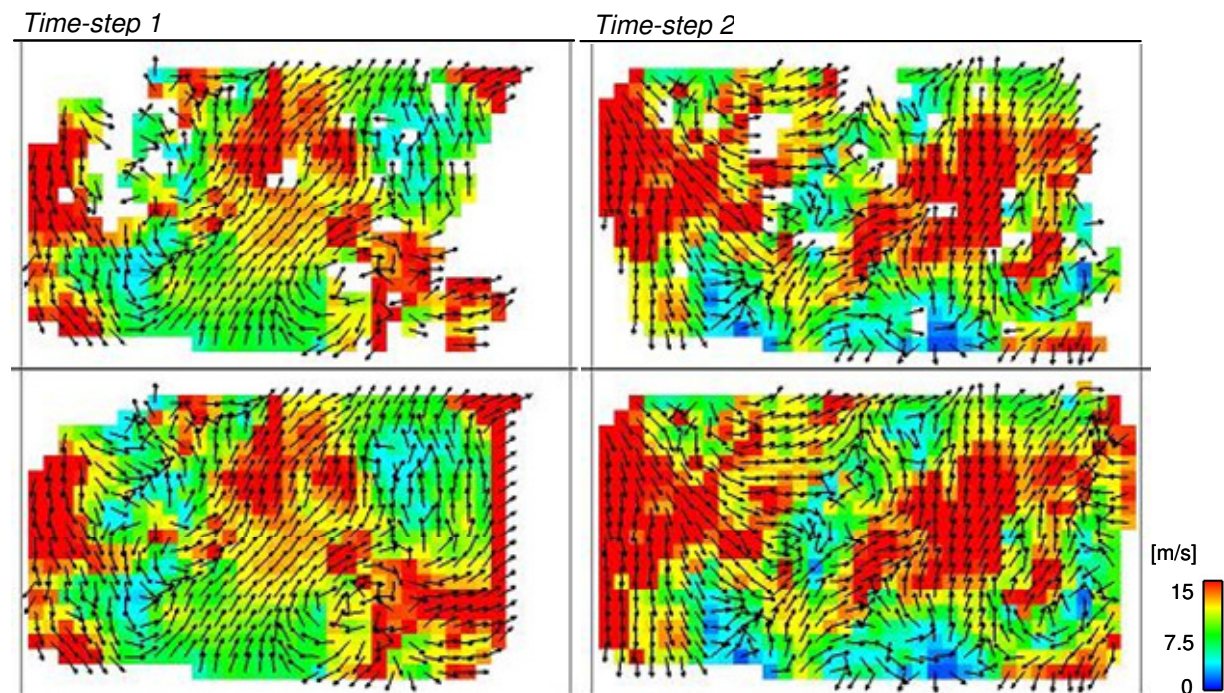


Figure 5.36: Difference of spatial resolution between various post-processing grids: a/ fine mesh b/ coarse mesh / “PIV-like” resolution (see also the diagram presented in Figure 5.11)

As depicted in Figure 5.36, a large difference exists between the “fine” mesh used for the post-processing of the CFD data and the coarser one, which is equivalent to the resolution of the PIV results (see §5.3.2 – data management and post-processing meshes). In the first case, the cells size in both directions were:  $\Delta z = 0.34$  mm and  $\Delta y = 0.6$  mm, whereas in the coarser configuration:  $\Delta z = 1.77$  mm and  $\Delta y = 1.74$  mm. This leads to the following ratios in the two different directions:  $\Delta z_{PIV} / \Delta z_{CFD} \approx 5.2$  and  $\Delta y_{PIV} / \Delta y_{CFD} \approx 2.9$ , which means that the fine grid was containing about 15 times more points than the coarser grid. All the results and analysis presented in the following paragraph are computed on the “PIV-like” grid to insure consistency in the comparison.

On the other hand, on the contrary to simulation results, the experimental data are showing some undesirable instantaneous effects, lacking information at certain time steps or snapshots. This is due to variable seeding properties and to the high repetition rate employed with the laser causing the PIV results to be unstable over time. This phenomenon is particularly influencing the quality and the relevance of the POD method by altering the correlation computation and then the resolution of the eigenvalues problem. In order to smooth down the inputs, a treatment of the raw data has been implemented in space and in time, to interpolate the original information in both directions. As it can be seen in Figure 5.37, the linear interpolation process employed here allows filling up the missing information without affecting the original data.



**Figure 5.37: PIV results in the valve plane – Top: raw data, Bottom: interpolated velocity field (over space and time)**

Based on the previously presented interpolated data set, the POD could be applied on each element containing information at every time step, guarantying the required conditions for the decomposition method.

Since the PIV acquisitions are offering a larger data set in time than the simulation results, Figure 5.38 is comparing the influence of the data set length on the POD decomposition by analysing the convergence of the kinetic energy. It appears that the longer the sample size is, the slower the energy is converging. With three hundred samples, the cumulative sum of energy is reaching a level of 50% of the total energy after approximately twenty modes, whereas with a sample size of

about nine hundred, thirty modes are requested. This difference is even increasing for higher level of energy. However, it is also possible to observe that, after a certain threshold, over a particular number of modes, the sum of eigenvalues resulting from the POD is reaching a limit. In Figure 5.38.b, the gap between the energy obtained with a sample size of 301 and 501 data is much higher than the difference existing between higher sample sizes results. This threshold is directly dependent on the complexity of the flow, requiring a larger number of modes to take into account the complete range of uncorrelated structures developing in the geometry.

Indeed, a preliminary study, based on a virtual simple flow made of basic sinusoidal signals with given proper frequencies and then, a limited number of modes, has shown that if the number of degrees of freedom is finite, the POD decomposition over a larger number of modes does not bring any further information. This means that the energetic convergence of the reconstructed field obtained thanks to the higher basis is equivalent to the one provided by the basis containing the exact dimension. The contribution of the last modes generated by the basis of higher dimension is purely negligible; the curve representing the cumulative energy of the different modes being asymptotic to the maximum level of energy (reaching 100%).

In the present case, even if a higher number of samples would have been desirable, due to the restricted length of the numerical results, for the following comparisons between experimental and CFD outcomes, the same sample size of 301 data will be employed to ensure consistency.

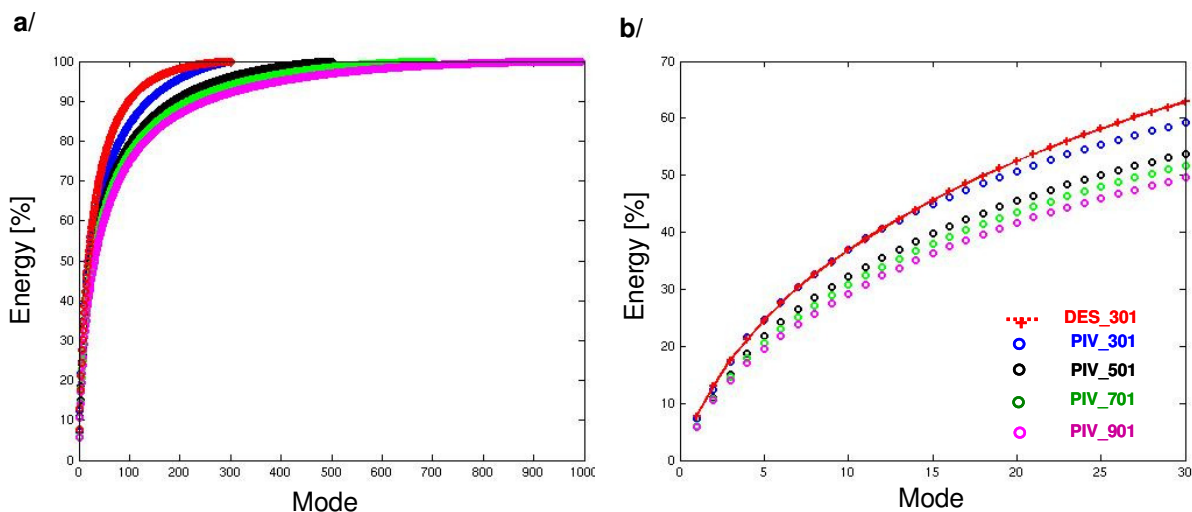


**Figure 5.38: : Influence of the sample size on the cumulative fluctuating kinetic energy convergence (from 301 modes to 901 modes)**

In Figure 5.39, the sum of the kinetic energy obtained between mode 1 and 30 are superimposed for CFD and PIV results, showing the influence of the window size on the CFD results. Subplots a/ and b/ are representing the DES results on both planes, while the SAS ones are displayed on c/ and d/. As it has already been mentioned, DES results are more sensitive to the window size than the SAS results, and are even better matching the PIV outcomes when the same post-processing area is used. Indeed, in the upper right corner of the graph, subplot b/, the first fifteen modes are almost perfectly coinciding between DES and PIV results. The SAS simulation results are being basically not influenced by the windowing effect as they are presenting the same absolute difference whatever the post-processing area.

As already mentioned, for any further direct comparison between CFD and experimental results, only the same window and the same sample size are considered for consistency reasons.

The former observations made by comparing each turbulence models individually with the PIV results are confirmed by the superimposition of all three cases together in Figure 5.40. The

energy content of the first mode is very well matching between DES and PIV results in the present case, showing a discrepancy of about 3% with the SAS model.

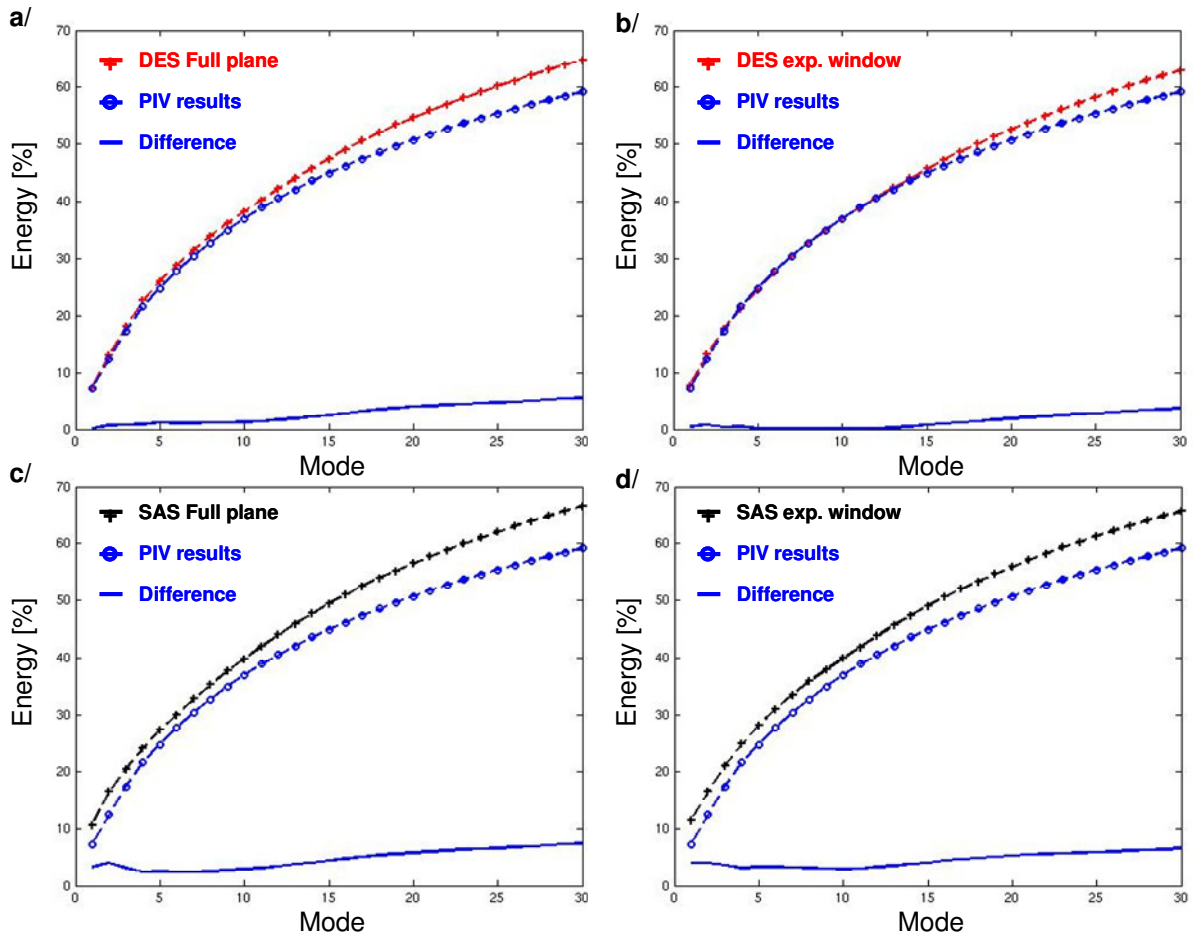


Figure 5.39: Windowing effect on CFD results – comparison with PIV measurements in the valve-plane

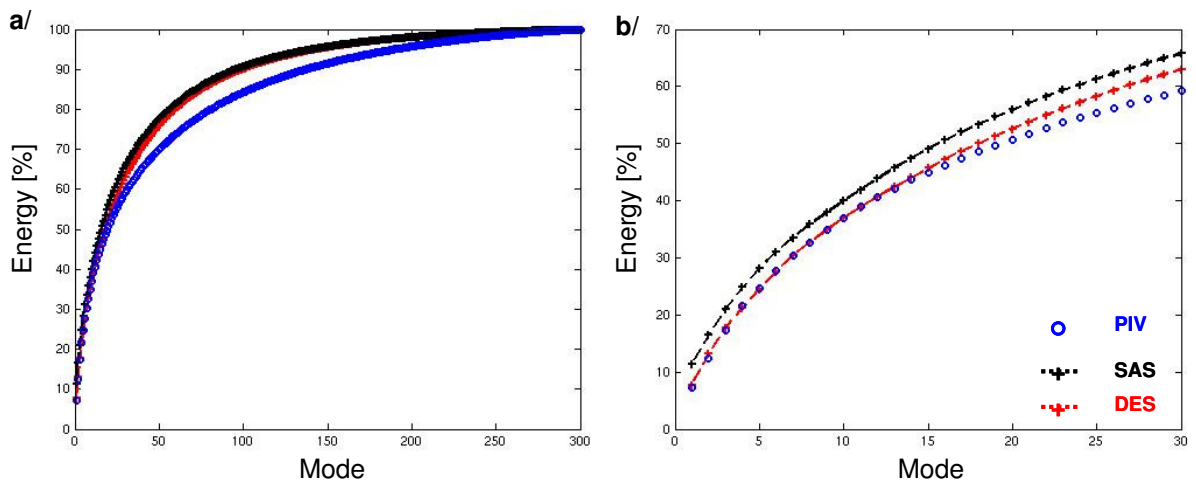
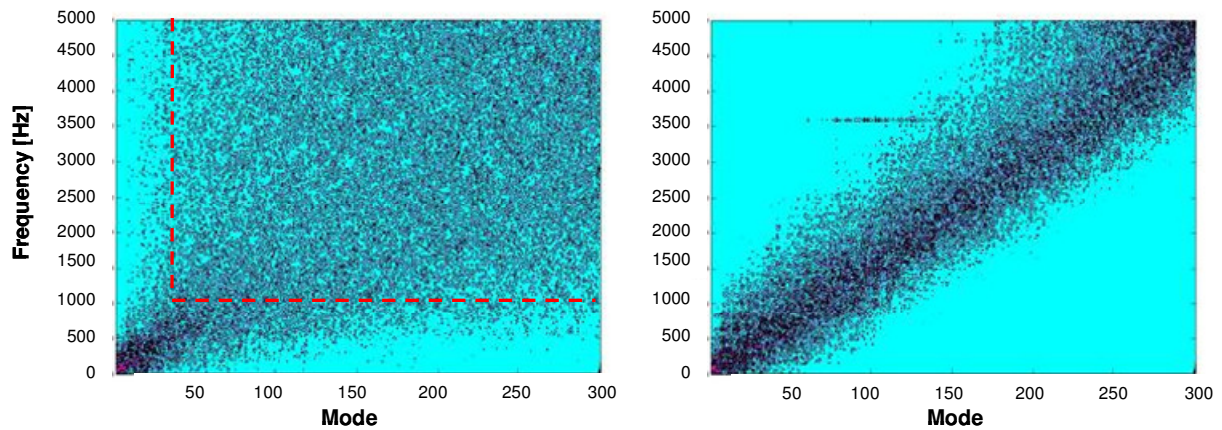


Figure 5.40: Eigenvalues comparison between both numerical results (DES and SAS) and experimental results for the case 100C3, in the valve plane – a/ 300 modes; b/ Zoom in the 30 first modes

However, the spectral analysis of the time coefficients associated to the different spatial modes is not so promising. Figure 5.41 and Figure 5.42 thereafter present the spectrograms obtained with the PIV results (case 100C3) compared to the DES, taken as reference.

First of all, in the linear representation, Figure 5.41, the spectrum seems to be widely diffuse in the higher frequency range and over a certain mode number. Actually, upon a value of about 1000Hz and 30 modes (region of the diagram contained in the upper right-hand-side, delimited by the dashed red lines), the signal obtained is very similar to pure white noise. Indeed, whereas the DES spectrogram is showing a particular pattern, forming a diagonal with well defined bounds, in the case of PIV results, the signal is totally scattered as soon as the previously mentioned domain is reached, for a frequency of around 1 kHz, after the first 30 modes.

In other words, this signifies that the spectral decomposition based on the experimental data will probably not offer such clearly differentiated frequency peaks or other distinct modes range with a prevailing characteristic frequency as the one determined by analyzing the CFD spectrograms.



**Figure 5.41: Linear representation of the spectrogram of the time coefficients associated to the 300 POD modes. Left: PIV results (distinction between a confidence area and a noisy, scattered region bordered by the dashed red lines, in the upper right-hand-side of the graph), right: DES**

Apparently the signal-to-noise ratio of the measurements is too low in the higher frequency range and higher mode numbers, implying a very high level of noise and preventing any investigations of the phenomena occurring in this domain. This last observation constitutes a major drawback since the main characteristic frequencies highlighted earlier were contained in this region (1.5 kHz, 2.5 kHz and 3.6 kHz). Evidence can be seen in Figure 5.41 again, where the 3.6 kHz frequency peaks found in the DES spectrogram cannot be distinguished from the surrounding noise in the PIV signal.

The logarithmic representation of Figure 5.42 offers a better visualization of the information contained in the lower frequency and mode's range. Indeed, compared to the CFD results, showing a clearly bounded pattern all along the frequency range, the PIV ones are only reliable until 1kHz after what the spectrum obtained for each mode is widely spread over a broad range of frequencies.



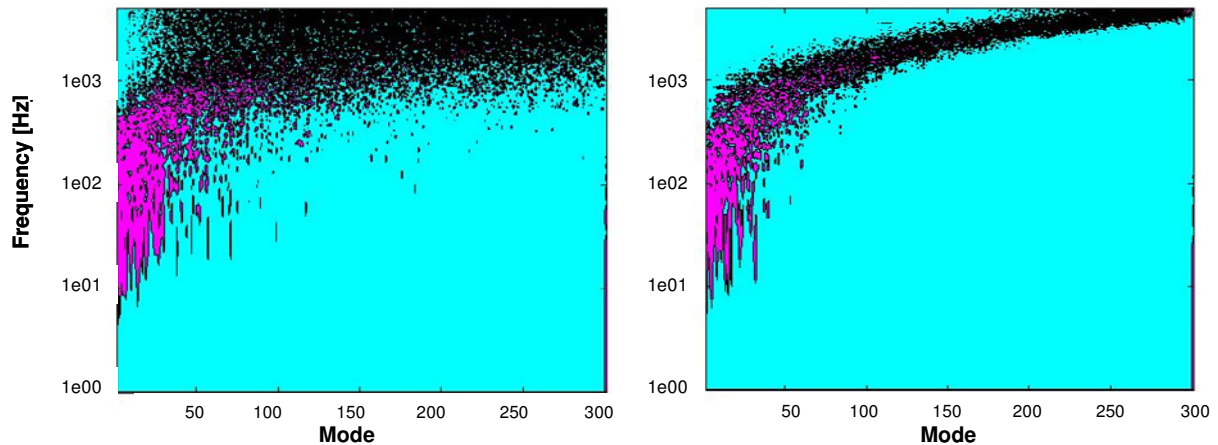


**Figure 5.42: Logarithmic representation of the spectrogram from Figure 5.41 – Left: PIV results; Right. DES results**

Unfortunately, based on the former observations resulting from the information of Figure 5.38, the increase of the number of samples used for the POD decomposition would not improve the resolution of the spectral analysis applied to the resulting modes. Indeed, as the energy decomposition of the flow over the successive POD modes is still sensitive to the sample size, it means that the description obtained with this orthogonal decomposition, or basically, the resulting basis, is not optimal or even complete. On one hand, this is certainly related to the existence of a large number of degrees of freedom or, in other words, to the complexity of the turbulent flow investigated, but also probably to the quality of the PIV measurements. Even though the cumulative energy computed for each mode is comparable between experiment and simulation results, the distribution over their spectra is rather different. Some energy peaks are really distinct on the CFD outputs at higher modes (for example, 3,6 kHz between mode 75 to mode 140) showing a better concentration of this energy and then, highlighting the predominance of particular frequencies. Increasing the sample size of the PIV results would only decrease the energy content of each mode without improving the time resolution at higher modes.

Next paragraph, establishing the correlation between the POD modes and the turbulence structure size, will support the assumption that this lack of performance of the high-speed stereo-PIV measurements, in the particular modes and frequency range described above, has probably to deal with a matter of spatial resolution. For that reason, PIV-results are missing the smallest structures that CFD can take into account, and which are fluctuating with the highest frequencies.

Therefore, since the spectral analysis of the experimental results is rather restricted, the focus of the following investigations has been put on a detailed study of the structures developing in the flow, based on the characteristic frequencies found in the CFD data spectrograms.

### 5.6.5 POD Modes Sizes

The POD method is supposed to decompose the original flow field into a finite ensemble of spatial modes, each of them representing a different class of eddies, with different size, orientation and energy content. Then, an interesting means of comparison would be to compare the number of structures present in the plane of interest as well as their averaged diameter. This

method could deliver some quantitative parameters to compare the outcomes of the different numerical models investigated and to check their validity.

As it has already been described in the work of Fogleman et al. [45], in order to determine the averaged number of vortices existing for each mode in the post-processing window, the number of times the velocity component parallel to the cylinder axis (Y-component) crosses zero as the diameter of the cylinder is swept (Z-direction) was calculated. This value should then represent an approximation of the number of vortices, which are aligned perpendicular to the cylinder axis. The diagram shown in Figure 5.43 is presenting the principle of “zero-crossings”, whereas Figure 5.44 gives an example of the distribution of positive and negative vertical velocities within the cylinder.

Based on the assumption that for a fully turbulent flow such as the one found in the cylinder of the engine considered here, all vortices are bounded by other vortices, without any gap in-between, the knowledge of the cylinder-bore and the zero-crossings count number should allow to compute the approximated eddies size.

However, since no information about the shape of the structures exists, no assumption about their “isotropy” can be stated. Thus, the other direction also needs to be studied, that means the zero-crossings values in the vertical direction (Y-axis) for the Z velocity-component should be computed.

Consequently, knowing the structures count number and the cylinder diameter, it is possible to compute an approximation of the mean diameter of vortices for each mode in both flow directions. This information represents a statistical measure of the turbulence level of the flow, depending on the POD mode considered (consequently on truncated energy levels).

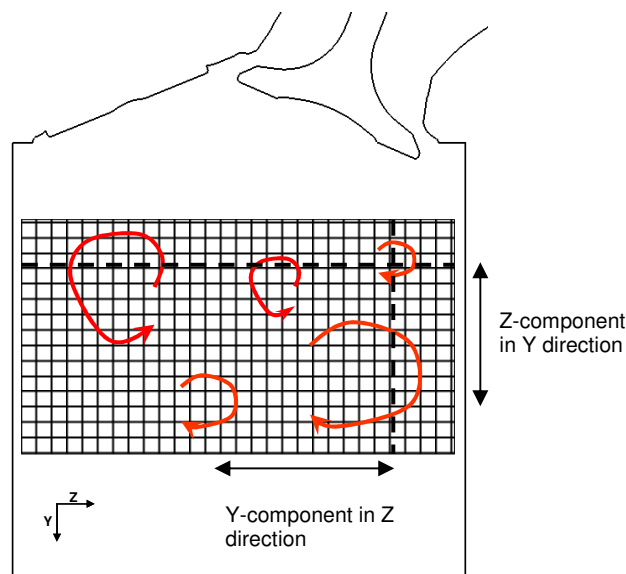


**Figure 5.43: Diagram of the “zero-crossings” calculation principle**

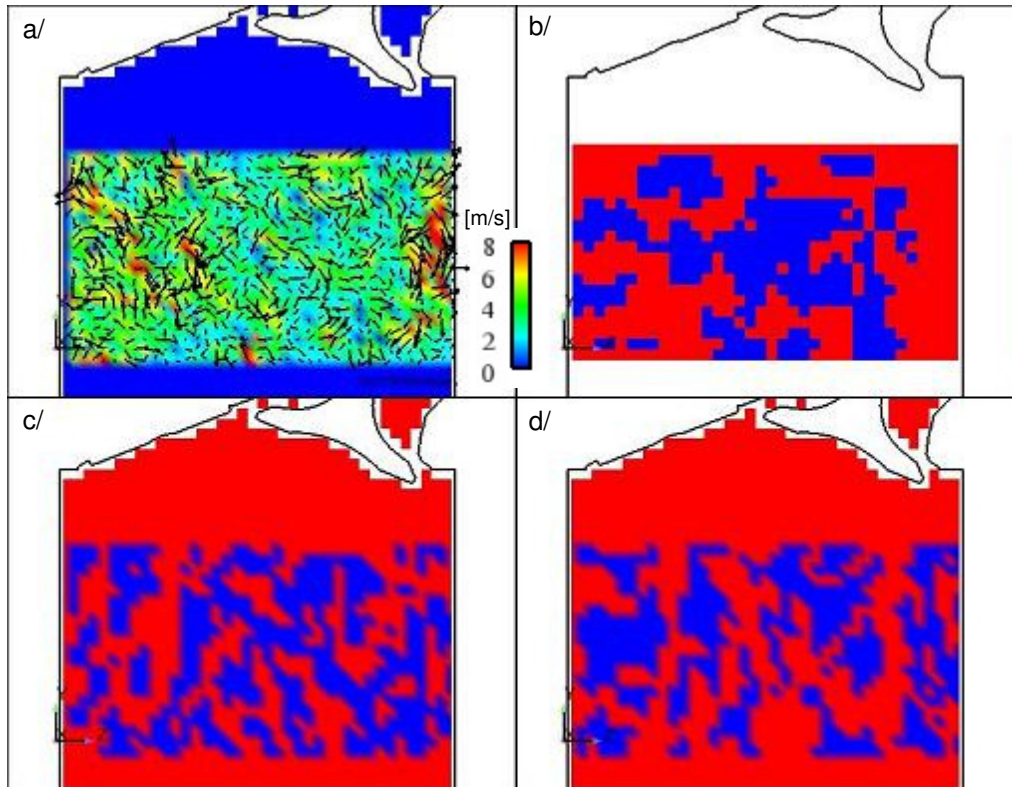


**Figure 5.44:** Example of zero-crossings determination for the Y-velocity component in the Z-direction (case 100C3 and the reconstructed velocity field fluctuating with 1.5kHz) – a/ reconstructed velocity field with vectors; b/ PIV results: sign of the Y-component (red:  $>0$ , blue:  $<0$ ); c/ DES results; d/ SAS results

### 5.6.5.1 Influence of the Post-Processing Resolution on the Resulting Structures Diameter and Count Number

Figure 5.45 hereafter is showing the influence of the spatial resolution of the post-processing window used to compute the number of zero-crossings values and, consequently, its influence on the approximated structures size.

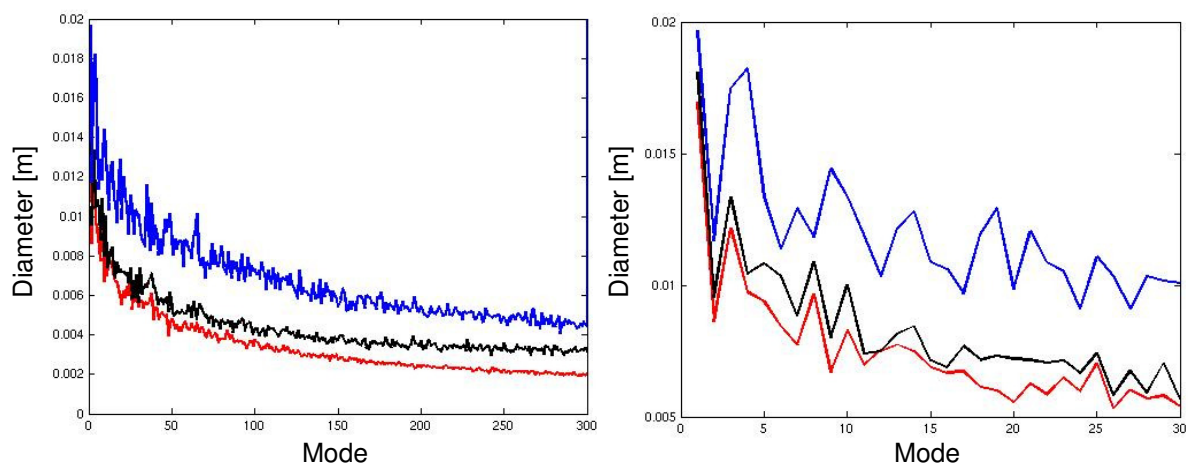


**Figure 5.45:** Influence of the spatial resolution on the zero-crossings computation and consequently, on the structure size – SAS original resolution (red), SAS low resolution (black), and PIV results (blue)

Beside the first few modes, for which the values obtained are almost similar, the diameter computed is directly dependent on the post-processing grid refinement: the finer the resolution is, the higher the number of zero-crossings, and then, the smaller the structures diameter. However, another important information provided here is concerning the presence and the amplitude of oscillations that are of higher intensity for lower resolutions. The fluctuations of the computed diameter over the mean, observed with coarser grids, is an evidence of the systematic error, which is induced by the post-processing domain employed.

In order to insure the consistency of the comparison between the different results, the same treatment will be applied to experimental and numerical data for further investigations.

### 5.6.5.2 Analysis of the Size of the Reconstructed Velocity Fields

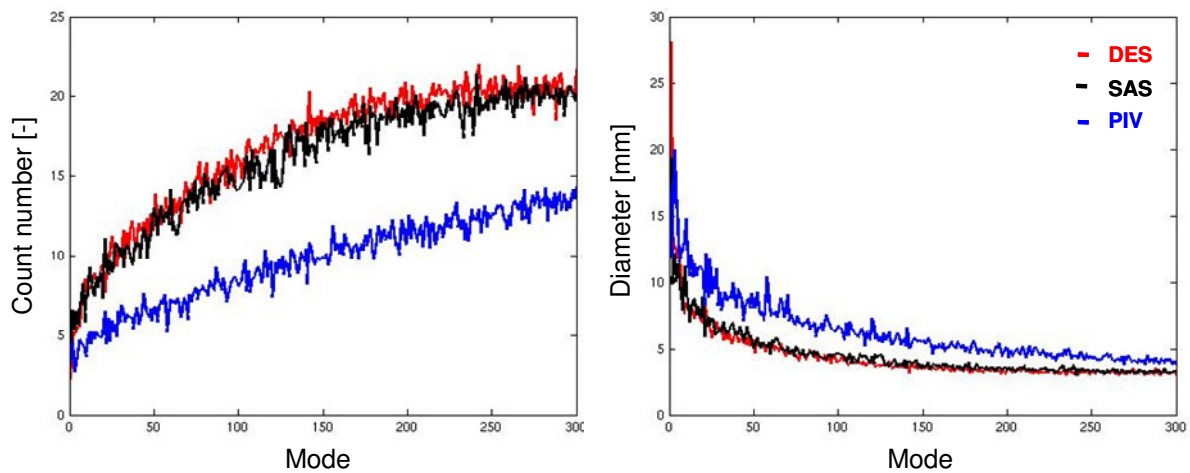


**Figure 5.46:** Comparison of count number of zero-crossings (a) and averaged characteristic length of the structures (b) for the Y velocity component along the Z direction

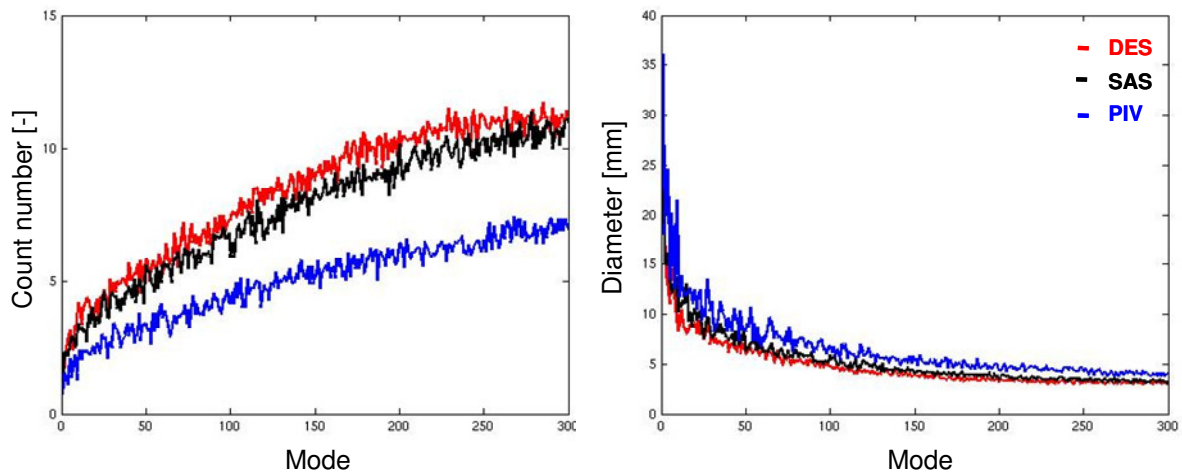


**Figure 5.47:** Comparison of count number of zero-crossings (a) and averaged characteristic length of the structures (b) for the Z velocity component along the Y direction

From the two former figures, a clear trend is made obvious by the comparison of CFD and PIV results. Except for the first mode, where all methods are delivering similar information, the number of vortices found with the numerical results is drastically superior to those resulting from the experimental investigation. Consequently, the structures diameter predicted by CFD will be smaller than the one based on PIV results. Actually, the smallest structures achieved here with

the PIV system are of about 4 mm diameter, which is the maximum resolution reachable with the optical system at stake (see §5.2.1).

On an overall aspect, the number of structures is increasing with the mode level, coinciding with the theory, which says that the most energetic flow structures, i.e. the largest ones, are represented by the lowest modes.

Tables 5-7 and 5-8 thereafter as well as the bar chart in Figure 5.48 are summarizing the different information plotted in Figures 5.46 and 5.47 for the two different spatial components.

**Table 5-7: Comparison of zero-crossings count number statistics**

		<i>Count [-]</i>			
		Min	Max	Mean	RMS
<b>Y-component Z-direction</b>	<b>DES</b>	2.3	22.0	17.0	4.0
	<b>SAS</b>	3.4	21.4	16.3	3.9
	<b>PIV</b>	2.7	15.3	9.9	2.8
<b>Z-component Y-direction</b>	<b>DES</b>	1.0	11.7	8.5	2.5
	<b>SAS</b>	1.1	11.4	7.8	2.4
	<b>PIV</b>	0.8	7.7	5.1	1.6

**Table 5-8: Comparison of approximated structures size**

		<i>Diameter [mm]</i>			
		Min	Max	Mean	RMS
<b>Y-component Z-direction</b>	<b>DES</b>	3.0	28.1	4.3	2.1
	<b>SAS</b>	3.1	19.4	4.4	1.8
	<b>PIV</b>	3.6	19.9	6.1	2.4
<b>Z-component Y-direction</b>	<b>DES</b>	3.0	33.1	4.7	2.6
	<b>SAS</b>	3.1	30.8	5.2	2.8
	<b>PIV</b>	3.6	36.0	6.4	3.5

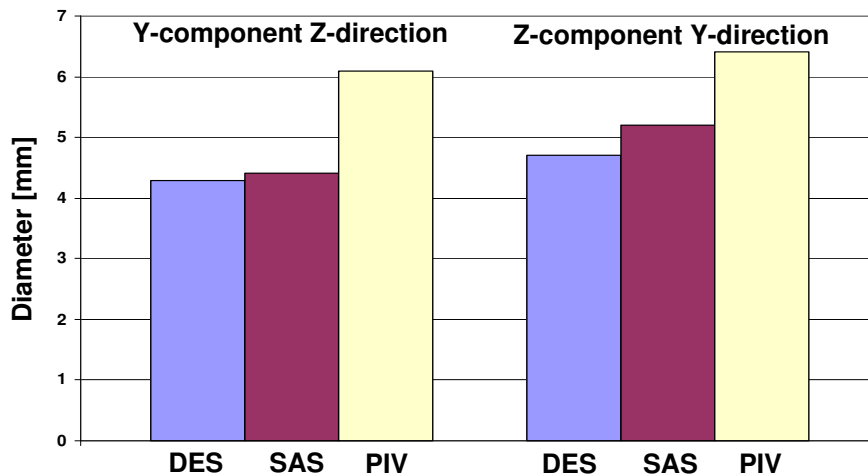


**Figure 5.48: Averaged structures diameter according to the velocity component normal to the direction considered**

The comparison between the structures size obtained for both directions as presented in the bar chart above, reveals a trend about the general geometry of the eddies present in this region of the cylinder and their anisotropic nature. Although the amplitude of the phenomenon is smaller for the PIV results as for the CFD ones, a systematic increase in the average structure diameter can be observed from the Z-direction to the Y-direction diameters for each methods employed (5%, 9% and 18% for PIV, DES and SAS respectively). This implies that the rotating structures have a stretched shape, whose longest dimension is orientated toward the main flow direction (Y-direction, downwards the cylinder).

Considering the spectral analysis conducted earlier on the time coefficients associated to each POD modes (see Figure 5.30), several characteristic frequencies have been highlighted. For the flow conditions considered and detailed here as example, 100 kg/h, 3mm valve-lift, the frequencies found on the POD modes spectrogram are similar to the one found by spectral analysis of the velocity fields in §5.5.1. Thus, some further information on the turbulent structures fluctuating with these frequencies could be gained by computing the size of the structures related to the corresponding modes.

As one can observe in Figure 5.49, which shows the eddies diameter for the DES results (on the “high-resolution” post-processing grid), the mean diameter (2,9mm) of the reconstructed velocity field (red curve), is corresponding to the average diameter of the structures contained in the different modes employed as a basis for this particular reconstruction (blue curve, range 96 → 146, as determined in §5.6.3 and summarized in Table 5-6). It is then possible to assume that there is a direct correlation between the sizes of the structures contained in each mode with the sizes of the turbulent structures effectively present in the flow. Following this assumption, it would be possible to estimate the dimension of the structures fluctuating with a certain frequency by computing the statistics of the POD modes required to reconstruct this field.

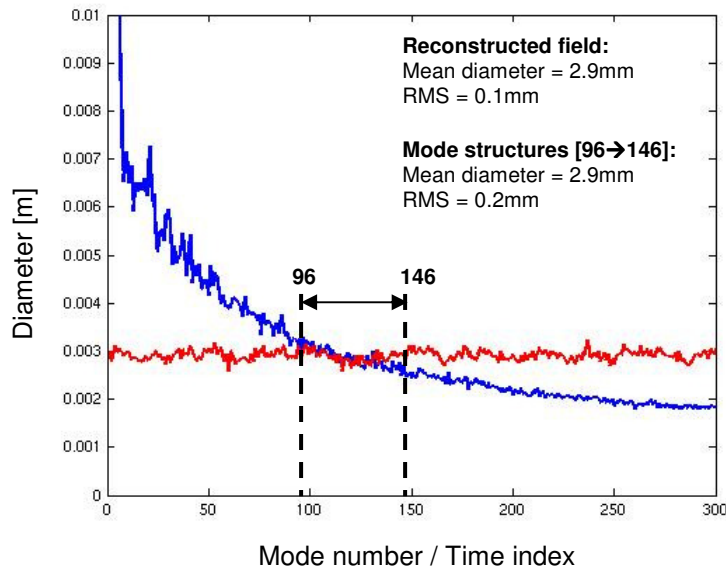


**Figure 5.49: Diameter of turbulent structures reconstructed (red curve) and structures size contained in each mode (blue curve). The X-axis corresponds to the mode number for the blue curve and to the time step for the red curve (time dependant mean diameter).**

In the results presented thereafter, the “low-resolution” grid shown in Figure 5.36 has been used for their post-processing, in order to stay consistent during the comparison between experimental and numerical outcomes. This coarser grid also allows handling the large amount of data generated by the simulation on the original fine mesh, which direct use is not realistic in terms of processing time and memory requirement, as already mentioned earlier (refer to §5.3.2).

The methodology implemented to generate the turbulent structures data gathered in the diagram from Figure 5.50 is following the main steps already described earlier in this chapter. But for a better understanding, the method will be summarized here again.

First of all, the main characteristic frequencies need to be defined thanks to the spectral analysis of the velocity fields from each configuration simulated. The signals used to conduct the FFT are the simulated velocity flow fields extracted from the fluid domain in the valve-plane and the cylinder center plane. The spectra, which are computed on each individual element or node, can be displayed all together as shown in Appendix A.2, and then deliver some valuable information concerning the regions of the flow that are fluctuating with those frequencies. Finding the origin of the fluctuations constitutes the first part of the process, next comes the evaluation of the approximated diameters of the structures present in the reconstructed flow. The modes range that will be employed for the reconstruction is based on the analysis of the POD time coefficients spectrogram, under the same principle as the one described in Figure 5.30. The previously defined frequencies, based on the spectra of original velocity data, serve as references for which to look for. Then a band of modes is filtered out the full set and will represent the range used for the reconstruction of the flow related to a particular frequency. Finally the zero-crossings analysis is conducted in both directions and delivers the average diameter of the vortices associated to this frequency.

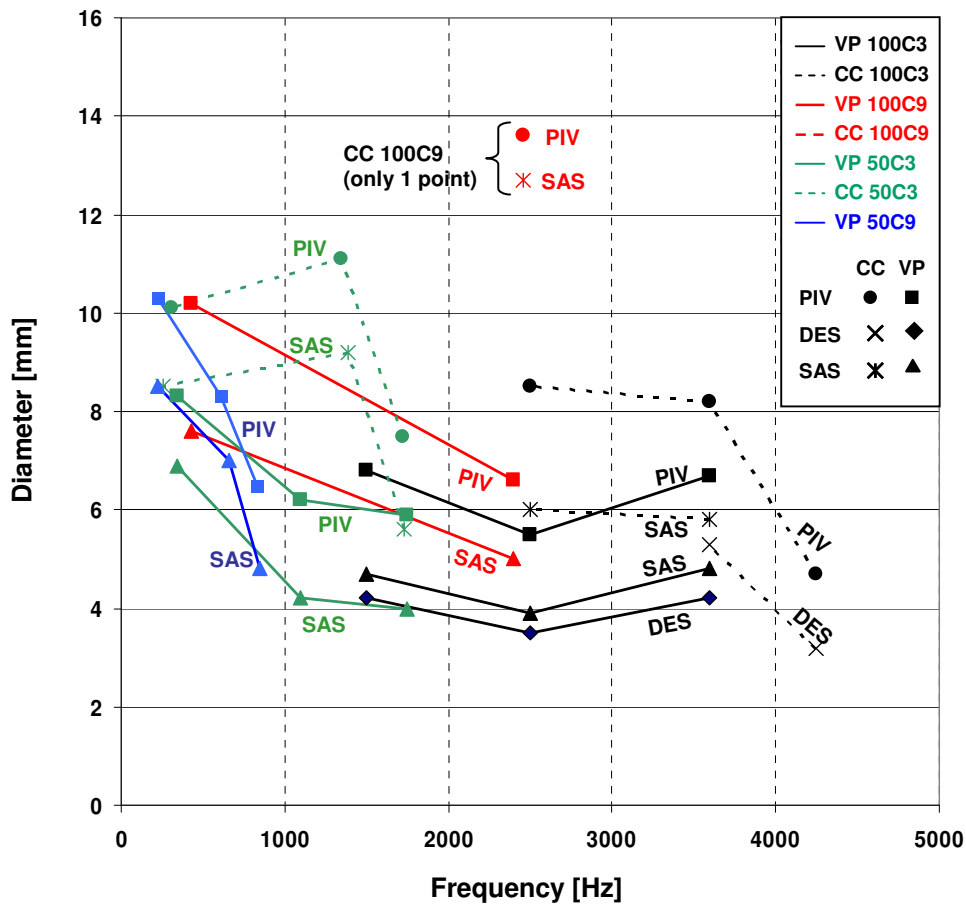


**Figure 5.50: Summary of average structure diameters and their corresponding fluctuation frequency for the four different configurations investigated and the two planes post-processed – Based on the zero-crossings analysis of the Y-component / Z-direction (VP: Valve Plane; CC: Cylinder Center plane; 50kg/h or 100kg/h flow rate; closed flap; 3mm or 9mm valve lift)**

A large amount of information is summarized in Figure 5.50, but the main aspects highlighted here are the relationship between the structures sizes and their associated frequencies, as well as the influence exerted by the diverse mass-flows and valve-lifts on these previously mentioned variables (diameter and frequency).

A curve-to-curve analysis of the previous diagram allows defining the major influence of the respective parameters investigated. First of all, considering the comparison between experimental and numerical results, a clear trend is crystallizing here. Experimental results are evolving parallel to the numerical results, but are always leading to a larger diameter, by about 35%. In the same way, for the only configuration simulated with both turbulence models (100C3), DES has been providing the smallest structures, with an offset of around 12% compared to the SAS results. With regards to the mass-flow, the tendency shows that the higher it is, the smaller the structures will get but their fluctuations occur at a higher frequency then.

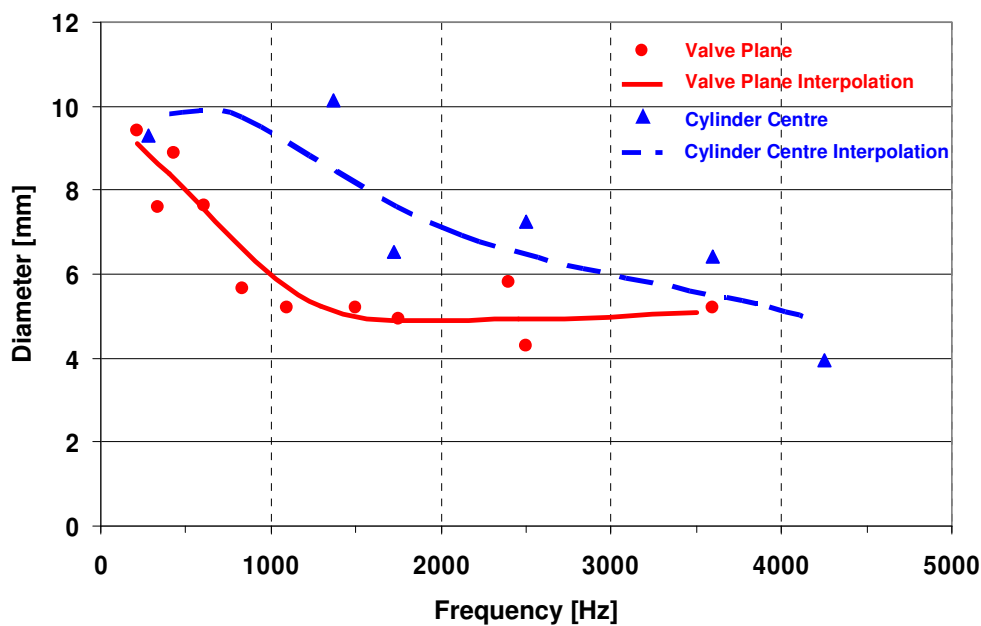
The valve-lifts employed seem to have a similar impact on the structures size, the higher the valve-lift, the larger the structures and the lower the frequencies.

Figure 5.51 thereafter shows the average structure size calculated for each characteristic frequency over the full range, comparing the two different planes studied, i.e. the valve plane and the cylinder centre plane. Here again, the general trend which shows the decrease of vortices diameter with the increasing frequency is standing out against the background. By comparing the interpolated curves for both planes, one can observe that the size of the energetic eddies identified thanks to this method are appreciably smaller in the valve plane than in the cylinder



centre one. For the first plane cited, the turbulence diameter is decreasing very fast over the lower frequency range, up to about 1 kHz, and then stabilizing at a value of about 5 mm until the highest frequencies. In the cylinder centre plane the vortices decreasing rate is steadier but reaching the same average value of approximately 5 mm at the highest frequencies.

Consequently, from this analysis, one can conclude that the structures size, depending on their excitation frequency, is generally not homogeneously distributed in the cylinder. Logically, the vortices induced by the intake port and valves are of a smaller size in the valve plane than in the other parts of the cylinder. However, with respects to the POD decomposition and the level of energy convected by the different eddies classes, it is also interesting to remark that some characteristic frequencies related to a certain modes range and then corresponding to a certain energy level are present in both planes. This is the case of the 5 mm structures fluctuating at frequencies over 3.5 kHz and which could be found in both planes.



**Figure 5.51: Overall comparison of the interpolated results obtained for the structure diameters in the valve plane and in the cylinder central plane**

Another important aspect while looking for the correlations existing between the different parameters investigated is appearing in Table 5-9, with regards to the influence of the mass flow on the resulting frequencies. For example, in the case of a valve-lift set to 3 mm, the division of the mass-flow from a factor 2, from 100 kg/h to 50 kg/h, is also found in the main characteristic frequencies, but not for all of them. Only the two highest frequencies are linearly scaling with this factor, going from 3600 Hz to 1750 Hz and from 2400 Hz to around 1100Hz. However, for the smallest frequency, 1400 Hz and 340 Hz, they are related to each other according to a quadratic relationship, by a factor 4. This major difference can be explained by the nature and the origin of these fluctuations. A first attempt of description of the possible sources of the flow perturbations has been made formerly in paragraph 5.5.1. After reconstruction of the velocity fields in the valve-plane, according to the filtered information based on the spectral analysis results, it appeared that the lowest frequency (around 1500 Hz) seemed to be related to the valve-shaft instabilities. The highest ones, 3600 Hz and 2500 Hz, were respectively thought to correspond to a combination of the instabilities induced by the flow splitter in the port and the clearance generated by the small valve lift for the first one, and to the turbulence provoked by the actuable

flap and other geometric protuberances upstream in the intake port for the second one. These last two phenomena are mainly driven by the general flow characteristics which explain their linear dependence on the mass-flow.

Conversely, the quadratic dependency observed for the valve shaft must be related to the relative complexity of the geometry faced by the flow in this region. As a rough approximation, the shaft is seen by the flow as a slanted cylinder, whose instabilities frequency can be estimated by the Strouhal definition:

$$Sr = f \frac{D}{U}, \quad (5.3)$$

with  $f$  the oscillation frequency,  $D$  the apparent cylinder diameter and  $U$  the mean velocity.

According to the numerous investigations found in the literature (see for example Achenbach [2]), for a Reynolds number smaller than  $3 \cdot 10^5$ , the Strouhal number is independent from  $Re$  and is approximated to a value of 0.2 (in the present case,  $Re_{D_H} \leq 6 \cdot 10^4$ , as shown in §5.2.2). Nevertheless, due to the complexity of the geometry in stake and, consequently, the large number of degrees of freedom existing, it is likely that these two dimensionless numbers are depending from each other. The following linear expression could be one form of the relationship between them:

$$Sr = \alpha Re + \beta \quad (5.4)$$

By substituting  $Sr$  by its definition given in Eq. (5.3), it yields

$$f = \alpha \frac{U^2}{\nu} + \beta \frac{U}{D} \quad (5.5)$$

which means that, in this case, the frequency would be quadratically proportional to the velocity. This assumption is also validated by the results obtained with the two other simulations, with a valve-lift of 9 mm. In this case, the only characteristic frequency observed with a mass flow of 100 kg/h is equal to 2422 Hz whereas the 50 kg/h flow conditions is presenting a frequency of 656 Hz. The quadratic correlation is here again respected, with a small deviation probably related to the influence of the linear term in Eq.5.5

With regards to the influence of the valve-lift, as far as the structures size is concerned, when the valve-lift is increasing the vortices are tending to become larger, as plotted in Figure 5.50. It should be noted that the valve displacements studied here are two extreme values, one being approaching the closing point, the other one being the maximum opening found in a 1.6L FSI® motored engine. As a matter of fact, the turbulent flow induced by this cylinder head and intake port is showing its sensitivity towards the valve position. Between both configurations, the flow topology is relatively different. Indeed, the larger valve-lift is offering less resistance to the flow, yielding a different distribution of the velocities around the shaft, and more particularly, decreasing the flow congestion occurring at the lower valve edge. The combination of all these effects is probably responsible for the drastic change in the characteristic frequencies observed with the 9 mm valve lift. For this last configuration, only one frequency (compared to the three found with the 3 mm valve lift) is revealed by the spectral analysis, at about 2400 Hz with a load of 100 kg/h and 650 Hz for 50 kg/h. The location of the frequency peaks within the geometry lets suppose that these fluctuations are partially taking their origin from the intake port since they occur over the flow splitter, but also that they may be reinforced by the passage through the shaft. This would also coincide with the former observation made during the mass flow influence

analysis, where the quadratic dependency of the frequency on the velocity has been highlighted, calling for a cylinder-induced oscillation.

**Table 5-9: Summary of main characteristic frequencies observed for each investigated cases – SAS Valve-plane**

<b>SAS Valve-Plane</b>			
	<b>100C3</b>	<b>50C3</b>	<b>Ratio</b>
<b>Frequency [Hz]</b>	3594	1750	~2
	2539	1094	~2.3
	1406	344	~4
	<b>100C9</b>	<b>50C9</b>	<b>Ratio</b>
	2422	656	~3.7

In addition to the ability of generating a low dimensional basis to describe complex turbulent flows, Proper Orthogonal Decomposition is offering the potential to transform the usual intuitive impression resulting from visual inspection of the velocity field into a quantitative form. This has been achieved by computing the zero-crossings of some specific velocity components along a certain direction. Therefore interesting data for comparison analysis between experimental and numerical outcomes such as the turbulent structures dimension found in both reconstructed fields and single POD modes could thus be delivered.

Nevertheless, the clear restriction of the exploitable post-processing window size corresponding to the optical measurements area is drastically reducing the amount of information that can be taken out of the flow thanks to the almost unlimited CFD outcomes. In order to take the maximum benefit from the high-resolution simulations results, further flow analyses such as structures visualization have been conducted and are presented thereafter.

## 5.7 Visualization of Turbulent Structures

### 5.7.1 3-D Visualization

According to the preliminary studies results showed in the former chapters 3 and 4, iso-surfaces of the second invariant of the velocity gradient tensor,  $Q$ , are offering a convenient way of representing vortical regions developing in the turbulent flow. This criterion has been employed here again for the qualitative level of information provided for 3D structures visualization.

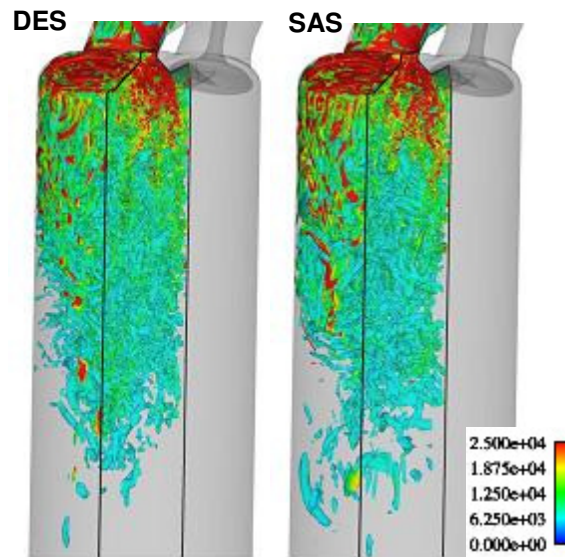


**Figure 5.52: 3D visualization of turbulent structures – half-section of an isosurface of positive  $Q$  ( $Q = 7e+06s^{-2}$ ) shaded with the vorticity**

Figure 5.52 shows an example of vortices visualization, representing the surface of a constant value of  $Q$  inside the cylinder being investigated. Both numerical models are depicting similar results, presenting relatively fine structures similar to hairpins developing, stretching and then breaking down later in the cylinder. This information is of first interest since it proves the ability of the SAS method enabling the flow fluctuations to develop with a LES-like resolution of the turbulence. On the other hand, although this representation depicts the 3-dimensional nature of the structures and their orientation in the geometry considered, it is rather difficult here to quantitatively differentiate both turbulence models.

### 5.7.2 Turbulence Models Comparison

An interesting evaluation parameter to differentiate the two different models is the actual turbulence length scale resolved by the different models. This turbulence length scale reads (see §3.2.5):

$$L_t = \frac{\sqrt{k}}{c_\mu^{1/4} \omega} \quad (5.6)$$

This length scale corresponds to the smallest structures resolved by the turbulence model. Figure 5.53 shows the evolution of this variable (normalized with the local mesh length scale,  $\Delta$ ) within the cylinder in a valve plane, and gives a comparison between the two different models at stake. According to previous studies of the turbulence energy spectrum resolution for isotropic

decaying turbulence, the same analysis of the length scale has proven that for a ratio under 0.2, most of the energetic eddies are properly resolved [91]. In the present case, both models are presenting a resolved turbulence length scale ratio located around this value of 0.2, attesting their global quality and their relevance. However, the DES model shows a more homogeneous distribution of this parameter throughout the complete field considered here, whereas the SAS method has some higher peaks in particular regions. This last observation leads to the assumption that the DES model should offer a slightly better resolution of the turbulent structures.

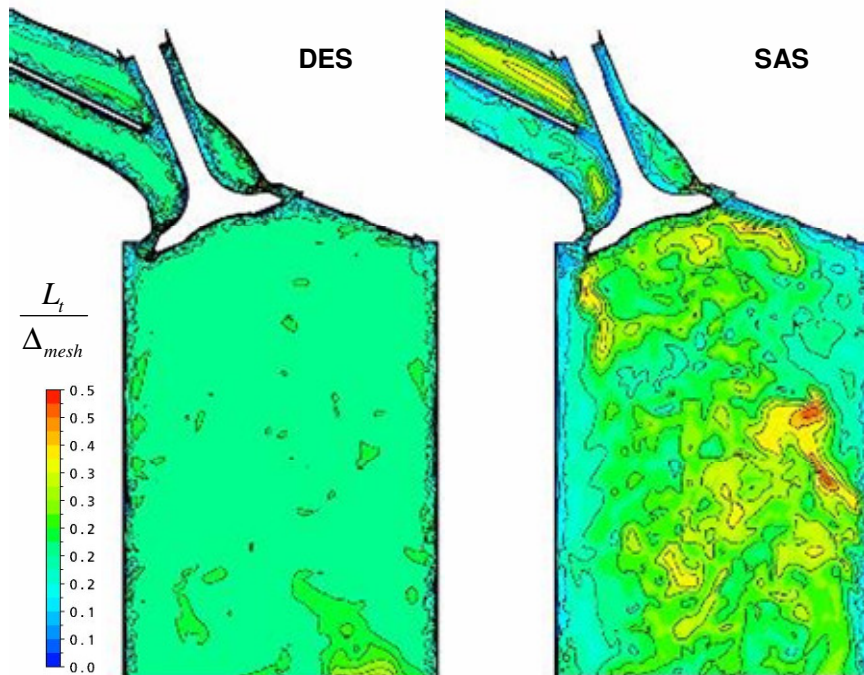


**Figure 5.53: Ratio between the smallest turbulent structures resolved by the two different turbulence models and the local mesh length scale**

The former observation is also supported by considering the ratio between the resolved part and the total amount of turbulent kinetic energy. The last term is basically the sum of the modeled energy and the resolved one. Indeed, the solver used for the simulation is delivering the required information concerning the statistical Reynolds stress computed for each velocity component, allowing determining the resolved part of the turbulent kinetic energy. Figure 5.54 thereafter is showing the distribution of this ratio within the cylinder, giving a clear and direct comparison mean between both numerical models. According to this analysis, the DES simulation based on the fine resolved mesh described earlier is solving above 90% of the turbulent kinetic energy and even reaching 100% in broad flow regions downstream of the valves. This proves the quality of the mesh employed and the efficiency of the zonal treatment implemented here, shifting very fast from a RANS formulation in the wall vicinity to a traditional LES formulation in the free stream flow. On the other hand, the URANS derivative method is also solving a large amount of the total turbulent kinetic energy. Although SAS results are not reaching the same level of resolution as DES, an average of about 75% to 80% is obtained throughout the full domain.

With regard to these two comparisons, both models are expected to deliver reliable information about the turbulent structures present in the flow. The methods employed to visualize the instabilities developing in the cylinder head will either confirm or invalidate the slight discrepancy observed in this paragraph.

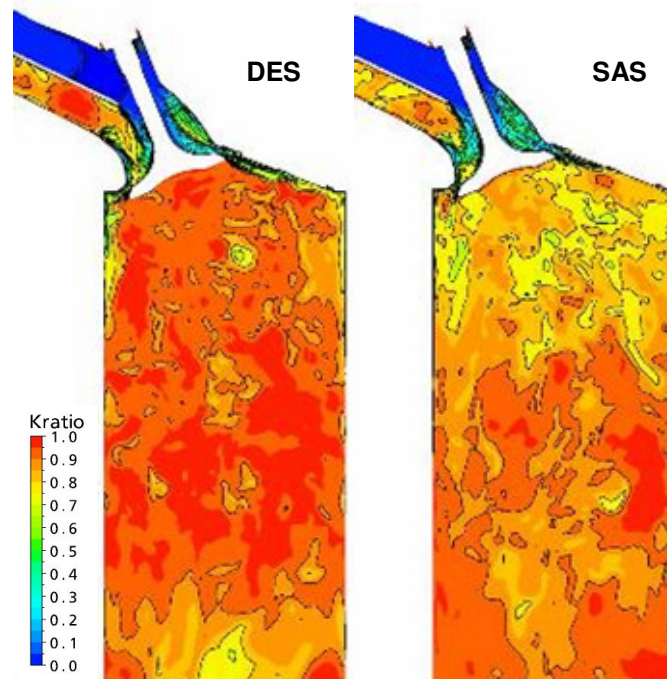


**Figure 5.54: Comparison of the ratio between the turbulent kinetic energy resolved and the total amount of this value**

### 5.7.3 2-D Visualization and Quantification of the Turbulent Structures

For a detailed and more quantitative insight into the turbulent structures, another method also based on the invariant of the velocity tensor,  $Q$ , is being investigated. For in-cylinder flows, and more particularly in DISI engines, a major issue is the generation of the appropriate mixing of air and fuel, to obtain an ignitable mixture at the right position. This implies that the development of turbulence has to take place very fast in the upper part of the cylinder, around the spark plug vicinity.

By considering different section planes of the previously mentioned  $Q$  iso-volume at various distances from the cylinder ceiling, it would be possible to study the distribution of turbulent structures. This distribution is realized in analogy with the droplets size distribution in a two-phase flow. In the present case, the sizes of the 2-D structures obtained on each horizontal cylinder cross-sections are characterized by an equivalent radius. Despite the restrictions related to a circular approximation of the real complex 3-dimensional geometry of the structures, this approach is offering interesting statistics about the turbulence in cylinders and needs to be considered.

On Figure 5.55 thereafter, the position of the different planes selected to analyze the distribution of the turbulent structures is presented. The first qualitative impression given by these 2-D structures is supporting the fact that the largest structures, containing the highest amount of vorticity, are concentrated in the upper part of the cylinder before decaying as they travel downward to the bottom of the geometry.

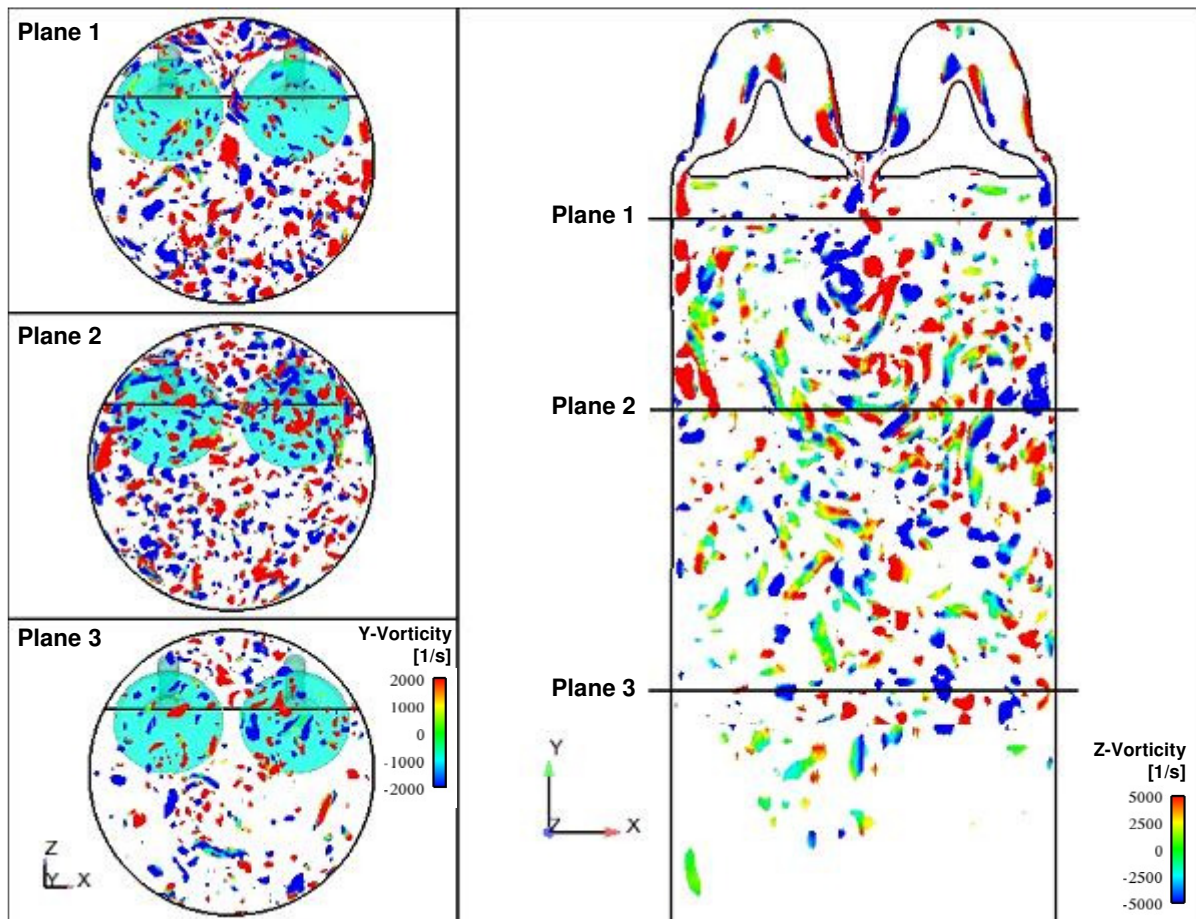


**Figure 5.55: Different section views of the isovolume of  $Q$ , representing the development of the turbulent structures within the cylinder, colored with the vorticity**

Besides the location and the size of the structures drawn by the intersection between the  $Q$ -isovolume and the planes, interesting information is provided by the color map employed, ranging from blue to red for the extreme negative and positive values of the vorticity. Therefore it is also possible to recognize the rotating direction of the eddies, and then the interaction between the flow and the geometric obstacles met within the engine port. For example, the contra-rotating structures developing between the two valves where the jets are crossing each other is very clear, with an alternation of positive and negative vortices (the sign is relative to the direct orientation of the coordinates system).

The value of the  $Q$ -invariant chosen earlier for the turbulence visualization is not arbitrary, but is based on the distribution of the parameter in the planes of interest. Figure 5.56 is showing the distribution of  $Q$  along two perpendicular profiles at three different levels in the cylinder (planes 1, 2 and 3 as defined in Figure 5.55). The two profiles are then plotted together as a function of the cylinder position and superimposed with the threshold defined by the criterion selected, here  $Q = 7e06 \text{ s}^{-2}$  (also written  $Q_c$ ). This value, corresponding to the filter employed to distinguish the core of the turbulence, allows the detection of isolated peaks of  $Q$ . The quantitative analysis and the control of the relevance of this criterion can be done by studying the cumulative probability function of  $Q$  as depicted in Figures 5.57 and 5.58. Some statistics about the distribution of  $Q$  have been summarized in Table 5.10, such as the maximum value of  $Q$ , and the percentage of distribution contained over different thresholds defined.

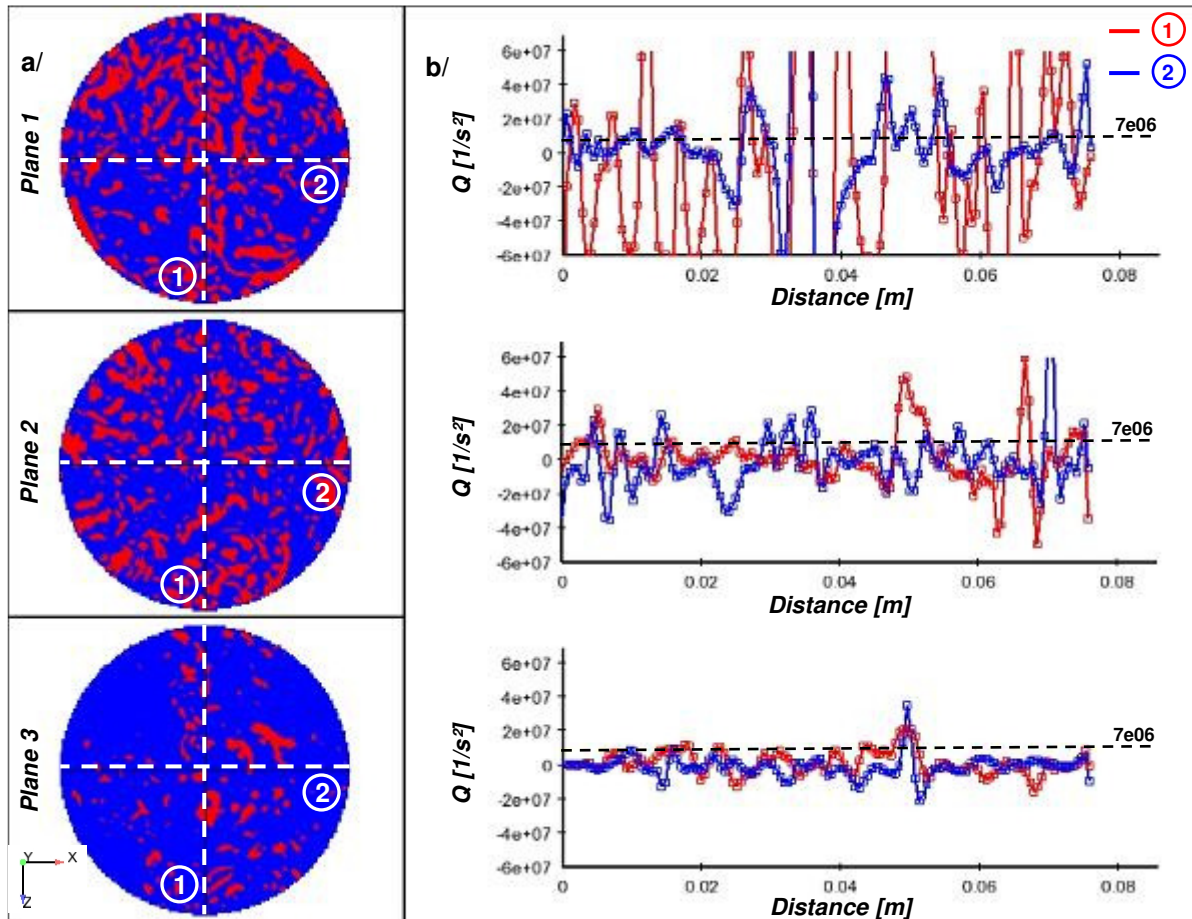


Figure 5.56: Instantaneous representation of the global  $Q$  invariant parameter distribution along two perpendicular directions of the cylinder. a/ Section cuts showing the two axis and the intersection area with the  $Q$ -isovolume ( $Q = 7e06 \text{ s}^{-2}$ ); b/  $Q$  distribution along the two axis defined in a/

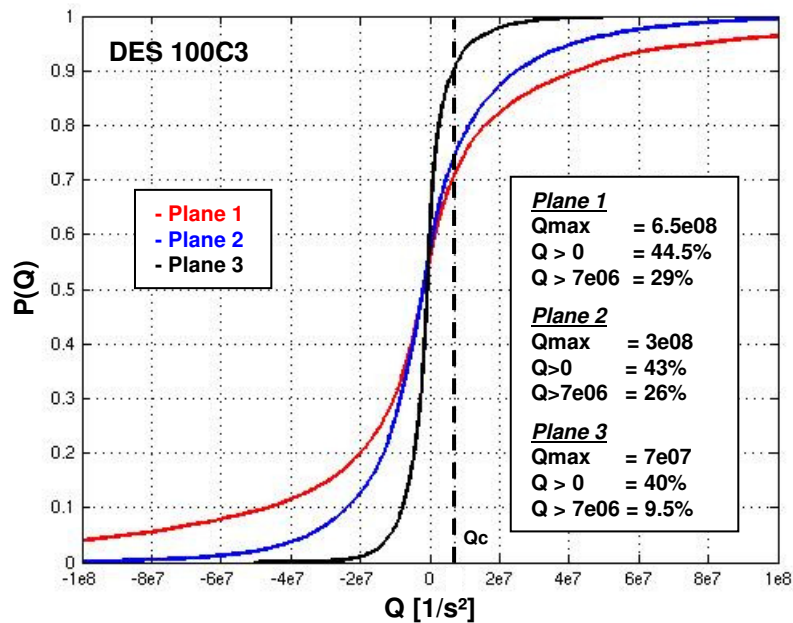


Figure 5.57: Probability function of the  $Q$  invariant calculated on each post-processing planes for the DES 100C3 simulation results (where  $Q_c$  is the criterion –  $Q_c = 7e06 \text{ s}^{-2}$ )



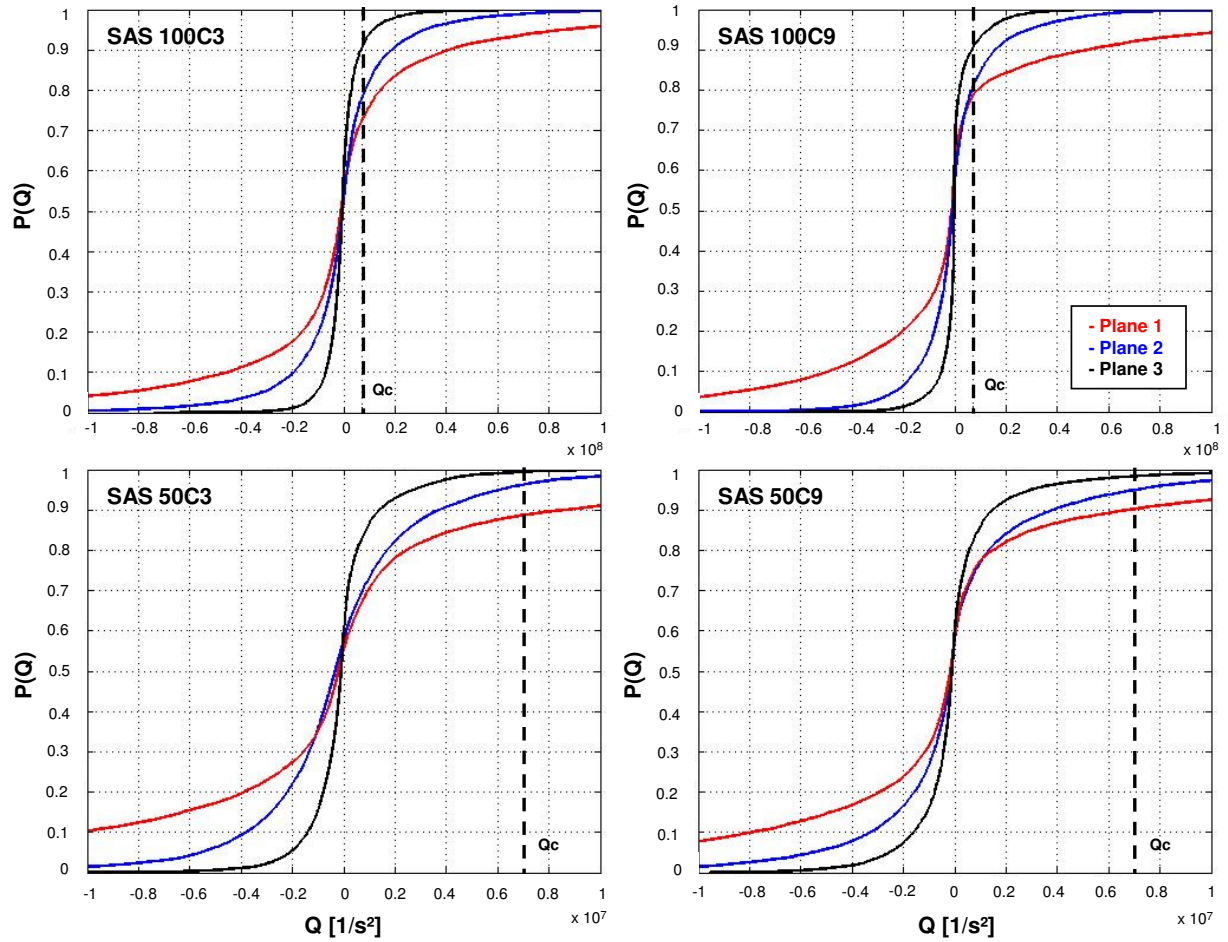


Figure 5.58: Probability function of the Q invariant calculated on each post-processing planes for the different SAS simulations (mass flow: 100 and 50 kg/h; valve-lift: 3 and 9 mm;  $Q_c = 7e06 \text{ s}^{-2}$ )

Table 5-10: Summary of the global distribution and extreme values of the variable Q according to different criteria on every post-processing plane (SAS results)

<i>Plane 1</i>					
		100C3	100C9	50C3	50C9
<b>Q max</b>	[1/s <sup>2</sup> ]	6.5e08	6.0e8	2.2e08	2.0e08
<b>Q &gt; 0</b>	[%]	47	40	44.5	42
<b>Q &gt; 7e06</b>	[%]	27.5	21.5	11.5	10

<i>Plane 2</i>					
		100C3	100C9	50C3	50C9
<b>Q max</b>	[1/s <sup>2</sup> ]	2.6e08	3.0e08	3.5e07	6.0e07
<b>Q &gt; 0</b>	[%]	45.5	43.5	42.5	42.5
<b>Q &gt; 7e06</b>	[%]	22	19.5	4	5

<i>Plane 3</i>					
		100C3	100C9	50C3	50C9
<b>Q max</b>	[1/s <sup>2</sup> ]	1.2e08	9.0e07	2.0e07	2.7e07
<b>Q &gt; 0</b>	[%]	42	38.5	40.5	40.5
<b>Q &gt; 7e06</b>	[%]	9.5	9.5	1	1.5

The DES and SAS results obtained with a mass-flow of 100 kg/h and a valve lift of 3 mm have been used as reference to set the value of the  $Q$  criterion. As it can be observed from the probability functions represented in Figures 5.57 and 5.58, according to the criterion chosen ( $Q = 7e06 \text{ s}^{-2}$ ), the peaks identified are containing about 30% of the total distribution of  $Q$  in the first plane, decreasing to nearly 10% in the lowest plane. The study of the relation existing between the threshold value and the quantity and width of the truncated peaks has shown that the position of the intersection point between the vertical line corresponding to the  $Q$ -criterion and the probability function is a determining factor. For positive values of  $Q$ , as long as this intersection is located in the region of high gradient of probability, the overall number of peaks is staying rather constant, while the size of the structures is decreasing relatively fast. Above a certain value, depending on the flow conditions, the gradient of the curve is approaching zero (the probability function approaching the horizontal). For a criterion chosen in this domain, the number of peaks is falling rapidly.

Thus, in the present case, under the flow conditions given, the criterion employed is crossing the curve of the probability function in the first region, allowing to take into account the maximum number of independent peaks, showing the highest amplitude.

For consistency reasons, during the comparison between the different cases, this legitimate value for  $Q$  has been kept constant all along the study, even for the 50 kg/h case. However, for this last condition, the smaller mass-flow induces a lower turbulence intensity, which implies a lower order of magnitude for the variables at stake during the computation of the  $Q$ -invariant. Thus, following the same logic as the one described above, the total number of structures identified will sink drastically as it can be observed in Figure 5.58 for SAS 50C3 and SAS 50C9. Indeed, one can observe on this graph that the criterion defined for the higher flow-rate is intersecting the probability function of  $Q$  much higher. This observation is confirmed while considering the information summarized in Table 5-10, where the residual probability of  $Q$  left over the criterion is only of about 10% in the first plane, this value decreasing to as few as 1% in the lowest plane.

The following figure, Figure 5.59, shows the superimposition of the probability functions resulting from the analysis of the different SAS simulations. According to this representation of the results, it is possible to draw some conclusions regarding the physics of the process.

First of all it is very interesting to remark that none of the probability functions of all cases depicted here are centered on 0, but  $P(Q) = 0.5$  is rather shifted towards the negative values of  $Q$  (refer to the table in Figure 5.57 and Table 5-10:  $P(Q > 0)$  is always smaller than 50%). Based on the definition of this variable, this implies that the flows (under the different conditions applied) developing within the cylinder are mainly driven by shear effects instead of vorticity (see §3.3.2.3). This underlines once again the importance of the accurate treatment of the different flow regions concerned by these high shear effects, such as the wake of the valves or any other geometrical obstacles.

On the other hand, the influence of the valve-lift is also made obvious from the actual analysis: the higher the valve-lift, the faster  $P(Q)$  is converging ( $P(Q) \rightarrow 1$ ). This influences directly the maximum amplitude of the  $Q$  variable, as well as its distribution. A higher valve-lift implies a lower value of  $Q$ , which means that the shear effects and then, the overall turbulence intensity, are decreasing. As a further consequence, eddies present in the flow are dissipating or shedding faster than the ones induced by smaller valve displacements.

The opposite effect can be observed with regards to the influence of the mass-flow on the  $Q$ -invariant: the lower the mass-flow, the faster  $P(Q)$  is converging ( $P(Q) \rightarrow 1$ ), and then the faster the turbulent structures are decaying in the flow.

All the qualitative trends described in this paragraph have to be quantified now, in order to better characterize the development and shedding process taking place within the cylinder of the particular engine type considered here.

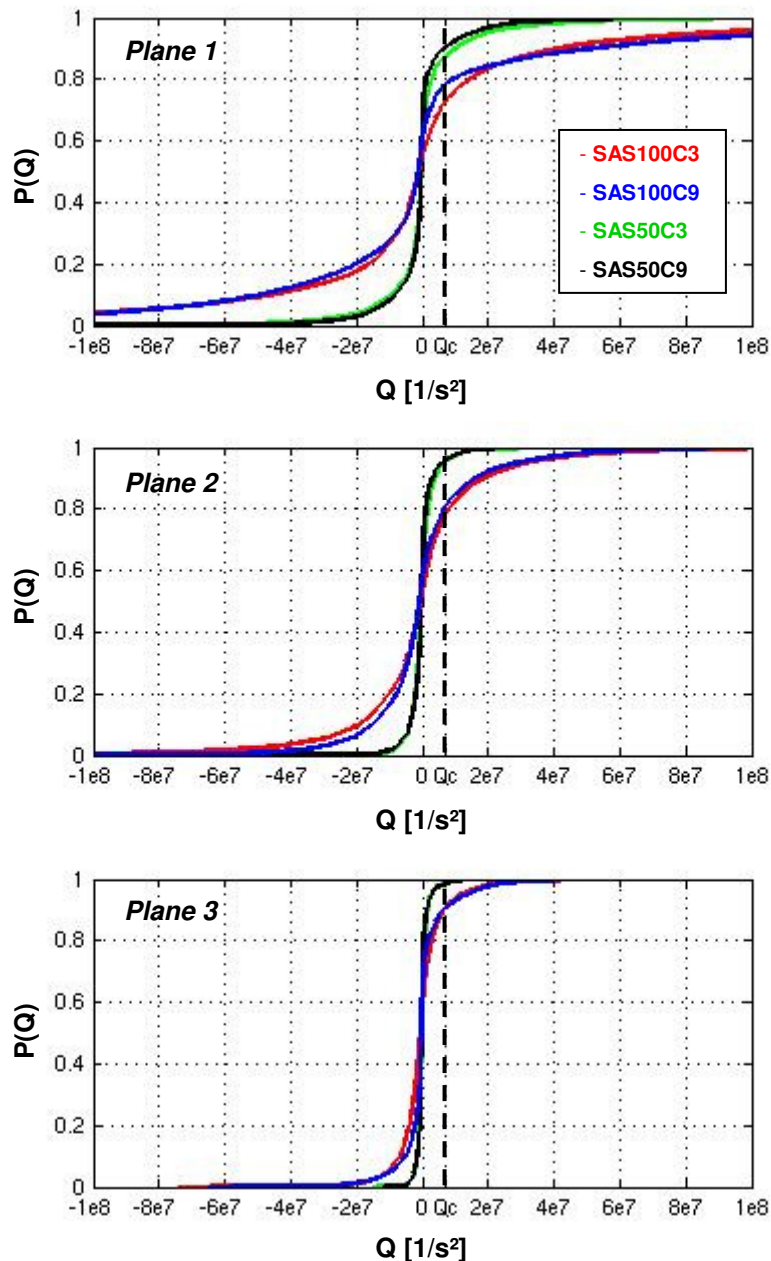


**Figure 5.59:** Superimposition of the probability function of the  $Q$ -invariant for the four different SAS simulations on each horizontal cylinder cross-sections

After having presented and justified the selection of the  $Q$ -invariant criterion, the quantitative description of the vortices based on the circular approximation mentioned earlier can be carried out. For this purpose, the distribution of the turbulent structures in the three different planes (see Figure 5.55) will be realized according to their equivalent radius. This radius is derived from the cross-sectional area formed by the intersection between the plane of interest and the previously defined  $Q$  iso-surface (2D structures displayed in Figure 5.55 planes 1, 2 and 3).

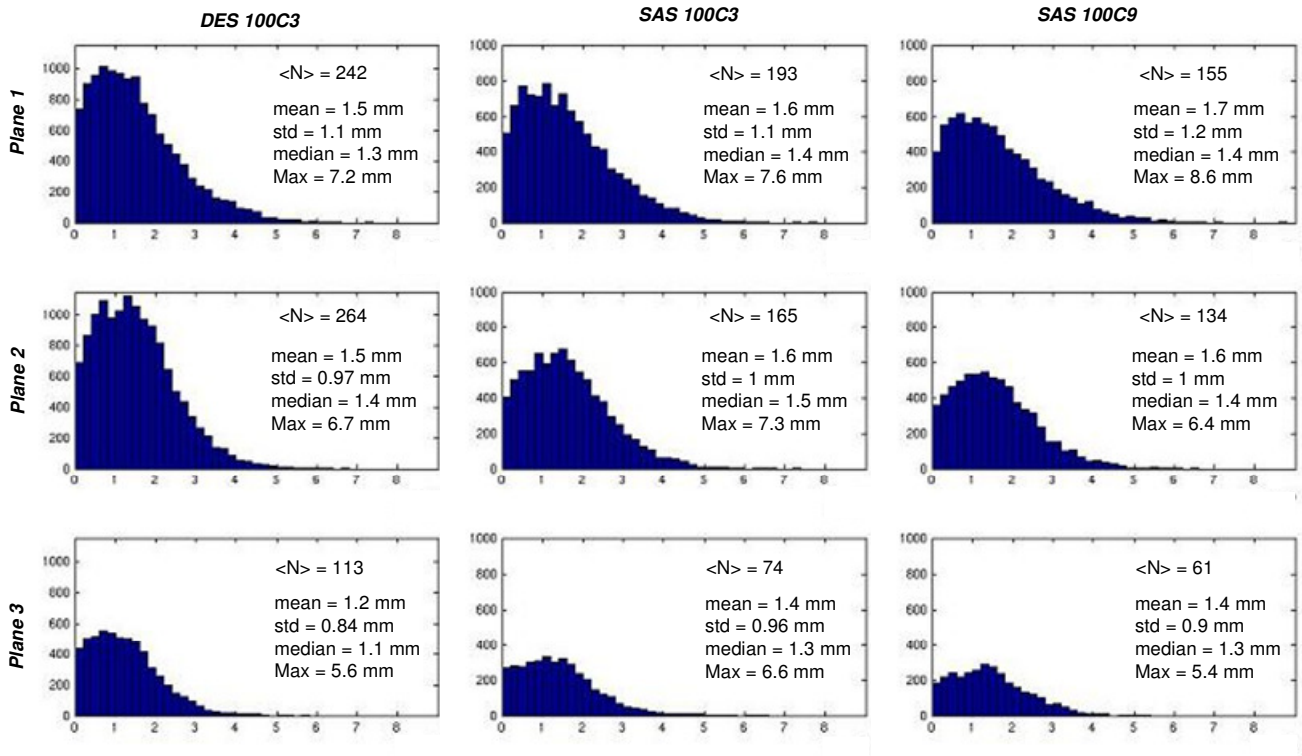


**Figure 5.60:** Distribution of the approximate radius of the 2-D turbulent structures defined by the selected range of  $Q$  – Mass flow = 100 kg/h (X-axis: radius [mm], Y-axis: count number [-])

A rather exhaustive mapping of the structures can be drawn such as the histograms plotted on Figure 5.60. Three different simulation results are presented, the two first ones are the DES and SAS used earlier with a 3mm valve-lift, the last one is a SAS simulation with a higher valve-lift (9mm). Different aspects of the structures statistics must be highlighted here, as they are displayed on the graph. First of all, the total number  $N$  of areas found on the surface and its mean value  $\langle N \rangle$  must be commented. These quantities give information about the development and the decay of the structures according to their distance to the valves. It has to be noticed that DES is offering the greatest number of turbulent structures and secondly that this number is increasing between plane 1 and plane 2 corresponding to a break-up of the former structures. While comparing the other details like the median, mean, max or standard deviation values different trends are becoming evident. First of all between DES and SAS (3 mm valve-lift), beside the number of structures solved by the different models, the distribution is also slightly different. For the DES results, the distribution is narrower, more concentrated around its mean value and the structures are generally smaller. Although the mean values are not very far from each other (1.5 mm for DES against 1.6 mm for SAS), the median presents a bigger discrepancy, showing that half of the resolved structures are below 1.3 mm for DES and 1.5 mm for SAS. Between the two different SAS simulations, the effect of the valve-lift is mostly acting on the

total number of structures obtained. These structures are getting a little larger as the valve-lift increases, but the general shape of the distribution is very similar.

The same tendency is emerging from the observation of the two other SAS simulations in Figure 5.61, based on a smaller mass-flow of 50 kg/h. At first, the average number of independent structures identified is of another order of magnitude, much smaller than the ones obtained above. This aspect is directly related to the selection of a unique  $Q$ -criterion for all cases investigated in order to guarantee the consistency of the analysis and to maintain the possibility to compare their respective distributions on a common basis.

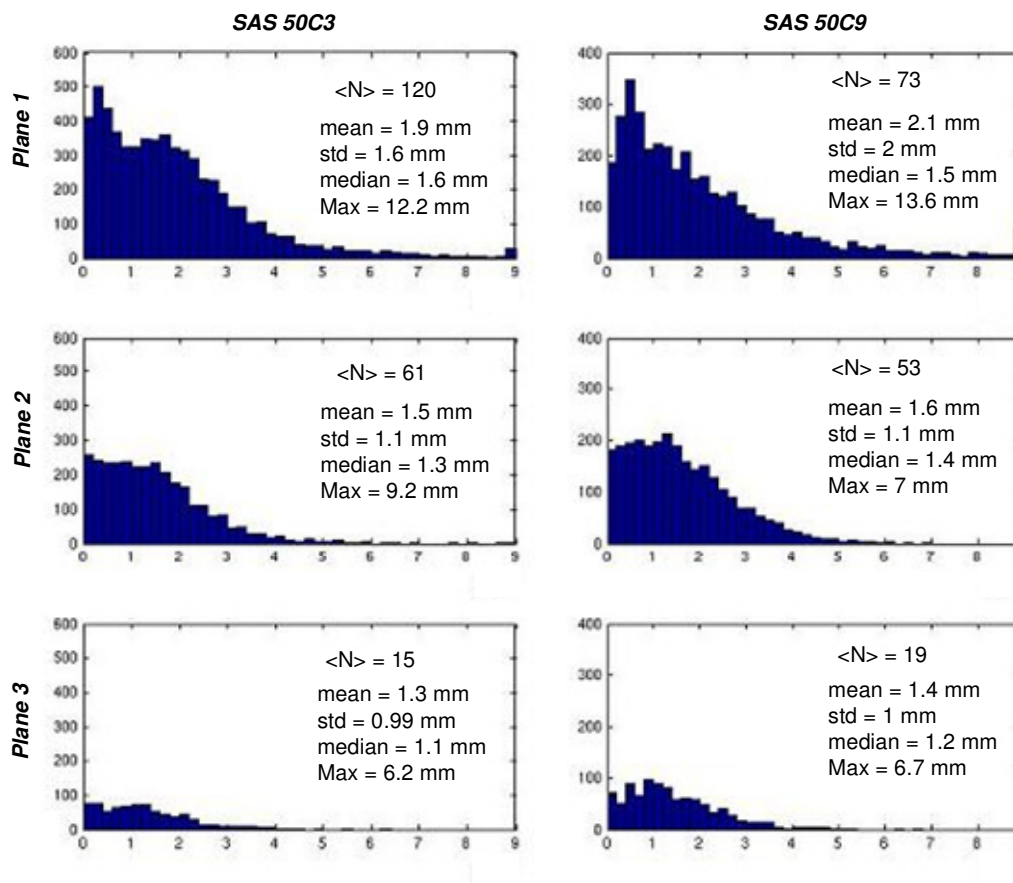


**Figure 5.61: Distribution of the approximated radius of the 2-D turbulent structures defined by the selected range of  $Q$  – Mass flow = 50 kg/h (X-axis: radius [mm], Y-axis: count number [-])**

For both simulation results displayed in the diagram above, the higher the distance from the intake valves, the smaller the structures mean diameters; the same effect being observable with the valve displacement. Indeed, the turbulent eddies size is decreasing with the valve lift.

Thanks to these two last simulations, the influence of the mass-flow can also be described. However, the difference existing between the results is not constant but depends on the distance to the intake valves. In plane 1, the equivalent radius of the structures computed for a mass-flow of 50 kg/h is about 20% larger than the one obtained for 100 kg/h. In plane 2 this offset is falling to 3% and in plane 3 both cases are providing similar results.

The forthcoming analysis of the normalized distribution of the vortices characteristic length will allow a direct comparison between the global shapes of all simulation results available.

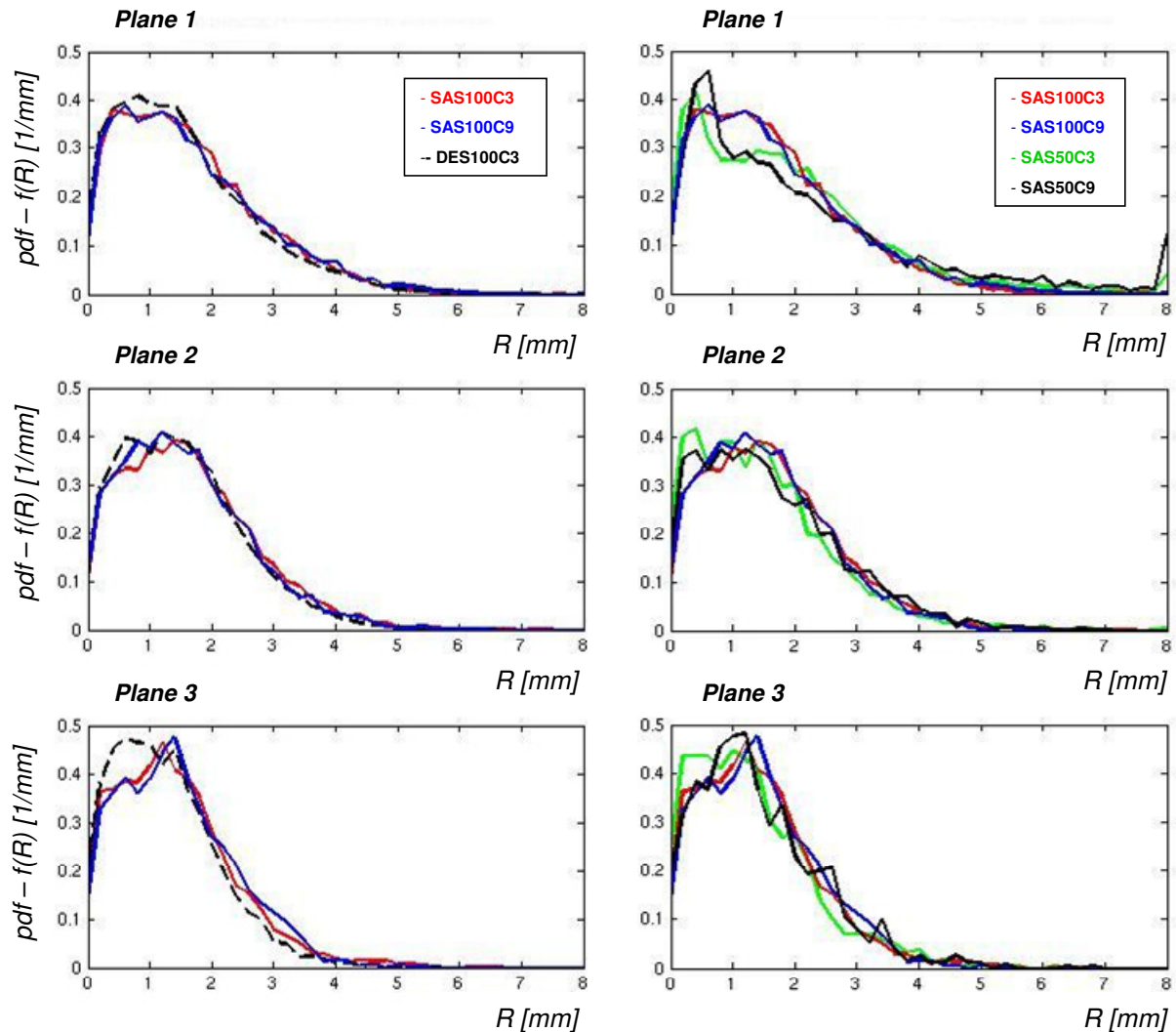


**Figure 5.62: Normalized distribution of the turbulent structures according to the  $Q$ -factor definition**

On Figure 5.62, the normalized distribution functions obtained with the different numerical methods and settings are superimposed.

In the left column of the graph, where the DES and SAS results with 100 kg/h mass-flow are compared, the similarity between the distributions of the two SAS simulations is obvious, whereas DES is showing a little difference. This last one is generally rounder at his maximum position but decreases rather fast in contrast with the two others. More generally speaking, all results are in a good agreement with regards to the global narrowing trend of the distribution as the structures are moving downward the cylinder.

In the right hand side of the previous graph, the four different SAS simulations are compared together. Although the trend observed before with the narrowing of the distribution away from the intake valves is verified, the shape of the normalized curves obtained with 50 kg/h in the first two planes are differing from the 100 kg/h results. Even if the mean diameter found with the lowest mass-flow was smaller than the one computed with the highest mass-flow, an outstanding

peak is appearing at a diameter of about 0.5 mm for both SAS 50C3 and SAS 50C9 results. This information is corroborating the high standard deviation observed during the distribution of the radius on the bar-charts in Figure 5.61. For both SAS simulations run with a mass-flow of 50kg/h, the standard deviation was of the same amplitude as the mean diameter itself, a proof of the data scattering.

Assuming that this characteristic of turbulence through the representation of the vortices normalized distribution could be a major factor of evaluation for the performance and quality of an intake-port, a proper mathematical model describing and predicting the distribution as a function of the different influent parameters would be of high interest. The description by such a universal model could help to understand the level of complexity of the system by defining the number of degrees of freedom required to describe the phenomena at stake. For example, the 100kg/h case seems to follow a simpler distribution law than the 50kg/h one. In the last case, the presence of several peaks in its distribution is significant from a more complex situation where more than just one parameter is necessary to accurately model the physics. However, to develop such a model that could determine the turbulent structures size distribution of any flow and geometrical conditions, some more investigations are required in order to get sufficient information or statistics concerning the physical properties and interdependence of the influent parameters.

To start with, the validation of the former results presented in Figure 5.62 is imperative. Unfortunately, the comparison with the measurement data could not be carried out since the computation of the  $Q$ -factor requires the calculation of velocity gradients. This last operation is only feasible if a certain spatial resolution is achieved, and, for the PIV measurements presented in this study, the focus has been set on the time-resolution and a compromise had to be made at the disadvantage of the spatial resolution. At this stage, some complementary measurements should be necessary to ensure the quality of the required gradient computation, and then to be able to conclude about the reliability of the numerical results shown here.

As far as the turbulence models are concerned, and as interpretation of the discrepancy observed between DES and SAS results, once again, without any validation data, it is rather difficult to assert that one is more accurate than the other. However, based on the former observations as well as on the resolved turbulence length scales presented in Figure 5.53, it can be assumed cautiously that the hybrid turbulence model, DES, enables a better resolution of the turbulence spectrum developing in the flow, taking into account a greater range of structures as well as their breakup and decay process.

More generally, for both models, the high level of spatial resolution obtained in the results has to be counterbalanced by the extremely high computational time required to reach it. For the present case almost six weeks on 32 CPU's are necessary to compute 5000 time steps with the mesh considered, generating hundreds of gigabytes of data. This would represent another limiting factor or at least a strong issue for the parametric study required to determine the universal mathematical model desired.

In the future, studies on coarser meshes and with higher time steps should be conducted to investigate the potential of obtaining sufficiently accurate results with reduced numerical effort. In this particular case, the SAS model should show its potential and its advantage on the DES method, which is much more dependent on these two parameters.





## 6 Summary & Conclusions

Gasoline direct-injection (GDI) technology and more particularly the stratified-charge combustion technique have the potential to provide significant improvements in fuel efficiency and thus to fulfil the need for further reductions in consumption and carbon dioxide emissions. However, this technology is facing some issues, since cyclic variations can occur under certain running conditions, especially in stratified mode. Indeed, one of the primary challenges with GDI engine design is to understand the mixing process taking place within the cylinder in order to better predict and control the undesirable fluctuations.

The present study investigates the origin of those fluctuations by analysing the turbulent cold airflow induced by the intake port and cylinder head of a direct injection spark ignition engine. The main focus of this study has been placed in the foundation of a universal post-processing method in order to facilitate the visualization and the quantification of the turbulent phenomena occurring in port and engine flows. The gradually increasing complexity of the experimental and numerical models employed throughout the different steps of the analysis has underscored the ever demanding needs for computational and storage capacity in such highly resolved unsteady investigations.

A first part made of three different preliminary studies and based on some simplified models allowed to investigate the influence of the main parameters on the numerical results and to adjust the setups of the turbulence models for the following analysis. This initial study also offered a benchmark between the most appropriate experimental techniques available to validate the highly refined CFD results, in time and space.

In spite of a good overall agreement with regards to the averaged velocity profiles, both analyses conducted with a tumble flap model and an intake port section model are showing some discrepancies between LDA measurements and unsteady CFD results. Depending on the blending factors chosen for the zonal treatment of the hybrid turbulence model, the shift between the URANS and the LES formulations and thus the sensitivity of the model can be triggered. However, while using different boundary conditions for experiments and numerics, and more particularly with different levels of initial turbulence, DES simulation cannot dissociates itself from URANS unless a geometrical singularity disturbs the flow (port's elbow, valve edge). This observation highlights the dependency of the turbulence models towards the boundary and initial conditions employed. Besides the quality of the experimental measurements, the similarity of these conditions has to be satisfied in order to guaranty the relevance of the simulation results. Finally, from the two first steps of the research strategy developed during this work, the restriction of the LDA measurements for validation purpose of advanced 3-D CFD results has been demonstrated. Indeed, this point-wise optical technique is not dedicated to the measurement of large planes and then prevents using the great potential of these CFD methods in terms of flow visualization and turbulent structures tracking.

Based on the former remarks, a planar time-resolved optical system known as High-Speed Particle Image Velocimetry (HS-PIV) has been employed for the rest of the analysis in order to gain more details on the development of turbulent flows within the cylinder and to validate the future simulation results. A particular attention has been given to the 2- and 3-dimensional post-processing of the unsteady data to describe the complex process associated to the origins of turbulence in internal combustion engines. The last stage of the preliminary study enabled to realize the constraints related to the optical measurements in a transparent cylinder as well as the acquisition frequency required to catch the instabilities induced by the system under realistic engine functioning conditions. Even if a good agreement was found between experimental and numerical results while considering the averaged velocity scalar and vector fields, the relatively

high data rate offered by the PIV system with a frequency of 5 kHz did not fully fulfill the requirements. However, the validation of the numerical method based on the global flow quantities has motivated further numerical investigations of the in-cylinder flow in terms of vortex visualization and thus to prove the potential of the zonal turbulence model to properly reproduce the behavior of these turbulent structures. This has been achieved through the use of two different criteria: low pressure iso-surfaces, as well as  $Q$  invariant contours. Although these two criteria are known to deliver similar information about the rotating structures encountered in turbulent flows, the second invariant of the velocity gradient tensor,  $Q$ , has been revealed as the most appropriate visualization technique to return and follow the vortices cores.

Finally, strong from all the experiences summarized before, the detailed analysis of the flow induced by the intake port and the cylinder head of a production engine could take place, offering new perspectives for the visualization and the quantification of the turbulence structures developing under various geometrical and functioning conditions.

The temporal development of the in-cylinder flow induced by a production FSI<sup>®</sup> engine cylinder-head in steady-state configuration has been investigated by means of stereoscopic HS-PIV and compared to simulation results obtained from two different turbulence models: the Detached Eddy Simulation and a URANS derivative model called Scale Adaptive Simulation. The focus of the work has been put on the high temporal resolution of the experimental results as well as on the extreme refinement of the numerical mesh employed. With regards to the first point, the repetition rate of the system reached a frequency of 20 kHz (10 kHz post-processed information) and, associated with the optimized optical test-bench, provided with sensibly improved results. In terms of numerical simulation, under the same initial and boundary conditions, both turbulence models are showing a good agreement with each other and are matching the experimental data. A detailed spectral analysis and the reconstruction of the velocity fields associated with the characteristic frequencies revealed the existence of, at least, three particular modes contributing to the flow fluctuations. Indeed, a clear relation could be established between the valve stem, the valve head and the flow splitter (tumble plate), and some fluctuating flow structures with well defined frequencies (respectively: 1.5 kHz, 2.5 kHz and 3.6 kHz). Although this method is bringing valuable information about the potential origins of the in-cylinder flow fluctuations, the FFT analysis conducted is presenting the major drawback to be a local technique, making it rather exhaustive, and then not very convenient for large flow-fields investigations.

For this reason, Proper Orthogonal Decomposition has been employed, non-conventionally, in order to offer the global approach desired. Indeed, this method offers the opportunity to decompose the unsteady turbulent flow in an ensemble of energy containing spatial modes and also supplies their associated time coefficients. Experimental and numerical results have all been submitted to the same study, and the spectral analysis of the time signal of each mode have been plotted together on a spectrogram to provide an overall view of the characteristic frequencies available. Even if the PIV mapping is slightly blurred in the higher frequencies, both numerical outcomes from DES and SAS are showing a similar and clear tendency. The same characteristic frequencies as the one found thanks to the standard local FFT investigation could be identified here as well. Once the modes ranges corresponding to the frequency peaks of interest are determined, a filtered flow reconstruction can be carried on, allowing to display the eddy structures fluctuating with this particular frequency and to track their physical origin. Following this qualitative representation, a “zero-crossings” analysis has been conducted in both vertical and horizontal directions of the flow in order to deliver the number and then the average diameter of the vortices.

Finally, while applying this analysis process to all configurations investigated, with various valve-lifts and mass-flows, and in different cylinder planes, some correlations and interdependencies between these parameters and the characteristic frequencies and turbulence sizes could be observed.

By comparing the interpolated curves obtained for the two different planes investigated, plotting the structures diameters as a function of their fluctuation frequencies, one could observe that the size of the energetic eddies identified thanks to this method are appreciably smaller in the valve plane than in the cylinder centre one. For the first plane cited, the turbulence diameter is decreasing very fast over the lower frequency range, up to about 1 kHz, and then stabilizing at a value of about 5 mm until the highest frequencies. In the cylinder centre plane the vortices decreasing rate is steadier but reaching the same average value of approximately 5 mm at the highest frequencies.

While evaluating the influence of the nature of the results, it appeared that experimental outcomes are presenting an almost constant offset toward numerical results, with structures sizes about 35% larger than the CFD estimations. In the same way, for the only configuration simulated with both turbulence models (100C3), DES was providing the smallest structures, with an offset of around 12% with the SAS results.

A relationship could also be set up between the mass-flow employed and the resulting fluctuations frequencies. Whereas a linear dependency exists between the two largest frequencies identified (3.6 kHz and 2.5 kHz) and the mass-flow, decreasing by a factor two when the mass-flow is halved, the smallest frequency (1.5 kHz), associated to the valve stem, is presenting a quadratic behavior (decreasing by a factor four). Due to the complexity of the geometry and the high number of degrees of freedom of the port-flow, the dependency between the Strouhal number of the slanted cylinder represented by the stem and the Reynolds number could explain this quadratic proportionality between the frequencies and the averaged flow velocity.

Although the valve-lift influence could be observed, provoking an increase of the structures sizes at larger valve-lifts, the impact on the frequencies is not so straightforward. Indeed, it has been found that the valve-lift, and more generally the position of the valve head, is strongly modifying the overall topology of the flow. At higher lifts, the valve is offering less resistance to the flow, yielding a different distribution of the velocities around the shaft and, more particularly, decreasing the flow congestion occurring between the lower valve edge and the seat. This is probably the reason for the drastic change observed with the 9 mm lift, showing only one characteristic frequency, compared to the three found with the 3 mm displacement.

Consequently, in addition to the ability of generating a low dimensional basis to describe complex turbulent flows, Proper Orthogonal Decomposition has shown its potential to transform the usual intuitive impression resulting from visual inspection of the velocity field into a quantitative form, which could be very useful for further optimization purposes.

Nevertheless, the clear restriction of the exploitable post-processing window size corresponding to the optical measurements area was drastically reducing the amount of information that can be taken out of the flow thanks to the almost unlimited CFD outcomes. In order to take the maximum benefit from the high-resolution simulations results, further flow analyses based on structures visualization have been conducted.

Therefore, a quantitative method has also been proposed, based on the second invariant of the velocity gradient tensor,  $Q$ , to get a better insight into the turbulence structures developing and decaying within the flow. In different cylinder cross-sections with an increasing distance from the valves, the structures containing the highest amount of vorticity could be isolated according to the  $Q$ -criterion (or threshold) selected. Those structures are approximated as circular forms, whose equivalent radii have been employed to determine their distribution functions. The resulting exhaustive statistics about the induced structures as well as a complete mapping of their distribution are offering a valuable data base for further comparative studies between numerical models but also suggest a new way of characterizing the turbulence level induced by the engine geometry considered. In the present case, from a numerical point of view, the small discrepancy observed between the DES and the SAS results lets suggest that the hybrid model enables a slightly better resolution of the turbulence spectrum developing in the flow, taking into account a

greater range of structures, but still emphasizes the very good performance of the URANS-derivative formulation. However, the experimental data available could not allow for any validation of these results.

Although the stereoscopic HS-PIV system employed for this study has proven its efficiency in terms of time resolution, this can not be done to the detriment of the spatial resolution which needs to be high enough in order to compute the velocity gradients required to validate the results obtained by CFD. The use of a larger CCD or CMOS sensor, with at least 2048 x 2048 pixels, should allow reaching finer vector spacing (same order as the one achieved by the CFD results) without overlapping operation, what would improve the quality of the optical measurements. On the other hand, some newly developed techniques such as tomographic PIV, which enables the instantaneous measurement of all three velocity components in a complete 3D measurement volume, could also represent an interesting solution.

Finally, within the framework of this thesis, it was found that the application of SAS to predict turbulent flows based on a modified URANS formulation provides a promising alternative to the LES derivative models such as DES. This method is relatively new in the field of engine simulation, the present work being the first application of SAS for engine flows, and further investigations need to be carried out in order to demonstrate its advantage in terms of computational costs and to support its implementation in the engine development process.

Ultimately, the combination of the innovative post-processing techniques developed here with an efficient unsteady simulation tool such as SAS and the reliable 3D validation data will provide the understanding required about the unsteady turbulent processes involved in the genesis of engines cyclic variations.

## Bibliography

- [1]. *Theoretical Background: Large-Eddy Simulation (Chapter 3)*, in *Large-Eddy Simulation for Acoustics*, pp. 111-112. C. Wagner, T. Hüttl, and P. Sagaut, eds. Cambridge University Press. New-York, USA, 2007.
- [2]. Achenbach, E., *Distribution of local pressure and skin friction around a circular cylinder in cross-flow up to  $Re=5.10^6$* . J. Fluid Mech., **34**: pp. 625-639, 1968.
- [3]. Adrian, R.J., *Particle-imaging techniques for experimental fluid dynamics*. Ann. Rev. Fluid Mech., **23**: pp. pp. 261-304, 1991.
- [4]. Adrian, R.J., *Bibliography of particle image velocimetry using imaging methods: 1917-1995*, in *TAM Report 817, UILU-ENG-96-6004*. 1996, University of Illinois.
- [5]. Ahmadi, G., *Lecture notes on Turbulence - Module ME637*. Turbulence & Multiphase Fluid Flow Laboratory - Clarkson University, USA, 2003.
- [6]. ANSYS-CFX, *CFX 11.0 Modeling Guide - Turbulence and Near Wall Modeling*. December 2006.
- [7]. Baby, X., A. Dupont, A. Ahmed, W. Deslandes, G. Charnay, and M. Michard, *A New Methodology to Analyse Cycle-to-Cycle Aerodynamic Variations*. SAE Paper No. 2002-01-2837, 2002.
- [8]. Balaras, E., C. Benocci, and U. Piomelli, *Two-Layer Approximate Boundary Conditions for Large-Eddy Simulations*. AIAA Journal, **34**(6): pp. 1111-1119, 1996.
- [9]. Ball, K., K. Sirovich, and L. Keefe, *Dynamical eigenfunction decomposition of turbulent channel flow*. International Journal for Numerical Methods in Fluids, **12**: pp. 585-604, 1991.
- [10]. Bardina, J.E., P.G. Huang, and T.J. Coakley, *Turbulence Modeling Validation, Testing and Development*, in *NASA Technical Memorandum 110446*. 1997.
- [11]. Barton, R.K., *An Empirical Model for Correlating Cycle-by-Cycle Cylinder Gas Motion and Combustion Variations of a Spark Ignition Engine*. SAE 710163, 1971.
- [12]. Batten, P., U. Goldberg, and S. Chakravarthy, *LNS - An Approach Towards Embedded LES*. AIAA Paper 2002-0427, 2002.
- [13]. Belamri, T., Y. Egorov, and F. Menter. *CFD Simulation of the Aeroacoustic Noise Generated by a Generic Side View Car Mirror*, in *13th AIAA/CEAS Aeroacoustics Conference*. 2007.
- [14]. Bendat, J.S. and A.G. Piersol, *Engineering Applications of Correlation and Spectral Analysis*. 2nd ed. John Wiley & Sons, Inc., 1993.
- [15]. Bensler, H., L. Kapitza, J. Raposo, and U. Reisch, *A New Experimental Method for Determining Port Generated Swirl Flow*. SAE Technical Paper Series 2002-01-2846, 2002.
- [16]. Berkooz, G., P. Holmes, and J.L. Lumley, *The Proper Orthogonal Decomposition in the Analysis of Turbulent Flows*. Annual Reviews in Fluid Mechanics, **25**: pp. 539-575, 1993.

- [17]. Bianchi, G.M., G. Cantore, and S. Fontanesi, *Turbulence modelling in CFD simulation of ICE intake flows: The discharge coefficient preview*. SAE 2002-01-1118, 2002.
- [18]. Bianchi, G.M., V. Michelassi, and R.D. Reitz. *Modeling the isotropic turbulence dissipation in engine flows by using the linear k-epsilon model*, in *ASME-ICE Division, Fall Technical Conference*. Ann Arbor, Michigan, USA, 1999.
- [19]. Blasius, H., *Das Ähnlichkeitsgesetz bei Reibungsvorgängen in Flüssigkeiten*. Forsch. Arb. Ing.-Wes, **134**, 1913.
- [20]. Bosch, *Kraftfahrtechnisches Taschenbuch*. Vol. 24. Auflage. Robert Bosch GmbH, Stuttgart, 2002.
- [21]. Broeze, J.J., *Combustion in Internal-Combustion Engines. II: The SI Engine*. Engineering, **169**, 1950.
- [22]. Campbell, J.W., G. Hardy, and F. Personeni. *Diesel Engine Intake Port - Flow Stability and application of CFD using a Hybrid-Low-Reynolds near wall method*, in *THIESEL - Conference on Thermo- and Fluid Dynamic Processes in Diesel Engines*. 2006.
- [23]. Celik, I. and I. Yavuz. *An assessment of turbulence length scales relevant to IC Engines*, in *ASME-ICE Division, Spring Technical Conference*. Fort Collins, Colorado, USA, 1997.
- [24]. Celik, I., I. Yavuz, and A. Smirnov, *Large eddy simulations of in-cylinder turbulence for internal combustion engines: a review*. International Journal for Engine Research, IMechE, **2**(2): pp. 119-148, 2001.
- [25]. Celik, I.B., I. Yavuz, A. Smirnov, J. Smith, E. Amin, and A. Gel, *Prediction of in-cylinder turbulence for IC engines*. Combustion Science & Technology, **153**: pp. 339-368, 2000.
- [26]. Chatterjee, A., *An introduction to proper orthogonal decomposition*. Current Science, **78**(7): pp. 808-817, 2000.
- [27]. Chiriac, R. and N. Apostolescu, *Cyclic Variability Patterns in a Spark Ignition Engine Fueled with LPG*. SAE Paper 2004-01-1920, 2004.
- [28]. Colin, O., O. Vermorel, S. Richard, and A. Benkenida. *Multi-cycle LES simulation of a port fuel SI 4 valve engine* in *Workshop "LES for piston engine flows"*. IFP, Rueil-Malmaison, France, 2006.
- [29]. Cordier, L. and M. Bergmann, *Proper Orthogonal Decomposition: an overview*, in *Post-Processing of Experimental and Numerical Data - Lecture Series 2003-03*. P. Millan and M.L. Riethmuller, eds. Rhode-Saint-Genèse, Belgium, 2003.
- [30]. Cosadia, I., J. Borée, G. Charnay, and P. Dumont, *Cyclic variations of the swirling flow in a Diesel transparent engine*. Experiments in Fluids, **41**: pp. 115-134, 2006.
- [31]. Courant, R., K. Friedrichs, and H. Lewy, *Über die partiellen Differenzgleichungen der mathematischen Physik*. Mathematische Annalen, **100**(1): pp. 32-74, 1928.
- [32]. Cucitore, R., M. Quadrio, and A. Baron, *On the effectiveness and limitations of local criteria for the identification of a vortex*. Eur. J. Mech. B/ Fluids, **18**: pp. 261-282, 1999.

- [33]. Davidson, L. *Evaluation of the SST-SAS Model: Channel Flow, Asymmetric Diffuser and Axi-symmetric Hill*, in *ECCOMAS CFD*. TU Delft, The Netherlands, 2006.
- [34]. Davidson, L. *The SAS model: A turbulence model with controlled modelled dissipation*, in *20th Nordic Seminar on Computational Mechanics*. Göteborg, 2007.
- [35]. Davidson, L. and S.-H. Peng, *Hybrid LES-RANS: A One-Equation SGS Model Combined with a  $k$ - $\omega$  model for Predicting Recirculation Flows*. *International Journal of Numerical Methods in Fluids*, **43**: pp. 1003-1018, 2003.
- [36]. Dean, R.B., *Reynolds number dependence of skin friction and other bulk flow variables in two-dimensional rectangular duct flow*. *Trans. ASME I: J. Fluids Eng.*, **100**: pp. 215-223, 1978.
- [37]. Deslandes, W., P. Dumont, A. Dupont, X. Baby, G. Charnay, and J. Borée, *Airflow Cyclic Variations Analysis in Diesel Combustion Chamber by PIV Measurements*. SAE Paper No. 2004-01-1410, 2004.
- [38]. Devesa, A., J. Moreau, T. Poinsot, and J. Helie, *Large Eddy Simulations of Jet / Tumble Interaction in a GDI Model Engine Flow*. SAE 2004-01-1997, 2004.
- [39]. Druault, P., P. Guibert, and F. Alizon, *Use of proper orthogonal decomposition for time interpolation from PIV data - Application to the cycle-to-cycle variation analysis of in-cylinder engine flows*. *Experiments in Fluids*, **39**: pp. 1009-1023, 2005.
- [40]. EC, *European Commission, Transport & Environment Department*. [http://ec.europa.eu/environment/air/transport/co2/co2\\_home.htm](http://ec.europa.eu/environment/air/transport/co2/co2_home.htm), 2008, December 17th.
- [41]. Ferziger, J.H. *The Physics and Simulation of Turbulence*, in *Introduction to turbulence Modeling - Lecture Series 2004-06*. von Kármán Institute for Fluid Dynamics - Rhode-Saint-Genèse - Belgium, 2004.
- [42]. Ferziger, J.H. and M. Peric, *Computational Methods for Fluid Dynamics*. 3rd ed. Springer, Berlin, 2002.
- [43]. Fiedler, H.E., *Control of free turbulent shear flows*, in *Flow Control: Fundamental and Practices - Lecture Notes in Physics m 53*, pp. 336-429. M. Gad-el-Hak, A. Pollard, and J.P. Bonnet, eds. Springer, 1998.
- [44]. Fischer, J., A. Velji, and U. Spicher, *Investigation in Cycle-to-Cycle Variations of In-Cylinder Processes in Gasoline Direct Injection Engines Operating With Variable Tumble Systems*. SAE Paper No. 2004-01-0044, 2004.
- [45]. Fogleman, M., J.L. Lumley, D. Rempfer, and D. Haworth, *Application of proper orthogonal decomposition to datasets of internal combustion engine flows*. *Journal of Turbulence*, **5-023**, 2004.
- [46]. Friedrich, R. and W. Rodi, *Advances in LES of Complex Flows*. Kluwer Academic Publishers, 2000.
- [47]. Geiger, J., *Untersuchung der Flammenausbreitung im Ottomotor bei unterschiedlichen Brennraumformen*. PhD Thesis. RWTH, Aachen, 1992.
- [48]. Germano, M., U. Piomelli, P. Moin, and W.H. Cabot, *A Dynamic Subgrid-Scale Eddy Viscosity Model*. *Phys. Fluids A*, **3**: pp. 1760-1765, 1991.
- [49]. Goehre, M., *Engine pre-development, Optical measurement methods, Volkswagen AG*. Personal communication with O. Imberdis, March, 2006.

- [50]. Goldstein, R.J., *Fluid Mechanics Measurements*, R.J. Goldstein. University of Alabama, 1996.
- [51]. Gordeyev, S., *POD, LSE and Wavelet decomposition: Literature Review*. 2000, Department of Aerospace and Mechanical Engineering, University of Notre Dame, IN.
- [52]. Goryntsev, D., M. Klein, and J. Janicka. *Charakterisierung der zyklischen Schwankungen in einem direkteinspritzenden Ottomotor mittels Grobstruktursimulation*, in *BMBF Workshop: Turbulenz in der Energietechnik*. Darmstadt, Germany, 2005.
- [53]. Goryntsev, D., M. Klein, A. Sadiki, and J. Janicka, *LES of Influence of Cyclic Variations on Fuel-Air-Mixing and Combustion in a DISI engine*. VDI-Berichte Nr. 1988: pp. 265-270, 2007.
- [54]. Goryntsev, D., O. Stein, M. Klein, and J. Janicka. *Characterization of Cyclic Fluctuations of the In-Cylinder Flow field of a Direct Injection SI Engine using Large Eddy Simulation*, in *Engine Combustion Processes, VII. Congress*. Haus der Technik e.V., Munich, 2005.
- [55]. Graftieaux, L., M. Michard, and N. Grosjean, *Combining PIV, POD and vortex identification algorithms for the study of unsteady turbulent swirling flows*. Meas. Sci. Technol., **12**: pp. 1422-1429, 2001.
- [56]. Grant, I. *Particle Image Velocimetry, A Review*. Proceedings of the Institution of Mechanical Engineers, Part C. Mechanical Engineering Science. Vol. 211 (1), pp. 55-76, 1997.
- [57]. Grosse, G. and W. Hentschel. *Stroemungsmessungen im Modell eines Schaltbaren Einlasskanals für einen Ottomotor mit Direkteinspritzung Mittels PIV und LDA*, in *10. GALA Fachtagung - Lasermethoden in der Stroemungsmesstechnik*. Rostock University, Germany, 2002.
- [58]. Haworth, D.C., *Large-Eddy Simulation of In-Cylinder Flows*. Oil & Gas Science and Technology - Rev. IFP, **54**(2): pp. 175-185, 1999.
- [59]. Haworth, D.C. and K. Jansen, *Large-Eddy Simulation on Unstructured Deforming Meshes: Towards Reciprocating IC Engines*. Computers and Fluids, **29**(5): pp. 493-524, 2000.
- [60]. Heisenberg, W., *Zur statistischen Theorie der Turbulenz*. Z. Phys., **Bd. 124**: pp. 628-657, 1948.
- [61]. Hélie, J., J.-M. Duclos, T. Baritaud, T. Poinso, and A. Trouvé, *Influence of mixture fluctuations on combustion in direct injection spark ignition engines simulations* SAE 2000-01-1226, 2000.
- [62]. Hentschel, W., B. Block, T. Hovestadt, H. Meyer, G. Ohmstedt, V. Richter, B. Stiebels, and A. Winkler, *Optical Diagnostics and CFD-Simulations to Support the Combustion Process Development of the Volkswagen FSI Direct-Injection Gasoline Engine*. SAE Paper No. 2001-01-3648, 2001.
- [63]. Heywood, J.B., *Fluid Motion within the Cylinder of Internal Combustion Engines - The 1986 Freeman Scholar Lecture*. Journal of Fluid Engineering, **109/3**, 1987.
- [64]. Heywood, J.B., *Internal Combustion Engine Fundamentals*. Mc Graw Hill, 1988.



- [65]. Hill, P.G., *Cyclic Variations and Turbulence Structure in Spark-Ignition Engines*. Combust. Flame, **72**: pp. 73-89, 1988.
- [66]. Holmes, P., J.L. Lumley, and G. Berkooz, *Turbulence, Coherent Structures, Dynamical Systems and Symmetry*, Cambridge University Press. 1996.
- [67]. Hunt, J.C., A. Wray, and P. Moin, *Eddies, stream, and convergence zones in turbulent flows*. Center for turbulence Research Report - CTR-S88, 1988.
- [68]. IEA, *International Energy Agency*. <http://www.iea.org/journalists/index.asp>, Statistics August 2008.
- [69]. Imberdis, O., H. Bensler, M. Hartmann, W. Hentschel, U. Schrottke, and D. Thévenin. *Analysis of Turbulent Flow Induced by a Simplified Steady-State Engine Port Model: LDA Measurements and CFD Simulation*, in *14. GALA Fachtagung - Lasermethoden in der Stroemungsmesstechnik*. Physikalisch-Technischen Bundesanstalt Braunschweig, Germany, 2006.
- [70]. Imberdis, O., H. Bensler, M. Hartmann, W. Hentschel, G. Ohmstede, and D. Thévenin. *Visualization and Characterization of Intake-port Model induced Turbulent Structures*, in *12th International Symposium on Flow Visualization* Göttingen, Germany, 2006.
- [71]. Imberdis, O., M. Hartmann, H. Bensler, D. Thévenin, and L. Kapitza, *A Numerical and Experimental Investigation of a DISI-Engine Intake Port Generated Turbulent Flow*. Journal of Engines - SAE 2007 Transactions, Paper 2007-01-4047, 2007.
- [72]. Jeong, J. and F. Hussain, *On the identification of a vortex*. Journal of Fluid Mechanics, **285**: pp. 69-94, 1995.
- [73]. Jones, W. and B.E. Launder, *The Prediction of Laminarization with a Two-Equation Model of Turbulence*. International Journal of Heat and Mass Transfer, **15**: pp. 301-314, 1972.
- [74]. Khalighi, B., *Intake-Generated Swirl and Tumble Motions in a 4-Valve Engine with Various Intake Configurations - Flow Visualization and Particle Tracking Velocimetry*. SAE 900059, 1990.
- [75]. Kim, J., P. Moin, and P. Moser, *Turbulence statistics in fully developed channel flow at low Reynolds number*. Journal of Fluid Mechanics, (177), 1987.
- [76]. Kolmogorov, A.N., *Die Energiedissipation für lokal isotrope Turbulenz*. Dokl. Akad. Wiss. USSR, **Bd. 32**: pp. 16-18, 1941.
- [77]. Kolmogorov, A.N., *Die lokale Struktur der Turbulenz in einer inkompressiblen zähen Flüssigkeit bei sehr großen Reynoldsschen Zahlen*. Dokl. Akad. Wiss. USSR, **Bd. 30**: pp. 301-305, 1941.
- [78]. Kraemer, S., *Untersuchung zur Gemischbildung, Entflammung und Verbrennung beim Ottomotor mit Benzin-Direkteinspritzung*. PhD Thesis. University of Karlsruhe (TH), 1998.
- [79]. Kyriakides, S.C. and A.R. Glover, *A Study of the Correlation Between In-Cylinder Air Motion and Combustion in Gasoline Engines*. IMechE, 1988.
- [80]. Launder, B.E. and B.I. Sharma, *Application of the Energy Dissipation Model of Turbulence to the Calculation of Flow Near a Spinning Disc*. Letters in Heat and Mass Transfer, **1**(2): pp. 131-138, 1974.

- [81]. Leonard, A., *Energy cascade in Large-Eddy Simulations of turbulent fluid flows*. Adv. Geophys., **18A**, 1974.
- [82]. Leschziner, M.A., *Modeling strongly swirling flows with advanced turbulence closure*. Advances in Numerical Simulations of turbulent Flows, ASME Publication, New-York, **Vol. 117**: pp. 1-10, 1991.
- [83]. Lesieur, M., P. Comte, F. Ducros, E. Lamballais, and O. Metais, *Large Eddy Simulations of Turbulent Shear Flows*. Notes on Numerical Fluid Mechanics - Computation and Visualization of 3-D Vortical and Turbulent Flows. Vol. NNFM64. Vieweg, 1996.
- [84]. Lien, F.S. and M.A. Leschziner, *Assessment of turbulence-transport models including non-linear RNG eddy-viscosity formulation and second-moment closure for flow over a backward-facing step*. Computers and Fluids, **23**: pp. 983-1004, 1994.
- [85]. Lugt, H.J. *The dilemma of defining a vortex*, in *Recent Developments in Theoretical and Experimental Fluid Mechanics*. Springer, 309-321, 1979.
- [86]. Lumley, J.L., *The structure of inhomogeneous turbulent flows*, in *Atmospheric Turbulence and Wave Propagation*, pp. 166-178. A.M. Yaglom and V.I. Tatarsky, eds. Nauka, Moscow, 1967.
- [87]. Lumley, J.L., *Coherent structures in turbulence*, in *Transition and Turbulence*, pp. 215-241. R.E. Meyer, ed, 1981.
- [88]. Lumley, J.L., *Engines: An Introduction*. Cambridge University Press, New York, USA, 1999.
- [89]. Menter, F.R., *Zonal two-equation  $k$ - $\omega$  turbulence model for aerodynamic flows*. AIAA Paper 1993-2906, 1993.
- [90]. Menter, F.R., *Two-Equation eddy viscosity turbulence models for engineering applications*. AIAA Journal, **32**(8): pp. 1598-1605, 1994.
- [91]. Menter, F.R., *Development Manager, Scientific Coordination, Ansys Germany*. Personal communication with O. Imberdis, May 16, 2007.
- [92]. Menter, F.R. and Y. Egorov. *Re-visiting the turbulent scale equation*, in *One hundred years of boundary layer research*. Goettingen, Germany, 2004.
- [93]. Menter, F.R. and Y. Egorov. *A Scale-Adaptive Simulation Model using Two-Equation Models*, in *AIAA paper 2005-1095*. Reno, NV, 2005.
- [94]. Menter, F.R. and Y. Egorov. *Turbulence Models Based on the Length-Scale Equation*, in *Fourth International Symposium on Turbulent Shear Flow Phenomena - Paper TSFP4-268*. Williamsburg, 2005.
- [95]. Menter, F.R. and Y. Egorov. *Turbulence Modeling of Aerodynamic Flows*, in *International Aerospace CFD Conference*. Paris, 2007.
- [96]. Menter, F.R. and M. Kuntz, *Development and application of a zonal DES turbulence model for CFX-5*. Ansys CFX Validation Report: pp. 3-7, 2003.
- [97]. Menter, F.R., M. Kuntz, and R. Bender. *A Scale-Adaptive Simulation Model for Turbulent Flow Predictions*, in *41st Aerospace Science Meeting & Exhibit, AIAA paper 2003-0767*. Reno, Nevada, USA, 2003.
- [98]. Moin, P. and R.D. Moser, *Characteristic-eddy decomposition of turbulence in a channel*. J. Fluid Mech., **200**: pp. 471-509, 1989.

- [99]. Nadarajah, S., S. Balabani, M.J. Tindal, and M. Yianneskis, *The turbulence structure of the annular non-swirling flow past an axisymmetric poppet valve*. Journal of Mechanical Engineering Science, **212(C6)**: pp. 455-471, 1998.
- [100]. Patterson, D.J., *Pressure Variations, A Fundamental Combustion Problem*. SAE Paper No. 660129, 1966.
- [101]. Piomelli, U., *Recent Advances in Turbulence Simulation*. Course presented at the von Kármán Institute for Fluid Dynamics, Rhode-Saint-Genèse, Belgium, 2002.
- [102]. Piomelli, U. *Introduction to Turbulence Modeling*, in *Lecture Series 2004-06*. von Kármán Institute for Fluid Dynamics - Rhode-Saint-Genèse, Belgium, 2004.
- [103]. Pischinger, S., M. Graf, R. Aymanns, B. Vogt, and F. Fricke. *Zyklische Schwankungen beim direkteinspritzenden Ottomotor*, in *BMBF Workshop "Turbulenz in der Energietechnik"* Darmstadt, Germany, 2005.
- [104]. Poinso, T. *LES for combustion*, in *Workshop "LES for piston engine flows"*. IFP, Reuil-Malmaison, France, 2006.
- [105]. Raffel, M., C.E. Willert, and J. Kompenhans, *Particle Image Velocimetry: A Practical Guide*, Springer Verlag Berlin Heidelberg. 1998.
- [106]. Ramos, J.I., *Internal Combustion Engine Modeling*. Hemisphere Publishing Corp., New York, 1989.
- [107]. Raposo, J., W. Hentschel, and W. Merzkirch. *Extraction of the Large Scale Structures in the In-Cylinder Flow of Internal Combustion Engines by means of POD and Wavelet Techniques*, in *8. GALA Fachtagung - Lasermethoden in der Stroemungsmesstechnik*. Freising / Weihenstephan, Germany, 2000.
- [108]. Reuss, D.L., R.J. Adrian, C.C. Landreth, D.T. French, and T.D. Fansler, *Instantaneous Planar Measurements of Velocity and Large-Scale Vorticity and Strain Rate in an Engine Using Particle-Image Velocimetry*. SAE 890616, 1989.
- [109]. Reuss, D.L., M. Bardsley, P.G. Felton, C.C. Landreth, and R.J. Adrian, *Velocity, Vorticity and Strain-Rate Ahead of a Flame Measured in an Engine Using Particle Image Velocimetry*. SAE 900053, 1990.
- [110]. Riethmuller, M.L. *Particle Image Velocimetry*, in *Von Kármán Institute of Fluid Dynamics, Lecture Series 1996-03*. Rhode-Saint-Genèse, Belgium, 1996.
- [111]. Rodi, W., *Experience with Two-Layer Models Combining the k-epsilon Model with a One-Equation Model Near the Wall*. AIAA Paper 91-0216, 1991.
- [112]. Rotta, J.C., *Turbulente Stroemungen*, Teubner. Stuttgart, Germany, 1972.
- [113]. Sagaut, P., *Large Eddy Simulation for Incompressible Flows*. Springer Verlag, 2001.
- [114]. Sagaut, P., S. Deck, and M. Terracol, *Multiscale and Multiresolution Approaches in Turbulence*. Imperial College Press, London, UK, 2006.
- [115]. Schumann, U., *Realizability of reynolds-stress turbulence models*. Physics of Fluids, **20(5)**: pp. 721-725, 1977.
- [116]. Schumann, U., *Stochastic backscatter of turbulence energy and scalar variance by random subgrid-scale fluxes*. Journal of Fluid Mechanics, **451**, 1995.
- [117]. Seidl, V., S. Muzaferija, and M. Peric, *Parallel Computation of Unsteady Separated Flows Using Unstructured, Locally Refined Grids*. Notes on Numerical Fluid

- Mechanics - Computation and Visualization of 3-D Vortical and turbulent Flows. Vol. NNFM64. Vieweg, 1996.
- [118]. Shuliang, L., L. Yufeng, and L. Ming, *Prediction of Tumble Speed in the Cylinder of the 4-Valve Spark Ignition Engines*. SAE 2000-01-0247, 2000.
- [119]. Sirovich, L., *Turbulence and the Dynamics of Coherent Structure: I, II and III*. Quarterly Applied Mathematics **45**: pp. 561, 1987.
- [120]. Smagorinsky, J., *General circulation experiments with the primitive equations*. Mon. Weath. Rev., **91**(3), 1963.
- [121]. Sohm, V.M., *Hybrid Turbulence Simulation to Predict Cyclic Variations in Internal Combustion Engines*. PhD Thesis - RWTH Aachen, Germany, 2007.
- [122]. Soltau, J.P. *Cylinder Pressure Variations in Petrol Engines*, in *Proc. of the Institution of Mechanical Engineers*. Vol. 2, 1960-1961.
- [123]. Sone, K. and S. Menon, *The effect of subgrid modeling on the in-cylinder unsteady mixing process in a direct injection engine*. ASME - Journal of Engineering for gas turbines and power, **125**(2): pp. 435-443, 2003.
- [124]. Sone, K., N.V. Patel, and S. Menon, *Large-Eddy Simulation of Fuel-Air Mixing in an Internal Combustion Engine*. AIAA 2001-0635, 2001.
- [125]. Speziale, C., *Galilean invariance of subgrid scale stress models in large-eddy simulations of turbulence*. Journal of Fluid Mechanics, **156**: pp. 55-62, 1985.
- [126]. Squires, K.D., *Detached-Eddy Simulation: Current Status and Perspectives*. ERCOFTAC Series: Direct and Large-Eddy Simulation, **5**: pp. 465-480, 2004.
- [127]. St.Hill, N., P. Asadamongkon, and K.C. Lee. *A study of turbulence and cyclic variation levels in internal combustion engine cylinders*, in *10th International Symposium on Applications of Laser Techniques to Fluid Mechanics*. Lisboa, Portugal, 2000.
- [128]. Stiesch, G., *Modeling Engine Spray and Combustion Processes*. Springer Verlag, 2003.
- [129]. Strelets, M. *Detached Eddy Simulation of Massively Separated Flows*, in *AIAA Paper 2001-0879, 39th Aerospace Sciences Meeting and Exhibit*. Reno, NV, 2001.
- [130]. Tennekes, H. and J.L. Lumley, *A First Course in Turbulence*, The Massachusetts Institute of Technology Press. USA, 1974.
- [131]. Thobois, L. and T. Poinso. *LES simulations of steady engine flow test benches and SI engine combustion*, in *Workshop "LES for piston engine flows"*. IFP, Rueil-Malmaison, France, 2006.
- [132]. Tropea, C., N. Damaschke, and H. Nobach, *Datenverarbeitung*. Lecture Notes - Fachgebiet Strömungslehre & Aerodynamik. TU Darmstadt, 2003.
- [133]. Vermorel, O., S. Richard, C. Angelberger, and A. Benkenida. *Predicting cyclic variability in a 4-valve SI engine using LES and the AVBP CFD code*, in *International Multidimensional Engine Modeling - User's Group Meeting*. Detroit, MI, USA, 2007.
- [134]. Vichnievsky, R. and B. Sale, *Etude de la Combustion sur le Monocylindre IFP Renault CNRS*. Journal de la Société des Ingénieurs Automobile, **31**, 1958.

- [135]. Vreman, B., B. Geurts, and H. Kuerten, *Realizability conditions for the turbulent stress tensor in large-eddy simulation*. Journal of Fluid Mechanics, **278**: pp. 351-362, 1994.
- [136]. White, F.M., *Fluid Mechanics*. 4th ed. McGraw-Hill, New York, NY, 1999.
- [137]. Wilcox, D.C., *Re-assessment of the scale-determining equation for advanced turbulence models*. AIAA Journal, **26**: pp. 1414-1421, 1988.
- [138]. Wilcox, D.C., *Turbulence Modeling for CFD*. 2nd Edition ed. DCW Industries, Inc., 1998.
- [139]. Willems, W., *Numerische Simulation turbulenter Scherströmungen mit einem Zwei-Skalen Turbulenzmodell*. PhD Thesis - RWTH Aachen, Germany, 1996.
- [140]. Williams, F.A., *Combustion Theory*. 2nd ed. Benjamin-Cummings, Menlo Park, CA, 1985.
- [141]. Wilson, N.D., A.J. Watkins, and C. Dopson, *Asymmetric valve strategies and their effect on combustion*. SAE 930821, 1993.
- [142]. Winsor, R.E. and D.J. Patterson, *Mixture Turbulence - A Key to Cyclic combustion Variation*. SAE 730086, 1973.
- [143]. Young, M.B., *Cyclic Dispersion in the Homogeneous-Charge Spark-Ignition Engine - A Literature Survey*. SAE Paper 810020, 1981.



## Appendix

### A.1 Sequence of instantaneous PIV acquisitions (§5.5)

The following figure represents a succession of High-Speed PIV acquisitions taken in the cylinder centre plane, between the two intake-valves. The laser pulse-rate of 10 kHz allows following the displacement and break-up process of certain flow structures (for example, those marked by black circles on the left and the right of the successive plots).

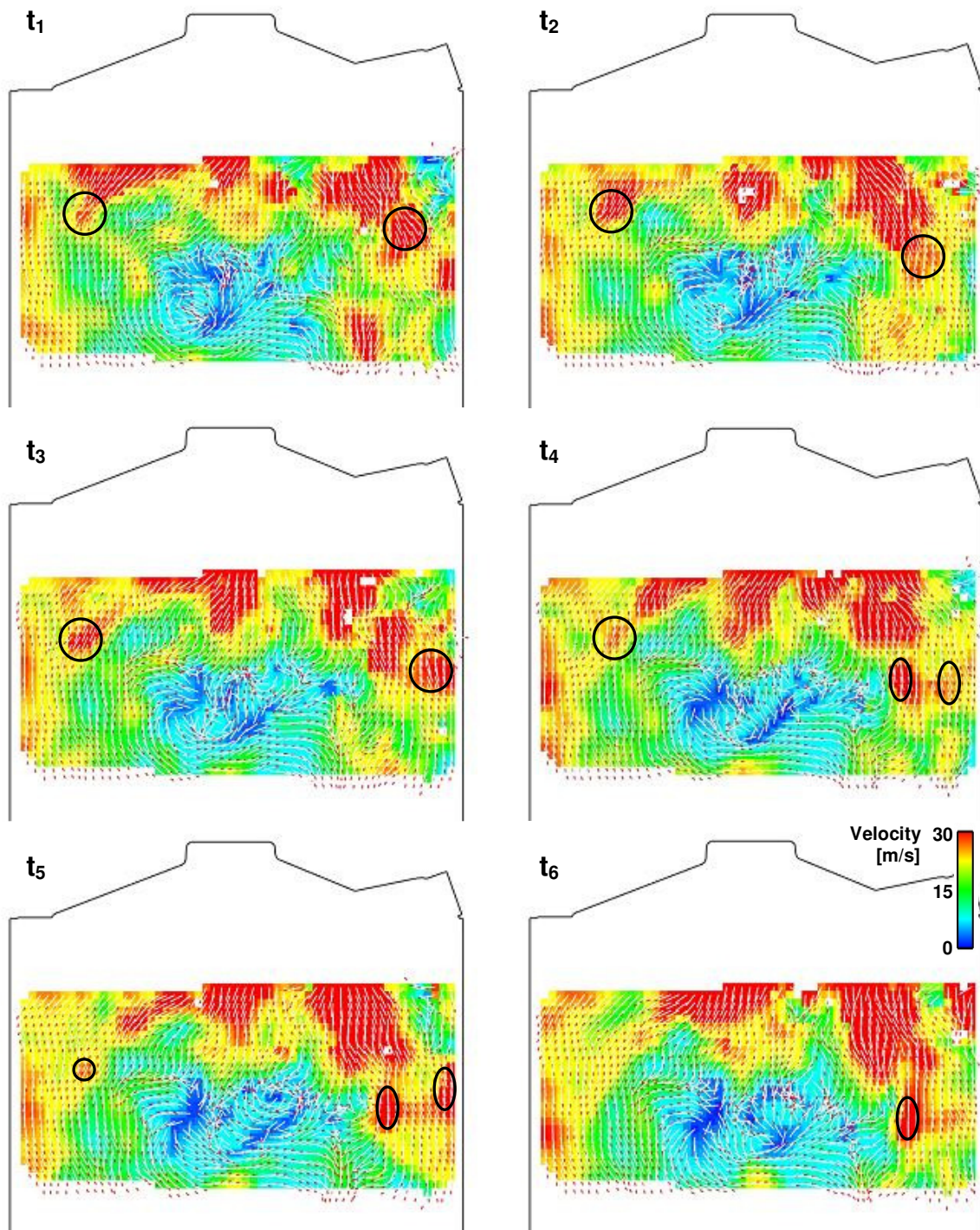


Figure A. 1: Instantaneous snapshots of 6 successive PIV acquisitions in the cylinder centre plane (10 kHz of pulse rate) shaded with the total velocity magnitude [0→30m/s] and instantaneous vectors

## A-2 Spectral Analysis of the FSI<sup>®</sup> Intake-Port Induced Turbulent Flow (§5.6.5)

The results presented thereafter are showing the spectra of the simulated velocity fields and the spatial distribution of the characteristic frequencies in the two planes of interest. These frequencies are determined by carrying a FFT analysis of the instantaneous simulation data, on every nodes of the plane considered (valve plane, or cylinder centre). It is reassuring to observe that the peaks obtained in the higher frequency range are matching the one from §5.5.1.

The principle of the method described here for the DES 100C3 results is applied in the same way to the Scale-Adaptive Simulation (SAS) results, for two different mass-flows (100 kg/h and 50 kg/h) and two different valve-lifts (3 mm and 9 mm).

### A-2.1 DES 100C3 Low-Resolution

Figure A.2 shows the superimposition of the spectra computed at each node of the 2-D Low-Resolution post-processing mesh, presented in §5.3.2 (Data Management & Post-Processing Mesh).

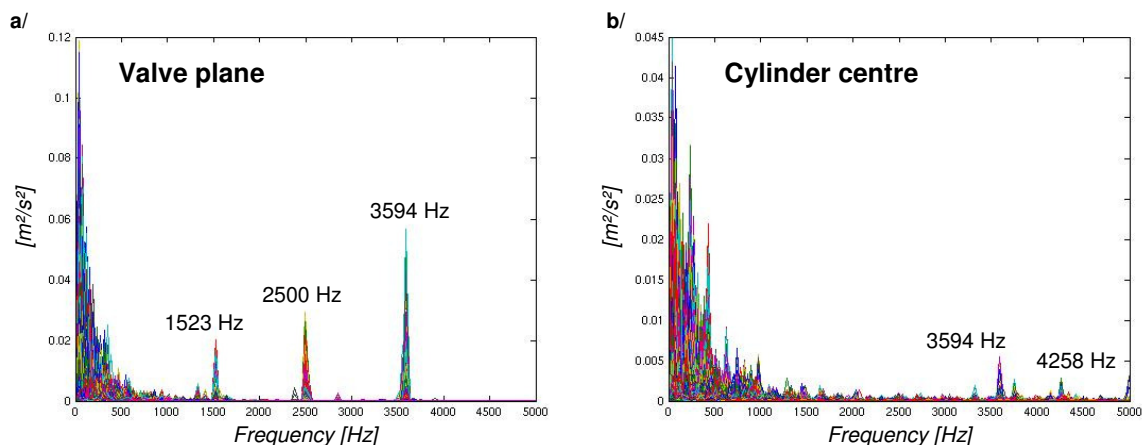


**Figure A.2: Spectra obtained by FFT of the DES 100C3 results (100 kg/h, tumble flap Closed, 3 mm valve-lift) and characteristic frequencies (in the higher frequency range). a/ 3 characteristic frequencies in the valve plane; b/ 2 characteristic frequencies in the cylinder centre plane.**

In order to determine the characteristic frequencies above, all located in the higher frequency range, the spatial coherence of the signal has been studied. Concretely, for a given frequency, the amplitude of the spectra corresponding to each node has been plotted in the 2-D plane, as shown in Figure A.3. Thus, only the three previously marked frequencies, also called characteristic frequencies, are presenting some remarkable regions of activity that can be isolated from their surrounding. These small localized regions of the flow are representative of the nodes, which are fluctuating with a common frequency, or are spatially correlated in frequency.

For lower frequencies, below 1000 Hz, no particular behavior could be identified in any part of the plane.



As mentioned before, Figure A.3 is displaying the spatial distribution of the amplitude of the FFT signals, filtered with each of the three characteristic frequencies. This representation allows identifying the regions of the flow showing a particular activity at a given frequency, and then, to track the potential origins of the perturbation.

The blur effect observed on the results shown thereafter is due to the spatial resolution employed. Indeed, for consistency in the comparison with the PIV results conducted in §5.6.5.2, the POD data processing needs to be based on the same resolution.

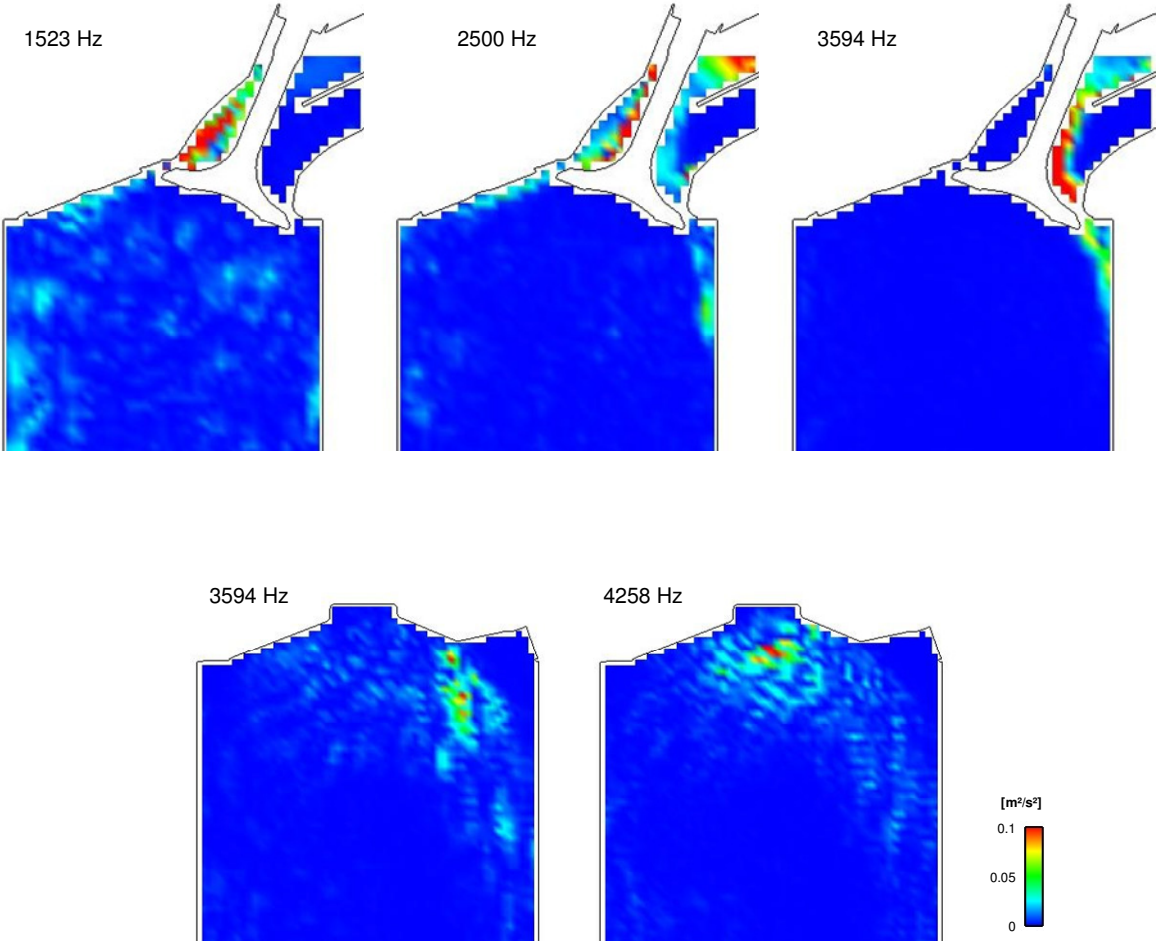


**Figure A.3: Spatial distribution of the local FFT-signals amplitude, filtered with the previously identified characteristic frequencies (top: valve plane, bottom: cylinder centre plane).**

## A-2.2 SAS 100C3 Low-Resolution

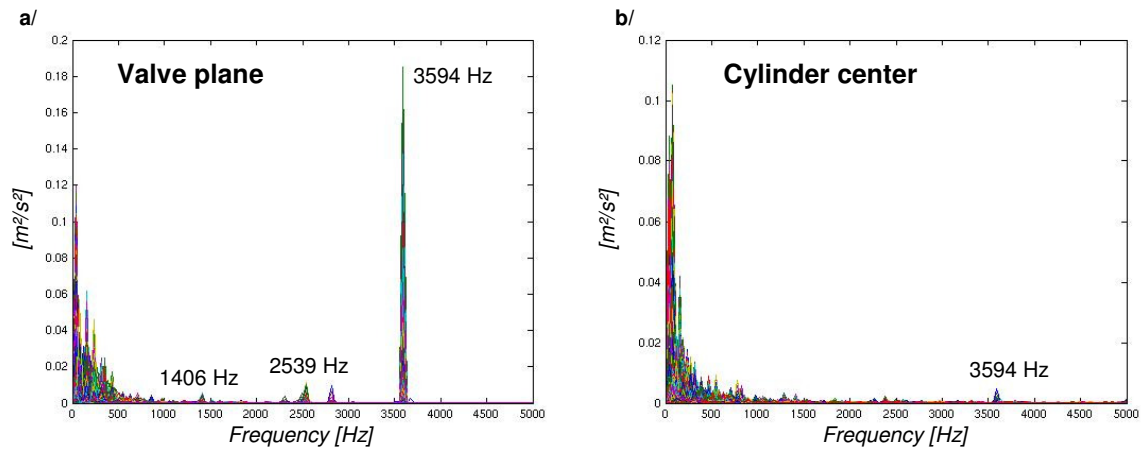


Figure A.4: Spectra obtained by FFT of the SAS 100C3 results (100 kg/h, tumble flap Closed, 3 mm valve-lift) and characteristic frequencies (in the higher frequency range). a/ 3 characteristic frequencies in the valve plane; b/ 1 characteristic frequency in the cylinder centre plane.

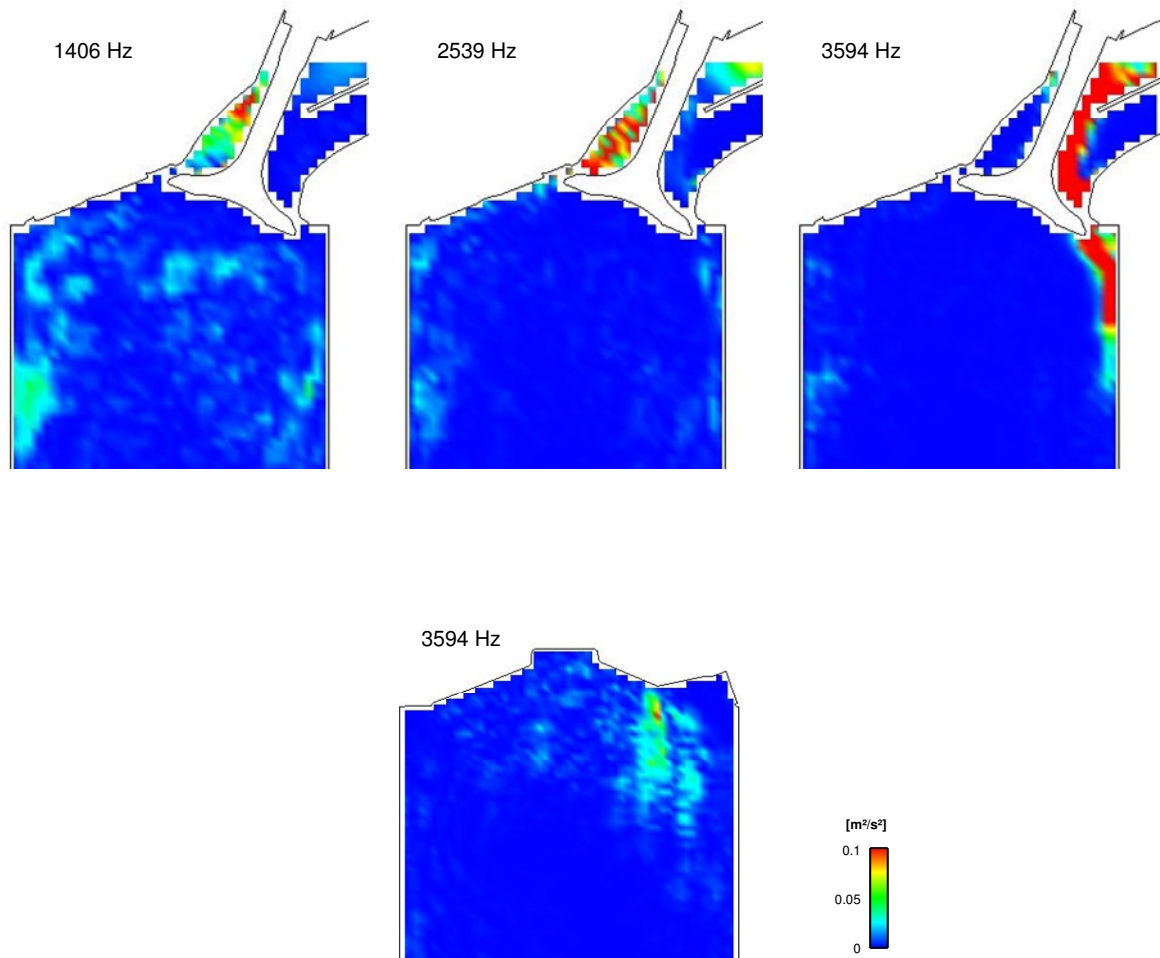


Figure A.5: Spatial distribution of the local FFT-signals amplitude, filtered with the previously identified characteristic frequencies (top: valve plane, bottom: cylinder centre plane).

### A-2.3 SAS 50C3 Low-Resolution

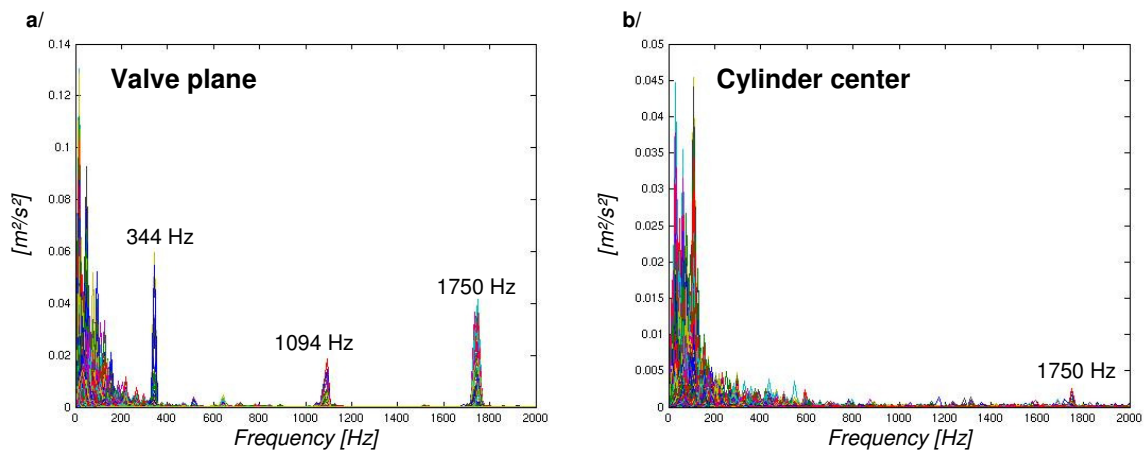


Figure A.6: Spectra obtained by FFT of the SAS 50C3 results (50 kg/h, tumble flap Closed, 3 mm valve-lift) and characteristic frequencies (in the higher frequency range). a/ 3 characteristic frequencies in the valve plane; b/ 1 characteristic frequency in the cylinder centre plane.

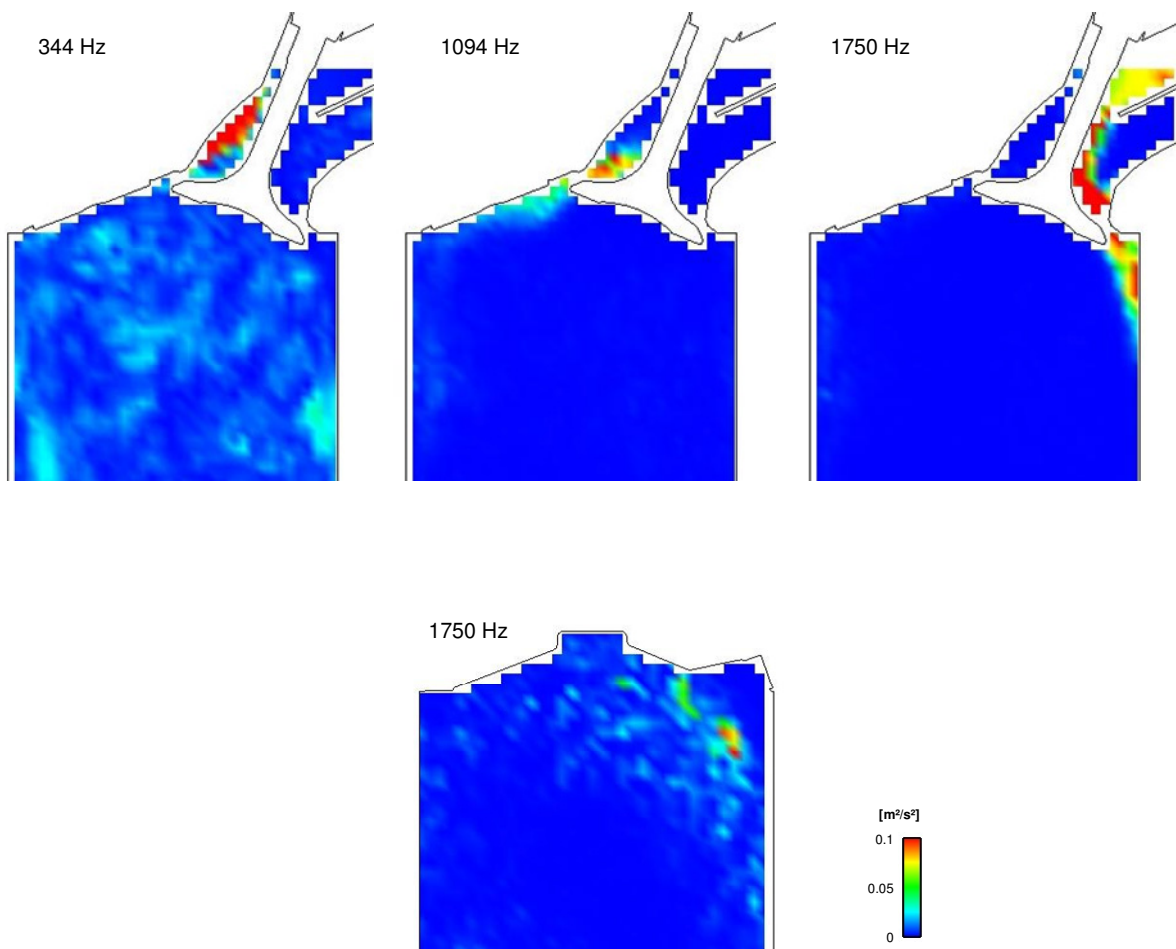


Figure A.7: Spatial distribution of the local FFT-signals amplitude, filtered with the previously identified characteristic frequencies (top: valve plane, bottom: cylinder centre plane).

## A-2.4 SAS 100C9 Low-Resolution

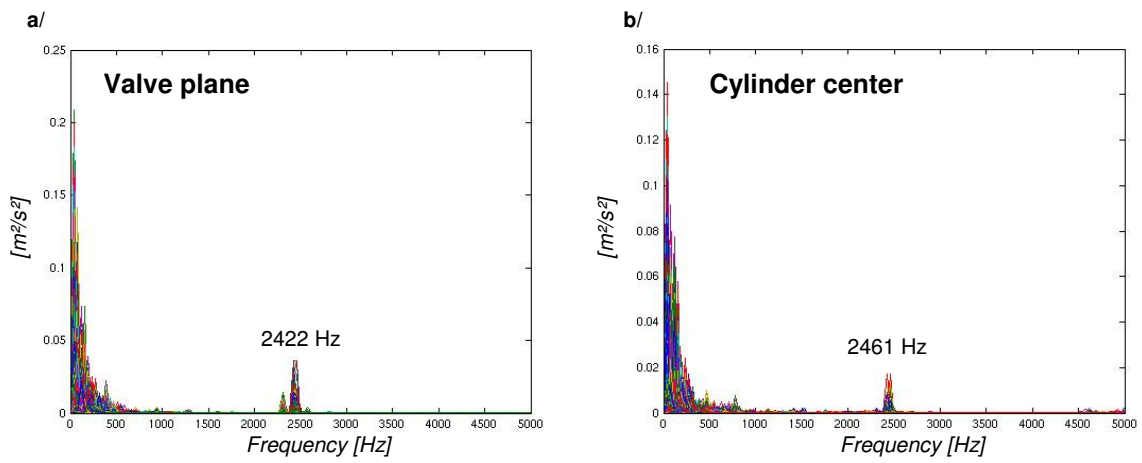


Figure A.8: Spectra obtained by FFT of the SAS 100C9 results (100 kg/h, tumble flap Closed, 9 mm valve-lift) and characteristic frequencies (in the higher frequency range). a/ 1 characteristic frequency in the valve plane; b/ 1 characteristic frequency in the cylinder centre plane.

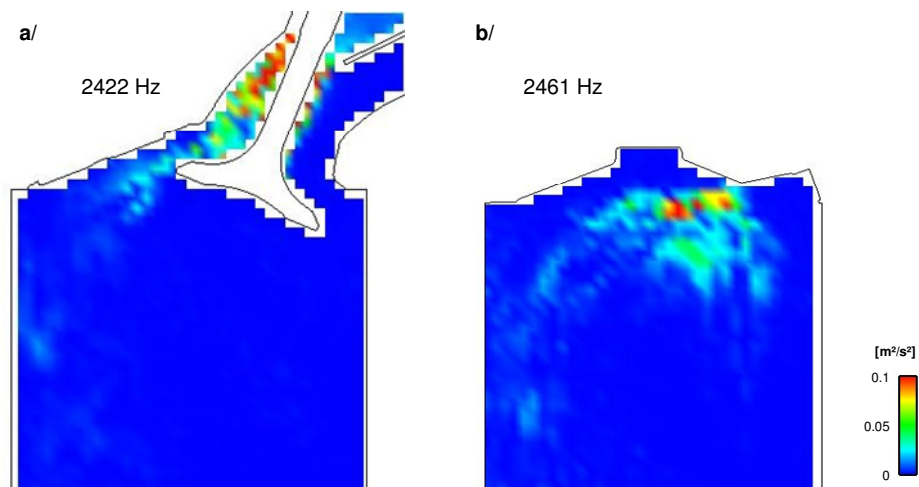
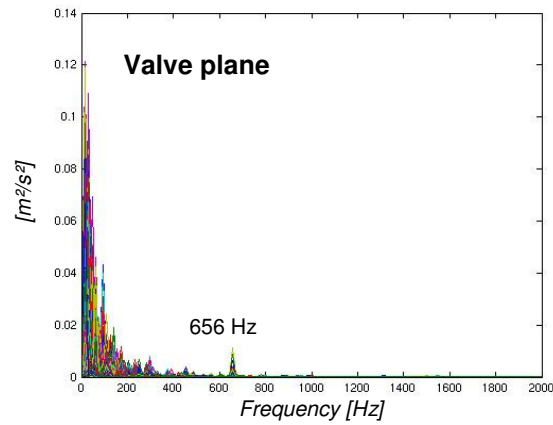


Figure A.9: Spatial distribution of the local FFT-signals amplitude, filtered with the previously identified characteristic frequencies (top: valve plane, bottom: cylinder centre plane).

## A-2.5 SAS 50C9 Low-Resolution

In this case, since no experimental data were available for the cylinder-centre plane, only the valve plane has been investigated and presented here.



**Figure A.10:** Spectra obtained by FFT of the SAS 50C9 results (50 kg/h, tumble flap Closed, 9 mm valve-lift) and characteristic frequencies (in the higher frequency range) - 1 characteristic frequency observed in the valve plane.

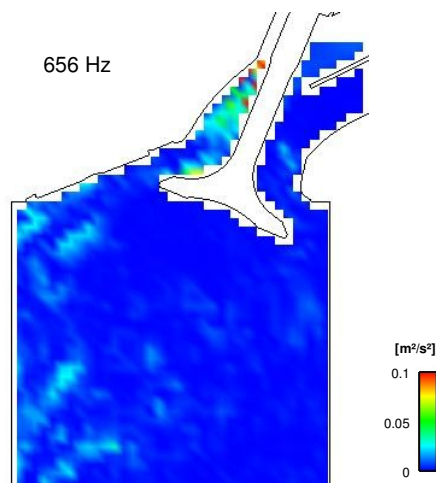


**Figure A.11:** Spatial distribution of the local FFT-signals amplitude in the valve plane, filtered with the previously identified characteristic frequency.



# Lebenslauf

## Persönliche Daten

Name	Olivier Imberdis
Geburtsdatum	28. Dezember 1979
Geburtsort	Verdun, Frankreich
Familienstand	ledig

## Bildungsweg

1994 – 1997	Lycée J.A. Margueritte, Verdun. Baccalauréat (Abitur) mit Auszeichnung Schwerpunkte Physik, Mathematik und Biologie
1997 – 1998	Universität von Metz (Frankreich) 2 Semester Studium – Schwerpunkt in Physik
1998 – 2003	Ingenieur Hochschule ESTACA (Ecole Supérieure des Techniques Aéronautique et Construction Automobile), Paris (Frankreich) Diplome d'Ingénieur - Master of Science (MSc)
2002 – 2003	University of Hertfordshire, Hatfield (Grossbritannien) Master of Science (MSc) in International Automotive Engineering mit Auszeichnung (“with Distinction”)

## Beruflicher Werdegang

2004 – 2007	Volkswagen AG, Konzernforschung, Wolfsburg Doktorand, Bereich Konzeptfahrzeuge – CAE-Verfahren
2007 – 2008	Volkswagen AG, Wolfsburg Internationaler Trainee, verschiedenen Geschäftsbereiche
seit 7/2008	IAV GmbH, Gifhorn / Paris Teil-Projektleiter Hybrid Antriebe, Bereich Fahrwerkelektronik

